94-612

COMMUNICATIONS
RESEARCH
LABORATORY

VALIDATION OF A SEA SWELL MODEL, ANALYSIS OF REAL MULTIPATH DATA, AND TESTING OF THE CHA TECHNIQUE WITH REAL AND SIMULATED DATA

by

T. Lo
L. Lai
J. Litva

Submitted to
Defence Research Establishment Ottawa
Scientific Authority: E. Bosse

Under DSS Contract 052SS.W7714-8-5674

Faculty of Engineering
McMaster University
Hamilton, Ontario
Canada L8S 4K1

April 1990

©Her Majesty The Queen in Right of Canada 1990

VALIDATION OF A SEA SWELL MODEL, ANALYSIS OF REAL MULTIPATH DATA, AND TESTING OF THE CHA TECHNIQUE WITH REAL AND SIMULATED DATA

T. LO, L. LAI, AND J. LITVA
COMMUNICATIONS RESEARCH LABORATORY
McMASTER UNIVERSITY
HAMILTON, ONTARIO

This report applies to
DSS Contract No.: 052SS.W7714-8-5674
"Collection of Data, Validation of Sea Swell Model and
Testing of the Correlation Height Analysis (CHA) Algorithm."

Date of Report: October 1989
Revised in April, 1990

TABLE OF CONTENTS

page

LIST OF FIGURES 4

LIST OF TABLES 10

1. INTRODUCTION 11

2. PROPAGATION AND MULTIPATH PROBLEM 14
   2.1 LOW-LEVEL TROPOSPHERIC PROPAGATION 14
   2.2 MULTIPATH PROBLEM ENCOUNTERED BY A LOW-ANGLE RADAR TRACKING SYSTEM 16
   2.3 MULTIPATH SIGNAL MODEL USED IN THE ANALYSIS . 18

3. SEA SWELL MODEL DEVELOPMENT 20
   3.1 SWELL SURFACE REALIZATION 21
   3.2 FRESNEL REGION 23
   3.3 INCREMENTAL FACET VOLTAGE 24
   3.4 FACET ORIENTATION ADJUSTMENT 27
   3.5 CURVED EARTH GEOMETRY 29
   3.6 ATMOSPHERE FACTOR 31
   3.7 DEPOLARIZATION 31

4. PRELIMINARY PROCESSING OF LAKE ONTARIO DATA . . . 35
   4.1 ENVIRONMENTAL AND METEOROLOGICAL DATA . . . 33
   4.2 FFT BEAMFORMING 36
   4.3 NULL HEIGHT ANALYSIS 37

5. SEA SWELL MODEL SIMULATION RESULTS

AND VALIDATION 40
5.1 PHASOR SIMULATION 40
5.2 INTERFERENCE PATTERN 41
5.3 COHERENT AND INCOHERENT FIELDS 42
5.4 TIME AND FREQUENCY DOMAIN ANALYSIS
OF SCATTERED FIELD 43

6. ANALYSIS AND PROCESSING OF COHERENT
AND DIFFUSE MULTIPATH DATA 45
6.1 ANALYSIS OF COHERENT COMPONENT
BASED ON NULL DEPTH 45
6.2 ESTIMATION OF DIFFUSE POWER 47
6.3 ANALYSIS IN TIME AND FREQUENCY DOMAIN . . . 49

7. PERFORMANCE OF CHA AND RML ALGORITHMS BASED
ON SIMULATED AND MEASURED DATA 53
7.1 PROPAGATION EFFECTS ON CHA 53
7.2 EFFECTS OF HIGH SEA STATES ON CHA 54
7.3 EFFECTS OF SEA SWELLS ON CHA 54
7.4 RML RESULTS BASED
ON LAKE HURON DATA 60

8. CONCLUSIONS AND RECOMMENDATIONS 62

REFERENCES 67
APPENDIX I THE LAKE ONTARIO TRIALS
APPENDIX II TONE REMOVAL

LIST OF FIGURES

Fig. 2.1 Geometry of the direct and indirect rays on a curved earth.

Fig. 3.1 Scattering geometry.

Fig. 3.2 Signal intercepted by a facet.

Fig. 3.3 The fall-off of the curved earth with respect to a flat earth.

Fig. 3.4 Curved earth geometry.

Fig. 3.5 Depolarization of a scattered wave.

Fig. 3.6 General orientation of the direction of propagation with respect to the reflecting plane.

Fig. 4.1 The FFT beamforming result of a typical data set prior to phase correction.

Fig. 4.2 The FFT beamforming result of the same data set used in Fig. 4.1 after phase correction.

Fig. 4.3 A typical profiler trace, dN/dh = –35 Nunit/Km.

Fig. 4.4 A typical profiler trace, dN/dh = –157 Nunit/Km.

Fig. 4.5 A typical profiler trace, dN/dh = –212 Nunit/Km.

Fig. 4.6 Refractivity gradient verse null height for 8.6 GHz signal, comparison of measured and estimated values.

Fig. 4.7 Refractivity gradient verse null height for 9.6 GHz signal, comparison of measured and estimated values.

Fig. 4.8 Angle–of–arrival verse refractivity gradient, comparison of measured and theoretical values.

Fig. 4.9 Comparison of the results of angles–of–arrival based on the FFT beamforming technique and null height information.

Fig. 5.1 Normalized Cornu spiral plot

(a) zero sea–state

(b) high sea–state

Fig. 5.2 Interference patterns of a vertically polarized signal. simulations are verified against real data. $f = 9.6$ GHz, $r = 11.972$ km, $\varepsilon_r = 80$, $\sigma = 4 \frac{mho}{m}$.

(a) $\frac{dN}{dh} = -222 \frac{Nu}{km}$, target height = 11.09 m, centre of aperture = 16.61 m, wave: height(rms) ≈ 0.2 m, length = 28–32 m, period = 10–20 seconds.

(b) $\frac{dN}{dh} = -157 \frac{Nu}{km}$, target height = 11.16 m, centre of aperture = 16.69 m, wave: height(rms) ≈ 0.5 m, length = 4–6 m, period = 10–20 seconds.

(c) $\frac{dN}{dh} = -131 \frac{Nu}{km}$, target height = 11.16 m, centre of aperture = 16.69 m, wave: height(rms) ≈ 0.5 m, length = 80–260 m, period = 5–22 seconds.

Fig. 5.3 Interference pattern with respect to atmospheric refraction. $f = 9.6$ GHz, $r = 11.972$ km, target height = 11.06 m, centre of aperture = 16.08 m, wave: height(p–p) = 0.1 m, length = 100 m, period = 10 m, propagation angle = 0 deg., $\varepsilon_r = 80$, $\sigma = 4 \frac{mho}{m}$.

(a) Amplitude

(b) Phase

Fig. 5.4 Interference pattern versus range of a horizontally polarized signal. $\frac{dN}{dh} = -157 \frac{Nu}{km}$, $f = 9.6$ GHz, $T_x = 10$ m, $R_x = 4.8$ m, $\varepsilon_r = 80$, $\sigma = 4 \frac{mho}{m}$, wave: height(p–p)λ = 0.1 m, length = 100 m, period = 10 m, propagation angle = 0 deg.

(a) Amplitude

(b) Phase

Fig. 5.5 Scattering coefficients versus surface roughness. $\frac{dN}{dh} = -157 \frac{Nu}{km}$, $f = 9.6$ GHz, $T_x = 11.06$ m, $R_x = 16.91$ m, $r = 11.972$ km, $\varepsilon_r = 80$, $\sigma = 4 \frac{mho}{m}$. 60 time samples at $\Delta t = 2$ seconds and 60 waves

superposed with length = 63–325 m, and period = 4.5–25 seconds.

(a) Vertical polarization

(b) Horizontal polarization

Fig. 5.6 Autocorrelation and energy spectral density of similar surface irregularities. $\frac{dN}{dh} = -157 \frac{Nu}{km}$, f = 10.2 GHz, T_x = 15 m, R_x = 9.5 m, r = 4.61 km, ε_r = 80, $\sigma = 4 \frac{mho}{m}$. 501 time samples at Δt = 0.016 second and 60 waves superposed with height(p–p) = 0.1–0.5 m, length = 20.5–50 m, and period = 2.1–4.9 seconds.

(a) Autocorrelation

(b) Energy spectral density

Fig. 5.7 Autocorrelation and energy spectral density of various surface irregularities. $\frac{dN}{dh} = -157 \frac{Nu}{km}$, f = 10.2 GHz, T_x = 15 m, R_x = 9.5 m, r = 4.61 km, ε_r = 80, $\sigma = 4 \frac{mho}{m}$. 501 time samples at Δt = 0.016 second and 60 wave superposed with length = 20.5–50 m, period = 2.1–4.9 seconds. —— height(p–p) = 0.1 m for all 60 waves, – – – height(p–p) = 0.1–0.5 m, –·– height(p–p) = 0.2–1 m.

(a) Autocorrelation

(b) Energy spectral density

Fig. 6.1 Specular reflection coefficient as a function of roughness parameter.

Fig. 6.2 Reflection coefficient as a function of depression angle. (Source: M. Hunter and T. Senior, "Experimental Studies of Sea–Surface effects on Low–Angle Radars," Proc. IEE, vol. 113, no. 11, Nov. 1966.)

Fig. 6.3 The diffuse signal power of vertical polarization as a function of roughness parameter.

Fig. 6.4 The diffuse signal power of horizontal polarization as a function of roughness parameter.

Fig. 6.5 Temporal auto–correlation function and power spectrum derived from a representative data set from Lake Huron trials. Recorded on Nov. 4, 1987, f = 10.2 GHz, horizontal polarization.

Fig. 6.6 Temporal auto–correlation function of backscattering signal. (Source: M. Long, *Radar Reflectivity of Land and Sea*, Artech House, Inc. 1983.)

Fig. 6.7 The power spectrum of the surface waves of the oceans. (Source: B. Kinsman, *Wind Waves*, Prentice–Hall, 1965.)

Fig. 6.8 Temporal auto–correlation function and power spectrum derived from a representative data set from Lake Ontario trials. Recorded on Nov. 17, 1988, f = 9.6 GHz, vertical polarization.

Fig. 6.9 Auto–correlation function and power spectrum derived from a representative data set from Lake Ontario trials. Recorded on Nov. 17, 1988, f = 9.6 GHz, horizontal polarization.

Fig. 6.10 Auto–correlation function and power spectrum derived from a representative data set from Lake Ontario trials. Recorded on Nov. 27,1988, f = 9.6 GHz, vertical polarization.

Fig. 6.11 Temporal cross–correlation function derived from a representative data set from Lake Huron trials. Recorded on Nov. 4, 1987, f = 10.2 and 8.05 GHz, horizontal polarization.

Fig. 6.12 Cross–correlation function derived from a representative data set from Lake Ontario trials. Recorded on Nov. 27,1988, f = 9.6 GHz, vertical polarization.

Fig. 7.1 Target heights given by CHA based on the data recorded on Nov. 25, 1988.

Fig. 7.2 Refractivity gradient measured during the period when the data used for Fig. 7.1 were recorded.

Fig. 7.3 Target heights given by CHA based on the data recorded on Nov. 25,

1988. The missing trace indicates the loss of track.

Fig. 7.4 MES verse SNR.

Fig. 7.5 The density distribution of the noise used in the simulation.

Fig. 7.6 The density distribution of the diffuse signal. f = 9.6 GHz, vertical polarization.

Fig. 7.7 The density distribution of the diffuse signal. f = 9.6 GHz, horizontal polarization.

Fig. 7.8 The density distribution of the diffuse signal. f = 8.6 GHz, vertical polarization.

Fig. 7.9 The density distribution of the diffuse signal. f = 8.6 GHz, horizontal polarization.

Fig. 7.10 The amplitude distribution of the interference pattern as a function of time. Swell propagation angle = 90 degrees.

Fig. 7.11 Target heights given by the CHA algorithm under single sea swell condition.

Fig. 7.12 The amplitude distribution of the interference pattern as a function of time. Swell propagation angle = 0 degrees.

Fig. 7.13 The amplitude distribution of the interference pattern as a function of time. Swell propagation angle = 45 degrees.

Fig. 7.14 The amplitude distribution of the interference pattern as a function of time. Swell propagation angle = 75 degrees.

Fig. 7.15 The amplitude distribution of the interference pattern as a function of time. Swell propagation angle = 85 degrees.

Fig. 7.16 Target heights given by the CHA algorithm under two sea swell condition.

Fig. 7.17 Target heights given by the RML algorithm based on the Lake huron data. Number of frequencies = 2.

Fig. 7.18 Target heights given by the RML algorithm based on the Lake huron data. Number of frequencies = 4.

Fig. 7.19 Target heights given by the RML algorithm based on the Lake huron data. Number of frequencies = 6.

Fig. 7.20 Relative height displacements, showing that the estimates given by using six frequencies are closer to the actual ones.

LIST OF TABLES

Table 7.1 Means and variances of the estimated target heights.

Table 7.2 The Lake Huron data files used for the estimation of target heights.

1. INTRODUCTION

Mathematical modelling and propagation data measurements of a continuous wave (CW) signal over a water path have been carried out by Defense Research Establishment Ottawa (DREO) in conjunction with McMaster University, so as to study the multipath phenomena and their effects on the performance of tracking radars operating against low flying objects and, eventually, to seek for solutions to improve their presently unsatisfactory performance. The mathematical model, which is originated from sea swell modelling, is developed to study the mechanism of the forward scattering from rough sea surfaces or/and sea swells. It is based on the theory of representing a sea surface by a continuum of aperture antennas. Simulations were carried out and results were satisfactory. Two multipath measurements were conducted in the past two years. One was over Lake Huron in November, 1987 and the other over Lake Ontario in November, 1988.

The objective of the trials is to investigate the performance of the Correlation Height Analysis (CHA) technique [1] affected by

- i) high sea states and surface roughness,
- ii) the effects of the sea swells, and
- iii) the changing propagation condition caused by the varying refraction gradient.

With regard to these items, a number of issues have been addressed in this report. They are:

1) the validation of the sea swell model by comparing the simulated data with real data,
2) the determination of the specular reflection coefficient by evaluating the power level of the coherent component from real data,

3) the determination of the diffuse power levels under various sea roughness parameters based on real data,
4) the determination of the characteristics of the diffuse component by the analyses of real multipath data in time and frequency domains,
5) the evaluation of the performance of the CHA technique using real data and simulated data, and
6) the evaluation of the performance of the RML algorithm technique using real data.

Two bases of measured data have been used in the analysis. One was obtained using the 32-element array developed in the Communications Research Laboratory (CRL), McMaster University. The other data base was obtained using the profiler provided by DREO. A detailed description of the Lake Huron measurements was given in the report which applied to DSS Contract W7714-7-5320. The Lake Ontario measurements are described in Appendix I.

This report consists of seven chapters. Following Chapter 1, the introduction, Chapter 2 gives a brief discussion of the propagation multipath problem. The theoretical background of the mathematical model and its development are described in Chapter 3. In Chapter 4 are given the results discussions based on the preliminary processing of the Lake Ontario data. In Chapter 5 are presented the simulation results from the sea swell model and the validation of the model by comparing them with the measured data. The analyses and processing of the coherent and diffuse signals are carried out in Chapter 4 based on both the Lake Huron and the Lake Ontario data. Chapter 7 gives the testing results of the CHA and RML algorithms using simulated and measured data. The report ends with the conclusions and recommendations given in Chapter 8.

2. PROPAGATION AND MULTIPATH PROBLEM

2.1 LOW-LEVEL TROPOSPHERIC PROPAGATION

When an electromagnetic wave propagates in the earth's atmosphere, it is generally refracted due to variation with altitude of the velocity of propagation, or the index of the refraction, which is defined as the ratio of the velocity of propagation in free space to that in the medium of interest. The major detrimental effect of refraction for low angle radar targets is the introduction of a discrepancy between the apparent and actual elevation angles of the target.

At microwave frequencies, the index of refraction, denoted by n, for air containing water vapor is

$$(n-1)10^6 = N = 77.6\,\frac{P}{T} + 3.73 \times 10^5\,\frac{e}{T^2} \tag{2.1}$$

where P = barometric pressure in millibars,
e = partial pressure of water vapor in millibars, and
T = absolute temperature in K.

The scaled-up parameter N is usually called refractivity. If, as in our case, the water vapor content of the air is measured in terms of relative humidity (RH) the partial pressure e is given by

$$e = e_s \times \mathrm{RH} \tag{2.2}$$

where [2]

$$e_s = 6.105\,\exp\left(25\frac{T-273}{T} - 5.2\,\ln\frac{T}{273}\right) \tag{2.3}$$

Since the change in refractivity near the earth's surface is of interest, an approximate relationship is given by [3],

$$\Delta N = -1.27\Delta T + 4.50\Delta e + 0.27\Delta P. \tag{2.4}$$

The curvature of the propagation path followed by a signal may be expressed as a function of the change in refractivity with respect to height. It is customary in practice to treat the ray paths in troposphere as straight lines. This is accomplished by replacing the earth with an imaginary earth whose effective radius is

$$R_e = \kappa R \tag{2.5}$$

where R is the radius of the real earth and the factor κ is given by

$$\kappa = (1 + 6.37\times10^{-3} \frac{dN}{dh})^{-1} \tag{2.6}$$

where dN/dh is the vertical gradient of refractivity. According to the values assumed by dN/dh, the propagation regimes can be defined as [3]

$$\frac{dN}{dh} = \begin{cases} > 0 & \text{(N unit/km)} \quad \text{subrefractive} \\ > -79 \text{ and } < 0 & \text{normal} \\ > -157 \text{ and } < -79 & \text{superrefractive} \\ < -157 & \text{ducting.} \end{cases} \tag{2.7}$$

Therefore, a ray with a sufficiently small initial elevation angle is refracted downward or upward (depending on the sign of dN/dh) with a curvature proportional to the rate of change in the refractivity with respect to elevation. In practice, when the propagation regime is defined as "superrefractive" or "ducting", sizable discrepancy may occur between the actual height of a target and its apparent height, thereby causing the performance of a low-angle tracking radar to be seriously degraded.

2.2 MULTIPATH PROBLEM ENCOUNTERED BY A LOW-ANGLE RADAR TRACKING SYSTEM

When a plane wave propagates from a source at a low elevation angle to an antenna, say the receiving antenna of a low-angle radar tracking system, the output of the antenna may consist of two signal components. One signal propagates along the direct path between the source and the antenna, and the other arrives via reflections from the earth's surface. The earth reflections can further be divided into two classes: specular and diffuse. This distinction, which is somewhat artificial, has been used by workers in the field to provide insight into the nature of multipath effects. The specular component, which is composed of only one or two strong reflected rays, is usually referred to as the coherent part of the reflected signal. The diffuse component, which results from scattering from the irregular surface, is known as the incoherent part of the reflected signal. In principle, a low-angle tracking radar will encounter both specular and diffuse multipath, which will introduce tracking errors to the system.

2.2.1 SPECULAR MULTIPATH

The geometry appropriate to the specular component of the multipath signal where it is reflected from a curved earth is given in Fig. 2.1. The source and the receiving antenna are separated by the range d. The point of reflection, indicated by P, determines d_1, d_2 and the grazing angle Ψ. h_1 is the height of the centre of the antenna aperture and h_2 is the height of the source. The angles–of–arrival for the direct and specular signals are θ_d and θ_s, respectively, and their expressions are given as [3]

$$\theta_d = \tan^{-1} \left[\frac{h_2 - \frac{d^2}{R_e} - h_1}{d} \right], \tag{2.8}$$

$$\theta_s = \tan^{-1} \left[\frac{h_1 + \frac{d_1^2}{R_e}}{d_1} \right], \tag{2.9}$$

where $d_1 = \frac{d}{2} + p \cos\left[\frac{\Psi + \pi}{2} \right]$,

$p = 2 \left\{ \frac{1}{3} \left[R_e (h_1 + h_2) + (\frac{d}{2})^2 \right] \right\}^{\frac{1}{2}}$, and

$\Psi = \cos^{-1} \left\{ \frac{1}{p^3} \left[2 \, Re \, (h_1 - h_2) \, d \right] \right\}$, for $h_1 \leq h_2$.

The specular signal is coherent with the direct signal in phase because the difference between the paths via which they propagate is constant. Therefore, the specular reflection is usually quantified by the complex specular reflection coefficient ρ_s, which is defined as the ratio of the magnitude of the specular signal to that of the direct signal. ρ_s depends on the reflection and absorption characteristics of the reflecting surface and the incident angle at which the signal impinge upon the reflecting surface.

2.2.2 DIFFUSE MULTIPATH

Energy from a source at low angle which is not absorbed or reflected specularly will be scattered at other angles due to the roughness of the sea surface. Since diffuse power is reflected by the surface irregularities in a random fashion, the reflections will reach the radar antenna incoherently and cause the received signal to take on noise–like characteristics. As one would expect, the incoherence of the diffuse multipath depends on the degree of the roughness of the surface. Since high sea states increase the diffuse component and reduce the level of the specular component, it follows that the performance of tracking techniques which solely rely on the amplitude and phase information provided by the specular multipath signal may be degraded to a marked extent.

2.3 MULTIPATH SIGNAL MODEL USED IN THE ANALYSIS

In formulating the signal model, we consider a linear array of N equally-spaced elements separated by a displacement *d*. If a signal arrives at angle θ_d with respect to the array boresight, the signal s received by the n^{th} element at time *t* is, under the multipath condition,

$$s(n,\ t) = s_d(n,\ t) + r_s(n,\ t) + r_d(n,\ t) + \eta(n,\ t) \tag{2.10}$$

where $s_d(n,\ t)$ = direct signal,

$r_s(n,\ t)$ = specular multipath return,

$r_d(n,\ t)$ = diffuse multipath return, and

$\eta(n,\ t)$ = additive Gaussian white noise of the element.

For simplicity, we neglect the noise for the time being. In the case of a smooth sea surface or low sea states, the diffuse portion of the received signal is negligible. Thus the received signal consists only of the direct signal and the specular multipath and Eq.(2.10) becomes

$$\begin{aligned} s(n,\ t) &= s_d(n,\ t) + r_s(n,\ t) \\ &= e^{j(\omega t + knd\sin\theta_d)} + \rho_s\, e^{j(\omega t + knd\sin\theta_s)} \\ &= [e^{jknd\sin\theta_d} + \rho_s\, e^{jknd\sin\theta_s}]\, e^{j\omega t} \end{aligned} \tag{2.11}$$

where θ_s is the angle–of–arrival of the specular signal, $k = \frac{2\pi}{\lambda}$, and ρ_s is the complex specular reflection coefficient. Since only the terms in the square brackets of Eq.(2.11) is of interest to us, the term $e^{j\omega t}$ can be discarded, giving

$$s(n) = e^{jknd\sin\theta_d} + \rho_s\, e^{jknd\sin\theta_s} \tag{2.12}$$

The amplitude of the received signal can be expressed as

$$|s(n)| = 1+|\rho_s|^2+2|\rho_s|\cos[knd(\sin\theta_d-\sin\theta_s)+\arg(\rho_s)] \tag{2.13}$$

where $\arg(\rho_s)$ is the phase of ρ_s and takes on the value of π in the case of low–angle propagation. If the term in the square bracket results in zero, $|s(n)|$ becomes maximum, which is known as a constructive effect. On the other hand, if the term takes on the value of π, $|s(n)|$ assumes the minimum value, which is , of course, known as a destructive effect.

In the case of a rough sea surface or high sea states, the diffuse portion of the received signal will be significant. The diffuse field is characterized as a continuum of reflections from different directions. Therefore, the diffuse signal $r_d(n,t)$ is not deterministic. However, its characteristics can be usually determined by using its first and second order statistics.

3 SEA SWELL MODEL DEVELOPMENT

The surface-reflected signal may be thought of as originating from the image of the target mirrored by the earth surface. That is, one assumes a Fresnel model for the reflected signal. In practice, the model is less than satisfactory if the surface is not perfectly flat. The algorithm derived by White and Gery [8] is essentially a two-dimensional model which considers variations in the scattering region to be limited only to one dimension. It is not applicable to a physical swell because of the limitation of the model to one-dimensional variation of the surface in the scattering region.

It is the purpose of this report to construct a model to describe the multipath scattering effect due to time-varying sea swells. The technique that is developed in this report is that of representing the facets by equivalent aperture antennas. Every facet has the same mathematical expression for radiation pattern but its position and surface curvature dictates its beam direction. It is assumed that no more than one scatterer can occupy any one cell at any time. A description of the model will be presented in the following sections. It will be accompanied by a discussion of a mathematical representation of a swell surface, as well as discussions of incremental facet voltages, facet orientations, curved earth geometry, atmospheric refraction and signal depolarization. It is then followed by simulation results, some of which are verified using experimental data which were obtained from scattering measurements on Lake Ontario.

To start, we consider the simple flat earth model illustrated in Figure 3.1, where h_1 and h_2 are, respectively, the heights of the receiver R_x and the transmitter T_x, which are separated by a distance r. In the figure, S is assumed to be the region illuminated by the energy source. As a result of the illumination, currents are induced on the surface which radiate in all directions (Huygens' Principle). Any incremental surface on S, such as the small rectangle, is assumed to be capable of capturing energy from the transmitter and re-radiating it in the direction of the receiver. The receiver related geometrical-parameters that are required for describing scattering by the elemental area, positioned at (x,y), are the direct signal path length r_1, elevation angle α_1, and azimuthal angle β_1. The corresponding transmitter related parameters are respectively, r_2, α_2, and β_2. The description of the approach that is used in modelling scattering from sea swells is given in the next section.

3.1 SWELL SURFACE REALIZATION

The surface of the ocean is never at rest. Its complex and varied movements may at times appear chaotic and unpredictable however; there is a pattern [5] to all this. Consider waves in deep water only, the three wave shapes that have been used for various theoretical analyses are the sine wave, the trochoid, and the cycloid. Although none of these fits the real wave under all circumstances, the sine wave more closely resembles the form of swells, the long waves with round tops and relatively low height that run out of the storm area and travel thousands of miles before breaking onshore. In addition to its uniform height and wavelength, it has a wave period between 10 to 30 seconds [6] and propagates in a constant direction and at a constant speed.

A random sea swell surface can be simulated by superposing a large number of sinusoidal surface waves with varying amplitudes, wave periods, wavelengths, propagation angles, and phase factors. The height of any incremental rectangle or so called facet is assumed to be described by the altitude of its centre above the mean value of the sea level. For an arbitrary facet with its centre coordinate (x_m,y_n), its wave height at any time t can be expressed as

$$z_{mn}(x_m,y_n,t) = \sum_{j=1}^{k} A_j \cos\left[\frac{2\pi}{T_j}t - \frac{2\pi}{L_j}(x_m\cos\theta_j + y_n\sin\theta_j) + \phi_j\right] \qquad (3.1)$$

where A_j, T_j, L_j, θ_j, and ϕ_j are the wave amplitude, the period, the wavelength, the propagation angle with respect to the positive x–axis, and the phase factor of the j–th wave, respectively. Initially, all of the facets will be of equal size. due to the perturbation of the surface, the facet sizes will no longer all be identical because their sizes will vary in a monotonic fashion with their tilt. The slopes of the facets are required in order to approximate the effective facet area and perform coordinate rotations. The slope angles can be defined as

$$\begin{aligned} \delta_x &= \tan^{-1}\left(\frac{\partial z_{mn}}{\partial x}\right) \\ \delta_y &= \tan^{-1}\left(\frac{\partial z_{mn}}{\partial y}\right) \end{aligned} \qquad (3.2)$$

The effective facet is then approximated to be a patch in rectangular shape with an area given by

$$\Delta A' = \Delta x' \cdot \Delta y' \simeq \left(\frac{\Delta x}{\cos\delta_x}\right)\left(\frac{\Delta y}{\cos\delta_y}\right) \qquad (3.3)$$

Equation (3.3) provides a satisfactory estimation of facet area if it is a plane surface. Inaccuracy may arise, however, when a curved or a perturbed surface is considered.

3.2 FRESNEL REGION

The area illuminated by the energy source in the x–y plane will be defined in this section. A family of ellipses [7] can be constructed corresponding to the path length difference between the direct and the indirect rays. The average phase of the radiation from each zone bounded by adjacent ellipses differs from that of the neighboring zone by just π; that is, the elementary waves from successive zones are in phase opposition. These half–period zones are called the Fresnel zones but are different from those defined in physical optics. The usual Fresnel zones are constructed in such a way that the consequent contributions of successive zones almost completely cancel, leaving the radiation from approximately half the area of the first zone as the end product. In the present instance, however, it is not evident that the contribution of the first zone alone predominates the total contributions of the entire surface.

The first Fresnel zone, in general, is considered to be the most significant area for reflection and diffraction, and is widely adopted by many researchers and investigators. However, the first six Fresnel zones are used in order to include the edge scattering effect that the first Fresnel region fails to account for. Its size depends mainly on the grazing angle, which in turn is a function of the height of the receiver and the transmitter geometry, as well as the separation between them. The smaller the grazing angle, the more elongated the elliptic zone. According to Kerr [7], the bounds of the n–th Fresnel zone, with origin at the datum level of the receiver axis, are given by

$$x_{\pm} \simeq r\left[1 - \frac{P_1 \pm P_2}{2P_3}\right] \qquad (3.4)$$

$$y_{\pm} \simeq \pm \frac{P_2}{2} \cdot \sqrt{\frac{n\lambda r}{P_3}}$$

with

$$P_1 = 1 + \frac{2h_2(h_1+h_2)}{\lambda r}$$

$$P_2 = \sqrt{1 + \frac{2\delta_0}{n\lambda}} \qquad (3.5)$$

$$P_3 = 1 + \frac{(h_1+h_2)^2}{n\lambda r}$$

$$\delta_0 = \frac{2h_1 h_2}{r}$$

where x_+ and x_- are the two ends along the major axis towards the receiver and transmitter, respectively; y_+ and y_- are the corresponding upper and lower bounds of the minor axis, δ_0 is the approximate path difference via the geometrical point of reflection. For the purpose of segmentation and without altering the essential reflecting area, the first six Fresnel regions are replaced by a rectangular area, S, as shown in Fig. 3.1.

3.3 INCREMENTAL FACET VOLTAGE

The illuminated region is then divided into a two-dimensional facet array of rectangular elemental scatterers. Each facet is represented by an equivalent aperture radiator [8,9] and its position is described by its x and y coordinates. The dimension of the facet is usually much less than the wavelength of the sea swell so as to be consistent with the assumption of one scatterer per cell at any time. Each cell intercepts the transmitted signal from the source and re-radiates some of the energy towards the receiving antenna. Assuming that the source is an isotropic radiator, the incident power density becomes

$$P_d = \frac{P_t}{4\pi R_d^2} \tag{3.6}$$

where P_t is the transmitted power and R_d is the direct path length. Consider a horizontally positioned patch of size Δx by Δy being illuminated by an incident signal at a grazing angle α_2, as shown in Figure 3.2, the power re-radiated by the patch can be expressed as

$$P_{rad} = \frac{|\Gamma|^2 \cdot \Delta A \cdot P_t}{4\pi R_2^2} \tag{3.7}$$

where $|\Gamma|$ is the modules of the reflection coefficient, ΔA ($=\Delta x \Delta y \sin\alpha_2$) is the effective differential intercepting area, and R_2 is the direct path length between the transmitter and the facet. The power density observed by the receiver is given by

$$P_{dr} = \frac{P_{rad}}{4\pi R_1^2} \cdot G_p \tag{3.8}$$

where R_1 is the direct path length between the facet and the receiver. G_p [10,11] is the maximum power gain of the facet along the patch-receiver line-of-sight. The product defines the maximum power gain as

$$G_p = \frac{j4\pi\Delta A}{(0.886\lambda)^2}\left[\frac{\sin(0.5\beta L_x u)}{(0.5\beta L_x u)}\right]\left[\frac{\sin(0.5\beta L_y v)}{(0.5\beta L_y v)}\right] \tag{3.9}$$

where β ($=2\pi/\lambda$) is the frees pace wavenumber, L_x ($=\Delta x \sin\alpha_2$) and L_y ($=\Delta y$) are the effective dimensions of the patch, and u and v ($u=\sin\theta\cos\phi$, $v=\sin\theta\sin\phi$) are functions of the angular displacement of the facet from a flat plane. A discussion of the facet geometry is given in section 3.4. In order to simplify the mathematical formulation, an isotropic receiving antenna is assumed. The incremental power that actually enters the receiving antenna is the product of the incident power density and the effective capture area in the direction of arrival which can be written as

$$\Delta P = \frac{\lambda 2}{4\pi} \cdot P_{dr} \tag{3.10}$$

If the antenna is matched to a 1-ohm resistive load, this will give rise to a voltage increment, which is denoted by

$$\Delta V_{nm} = \sqrt{\Delta P} \tag{3.11}$$

where the subscript nm signifies the two dimensional facet array due to surface segmentation. The phase delay due to the path difference between the direct signal and the facet-reflected signal can be defined to be

$$\Delta\phi_{nm} = -\beta(R_1+R_2-R_d) \tag{3.12}$$

The total multipath return voltage is equal to the phasor sum of all the incremental voltages over the entire illuminated surface and is given by

$$V_r = \sum_n \sum_m \Delta V_{nm} \cdot D_{nm} \cdot \Gamma_{nm} \cdot e^{j\Delta\phi_{nm}} \tag{3.13}$$

where D_{nm} is the local divergence factor and Γ_{nm} is a complex quantity which consists of local Fresnel reflection coefficient, as well as depolarization parameters. Both D_{nm} and Γ_{nm} will be addressed separately in the upcoming sections.

3.4 FACET ORIENTATION ADJUSTMENT

At this point, the formulation in (3.9) has not been developed to fully represent the physical situation of the scattering mechanism. Information on how the reflected energy of the facet is related to the receiving antenna is required. In other words, the facet's geometrical profile, its tilt and orientation, needs to be considered. It is desired to rotate the original facet coordinate system (x-y-z) so that it coincides with the system which describes the beam direction. In that way, the patch gain along the receiver's line-of-sight can be calculated.

The overall coordinate rotation is highlighted by the matrix expression in (3.14) which is consisted of four steps. Starting from the rightmost matrix expression, the facet is rotated by an angle of δ_x with respect to the y-axis in the first matrix and by that of δ_y with respect to the x-axis in the second matrix. These two coordinate rotations are focused on the tilt of the facet with respect to the x-y plane. By doing so, the tilted facet is thus related to its hypothetical untilted counterpart in terms of the two operations. The last two matrices are emphasised on relating the beam direction to the transmitting source. The facet is rotated with respect to the z-axis and y-axis by an angle of β_2 and α_2, respectively. In this case, the actual captured energy can be calculated in terms of the orientation of the facet.

$$\begin{bmatrix} u' \\ v' \\ w' \end{bmatrix} = \begin{bmatrix} \sin\alpha_2 & 0 & -\cos\alpha_2 \\ 0 & 1 & 0 \\ \cos\alpha_2 & 0 & \sin\alpha_2 \end{bmatrix} \begin{bmatrix} \cos\beta_2 & -\sin\beta_2 & 0 \\ \sin\beta_2 & \cos\beta_2 & 0 \\ 0 & 0 & 1 \end{bmatrix} \cdot$$

$$\begin{bmatrix} 1 & 0 & 0 \\ 0 & \cos\delta_y & \sin\delta_y \\ 0 & -\sin\delta_y & \cos\delta_y \end{bmatrix} \begin{bmatrix} \cos\delta_x & 0 & \sin\delta_x \\ 0 & 1 & 0 \\ -\sin\delta_x & 0 & \cos\delta_x \end{bmatrix} \begin{bmatrix} u \\ v \\ w \end{bmatrix} \quad (3.14)$$

The formulation of (3.14) relates the angular displacement of the beam direction of the facet to the energy incident direction only. It is necessary to establish the relationship between the incident and the reflected beam direction, as well as the receiving antenna. By negating the elements of the first two columns of the product of the matrix multiplication in (3.14), the angular displacement of the reflected beam is obtained. To complete the formulation, the direction cosines of the facet–receiver vector $[u, v, w]^T$ in (3.14) can be written as

$$\begin{aligned} u &= \cos\alpha_1\cos(\pi+\beta_1) \\ v &= \cos\alpha_1\sin(\pi+\beta_1) \qquad (3.15) \\ w &= \sin\alpha_1 \end{aligned}$$

The direction cosines u and v in (3.9) are required to be replaced by u' and v' as derived in (3.14). It is well known that matrix multiplications are not commutative and the technique of coordinate rotation appears to be in jeopardy, if the result depends on the order in which the transformations are applied. It has been shown by Goldstein [12], however, that the order in which the sequence of operations carried out is unimportant in the case of infinitesimal rotations, that is when δ_x, δ_y, α_2, and β_2 may be considered to be small.

For a low–level target, α_2 is always small as the range between the receiving antenna and the source is usually long enough. Since the major axis of the illuminated Fresnel region is much larger than its minor axis, β_2 is small as well. It is believed that coordinate rotation error due to α_2 and β_2 is insignificant. From the simulations, a rapid change was observed in the interference pattern when the steepness (a ratio of the peak to peak waveheight to its wavelength) of the surface was increased to 0.03. This implied that δ_x and δ_y should be no more than 3.43 degree before exceeding the limit of the coordinate rotation method. However, this is only a crude evaluation. Unsatisfactory results may also due to the facet area approximation as well. A more detailed study is needed in order to determine the accuracy of the method.

3.5 CURVED EARTH GEOMETRY

In upgrading the geometry used by our model from a flat earth approximation to a full curved earth geometry, there are two main effects that must be taken into consideration. Firstly, the phase difference between the direct and the indirect signals must be modified. The path length difference δ_0 in (3.5) is no longer valid and must be changed to account for the earth's curvature. Second, reflection from a curved earth is accompanied by a divergence of the ray bundles, thereby resulting in a reduction in the power of the reflected signal.

The sagitta equation [9,13] from physical optics is used to approximate the fall–off of the curved earth with respect to a flat earth. The fall–off (Δh), as shown in Figure 3.3, is the difference in the distance of a point on the flat earth from that of the corresponding point on a curved earth, and with respect to the centre of the earth, i.e.

$$\Delta h \simeq \frac{r^2}{2a} \qquad (3.16)$$

where r is the horizontal range of the receiver and the transmitter and a is the true earth radius. Due to the earth's surface curvature, the actual receiver and target heights become diminished, by a difference of Δh_1 and Δh_2, respectively, when viewed by a facet situated within the illuminated region. This is illustrated by Figure 3.4. The corresponding geometrical parameters α_1, α_2, R_1, and R_2, which can be easily deduced from the flat earth model, are varying accordingly as indicated in Figure 3.4 as well. They are being re-defined as

$$\begin{aligned}
\alpha_1' &= \tan^{-1}\left[\frac{h_1 - \Delta h_1 - z_{mn}}{\sqrt{(x_m^2 + y_n^2)}}\right] \\
\alpha_2' &= \tan^{-1}\left[\frac{h_2 - \Delta h_2 - z_{mn}}{\sqrt{((r - x_m)^2 + y_n^2)}}\right] \\
R_1' &= \sqrt{x_m^2 + y_n^2 + (h_1 + \Delta h_1 - z_{mn})^2} \\
R_2' &= \sqrt{(r - x_m)^2 + y_n^2 + (h_2 - \Delta h_3 - z_{mn})^2}
\end{aligned} \tag{3.17}$$

where

$$\begin{aligned}
\Delta h_1 &= \frac{x_m^2}{2a} \\
\Delta h_2 &= \frac{(r - x_m)^2}{2a} \\
\Delta h_3 &= \frac{r^2}{2a} - \Delta h_1
\end{aligned} \tag{3.18}$$

A divergence factor [14] is adopted to include the effect that the earth's curvature diminishes the power of the reflected signal. It is obtained by comparing the energy flux in the neighborhood of the receiver to the energy flux that would be received in free space at a distance R_1+R_2 and is given by

$$D_{nm} = \sqrt{\left\{1 + \frac{2R_1R_2}{a(R_1+R_2)\sin\alpha_2}\right\} \cdot \left\{1 + \frac{2R_1R_2}{a(R_1+R_2)}\right\}} \qquad (3.19)$$

where α_2 is the grazing angle, i.e. the angle subtended between the incident ray and the point of specular reflection, with respect to the earth surface. The definition of grazing angle does not include the effect of local surface roughness since it uses the smooth earth as its reference. The effect of surface roughness is accounted for through the mechanism of rotation of the facets, discussed earlier, to form an arbitrary rough surface.

3.6 ATMOSPHERIC FACTOR

The foregoing equations were derived on the assumption that both the direct and the scattered rays propagate in straight lines with constant velocity. In reality, none of these conditions hold. As discussed in Section 2.1, the propagation ray path of a microwave signal is bent due to different refraction coefficients at different elevations in the atmosphere. The introduction of κ factor is one way to compensate for the path curvature. That is,

$$a_e = a\left[\ 1 + 0.00637\frac{dN}{dh}\ \right]^{-1} \qquad (3.20)$$

We include tropospheric refraction in our modelling by replacing the true value of earth's radius by an effective earth radius (a_e) subject to the factor dN/dh.

3.7 DEPOLARIZATION

Whenever linearly polarized waves are reflected from a surface where normal does not lie in the plane of incidence, they are depolarized into vertical and horizontal components. Depolarization always occurs when the reflecting surface is tilted simultaneously about both the x and y axes. The tangent plane approximation [14,15] is a standard method for relating incident and scattered fields at a surface. The approximation is based on the assumption that the current flowing at each point on a surface is the same as it would flow (at each point) if the surface were flat and tangent to the actual surface. In order to represent scattering from a surface, scattered fields are constructed by adding the complex fields with phase distributions determined by the distances of the individual surface elements from the receiving antenna. Unfortunately, the technique is restricted to surfaces having radii of curvature large compared to a wavelength and the direction of reflection has to be known in order to evaluate the scattering parameters. Due to the simplicity of the tangent plane approximation, it is used, with constraints, to test the applicability of the model. In fact, the scattering parameters are believed and observed to be small because of the smooth surface assumption.

Consider an electromagnetic wave E_2, which is resolved into its vertical (E_2^-) and horizontal (E_2^+) components, striking a tilted surface at an angle of incident θ_2 ($=-\alpha_2+\frac{\pi}{2}$) and scattering into the direction [θ_1 ($=-\alpha_1+\frac{\pi}{2}$) and β_3 ($=|\beta_1|+|\beta_2|$)], as illustrated in Figure 3.5. The notation used here is consistent with that used previously. Following Mitzner [15] while at the same time referring to our coordinate system, the incident and reflected fields can be related linearly in a linear medium by

$$\begin{bmatrix} E_1^- \\ E_1^+ \end{bmatrix} = \begin{bmatrix} \Gamma_c^- & \Gamma_x^- \\ \Gamma_x^+ & \Gamma_c^+ \end{bmatrix} \begin{bmatrix} E_2^- \\ E_2^+ \end{bmatrix} \quad (3.21)$$

where E_1 and E_2 are, respectively, the reflected and the incident fields. The matrix elements Γ_c^-, Γ_x^-, Γ_c^+, Γ_x^+ are local co-polarization (with subscript $_c$) and cross-polarization (with subscript $_x$) scattering parameters due to the incident wave depolarization and are defined as follows:

$$\begin{aligned}\Gamma_c^- &= R^-\cos\xi_1\cos\xi_2 + R^+\sin\xi_1\sin\xi_2\\ \Gamma_c^+ &= R^-\sin\xi_1\sin\xi_2 + R^+\cos\xi_1\cos\xi_2\\ \Gamma_x^- &= R^-\cos\xi_1\sin\xi_2 - R^+\sin\xi_1\cos\xi_2\\ \Gamma_x^+ &= R^-\sin\xi_1\cos\xi_2 - R^+\cos\xi_1\sin\xi_2\end{aligned} \qquad (3.22)$$

where R^- and R^+ are the horizontal and vertical Fresnel coefficients [14], respectively. ξ_2 (ξ_1), as illustrated by Figure 3.6, is the acute angle between the unit vector t along the intersection of the reflection plane with the wave fronts and the unit vector e_2 (e_1) normal to the incident plane (reflection plane). The Fresnel coefficients are given by

$$\begin{aligned}R^- &= \frac{\cos\upsilon - \sqrt{(Y^2-\sin^2\upsilon)}}{\cos\upsilon + \sqrt{(Y^2-\sin^2\upsilon)}}\\ R^+ &= \frac{Y^2\cos\upsilon - \sqrt{(Y^2-\sin^2\upsilon)}}{Y^2\cos\upsilon + \sqrt{(Y^2-\sin^2\upsilon)}}\end{aligned} \qquad (3.23)$$

with

$$\begin{aligned}Y^2 &= \frac{\varepsilon_r}{\mu_r}\\ \varepsilon_r &= \frac{\varepsilon}{\varepsilon_0} + i60\lambda\sigma\\ \mu_r &= \frac{\mu}{\mu_0}\end{aligned} \qquad (3.24)$$

and

$$\begin{aligned}
\sin\xi_1 &= -\,\frac{\sin\theta_2\sin\beta_3}{\sin\chi} \\
\cos\xi_1 &= \frac{\sin\theta_1\cos\theta_2 + \cos\theta_1\sin\theta_2\cos\beta_3}{\sin\chi} \\
\sin\xi_2 &= -\,\frac{\sin\theta_1\sin\beta_3}{\sin\chi} \\
\cos\xi_2 &= \frac{\cos\theta_1\sin\theta_2 + \sin\theta_1\cos\theta_2\cos\beta_3}{\sin\chi}
\end{aligned} \tag{3.25}$$

with

$$\sin^2\chi = 1 - (\cos\theta_1\cos\theta_2 - \sin\theta_1\sin\theta_2\cos\beta_3)^2 \tag{3.26}$$

where υ is the local angle of incidence, subtended by the incident wave vector and the local normal of the surface, Y is the normalized admittance, ε_r and μ_r are the relative permittivity and permeability, respectively; ε, μ, and σ are the dielectric constant, permeability, and conductivity of the surface, respectively; and λ is the operating wavelength. Moreover, χ is twice the true angle of incidence or reflection.

At this point, the sea swell model has been basically formulated and almost all the possible factors have been incorporated into the model. Simulation results will be presented in Chapter 5.

4. PRELIMINARY PROCESSING OF THE LAKE ONTARIO DATA

4.1 ENVIRONMENTAL AND METEOROLOGICAL DATA

There were two environmental and meteorological data bases which were collected during the experiment. The first base includes hourly records of (1) water level, (2) air temperature, (3) vapour pressure, (4) water temperature, and (5) wind speed and direction. This data base was provided by the Canadian Centre for Inland Waters (CCIW) in Burlington, Ontario. These measurements were made at the Burlington Pier Station, which was located several hundreds of meters away from the lake shore. Thus, these meteorological data may closely represent the conditions over the transmitting path. Sea states or the rms roughness parameter were derived from the wind speed, duration, and direction data by using the Parametric Hindcasting by the Effective Wave (PHEW) procedure [16]. All these environmental data provide the information which can be correlated with the electromagnetic field data to give insights into the multipath phenomenon.

The second data base was recorded by the meteorological sensors mounted on the profiler trolley. It includes (1) temperature, (2) humidity, and (3) atmospheric pressure at different heights. This data base can be used to estimate the refractivity of the propagation medium. As given earlier, the refractivity, N, of air mixed with water vapor is

$$N = 77.6 \frac{P}{T} + 3.73 \times 10^5 \frac{e}{T^2} \tag{4.1}$$

Since P, T, and e are changing with the elevation h, N is in turn a function of elevation. In Fig. E1 through E12 are depicted the representative results of the refractivity gradient with respect to the profiler height for different propagation conditions during the measurement. The profiler height at zero is corresponding to 7.5 m above the water level. Each star in these figures indicates an individual value of the refractivity at a specific height, whereas the continuous straight line represents the first order regression estimation of the refractivity. The slope of the straight line gives the refractivity gradient, $\frac{dN}{dh}$, with respect to the profiler height. The use of the linear regression for the approximation of the refractivity gradient is based upon the assumption that the refractivity gradient is a linear function of elevation. In some cases, this linearity holds, as illustrated in Figs. E3, E4, E5, E6, and E9. However, in many cases, the linearity is not obvious or does not hold at all. In Fig. E1, E2, and E7 the gradient behave irregularly, whereas in Fig. E11 the gradient is not linear at all. Furthermore, the parameters related to the refractivity were measured at the receiver site. They might not truly represent the propagation conditions along the transmitting path. This may explain the inconsistence between the measured and estimated gradient obtained from the information provided by the null positions of the interference patterns, as shown by the results described in the next two sections. Nevertheless, the information given by the measure gradient may provide insights into some unusual propagation phenomenon.

4.2 FFT BEAMFORMING

The FFT beamforming technique has been applied to the Lake Huron data for analysis. Because the profiler is virtually a synthetic aperture antenna, FFT beamforming can be used to obtain useful information such as angles–of–arrival and sidelobe characteristics. In Fig. 4.1 is given the FFT beamforming result of a typical data set prior to the phase correction. The average sidelobe level is relatively high and the sidelobe distribution is irregular. Moreover, there is no clear indication of the angles–of–arrival of the direct and indirect signals. On the other hand, from Fig. 4.2, showing the FFT beamforming result of the same data set after the phase correction, it can be observed that the average sidelobe level goes down by about 5 dB. In addition, the angles–of–arrival are clearly shown. In Figs. E13 (a, b, c, d) through E22 (a, b, c, d) are given the FFT beamforming results based on the profiler data for both 9.6 GHz and 8.6 GHz frequencies and for both vertical and horizontal polarizations. By comparing these results, it can be observed that the angles–of–arrival for both frequencies and both polarizations are the same.

4.3 NULL HEIGHT ANALYSIS

It is known that the null positions in an interference pattern are sensitive to angles–of–arrival of the direct and indirect signals, which are in turn dependent on the refractivity gradient. Therefore, by measuring the heights of the nulls, we can, using the known configuration geometry, derive the information of the refractivity gradient and angles–of–arrival of the direct and indirect signals. In Figs. 4.3 through 4.5 are given amplitudes of the interference patterns signatures which were recorded at both 8.6 GHz and 9.6 GHz and for vertical polarization under representative propagation conditions. In Fig. 4.3, the pattern null for 9.6 GHz is at 21.8 m above sea surface. The estimated gradient of refractivity ($\frac{dN}{dH}$) is –35 N unit/Km, which is close to the value –39 N unit/Km assumed under a normal propagation condition. The null height for 9.6 GHz in Fig. 4.4 is 17 m above the sea surface, indicating that the propagation condition was between superrefractive and ducting; that is, $\frac{dN}{dH}$ = –157 N unit/Km. In this case the effective earth radius is infinitive. The null for 9.6 GHz in Fig. 4.5 is situated at 14.5 m above water level, showing that the propagation condition was in the ducting regime and that $\frac{dN}{dH} = -212$ N unit/Km. In Figs. 4.6 and 4.7 are plotted the estimated refractivity gradient as a function of null height for both 8.6 GHz and 9.6 GHz, respectively. The measured values of the gradient are also superimposed on the plots for comparison. It can be seen that there are apparently discrepancies between the measured and estimated values. Furthermore, the discrepancies can be described by a linear factor. That is, if a linear regression is performed on the measured values to obtain the their expected values, the slope of the resulted line differs by a constant from the that defined by the estimated values. Another observation about the interference patterns is that the depths of the nulls are, in general, inversely proportional to the gradient of refractivity.

The angles–of–arrival can also be derived from the heights of the nulls in the interference patterns. Fig. 4.8 shows a set of angle–of–arrival results as a function of the measured refractivity gradient. The continuous lines which represent the theoretical values are added to the plot for comparison. Although discrepancies can be found between them, they agree with each other to a certain extent. The angular separation of the direct and indirect signals decreases as the gradient of refractivity increases. A set of angle–of–arrival results based on the information given by the null positions are summarized and compared with the FFT beamforming results in Fig. 4.9. In spite of the differences between the results derived from null heights (NH) and the FFT results, they are strongly correlated with each other. For instance, the correlation coefficients between the FFT results and the results by null height analysis are 0.62 and 0.56 for the direct and indirect signals. The angular separations given by FFT are normally larger than that given by the null heights. Due to the fact that the null height analysis only relies on the information provided by the amplitude of the interference pattern whereas the FFT is a function of both amplitude and phase, the cause of the discrepancy between the results is two-folded. First, there are errors in determining the true null locations because of the noise in the amplitude signatures of the profiler. Secondly, although phase correction was applied to the profiler data, there still remained some phase residual errors which may cause bias in the FFT results.

5. SIMULATION RESULTS AND MODEL VALIDATION

5.1 PHASOR SUMMATION

It has been mentioned previously that the total scattered field is obtained by summing the incremental facet voltages over the entire illuminated surface. For all those facets with the same y-coordinate, phasor summations are first carried out by adding the incremental facet voltages across the x-axis. A set of strip voltages, parallel to the x-axis but along the y-axis, are then formed. The resultant can be found by repeating the summation to those strips along the y-axis. A Cornu spiral, as shown in Figure 5.1a, can be obtained by plotting the real part of the voltage versus its imaginary part. Each line segment represents the intermediate result of the voltage summation of two strip voltages. The spiral is found to be symmetrical about the x-axis but not the y-axis as long as the sinusoidal simulated swell propagates along the x-axis. For zero sea-state, the resultant magnitude, measured between the centers of the two spirals, gives an accurate estimation of the magnitude of the reflection coefficient. This surface summation resembles the classical Fresnel integral [17] of the Fresnel diffraction. The shape of the spiral will be drastically distorted when the perturbation of the surface increases. This distortion is due to the slope of the tilted surface as both the magnitude and the phase of the facet may be disturbed in a random fashion. Figure 5.1b is one of the examples obtained at sea state 2.

5.2 INTERFERENCE PATTERN

The total signal at the receiver in Figure 3.1 is a combination of the direct and the scattered components. As a result of the variation in the phase difference between the two components along h_1, an interference pattern is formed. This pattern can be obtained by sampling the vertical aperture of the antenna. Simulation results at various atmospheric refractions are shown in Figure 5.2 by observing the pattern at a frozen time-frame and they are well attested by the experimental results obtained from Lake Ontario in November 1988. Referring to the simulation results in Figure 5.2, twenty different sinusoidal sea waves are added together to form the sea surface. The wavelengths for sea waves range from 60 to 320 meters and their period spread from 5 to 20 seconds. Propagation angles, amplitudes, and phases of the waves are randomly selected so that a random sea surface is obtained. By the central limit theorem, the amplitude of this random surface is approximately of Rayleigh distribution. Although the amplitudes of the waves are randomly chosen, they are normalized so that the overall rms wave height is equal to that of the desired sea state. Consistent agreement between simulations and real data in Figure 5.2 has thus demonstrated the effectiveness of the model. Discrepancies in null position between the two results may be lessened by increasing the grid resolution of the illuminated region. However, it could be as well due to the error arisen from the coordinate rotation method. Improvement technique which focused on the particular problem is undergoing.

In addition, Figure 5.3 illustrates how the interference pattern changes as the refraction index gradient varies. Another type of interference pattern is illustrated in Figure 5.4. This is derived by varying the separation between the receiver and the transmitter while keeping their heights constant. The drop in power level with range is consistent with the inverse relationship between the power and distance squared.

5.3 COHERENT AND INCOHERENT FIELDS

The field scattered by a rough surface can be considered to be the sum of two components: a specular component (coherent) and a so-called diffuse component (incoherent). Beard, Katz, and Spetner [18], introduced a model for forward scattering that consisted of these two fields. The result of their model have been shown to be consistent with measurements. Based on their measurements, they concluded that the coherent field was Gaussian distributed and the incoherent field was close to being Rayleigh distributed in terms of ocean roughness. The roughness factor is defined as a root mean square value of the product of the standard deviation of the surface and the grazing angle normalized by the operating wavelength.

As generally accepted, the coherent field is the mean value of the resultant of the scattered signal. To assist in the comparison of the swell model results with Beard's [19] results, every facet in the swell model is normalized by its local reflection coefficient before the scattered resultant is computed. The average of the diffuse return over a number of time samples is then normalized by the direct component. According to Beard et al. [18], the incoherent field is represented by the standard deviation of the total received signal. Both the coherent and the incoherent components are given by

$$\frac{C}{Dr} = \frac{< S >}{D} \qquad (5.1)$$

$$\frac{I}{D} = \frac{< \nu - T >}{D} \qquad (5.2)$$

where S is the total scattered field, D is the direct signal, T is the total received field (i.e. S+D), and ν is the time average of T. Simulated results based on (5.1) and (5.2) are shown in Figure 5.5 where sixty sinusoidal surface waves are used and sixty time samples for every .2 seconds are taken. The coherent component appears to be normally distributed for low surface roughness. Notable deviations from the Gaussian curve for high surface roughness describes Beard's experimental data appropriately. The incoherent part mimics a Rayleigh distribution and will take on a slightly higher value if normalized by the reflection coefficient. The behaviour of the coherent and the incoherent fields are found to be sensitive to the randomness of the simulated surface. As more and more number of swells are added, the characteristics of both coherent and incoherent fields become palpable and consistent. Results in Figure 5.5 demonstrate that our simulated data do comply with Beard's prediction which further validates our swell modeling technique. The most important of all is the appropriateness of using a large number of swells to generate a random sea surface. However, shadowing due to higher sea–states has not been included.

5.4 TIME AND FREQUENCY DOMAIN ANALYSIS OF THE SCATTERED FIELD

The scattering problem of the swell surface are further analyzed by statistically sampling the multipath signals over the entire Fresnel region. Taking a set of time samples allows us to look at the problem in both the time and frequency domains. Five hundred time–sampled multipath returns are obtained over a surface composed of sixty waves with wavelength varies from 20 to 50 meters and periodicity ranges from 2 to 6 seconds. The sampling interval is 0.016 second for a duration of 8 seconds. The autocorrelation of the time samples are shown in Figure 5.6 and 5.7. Surfaces of the same mean waveheight exhibit relatively the same correlation characteristics, as shown in Figure 5.6a, while high correlationship of the surface irregularities appears as the surface roughness increases, as illustrated in Figure 5.7a. Their corresponding energy density spectrum are readily obtained by Fourier transform the autocorrelation as depicted by Figure 5.6b and 5.7b.

6. ANALYSIS AND PROCESSING OF COHERENT AND DIFFUSE MULTIPATH DATA

6.1 ANALYSIS OF THE COHERENT COMPONENT

Since the specular signal is coherent with the direct signal in phase, an interference field results. When this field is sampled vertically by an sampled aperture antenna, an interference pattern with maxima and minima will be observed, which is described by Eq.(2.13). For convenience, Eq.(2.13) is reproduced here,

$$|s(n)| = \{1+|\rho_s|^2+2|\rho_s|\cos[knd(\sin\theta_d-\sin\theta_s)+\arg(\rho_s)]\}^{1/2} \tag{6.1}$$

A maximum results when the term $\cos[\cdot] = 1$, giving

$$P_{max} = |s(n)| = [\ 1 + |\rho_s|^2 + 2|\rho_s|\ ]^{1/2} \tag{6.2}$$

On the other hand, a minimum occurs when $\cos[\cdot] = -1$, resulting

$$P_{min} = |s(n)| = [\ 1 + |\rho_s|^2 - 2|\rho_s|\ ]^{1/2} \tag{6.3}$$

Taking the ratio of P_{max} over P_{min} and expressing it in terms of decibel, we have

$$\begin{aligned}\gamma &= 20\ \log(\frac{P_{max}}{P_{min}}) \\ &= 20\ \log(P_{max}) - 20\ \log(P_{min}),\end{aligned} \tag{6.4}$$

which is the null depth of the interference pattern. Therefore, by measuring the null depth of the interference pattern, the specular reflection coefficient can be estimated by using the relations between Eqs.(6.2), (6.3), and (6.4).

The specular reflection coefficient is a function of the roughness of a sea surface. Therefore, it is usually correlated with the roughness parameter, which is proportional to the rms wave height of the sea surface, σ_h, and sine of the grazing angle, $\sin(\psi)$, and is inversely proportional to the wavelength of the carrier signal, λ; that is,

$$\text{roughness} = \frac{\sigma_h \sin(\psi)}{\lambda}. \tag{6.5}$$

If ψ is small, then $\sin(\psi) \simeq \psi$. Thus,

$$\text{roughness} \simeq \frac{\sigma_h \psi}{\lambda}. \tag{6.6}$$

In Fig. 6.1, the specular reflection coefficient is plotted against the roughness for both horizontal and vertical polarizations. In our case, σ_h took on the values from 0 to 0.5 m, ψ ranged from 1.87 to 2.33 mrad, and λ had the values of 0.003125 m and 0.003488 m. For comparison, in the same figure is superimposed a theoretical model for the specular reflection coefficient [20] described by the following,

$$\rho_s = \exp\left[-2\left[\frac{2\pi\ \sigma_h \sin\Psi}{\lambda} \right]^2 \right], \tag{6.7}$$

which is represented by the continuous line. As one can see, the estimated reflection coefficients exhibit a downward trend as the roughness increases. This qualitatively agrees with the theoretical model. However, near the zero roughness region, relatively low values are observed. It is believed that this was because of the propagation condition, especially for very small grazing angle. It is interesting enough that in their early work on low–angle propagation some researchers [21] also experienced the falling of the specular reflection coefficient when grazing angle was small. For instance, Fig. 6.2 shows the measured specular reflection coefficients verse the depression angle which is equivalent to the grazing angle in most practical cases. These results were based on experimental studies of sea–surface effects on low–angle radars at X–band frequency (λ=3.2cm). The reflection coefficient of the horizontal polarization drops as the depression angle approaches zero.

6.2 ESTIMATION OF DIFFUSE POWER

The diffuse power is defined as the ratio of the incoherent component to the coherent component. It is estimated based on the profiler traces. As given in the signal model, the total received signal consists of four components, namely the direct signal, specular reflection, diffuse reflection, and channel noise. Thus, we can represent the diffuse component in terms of the other components by rewriting Eq.(2.10) as,

$$r_d(n,t) = s(n,t) - [s_d(n,t) + r_s(n,t)] - \eta(n,t), \tag{6.8}$$

where the terms in the square bracket can be estimated by synthesis of the direct and specular signals,

$$s_d(n,t) + r_s(n,t) = \tilde{s}_d(n,t) + \tilde{r}_s(n,t) + e(n,t) \tag{6.9}$$

where $\tilde{s}_d(n,t)$ = synthesized direct signal,

$\tilde{r}_s(n,t)$ = synthesized specular signal, and

$e(n,t)$ = residual error by synthesis.

It follows that the estimated diffuse signal $\tilde{r}_d(n,t)$ is

$$\begin{aligned}\tilde{r}_d(n,t) &= s(n,t) - \tilde{s}_d(n,t) - \tilde{r}_s(n,t) \\ &= r_d(n,t) - e(n,t) - \eta(n,t)\end{aligned} \tag{6.10}$$

The estimated power of $\tilde{r}_d(n,t)$ is given by the following

$$\begin{aligned}\tilde{\sigma}_d^2 &= \mathrm{var}[\tilde{r}_d(n,t)] \\ &= \mathrm{var}[r_d(n,t)] + \mathrm{var}[e(n,t)] + \mathrm{var}[\eta(n,t)] \\ &= \sigma_d^2 + \sigma_e^2 + \sigma_n^2.\end{aligned} \tag{6.11}$$

$\tilde{\sigma}_d^2$ is expected to give a good estimation of σ_d^2 provided that σ_e^2 and σ_n^2 are much less than σ_d^2. In the profiler case, σ_e^2 is expected to be relatively small since a large aperture is sampled over a relatively long period. Moreover, the receiver noise power σ_n^2 is considered to be relatively small since the source power was at a relatively high level.

Fig.6.3 and 6.4 depict the diffuse power as a function of the roughness parameter of the sea surface for vertical and horizontal polarizations, respectively. They were derived based on the Lake Ontario data. Each point represented by a small triangle was obtained from one individual profiler trace, whereas a large number of points are within the roughness region from 20 to 40 mrad. Although it is not obvious, the diffuse power rises slowly as the roughness parameter increases. Several limitations on the results should be pointed out here. First, as shown above, the noise power was included in the results. Secondly, since a profiler trace was sampled along time and elevation together, the grazing angle for each sampled point was different from the other. Thus, we had to compromise the accuracy of the roughness parameter by using the grazing angle for the middle point of the vertical aperture for each profiler trace. Finally, the range of the roughness parameter is limited and the maximum value is only up to 50 mrad. This disables us to examine the behavior of the diffuse power beyond the roughness of 50 mrad.

6.3 ANALYSIS IN TIME AND FREQUENCY DOMAIN

In the time and frequency domain, the auto-correlation, the cross-correlation, and the power spectra of the diffuse signal are of interest. These statistic characteristics can provide important information about the nature of the diffuse component in the received signal. The analysis is performed based on the Lake Huron data as well as the Lake Ontario data.

For a discrete signal x(t) of a time-limited length N, the estimate of its auto-correlation function is given by

$$R_x(\tau) = \frac{1}{N} \sum_{i=0}^{N-\tau} x(t_i)\ x(t_i+\tau) \qquad (6.12)$$

for a time lag τ. Similarly, the estimate of the cross-correlation function of two discrete signals x(t) and y(t) is

$$R_{xy}(\tau) = \frac{1}{N} \sum_{i=0}^{N-\tau} x(t_i)\ y(t_i+\tau) \tag{6.13}$$

By recalling that the auto-correlation function and the power spectral density of a wide-sense stationary random process form a Fourier transform pair, the power spectrum of the diffuse signal is readily computed by performing a Discrete Fourier transform (DFT) on its auto-correlation function. It is given as following,

$$P_x(f) = \sum_{k=0}^{N-1} R_x(\tau)\ e^{-j2k\pi f\tau} \tag{6.14}$$

Fig. 6.5(a) shows the auto-correlation function of the diffuse component of the received signal derived from a data set of the the Lake Huron data base. This data set was recorded at 10.5 GHz for horizontal polarization. The sea state was about 3 when the data were taken. Appendix II describes the extraction of the diffuse signal from the modulated signal. It can be observed that the auto-correlation function falls rapidly near time zero from unity to 0.85. Due to the limited frequency resolution resulted from the relatively low sampling rate (62.5 samples per second), more detailed examination over this short time interval could not be carried out. Thus, it is difficult to determined that the rapid drop in the auto-correlation function was due to rapid change in amplitude and phase of the reflected signal or simply due to Gaussian white noise of the receiver. From the auto-correlation function, one can say that it took almost two seconds for the signal to decorrelated and the signal consisted of at least one sinusoidal component. Since there was no similar measurement of this sort, at least to our knowledge, no comparison can be made to justify the characteristics of the diffuse signal that we found from its auto–correlation function. Nevertheless, we believe that some characteristics of forward scattering are, to certain extent, similar to that of back scattering and therefore it is reasonable to compare them. The auto–correlation function derived from a back scattering measurement [22] is recaptured in Fig. 6.6. A strong resemblance between the two figures can be easily observed although the periods are different from each other. Fig. 6.5(b) depicts the amplitude of the power spectrum resulted from the DFT of the auto–correlation function shown in Fig. 6.5(a). One can see that most of the energy concentrates within the frequency band from 0.2 Hz to 1.0 Hz. By examining the power spectrum of the surface waves of a sea [23] given by Fig. 6.7, it is apparent that the resulted energy frequency band falls into the gravity wave frequency band. Based on this, it is reasonable for us to argue that the receiving antenna actually saw the activities of gravity waves on the sea surface.

A group of auto–correlation functions are shown from Fig.6.8(a) through 6.10(a). They are the results based on the Lake Ontario data. Again, a striking resemblance can be observed between these results and those of Lake Huron data. However, longer decorrelation times are observed in these functions. There are two points which should be stressed here. First, since the two data bases are collected under different conditions and in different experimental settings, the comparison carried out between the results of these two data bases can only be made qualitatively. Second, since the profiler data were obtained by sampling the field in both temporal and spatial domains, the resulted auto–correlation functions are also in these two domains. This should be generally understood although only the time scale is shown in Figs. 6.8(a) through 6.10(a). The auto–correlation functions in Fig. 6.8(a) and 6.9(a) were derived from the data recorded at 9.6 GHz for both vertical and horizontal polarized channels, respectively, on a rough day (Nov. 17, 1988). It can be seen that they are extremely similar to each other and have almost the same zero crossings. This suggests that for configurations that are similar to ours, the transmission via either a vertical or a horizontal polarized channel has no advantage over the other in terms of auto-correlation characteristics. The auto-correlation function in Fig. 6.10(a) was derived from the data recorded at 9.6 GHz for the vertical polarized channel on another rough day (Nov. 27, 1988). The power spectra that are corresponding to the three auto-correlation functions are shown in Figs. 6.8(b) through 6.10(b), respectively. These power spectra further provide evidence that the diffuse energy concentrates within the gravity wave frequency band.

In Fig. 6.11 is shown the cross-correlation function of the diffuse signals from two different frequency channels of the Lake Huron data. The first sequence is the one from which the auto-correlation function in Fig. 6.5 was derived. The other sequence was recorded at the same time but at the frequency of 8.05 GHz. The cross-correlation function indicates that the diffuse signals were highly correlated. This fact is also supported by the cross-correlation function based on Lake Ontario data, as shown in Fig. 6.12. The two diffuse signals from which the cross-correlation was derived were recorded at 8.6 and 9.6 GHz for vertical polarization on Nov. 17, 1988.

7. PERFORMANCE OF CHA AND RML ALGORITHMS BASED ON SIMULATED AND MEASURED DATA

7.1 PROPAGATION EFFECTS ON CHA

The CHA technique is based on the use of deterministic physical modelling. A refined signal model is used to generate radar data that can be correlated with the real radar data to estimate the target height. One of the key characteristics of this technique is to make use of the target range information so that phase difference between the signal via the direct and indirect paths can be accurately estimate. However, the bending of the microwave path due to the change in refractivity would set off this accuracy. In order to account for this propagation effect, the refractivity gradient is incorporated into the model as a parameter. The values of this parameter directly affect the accuracy of the estimated target heights. The following example illustrates the effect of the refractivity gradient, based on the Lake Ontario data.

In Fig. 7.1 are shown two traces of target heights over a period of two hours and 20 minutes on Nov. 25, 1988. For both height traces, the receiver apertures were taken to be 4.6 m long, with one centered at 18.9 m and the other at 23.5 m above the water level. Each height indicated by a marker was obtained from a single profiler trace, whereas a constant refractivity gradient was used in the CHA algorithm for all the results. It can be seen that both height traces exhibit similar fluctuation pattern and have the same variation of 1.5 m. By correlating these height results with the measured refractivity gradient over the same period, shown in Fig. 7.2, we can observe that a strong negative correlation exists between them. That is to say, the change in the target heights is inversely proportional to the change in the gradient. In fact their correlation coefficient is – 0.68.

In Fig. 7.1, there exists the discrepancy between the two target height traces. It is believed that this discrepancy caused by the non–linearity of different refractivity gradient. In other words, the changing rate of the refractivity at one elevation differs from that at other elevations. Thus, the curvatures of the bent signal paths are different. When a receiver is place at different elevations, the estimated target heights will be inconsistent.

Another degrading effect of the change in the refractivity gradient on the CHA algorithm is that it causes the algorithm to lose track of the target. It is known that the performance of CHA (dual frequency case) depends on the phase difference of the direct and indirect signals at the centre of the aperture. When the difference is 0 or π, poor performance may be yielded.. Fig. 7.3, which shows a set of CHA results, demonstrates this effect. The data used to produce the results were the same as described above, except that the aperture was centered at 15.0 m above water level. It is clear that initially the algorithm tracked the target. However, as the refractivity gradient fell to certain values, causing the phase difference at the centre of the aperture to approach zero, the algorithm lost the target track. When the gradient increased again, the algorithm regained the track. Fortunately, this undesirable effect can be eliminated by using three or more radar frequencies.

7.2 EFFECTS OF HIGH SEA STATES ON CHA

It is known that sea surface roughness increases the diffuse component in the received signal. The effect is that the signal takes on noise–like characteristics. This can be manifested by comparing profiler traces recorded for different sea states. Fig. E14 (e) and E21 (e) show the interference patterns for sea state 1 and sea state 3, respectively. These two pattern have the same null position, but their noise levels are different. It is clear that a higher level of noise power in the pattern results from a higher sea state. Therefore, one will expect that the bias and variance of the estimated target heights under the condition of high sea states are larger than that under the condition of low sea states. For example, by applying CHA to the data shown in Fig. E14 (e) and E21 (e) for the same aperture length of 4.6 m, the estimated target height was 11.2 m for Fig. E21 (e) and 12.1 m for Fig. E14 (e), whereas the actual target height is 11.1 m. The lower sea state data yielded a smaller error.

However, in order to see the effect of sea roughness on the CHA algorithm, the characteristics of the noise caused by it must be determined and understood. In developing the signal model for CHA, it is assumed that the received signal consists only of three components: the direct signal, the specular signal, and the receiver noise. The receiver noise is characterized as an independent Gaussian process. When the diffuse signal is present, the algorithm simply treats it as noise. If the diffuse signal is Gaussian or nearly Gaussian, the analysis of the effect of sea roughness on CHA can be simplified as the analysis of the performance of CHA under different signal–to–noise ratio (SNR). This can be readily accomplished by simulations. In Fig. 7.4 is given the simulation results of the SNR performance in terms of mean squared error (MSE). In the simulation, the same configuration as in the Lake Ontario measurement was used. The aperture is 2.3 m long and centered at 17.7 m above water level. Accordingly, the angular separation of the direct and indirect signals are 11% BW. Each point in Fig. 7.4 was obtained by 512–ensemble averaging. The density function of the simulated noise is depicted in Fig. 7.5 and compared with the normal density function. It can be seen that the characteristic of the simulated noise is very close to Gaussian.

In actual practice, however, the characteristics of the noise due to sea roughness is somewhat complicated. In a previous section, the auto–correlating characteristic of the noise (or the diffuse component) has been investigated. It was concluded the noise was temporally and spatially correlated. However, it is equally important to identify the distribution characteristic of the noise itself. In Fig. 7.6 trough 7.9 are shown the density functions of the diffuse signals, which are corresponding to the amplitudes of the interference pattern in Fig. E14 (e) and (f). These data were recorded for a rough sea. It is clear that the density functions of the noise components have longer tails and narrower main lobes than normal density function. That is to say, the noise due to the diffuse multipath is not Gaussian nor near Gaussian. If the CHA algorithm with the Gaussian noise model is used, it is expected that larger bias and variance will occur. In Fig. 7.4, the + symbols represent the CHA results based on the Lake Ontario data. Although these results are statistical insignificant because each point was derived from only one ensemble, they may, to certain extent, show the effect due to the sea roughness.

7.3 EFFECT OF SEA SWELLS ON CHA

Since we did not encountered sea swells during both the Lake Ontario trials and the Lake Huron trials, we have to rely on the simulated data for the analysis of the effect of sea swells on CHA.

In the simulation, the geometric configuration is based on the setting used in the Lake Huron trials. That is,

range = 4610 m,
number of elements = 32,
receiver antenna aperture = 7.84 m to 9.66 m above mean water level, and
target height = 15.3 m above the mean water level.

The refractivity gradient is assumed to be –39 NU/Km, the normal condition. Two frequencies are used: 8.05 GHz and 9.6 GHz. A sea swell is approximated by a sine wave with its amplitude being 0.5 m peak to peak, its wavelength being 50 m, and its period being 2.1 seconds. 128 snapshots are taken with a sampling rate of 62.5 samples/second, resulting a sampling time interval which just equals the period of the swell. Several representative examples for the sea swells are simulated to show the effects on the CHA algorithm.

Example 1: An extreme case is simulated here. The swell propagates in the direction perpendicular to the transmitting path. Since the phase front of the sea wave is parallel with the long dimension of the Fresnel Zone, the phase difference between the direct and indirect signals is modulated by the swells. Accordingly, the interference pattern also varies with the motions of the swells, as illustrated by the simulated amplitude of the interference pattern for 9.6 GHz shown in Fig. 7.10. The null moves towards and then apart from the aperture centre as a sea swell cycle completes in 2 seconds. Thus, it is not surprising that target heights estimated by the CHA algorithm fluctuate from 13.9 m to 16.35 m, as shown in Fig. 7.11.

Example 2: Another extreme case is presented here. The swell propagates in the direction along the transmitting path. From the simulated interference patterns shown in Fig. 7.12, there are seemingly regular perturbations in the interference patterns in the two second interval. However, since these perturbations are small in magnitude, only small fluctuations are introduced in the target heights given by the CHA algorithm, as manifested by the results shown in Fig. 7.11. On the other hand, a significant deviation from the actual target height is clearly observed.

Example 3: In this example, the swell propagates in the direction of 45 degrees with respect to the transmitting path. The perturbation in the amplitude of the interference pattern is similar to that in Example 2. It is in fact smaller, as shown in Fig. 7.13. Thus, it is not surprising that the effect on CHA is about the same as in Example 2, as depicted in Fig. 7.11. Based on this result, it can be argued that if the swell propagation angle with respect to the transmitting path is within –45 to 45 degrees, the swell effect on CHA is relative small.

Example 4: The swell propagation angle is now set to be 75 degrees with respect to the transmitting path. From the interference patterns shown in Fig. 7.14, it can be seen that the null appears, disappears, and reappears as the wave completes a full cycle. Referring back to Fig. 7.11, the target height results given by CHA are not better than that in Example 1.

Example 5: Based on the results in Example 4, it is expected that swells with propagation angles between 75 and 90 degrees will have similar effects on the CHA algorithm. The case given here is that the swell propagate at an angle of 85 degrees with respect to the transmitting path. Fig. 7.15 shows that the null of in the interference patterns appears and disappears repeatedly. The CHA results are again similar in Example 1, as shown in Fig. 7.11.

Example 6: This is a two-swell case. Two sinusoidal sea waves propagate in the directions of 90 and 80 degrees with respect to the transmitting path. These equi-amplitude swells interfere with each other, generating a relatively complicated surface. Since the propagation angles of both waves are close to 90 degrees, it is expected that the effect on the CHA results may be at least as large as in the single wave case. In Fig. 7.16 are compared the target height results with those in Examples 1 and 5. Similar behaviour is evidently presented.

In Examples 1,4,5, and 6, sizable errors in the target heights are observed. These errors are likely related to the aspect sensitivity [24]. In these cases where the swell propagation angle is close to 90 degrees with respect to the transmitting path, the scattering takes place from a surface perturbed by a regular structure, much like a diffraction grating, and the distance between the crests of the perturbation is considerably larger than the width of the Fresnel regions in which the beam is formed. It is also observed from these examples that sudden jumps from one value to another occur in the target height results, whereas this does not occur in Examples 2 and 3. It is believed that these sudden jumps are caused by the focusing and defocusing effects induced by the very small number of crests and troughs which are illuminated by the antenna beam [24]. During focusing and defocusing, the reflected signal received by the receiving antenna is enhanced and reduced, resulting the fluctuation in amplitude and phase of the total received signal. Therefore, the fluctuation in the target heights occurs.

7.4 RESULTS FROM RML BASED ON LAKE HURON DATA

Frequency diversity is known as a way to improve the performance of a low-angle radar tracking system. Many estimation algorithms or techniques make use of multi-frequency data from the radar system. One of these techniques is the Refined Maximum Likelihood (RML) estimator [25] developed at DREO, which uses the same multipath model as in the CHA technique. The results of the target heights to be presented were obtained by using this estimator.

The testing of this technique was based on the Lake Huron data. The target simulated by a beacon were at six different heights ranging from 3.5 m down to 18.5 m about the sea level. Equivalently, the angular separations were from 10% to 60% of a beamwidth. To show the advantageous effect of using frequency diversity on the estimation, two frequencies, four frequencies, and six frequencies were used for estimating the target heights. The roughness of the water surface for these data was about 1.5m to 2.0m in terms of wave heights. The normal propagation condition was assumed in the refined signal model. In other words, the effective earth radius factor κ was set to be 4/3. Such a value was taken because no enough atmospheric data were available for estimating the index of refractivity.

In Table 7.1 are listed the data files and frequencies that were used in the testing. A large effort was made to keep the consistence of frequencies that were used for the estimation of each height. If the data of the required frequency was corrupted, another data set of the closest frequency would be chosen. It should be pointed out that except for the data used in two-frequency cases, the multi–frequency data were not recorded simultaneously. Instead, they were recorded several seconds apart. It was assumed that in such a short period, propagation condition did not change much. Based on this, these data of different frequencies can be jointly used in our case.

The estimated target heights are depicted in Fig. 7.17 through 7.19 for two–frequency, four–frequency, and six–frequency runs, respectively. These results were obtained on a single–snapshot basis; i.e. the nth estimated height was resulted from the nth snapshot of each frequency data set. For comparison, we tabulate the statistical parameters of the results in Table 7.2. The angular separation of the direct and indirect signals is given in terms of an antenna beamwidth. The most significant parameter is the variance of the estimates of the target heights. It can be observed that the variance increases as the angular separation of the signals decreases. On the other hand, the variance decreases as the number of frequencies increases. There are obviously differences between the actual and estimated target heights. However, these differences do not reflect the true performance of the tracking technique since the actual values of refractivity gradient, which directly affected the angles–of–arrival, were not known for the data used. Instead, if the relative displacements between the target heights are examined, the performance improved by frequency diversity becomes clear. This is illustrated in Fig. 7.20. As it can be seen, the six–frequency estimates are generally closer to the actual than the others. Although there were many factors that might contribute to errors in the estimates, it is certain that the tilt of the antenna array, its vibration due to strong wind, and the calibration errors were the three main factors among them.

8. CONCLUSIONS AND RECOMMENDATIONS

This report has presented the work and results of (1) the sea swell model and its validation, (2) the analyses of real multipath data collected from Lake Ontario in 1988 and from Lake Huron in 1987, and (3) the effects multipath phenomena on the performance of the CHA algorithm. The objective of this study was to carry out the investigation and analyses the performance of the CHA algorithm under the conditions of (1) high sea states, (2) sea swells, and (3) varying refraction gradient.

A three–dimensional sea swell multipath model has been developed and verified against experimental results with a satisfactory agreement. In the present model, the sea clutter and shadowing are not included. Simulation results displayed the characteristics of the coherent and the incoherent fields, which further justified Beard's model. Despite of the limitation in locating the beam direction of a local facet and the incompleteness of the depolarization technique, the model has provided insight into the multipath return and the modelling of the swell surface. It may be still a long way to become a general solution on the problem of multipath scattering. Nevertheless, the yielded results were adequate and the method is promising.

The measured data from the Lake Ontario trials showed that during the measurements, normal, superrecfractive, and ducting propagation conditions were encountered. As well, the discrepancy between the estimated and measured refractivity gradient indicated that the propagation medium was non–homogeneous. The angle–of–arrival results derived from the FFT and the null positions were consistent, although residual phase errors caused some deviations.

Analysis results showed that the coherent and incoherent components of the multipath signal were a functions of the surface roughness parameter. The specular reflection coefficient was inversely proportional to the roughness parameter. However, an interesting fact was that at near zero roughness parameter, the specular reflection coefficient decreased. It is thought that this was because of very small grazing angle. The diffuse component was found to be increasing as the roughness increased. Unfortunately, due to the limitations in evaluating the roughness parameter, no quantitative comparison was made between the estimated diffuse power levels with theoretical values.

Based on both the Lake Huron data and the Lake Ontario data, the auto–correlation functions of the diffuse signals were evaluated. For high sea states, the diffuse signal was temporally and spatially correlated with itself. The diffuse signal via a frequency channel was also found to be correlated with that via another frequency channel. As well, the power spectra derived from the diffuse signals were observed within the gravity wave frequency wave band. It was, unfortunately, realized during the analysis that the data sampling rate was too low to fully characterize the diffuse component of the multipath signal.

The performance of the CHA algorithm has been evaluated using simulated and real data. It was clear that the algorithm was sensitive to the change in refractivity gradient. The worst effect was that the change in propagation centre of the aperture. Based on the real multipath data, the roughness of the sea would cause the received signal to take on noise-like characteristics. It was found that the density function of this sort of noise was non-Gaussian. The non-Gaussian noise may introduce more bias and variance into the tracking accuracy if algorithms that are based on the Gaussian noise model, such as CHA, are used for tracking. The effect of sea swells on the CHA algorithm was studied by simulations. It was found that sea swells generally introduce bias into the CHA results. As expected, the errors are also due to focusing and defocusing effects. The magnitude of the errors depends on the aspect sensitivity. Based on the Lake Huron data, frequency diversity was used to improved the performance of the RML technique. A remarked improvement was observed, especially for small separation between the direct and indirect signals. Generally, the more number of frequencies are used, the better performance can be obtained.

It has been shown that the performance of the CHA algorithm was degraded by changes in propagation condition, rough sea surfaces, and sea swells. Some recommendations are made for overcoming and reducing these adverse effects.

(1) Frequency diversity is strongly suggested for the use in CHA because of at least two reasons. (a) It has been shown the performance of CHA was improved markedly by using more than three frequencies data. (b) Frequency diversity can reduce CHA's sensitivity to the centre phase difference.

(2) The noise-like diffuse multipath must be understood as completely as possible in terms of its statistic characteristics such as its density distribution function, temporal auto-correlation, and spatial correlation.

(2) The noise-like diffuse multipath must be understood as completely as possible in terms of its statistic characteristics such as its density distribution function, temporal auto-correlation, and spatial correlation. In so doing, signal processing techniques such as adaptive filtering can be applied to reduce the noise level. As well, a specific noise signal model signal can be designed according to the noise characteristics and can be incorporated into the CHA algorithm to reduce bias and variance in the tracking accuracy.

(3) Upon understanding and determining the characteristics of the errors brought about by sea swells, compensation factors can be incorporated into the CHA algorithm to correct these errors.

Consequently, the work in the near future will include:

(1) to design a experiment to acquire multipath data that are suitable for fully characterizing the temporal and spatial auto-correlation of the diffuse multipath,

(2) to also collect multipath data suitable for determining depolarization characteristics and explore the feasibility of using cross-polarized diffuse component to cancel the co-polarized component so that the specular component in the co-polarized channel can be enhanced, and

(3) to improve the sea swell model and enhance the software by comparing real data with the predictions by the model. In addition, much more simulations must be thoroughly carried out to fully understand and characterize the CHA errors brought about by sea

swells so that proper steps can be taken to correct these errors. However, carrying out this task is extremely time consuming because the simulation part will take up a tremendous amount of computer cpu time.

REFERENCES

[1] Rook, B.J. and Litva, J., "An improved CHA algorithm for tracking low–angle targets (U)", CRC Report, no. 1356, April 1982.

[2] F. A. Berry, Jr. and E. Bollay (Ed.) *Handbook of Meteorology*, McGraw–Hill Book Company, 1945.

[3] J. Litva and P. Bauman, "Studies of Correlation Between Meteorological and Low–Level Radar Angle–of–Arrival Measurements," CRL Report No. 174, McMaster University, 1986.

[4] White, W.D. and Gery, S.W., "Final report on low angle radar study", AIL Report, no. 4251–TR1, Nov. 1969.

[5] Smith, F.G.W., *The Seas in Motion*, Thomas Y. Crowell Company, New York, 1973.

[6] Capurro, L.R.A., *Oceanography for Practicing Engineers*, Barnes & Noble, Inc., New York, 1970.

[7] Kerr, D.E., *Propagation of Short Radio Waves*, (Edited by D.E. Kerr–MIT Radiation Series), Dover Publications, Inc., 1965.

[8] Litva, J., personal notes, Jan. 1988 and discussions.

[9] Bauman, P. and Litva, J., "Modeling and analysis of the effect of the sea swell on low angle tracking performance", CRL Report, no. 193, June 1988.

[10] Stutzman, W.L. and Thiele, G.A., *Antenna Theory and Design*, John Wiley & Sons Inc., 1981.

[11] Balanis, C.A., *Antenna Theory Analysis and Design*, Harper & Row, New York, 1982.

[12] Goldstein, H., *Classical Mechanics*, 2nd Edition, Addison–Wesley Publishing Company, Inc., 1980.

[13] Dolukhanov, M., *Propagation of Radio Waves*, translated by Boris Kuznetsov, Mir Publishers, Moscow 1971.

[14] Beckmann, P. and Spizzichino, A., *The Scattering of Electromagnetic Waves from Rough Surfaces*, Artech House, Inc., 1987.

[15] Mitzner, K.M., "Change in polarization on reflection from a tilted plane", *Radio Science*, vol. 1 (New series), no. 1, pp. 27–29, Jan, 1966.

[16] C. A. Fleming, K. L. Philpott, and B. M. Pinchin, "Evaluation of Coastal Sediment Transport Estimation Techniques," Report No. C2S2–10, National Research Council, Canada, May 1984.

[17] Jenkins, F.A. and White, H.E., *Fundamentals of Optics*, McGraw–Hill Book Company, Inc., 1957.

[18] Beard, C.I., Katz, I., and Septner, L.M., "Phenomenological vector model of microwave reflection from the ocean", *IRE Transactions on Antennas and Propagation*, pp. 162–167, April 1956.

[19] Beard, C.I., "Coherent and incoherent scattering of microwaves from the ocean", *IRE Transactions on Antennas and Propagation*, pp. 470–483, Sept. 1961.

[20] D. K. Barton, "Low–Angle Radar Tracking," Proc. IEEE, vol. 62, no. 6, June 1974.

[21] M. Hunter and T. Senior, "Experimental Studies of Sea–Surface Effects on Low–Angle Radars," Proc. IEE, vol. 113, no. 11, Nov. 1966.

[22] M. W. Long, *Radar Reflectivity of Land and Sea*, Artech House, Inc., 1983.

[23] B. Kinsman, *Wind Waves*, Prentice–Hall, Inc., 1965.

[24] J. Litva, "On Scattering of Electromagnetic Waves from Sea Swells," CRL Report No. 175, McMaster University, 1986.

[25] R. M. Turner and E. Bosse, "Maximum Likelihood Processing for Low Angle Tracking Using a Highly Refined Multipath Signal Model," 21st Asilomar Conference on Signals, Systems and Computers, Pacific Grove, CA, Nov. 2–4,, 1987.

APPENDIX I. THE LAKE ONTARIO MEASUREMENTS

The measurements were successfully carried out on Lake Ontario, south of Burlington, Ontario, in November 1988. The profiler was sited at the shell Pier in Oakville and looked out over Lake Ontario, whereas th e beacon was mounted on the tower which was situated on the CCIW platform. Specifically, the beacon was located at 79°45'36"W and 43°16'13"N and the receiver at 79°43'14"W and 43°22'26"N. This particular location was chosen because it offers relatively high sea states due to westerly or easterly winds in late November. Continuous wave (CW) signals from the beacon were recorded using profiler The profiler consists of a reference receiver mounted at the top of the receiver tower, at the height of 27.4m above International Great Lakes Datum (IGLD), and a portable coherent receiver mounted on a vertical trolley. The incoming fields were sampled and recorded as the portable receiver moved up and down over the vertical aperture from 7.4m to 25.8m above IGLD. The diffraction limited beamwidth of this synthetic antenna is 1.5 milliradians (mrad). The receiver on the trolley recorded both the amplitude and phase distributions at two frequencies 8.6 GHz and 9.6 GHz and for both horizontal and vertical polarizations. In addition, meteorological sensors were mounted on the trolley, from which would be derived the refractive index gradient. The height of the beacon was 11.5m above IGLD and the range between the transmitter and the receiver was 11.97 km.

In addition to the meteorological data recorded by the profiler, sea states conditions, which where derived from wind speed and direction data using hindcasting technique, were provided by Canada Centre for Inland Water.

Although fair amount of effort was spent on aligning the profiler tower, it was still bowed or bent. As a result, the recorded data were inevitably contaminated with phase errors tue to non–linearity of the tower. To eliminate these phase errors, a method was used. A set of phase data which was recorded on a very calm day was selected and then compared with the synthetic phase data which were derived from the known geometry. Their differences would be the estimated phase errors due to the non–linearity. This method lay, of course, in the assumption that the model which was used to derive the synthetic phase is valid in our case. To justify this calibrating method, we carried out the direct measurement of the non–linearity of the tower using a powerful and accurate transit. Horizontal displacements at different heights (2.5 meters apart) of the tower were measured with respect to a fixed point of the tower. By dividing these displacements by the wavelength of a certain frequency signal, they were converted into the phase errors for that frequency. In Fig. A1 are superimposed the measured phased errors on top of the estimates. They agree with each other to a remarkable extent, giving us a sense of confidence about the method of estimating the phase errors.

APPENDIX II. TONE REMOVAL

In the Lake Huron trials, a baseband signal was produced and stepped up to carrier frequency for transmission. Consequently, the received signal must be a baseband signal after demodulation. However, this baseband frequency, or tone frequency, might have been distorted slightly due to propagation over the water path. Thus to remove tone frequency, we must first estimate this frequency. This can be accomplished by taking the mean value of the DFT estimates of all the 32 channels. Upon completing the estimation, the tone can be removed as follows.

Let the received signal at the n^{th} element before tone removal be

$$s(n) = A\, e^{j(2\pi f_t t+\phi)}$$

where A is the amplitude, f_t is the tone frequency, t is time, and ϕ is the initial phase. By generating a signal

$$\tilde{s}(n) = e^{j(2\pi \tilde{f}_t t)},$$

where $\tilde{f}_t$ is the estimated tone frequency, and multiplying its conjugate to s, we have the tone removed signal

$$\begin{aligned} r(n) &= s(n)\, \tilde{s}^*(n) \\ &= A\, e^{j(2\pi f_t t+\phi)}\, e^{-j(2\pi \tilde{f}_t t)} \\ &= A\, e^{j(2\pi\delta t+\phi)}, \end{aligned}$$

where δ denotes the discrepancy between f_t and $\tilde{f}_t$. $e^{j2\pi\delta t}$ is the residual error for the tone removed signal.

If we further assume that the coherent component of the received signal are constant within a short time interval, the diffuse component can be extracted from r(n) by removing its dc component. Furthermore, for extracting the optimal information about the diffuse component, the signal should be taken from the element where a null in an interference pattern occurred because at this element the power ratio of the diffuse component to the coherent component of the signal was maximum.

FIGURES AND TABLES

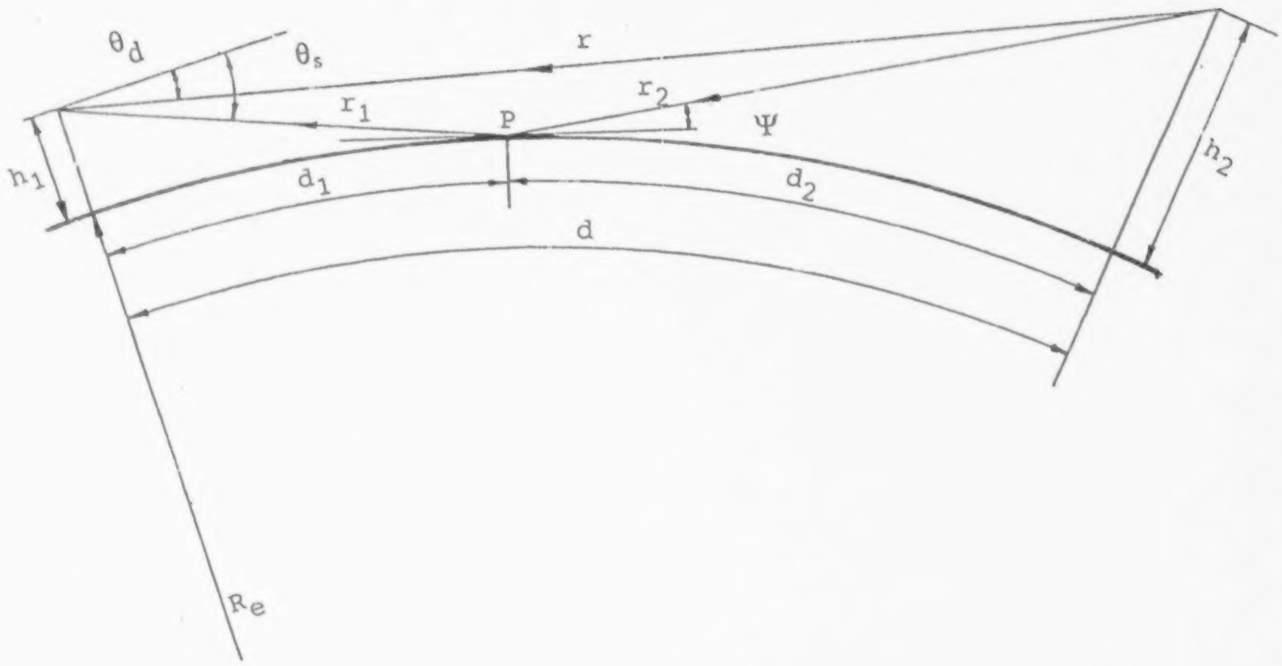
θd
θs
r
r1
r2
P
Ψ
h1
h2
d1
d2
d
Re

Fig. 2.1 Geometry of direct and indirect rays on a curved earth.

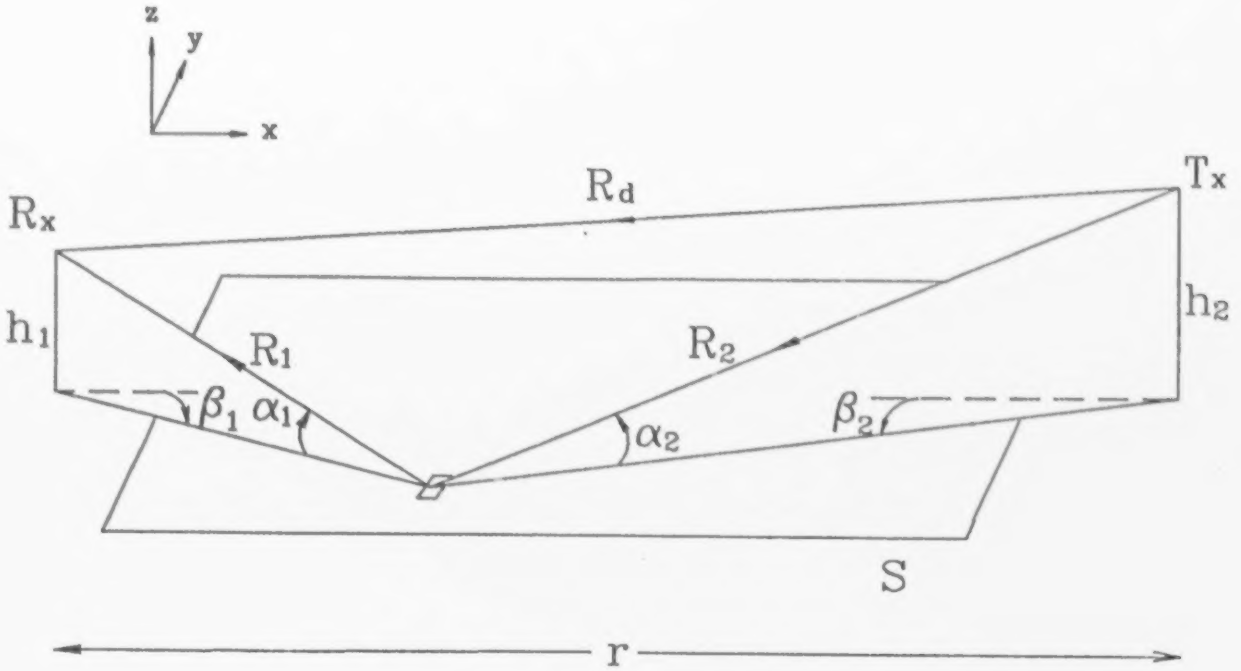
z
y
x
R_x
R_d
T_x
h_1
h_2
R_1
R_2
β_1
α_1
α_2
β_2
S
r

Figure 3.1: Scattering geometry

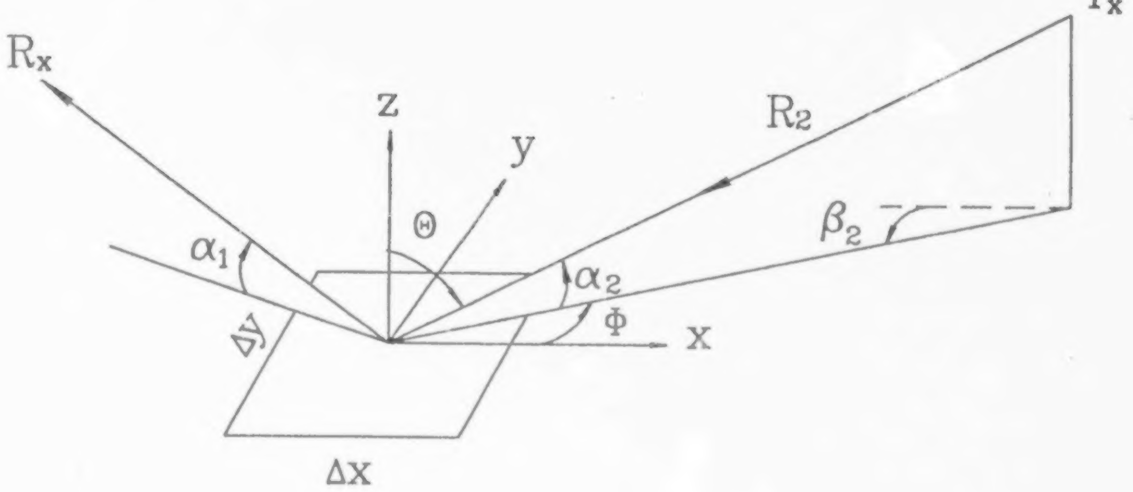
R_x
z
y
R_2
T_x
Θ
α_1
α_2
β_2
Φ
x
Δy
Δx

Figure 3.2: Signal intercepted by a facet

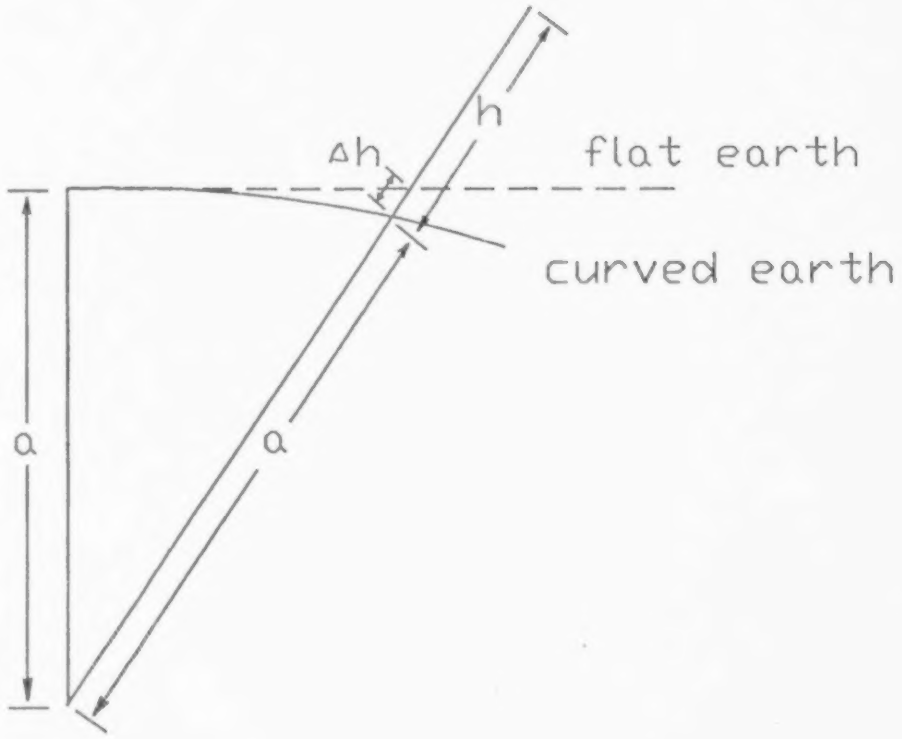
h
Δh
flat earth
curved earth
a
a

Figure 3.3: The fall–off of the curved earth with respect to a flat earth

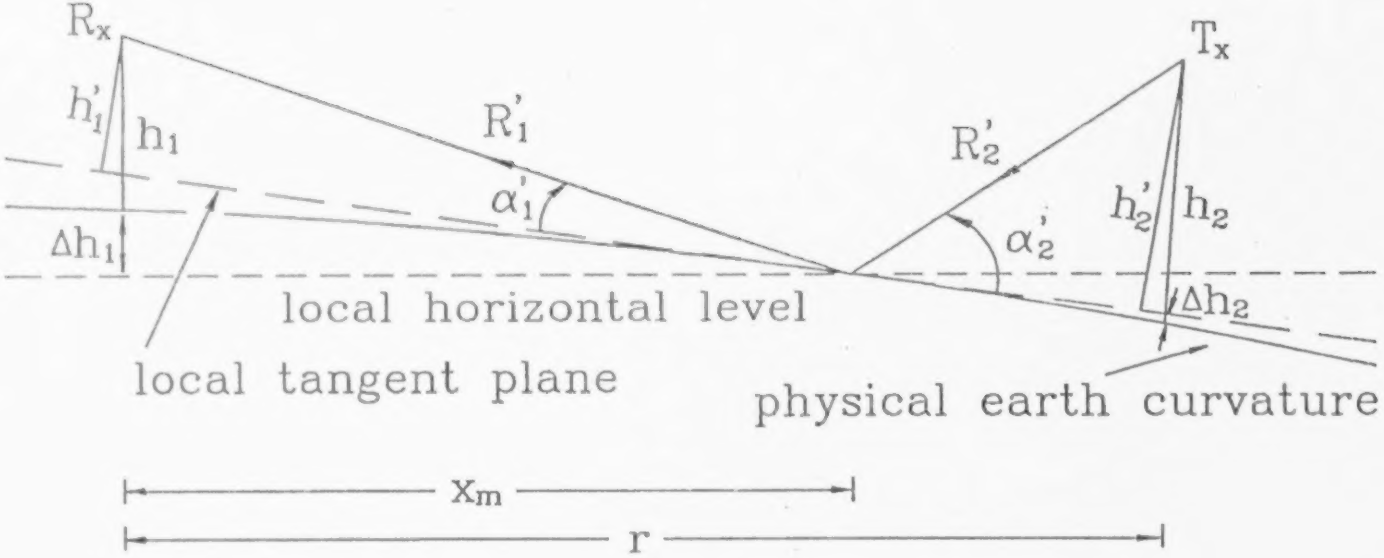
R_x
T_x
h_1'
h_1
Δh_1
R_1'
α_1'
R_2'
α_2'
h_2'
h_2
Δh_2
local horizontal level
local tangent plane
physical earth curvature
x_m
r

Figure 3.4: Curved earth geometry

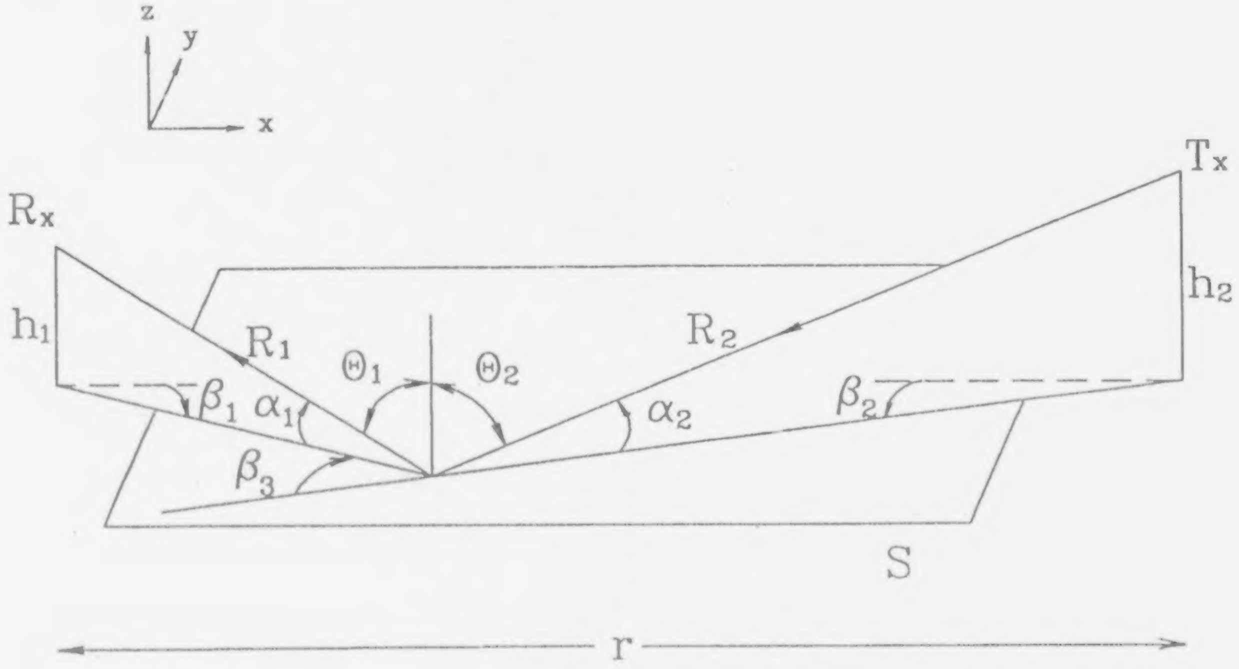
z
y
x
R_x
T_x
h_1
h_2
R_1
R_2
Θ_1
Θ_2
α_1
α_2
β_1
β_2
β_3
S
r

Figure 3.5: Depolarization of a scattered wave

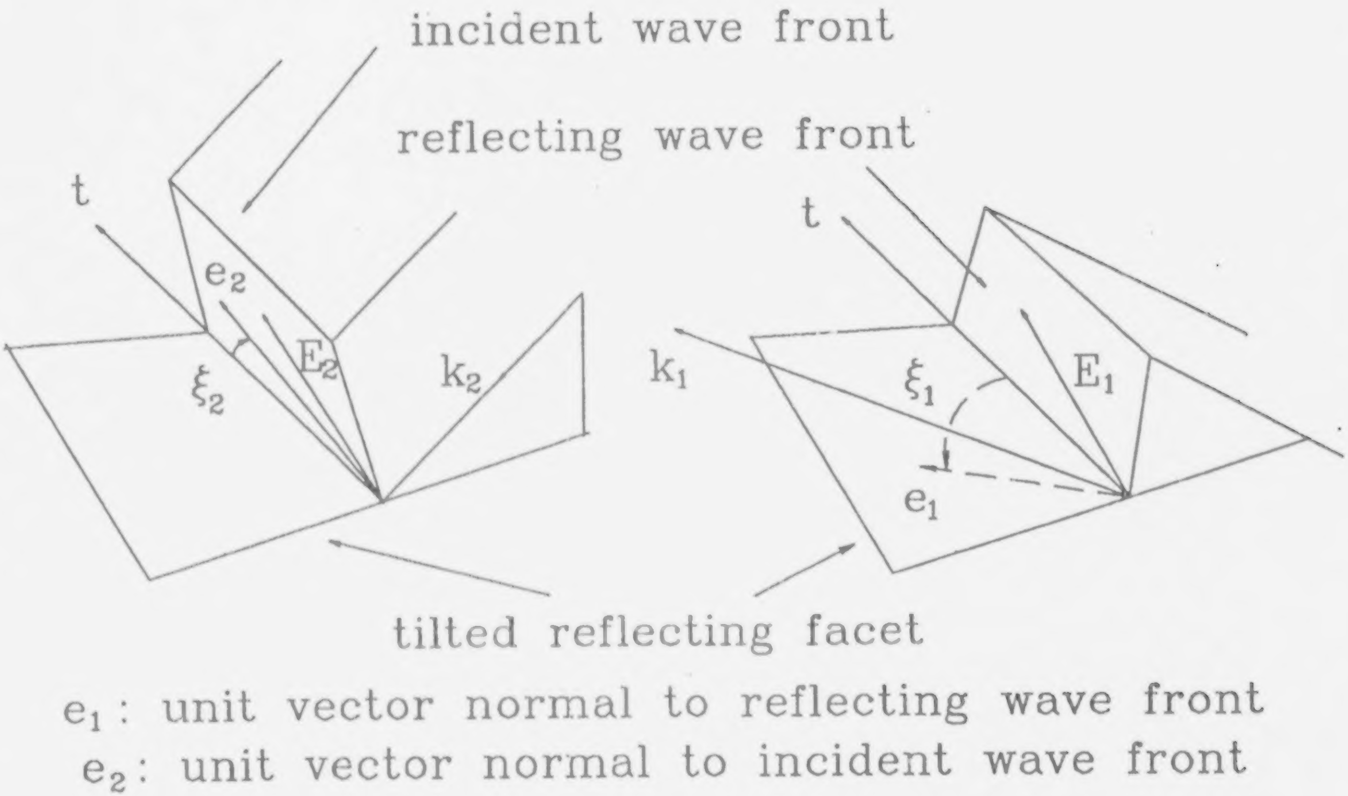
incident wave front
reflecting wave front
t
e_2
E_2
ξ_2
k_2
t
k_1
ξ_1
E_1
e_1
tilted reflecting facet
e_1 : unit vector normal to reflecting wave front
e_2: unit vector normal to incident wave front

Figure 3.6: General orientation of the direction of propagation with respect to the reflecting plane

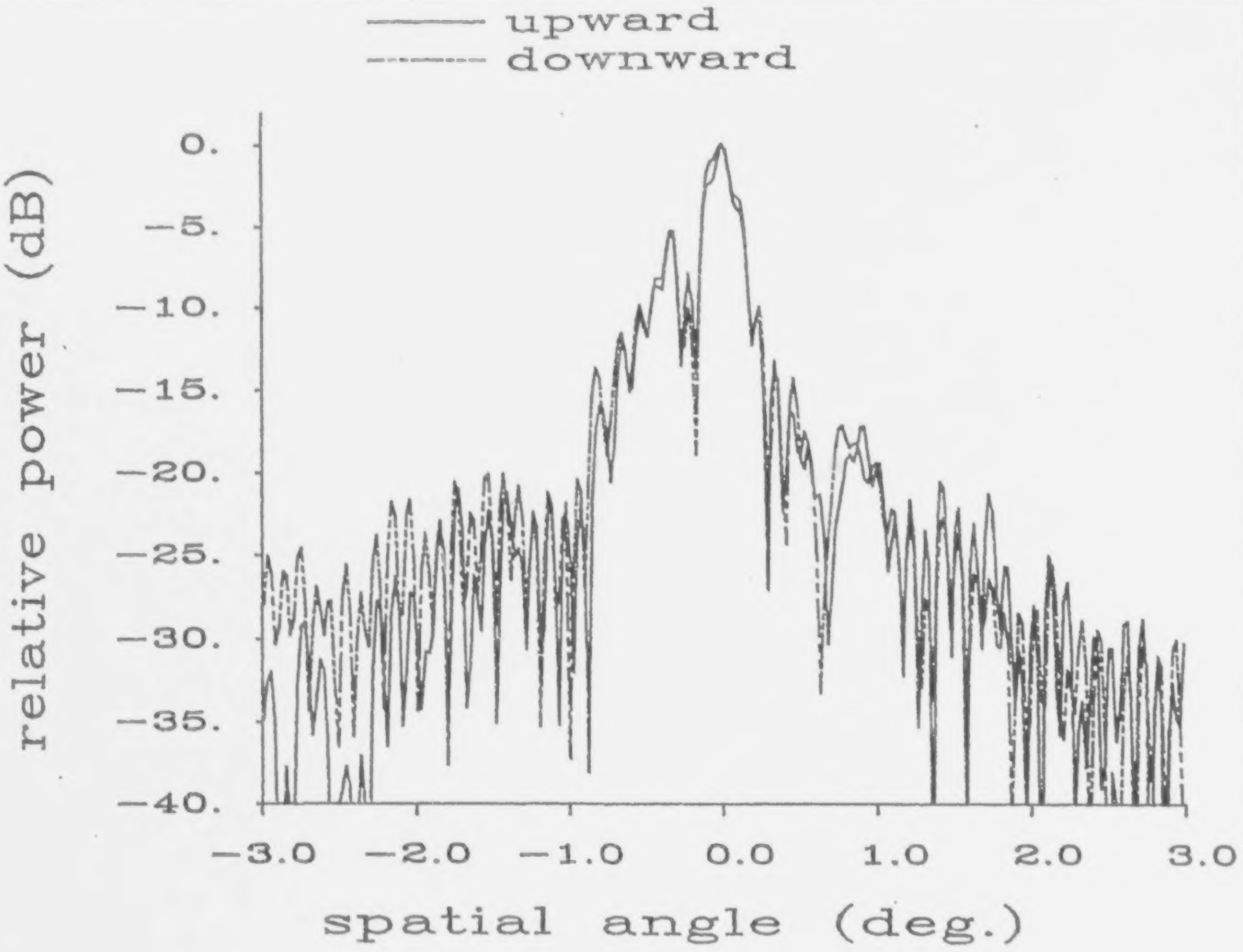

Fig. 4.1 The FFT beamforming result of a typical data set prior to phase correction.

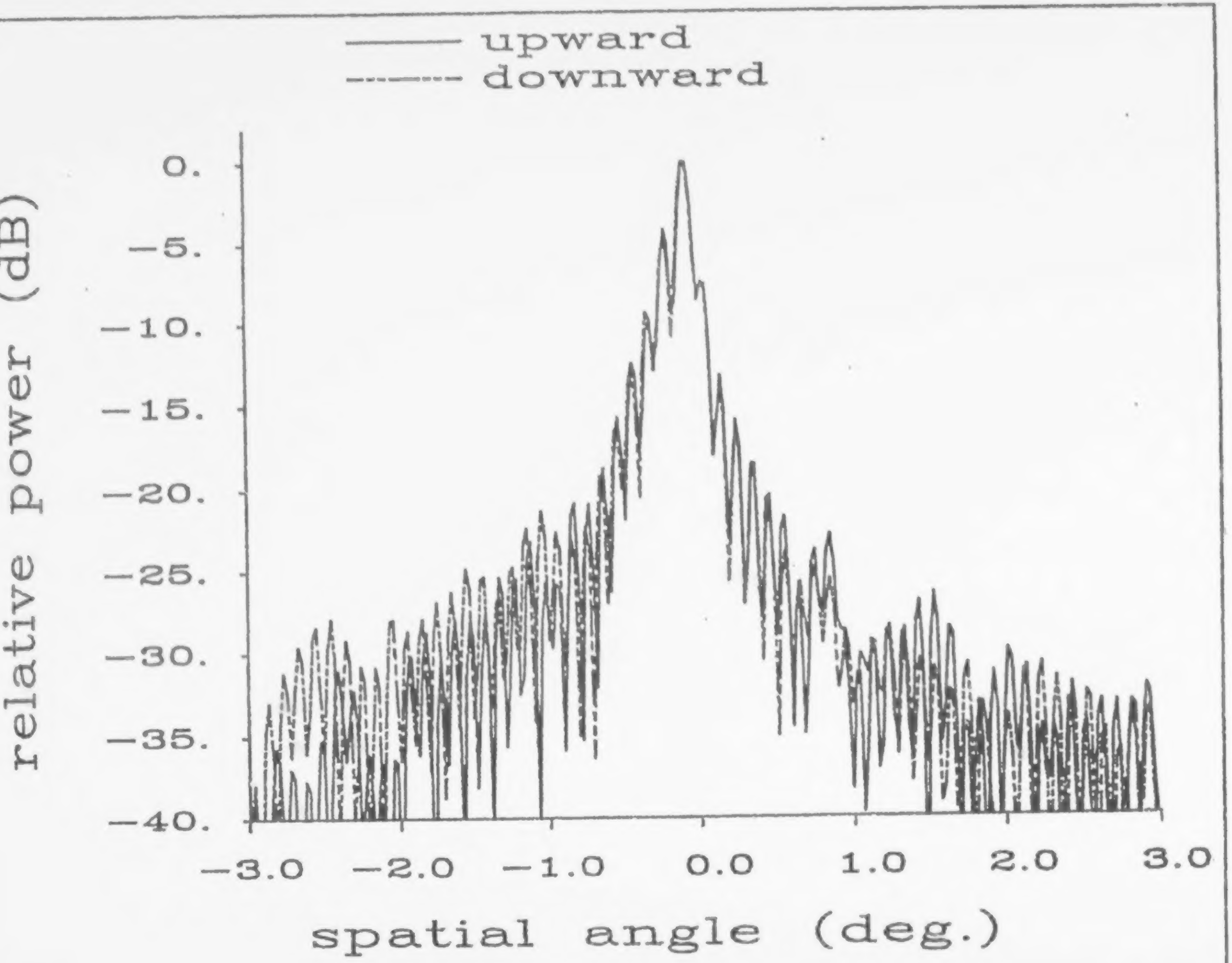

Fig. 4.2 The FFT beamforming result of the same data set used in Fig. 4.1 after phase correction.

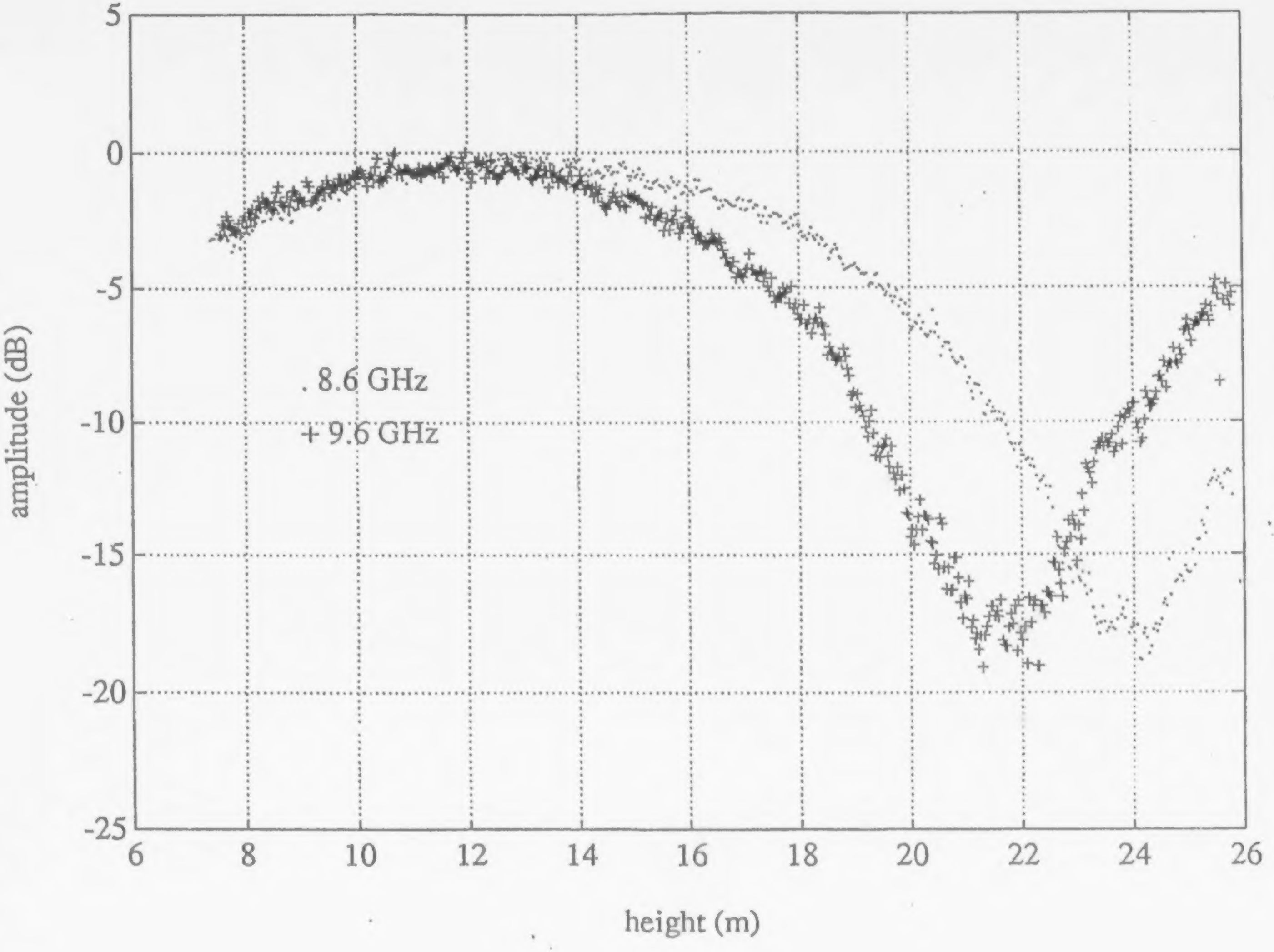

Fig. 4.3 A typical profiler trace, dN/dh = –35 Nunit/Km.

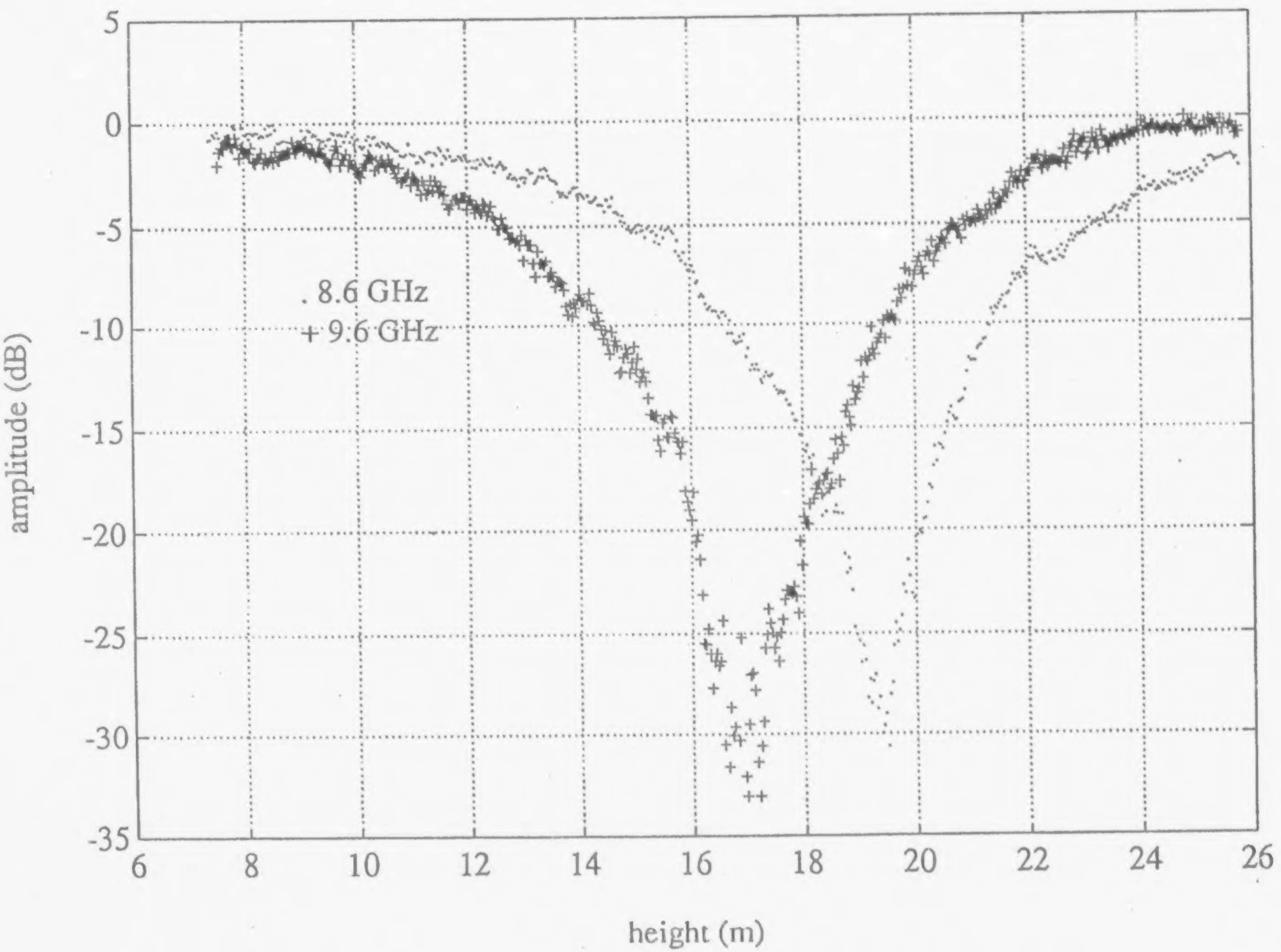

Fig. 4.4 A typical profiler trace, dN/dh = –157 Nunit/Km.

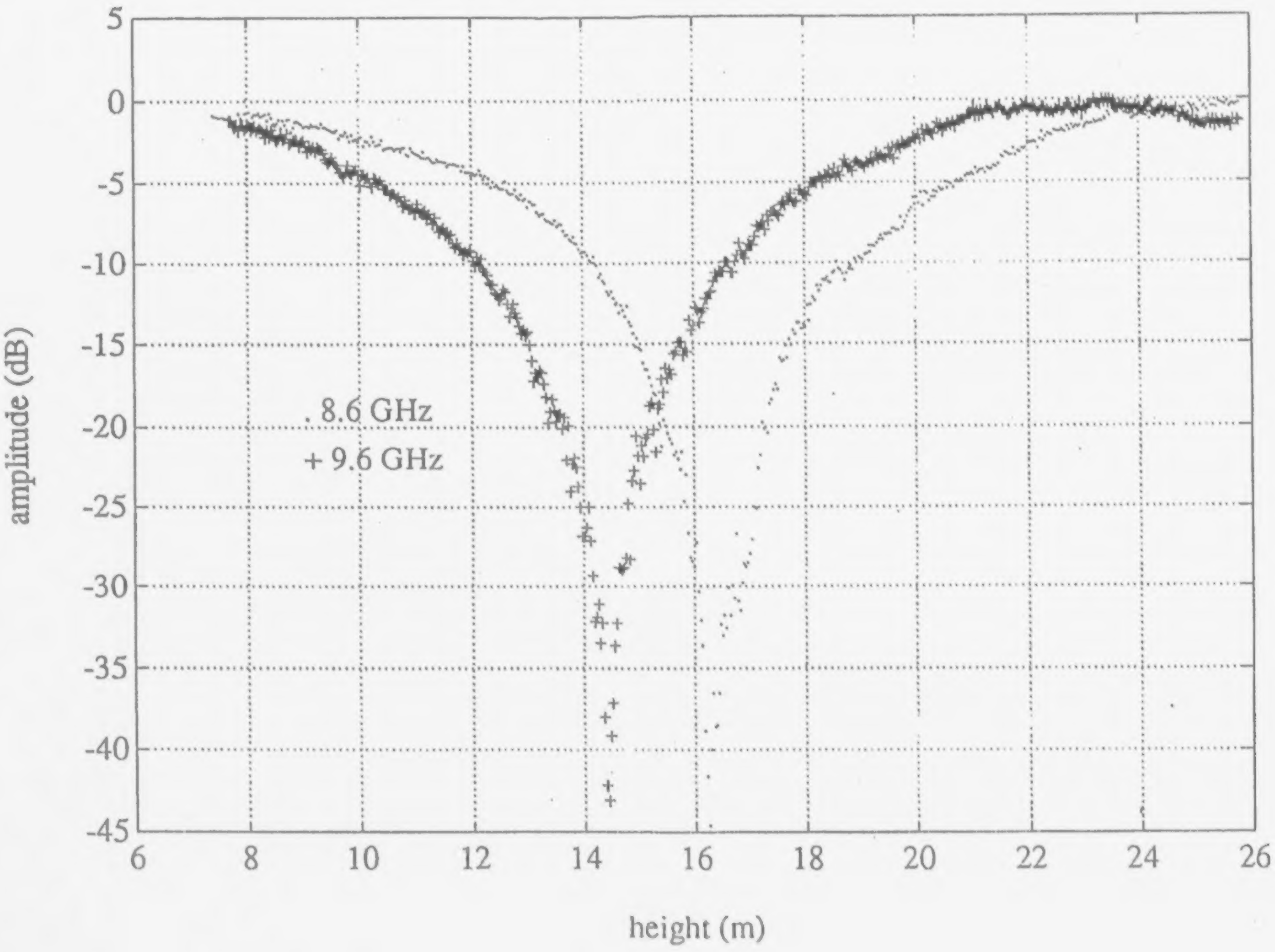

Fig. 4.5 A typical profiler trace, dN/dh = –212 Nunit/Km.

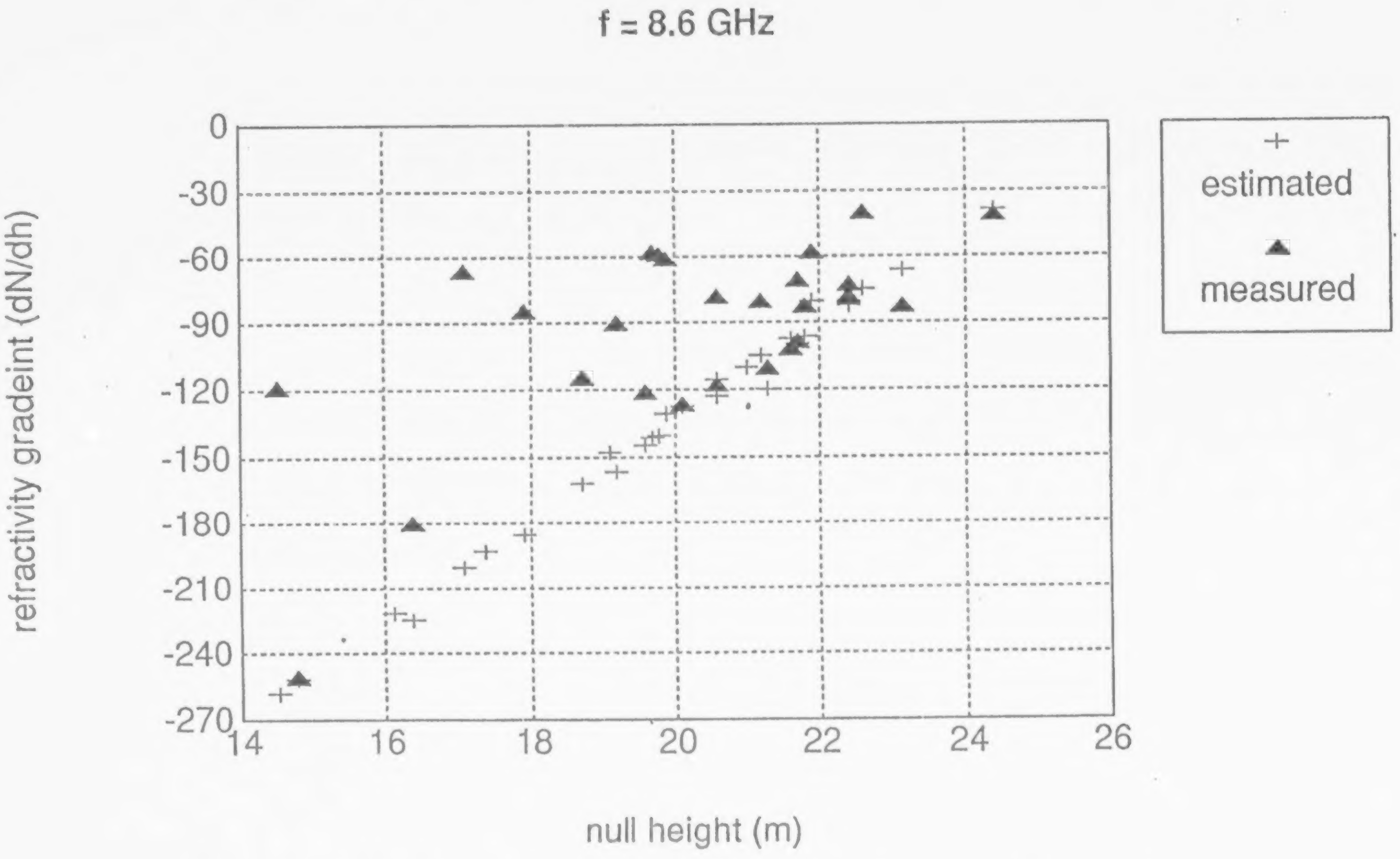

Fig. 4.6 Refractivity gradient verse null height for 8.6 GHz signal, comparison of measured and estimated values.

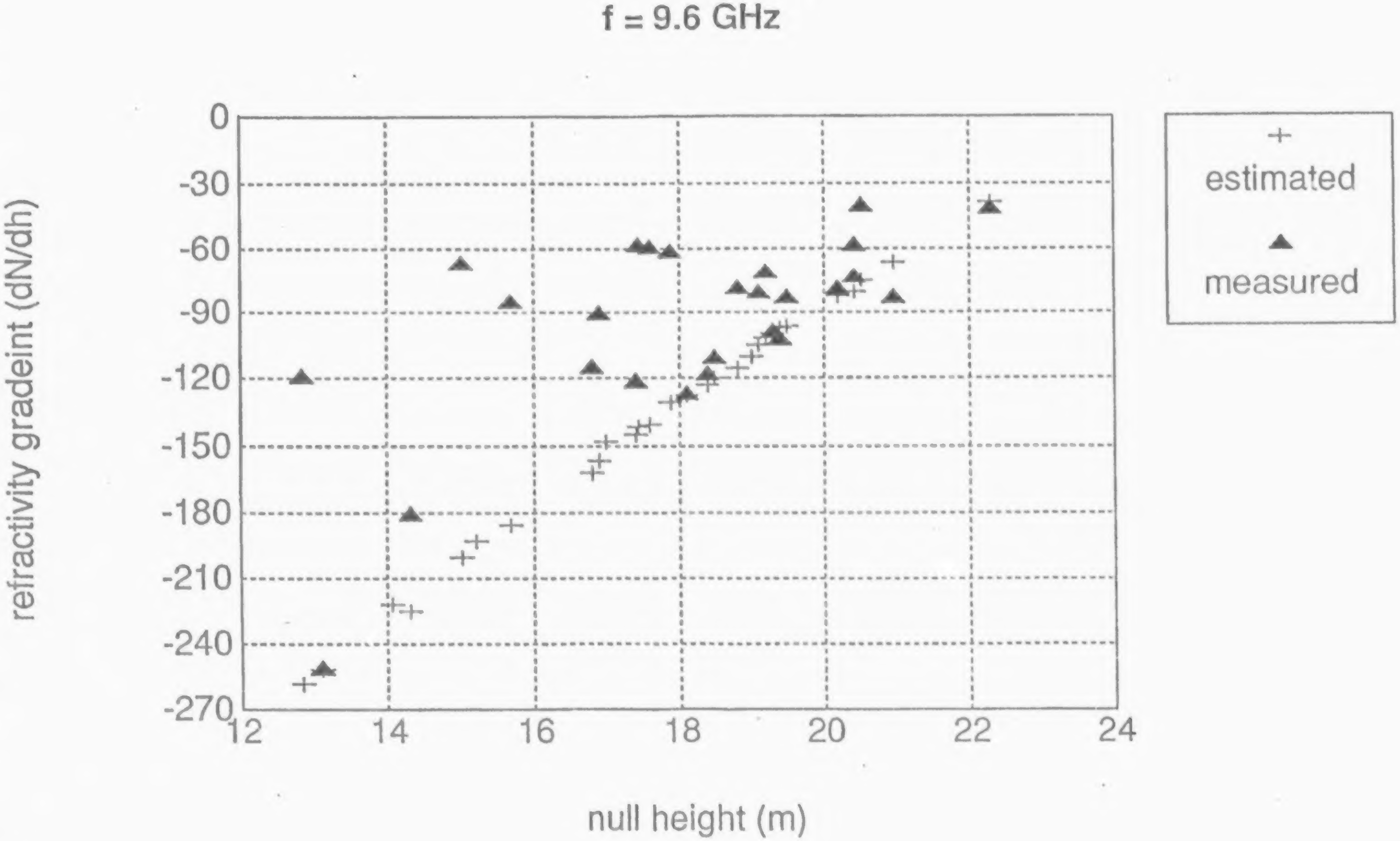

Fig. 4.7 Refractivity gradient verse null height for 9.6 GHz signal, comparison of measured and estimated values.

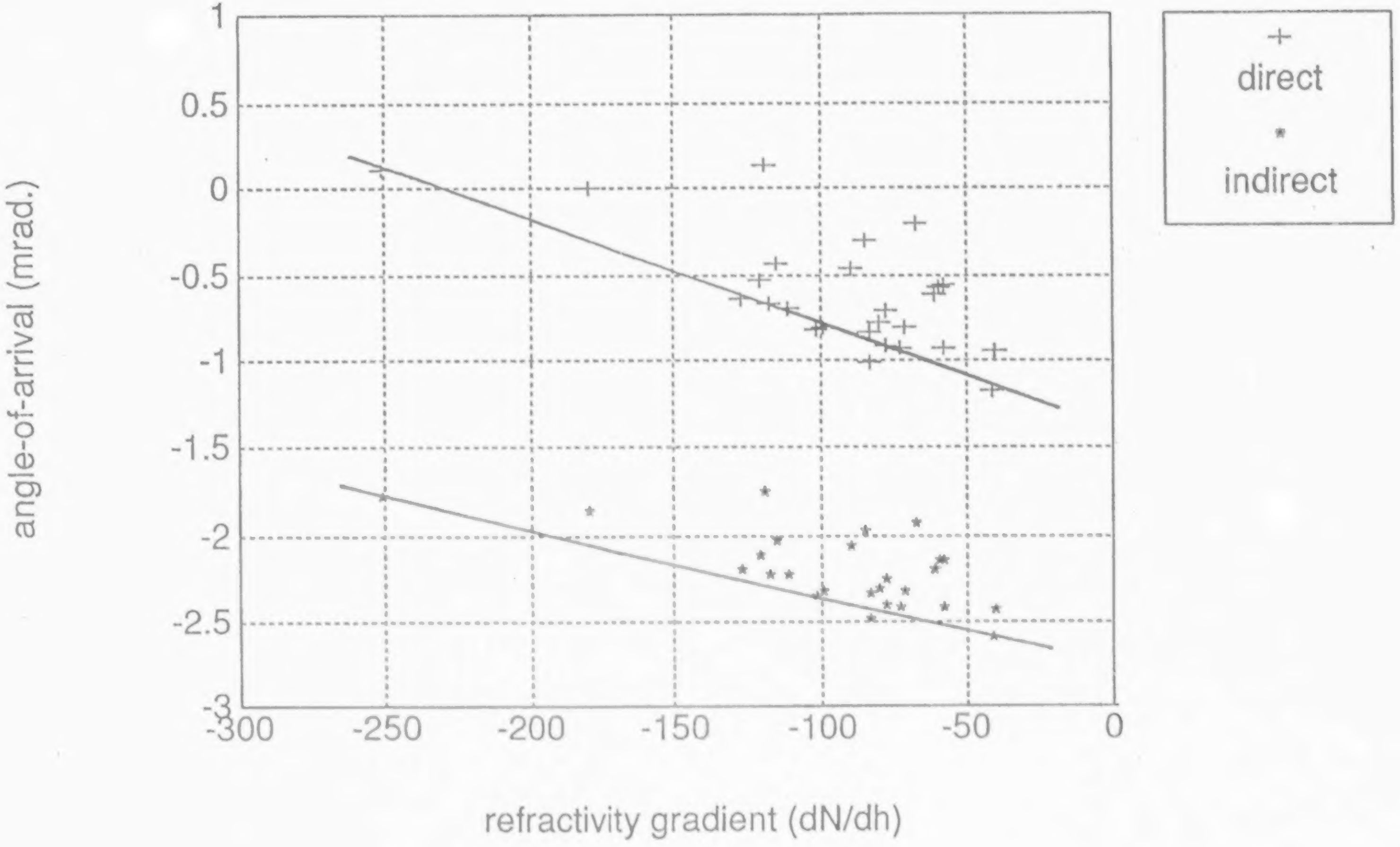

Fig. 4.8 Angle-of-arrival verse refractivity gradient, comparison of measured and theoretical values.

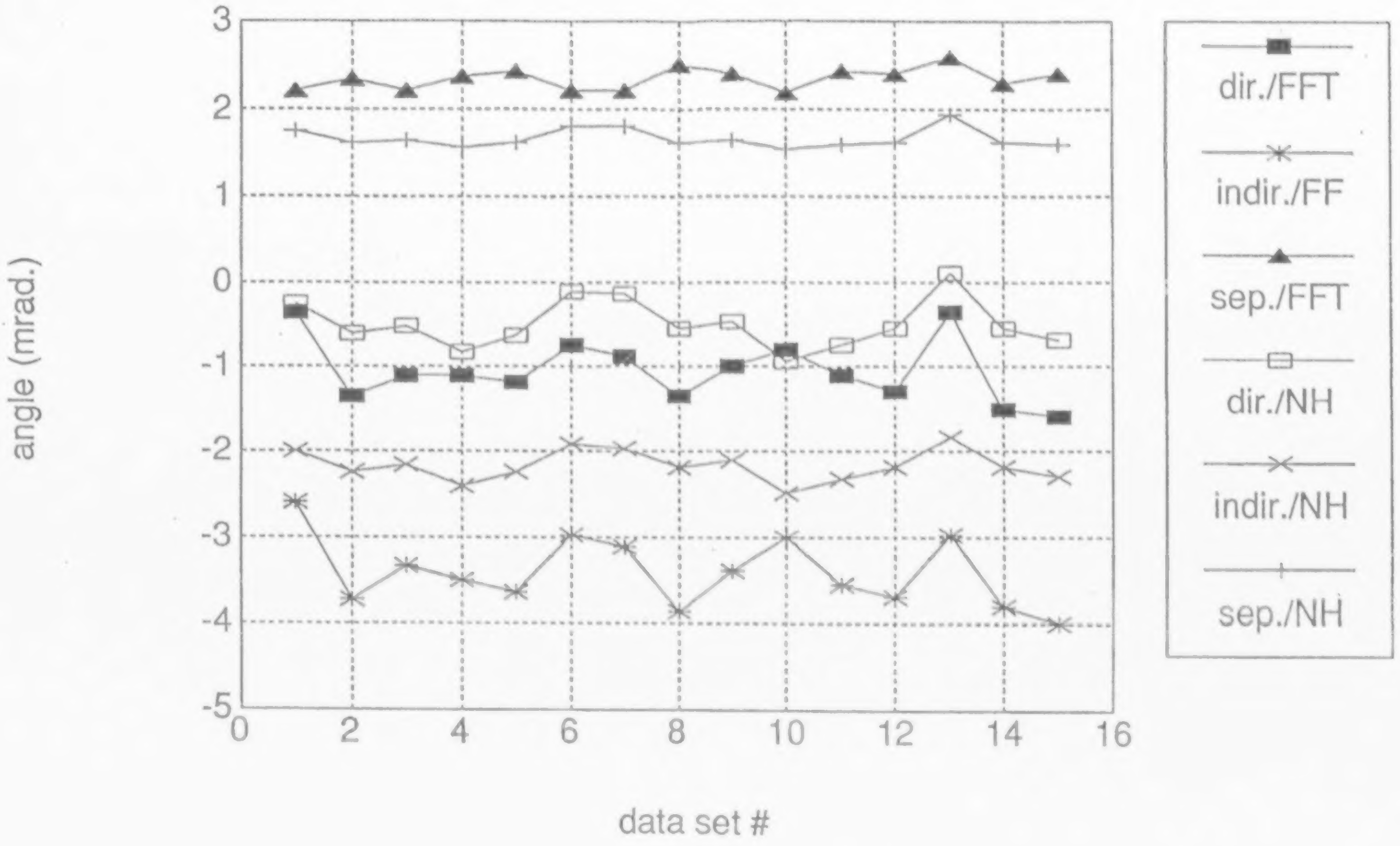

Fig. 4.9 Comparison of the results of angles-of-arrival based on the FFT beamforming technique and null height information.

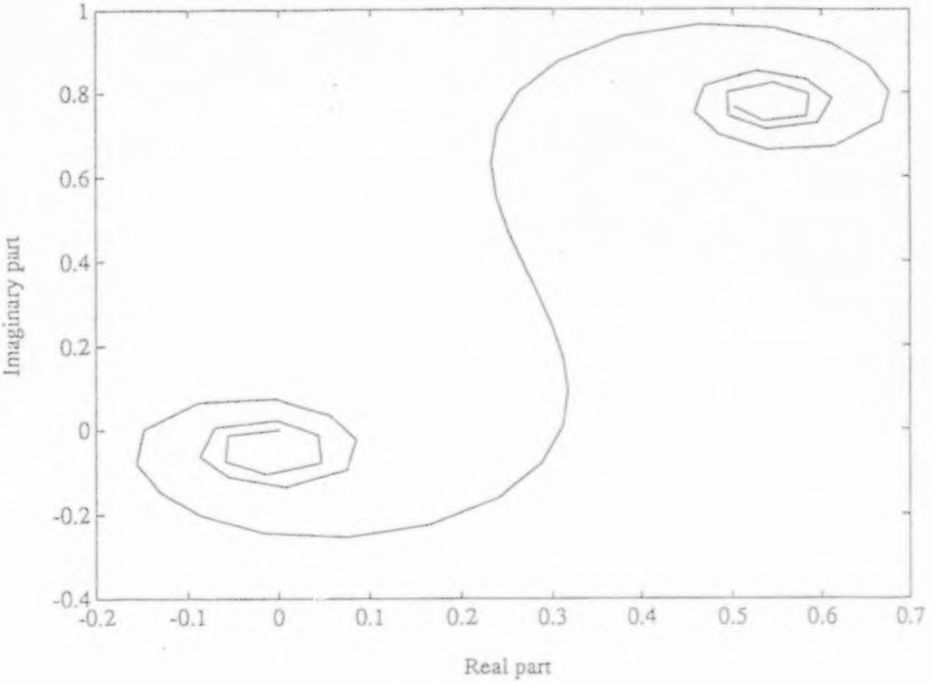

(a) zero sea–state

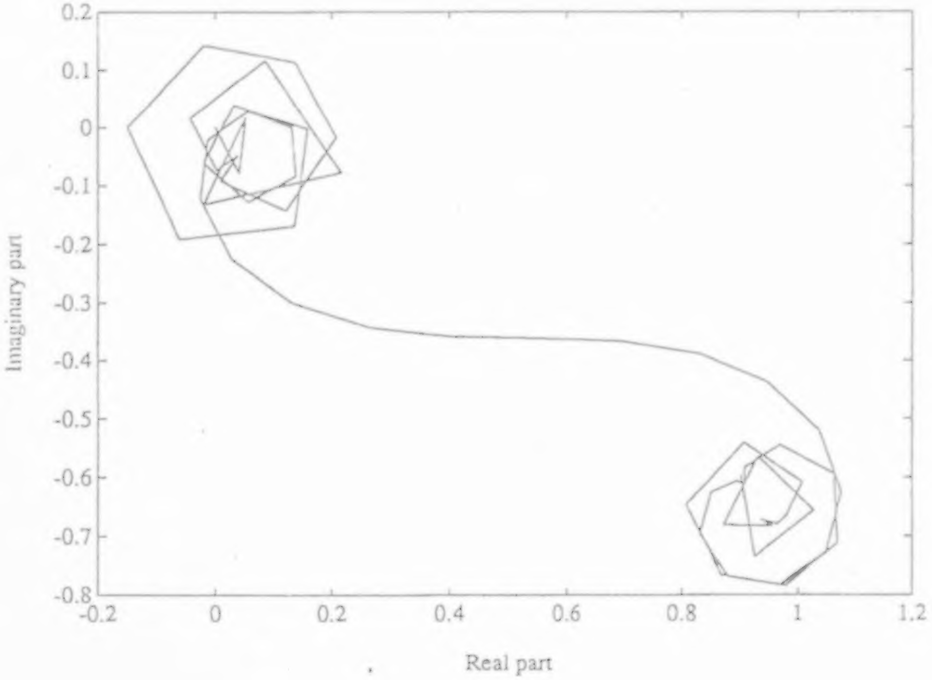

(b) high sea–state

Figure 5.1: Normalized Cornu spiral plot

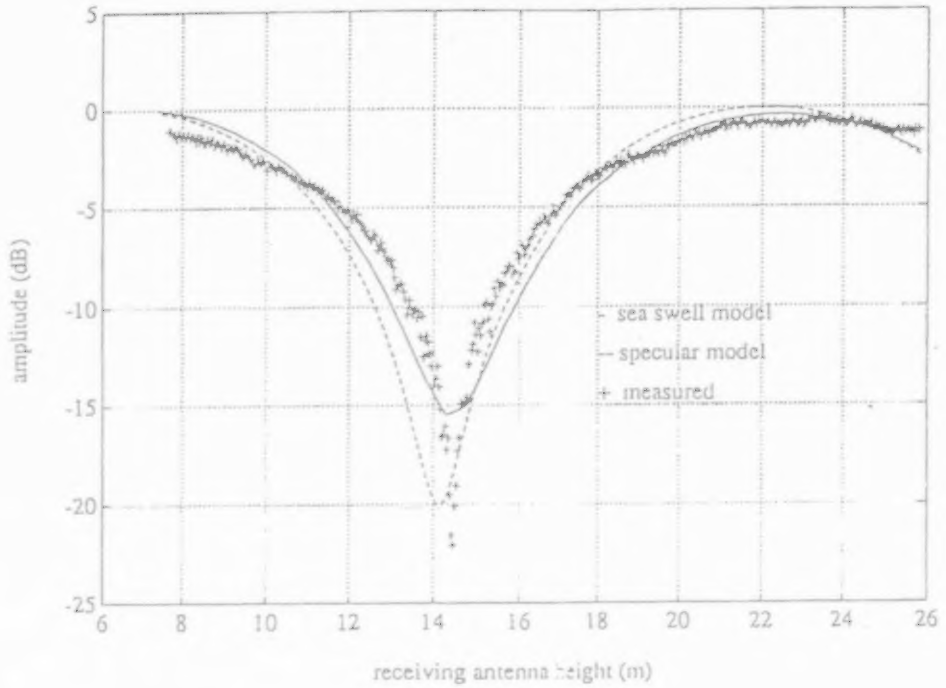

(a) dN/dh = –222 Nu/km, target height = 11.09 m, centre of aperture = 16.61 m, wave: height(rms) ≈ 0.2 m, length = 28–32 m, period = 10–20 seconds.

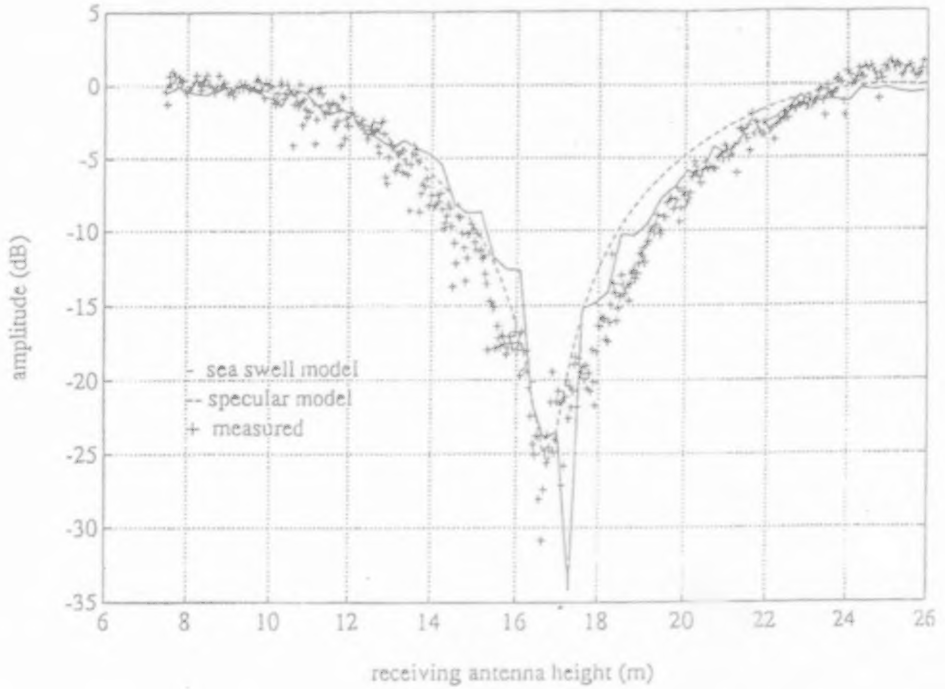

(b) dN/dh = –157 Nu/km, target height = 11.16 m, centre of aperture = 16.69 m, wave: height(rms) ≈ 0.5 m, length = 4–6 m, period = 10–20 seconds.

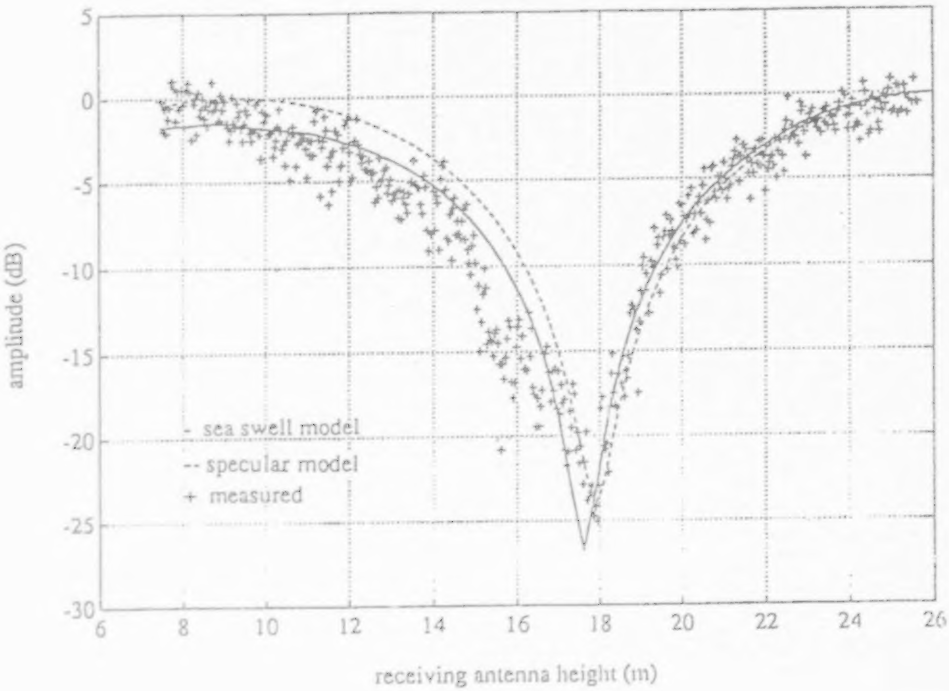

(c) $dN/dh = -131$ Nu/km, target height = 11.16 m, centre of aperture = 16.69 m, wave: height(rms) ≈ 0.5 m, length = 80–260 m, period = 5–22 seconds.

Figure 5.2: Interference patterns of a vertically polarized signal. Simulations are verified against real data. $f = 9.6$ GHz, $r = 11.972$ km, $\varepsilon_r = 80$, $\sigma = 4$ mho/m.

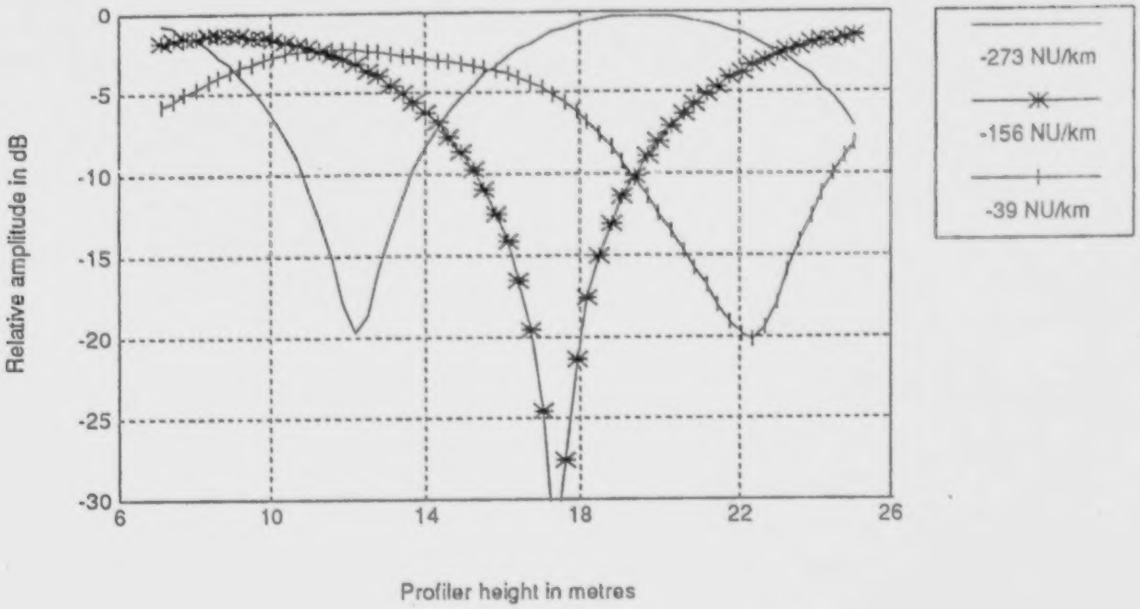

(a) Amplitude

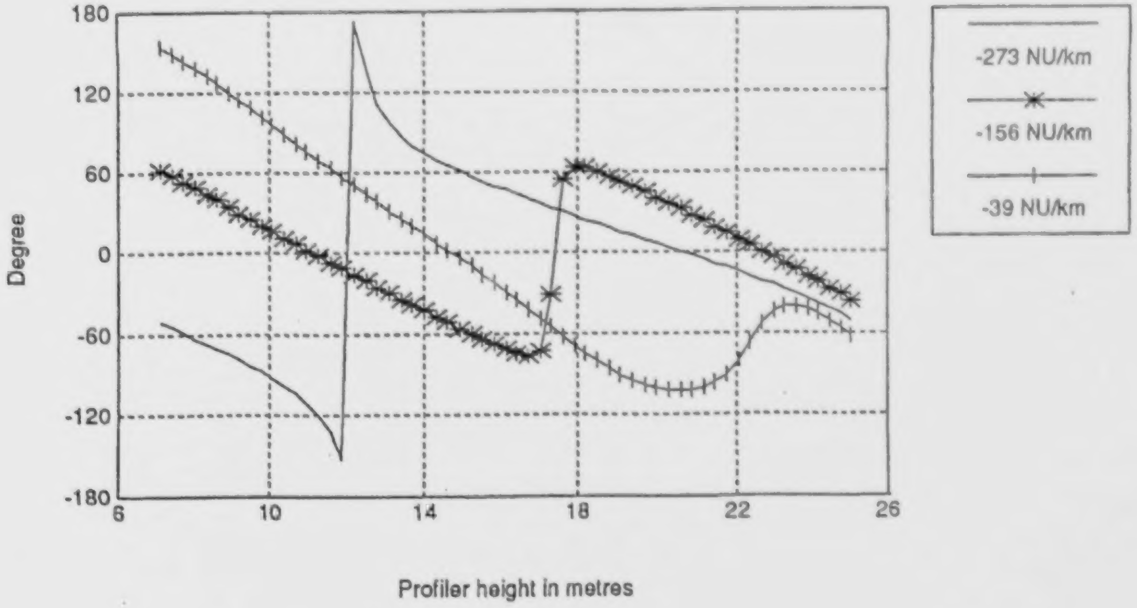

(b) Phase

Figure 5.3: Interference pattern with respect to atmospheric refraction. f = 9.6 GHz, r = 11.972 km, target height = 11.06 m, centre of aperture = 16.08 m. wave: height(p–p) = 0.1 m, length = 100 m, period = 10 m, propagation angle = 0 deg., ε_r = 80, σ = 4 mho/m.

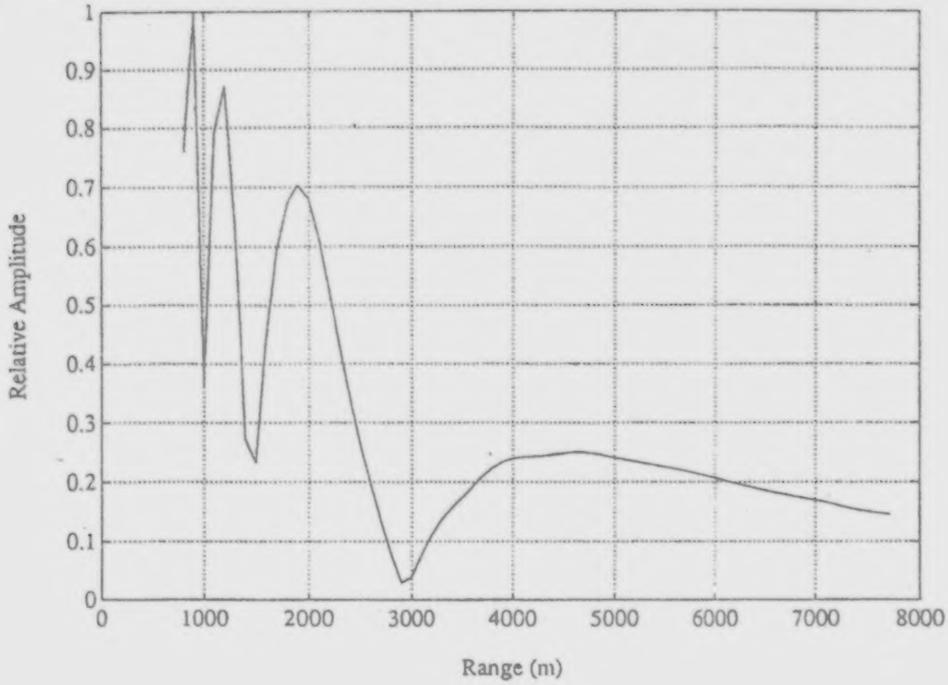

(a) Amplitude

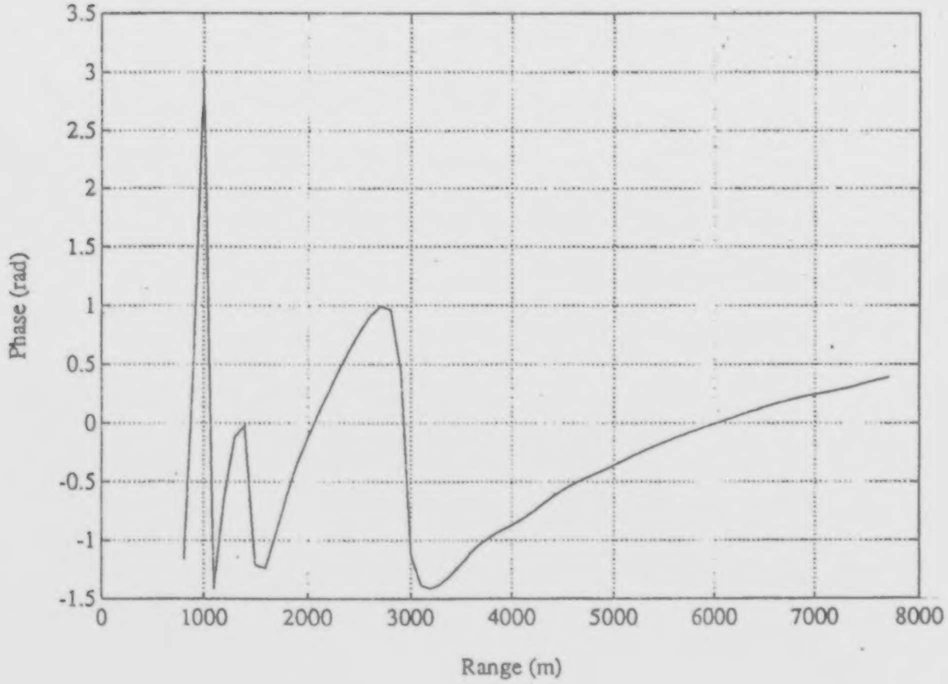

(b) Phase

Figure 5.4: Interference pattern versus range of a horizontally polarized signal. dN/dh = –157 Nu/km, f = 9.6 GHz, T_x = 10 m, R_x = 4.8 m, ε_r = 80, σ = 4 mho/m, wave: height(p–p) = 0.1 m, length = 100 m, period = 10 m, propagation angle = 0 deg.

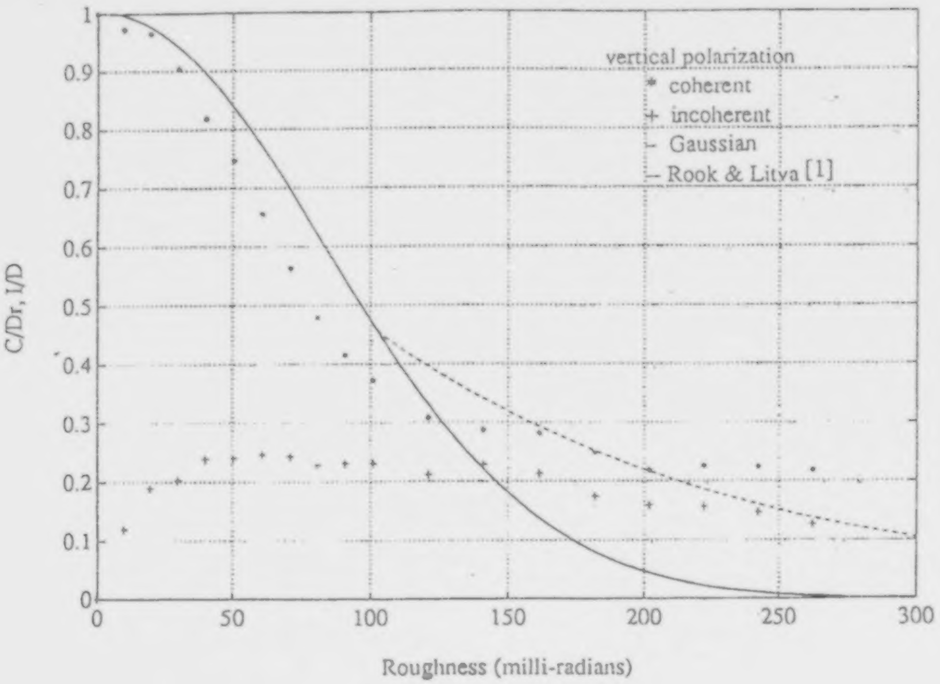

(a) Vertical polarization

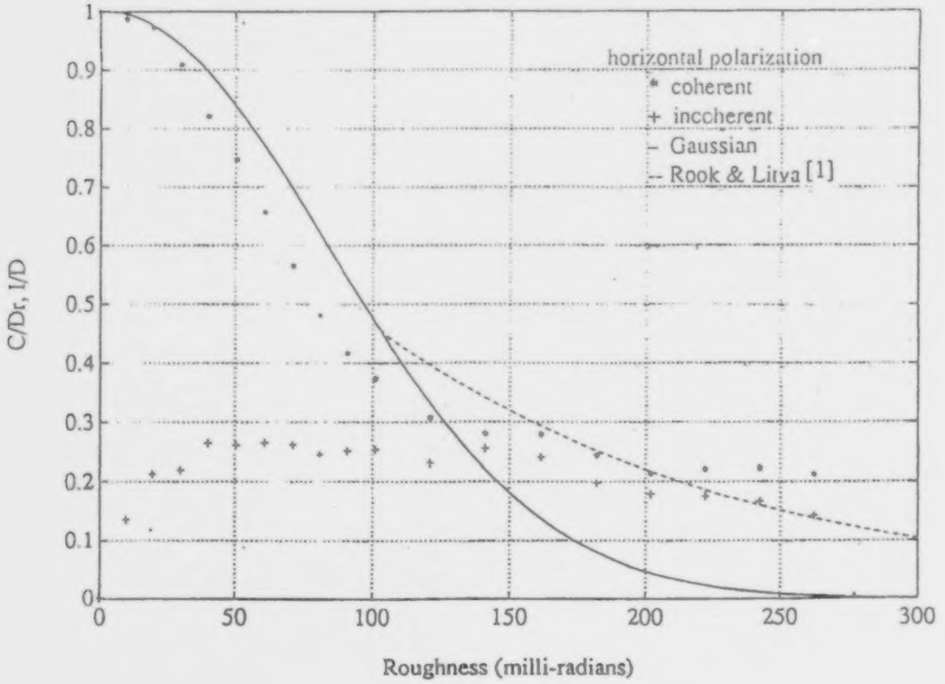

(b) Horizontal polarization

Figure 5.5: Scattering coefficients versus surface roughness. dN/dh = –157 Nu/km, f = 9.6 GHz, T_x = 11.06 m, R_x = 16.91 m, r = 11.972 km, ε_r = 80, σ = 4 mho/m. 60 time samples with Δt = 2 seconds and 60 waves superposed with length = 63–325 m, and period = 4.5–25 seconds.

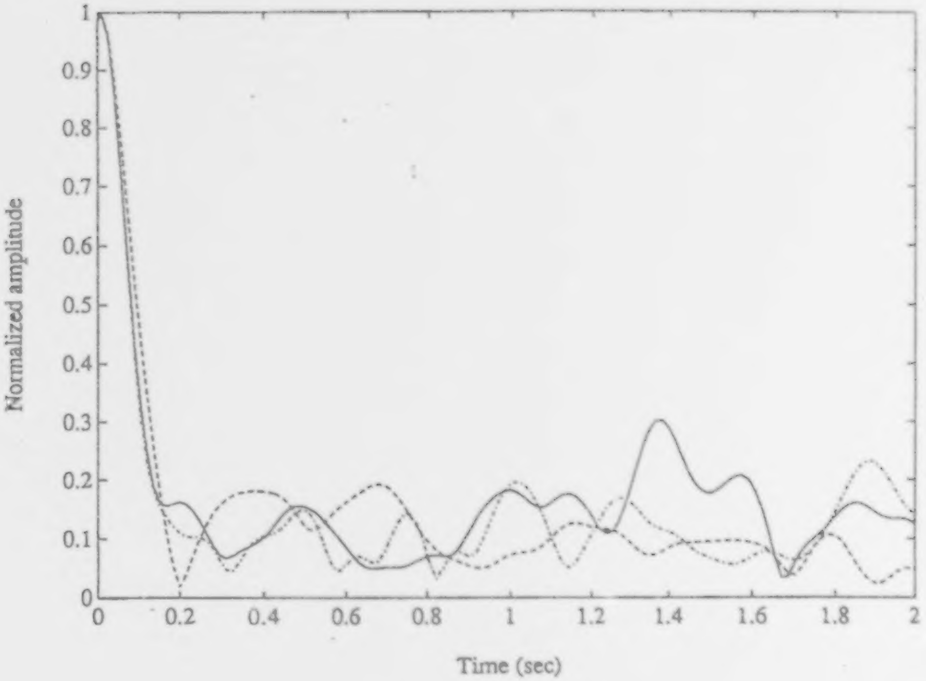

(a) Autocorrelation

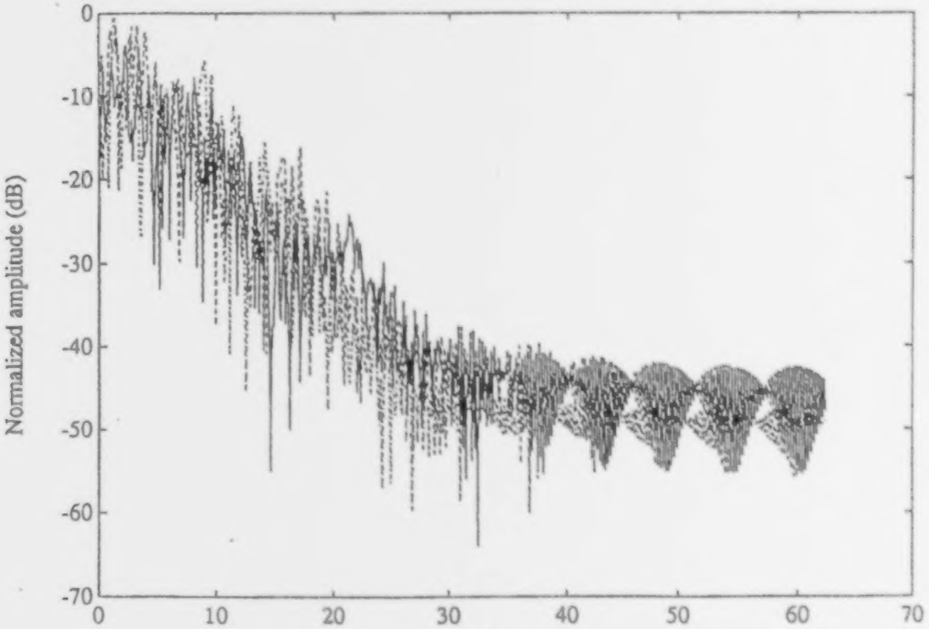

(b) Energy spectral density

Figure 5.6: Autocorrelation and energy spectral density of similar surface irregularities. dN/dh = −157 Nu/km, f = 10.2 GHz, T_x = 15 m, R_x = 9.5 m, r = 4.61 km, ε_r = 80, σ = 4 mho/m. 501 time samples with Δt = 0.016 second and 60 waves superposed with height(p–p) = 0.1–0.5 m, length = 20.5–50 m, and period = 2.1–4.9 seconds.

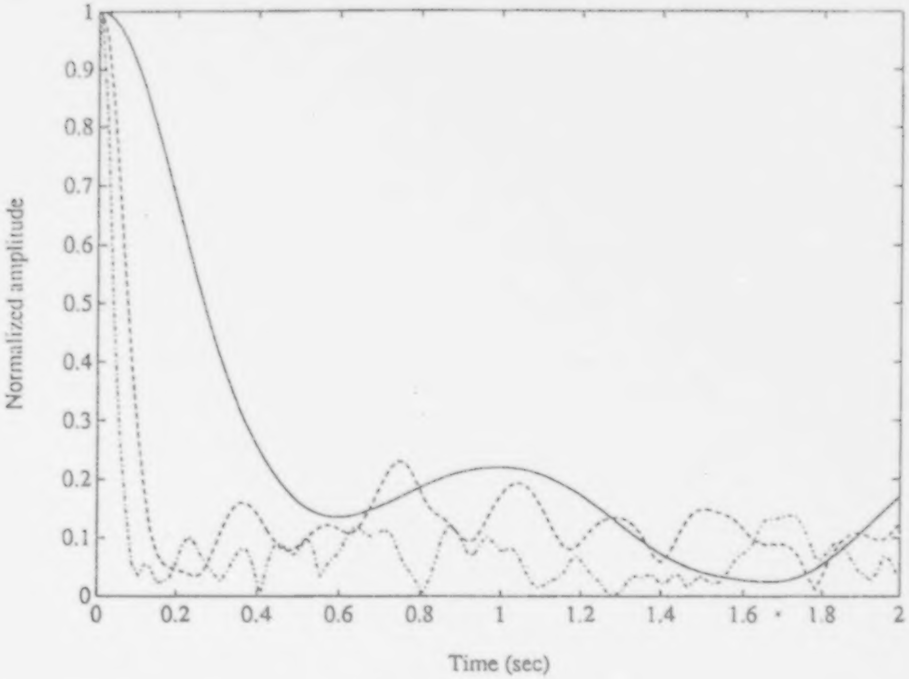

(a) Autocorrelation

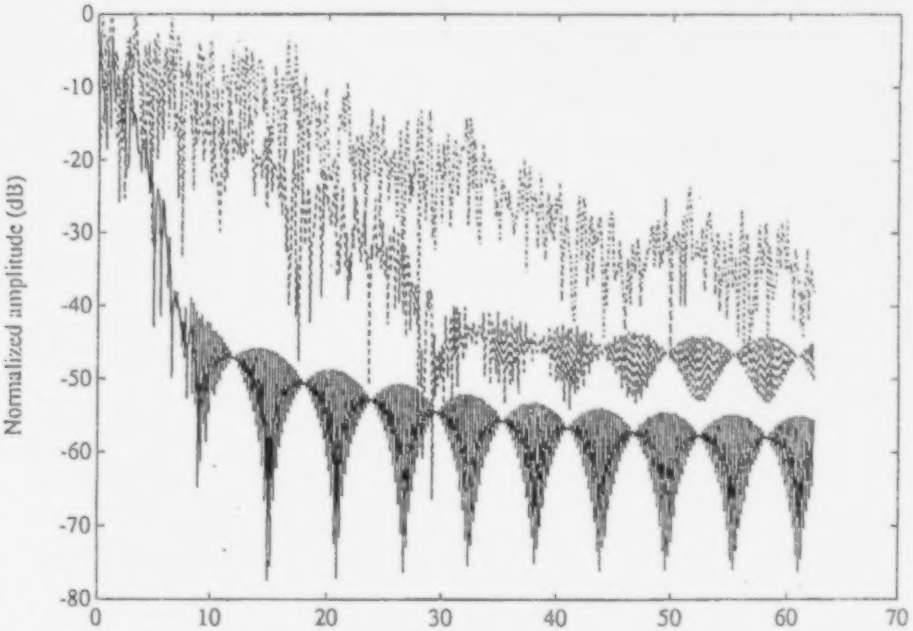

(b) Energy spectral density

Figure 5.7: Autocorrelation and energy spectral density of various surface irregularities. dN/dh = –157 Nu/km, f = 10.2 GHz, T_x = 15 m, R_x = 9.5 m, r = 4.61 km, ε_r = 80, σ = 4 mho/m. 501 time samples with Δt = 0.016 second and 60 wave superposed with length = 20.5–50 m, period = 2.1–4.9 seconds. —— height(p–p) = 0.1 m for all 60 waves, - - - height(p–p) = 0.1–0.5 m, –·– height(p–p) = 0.2–1 m.

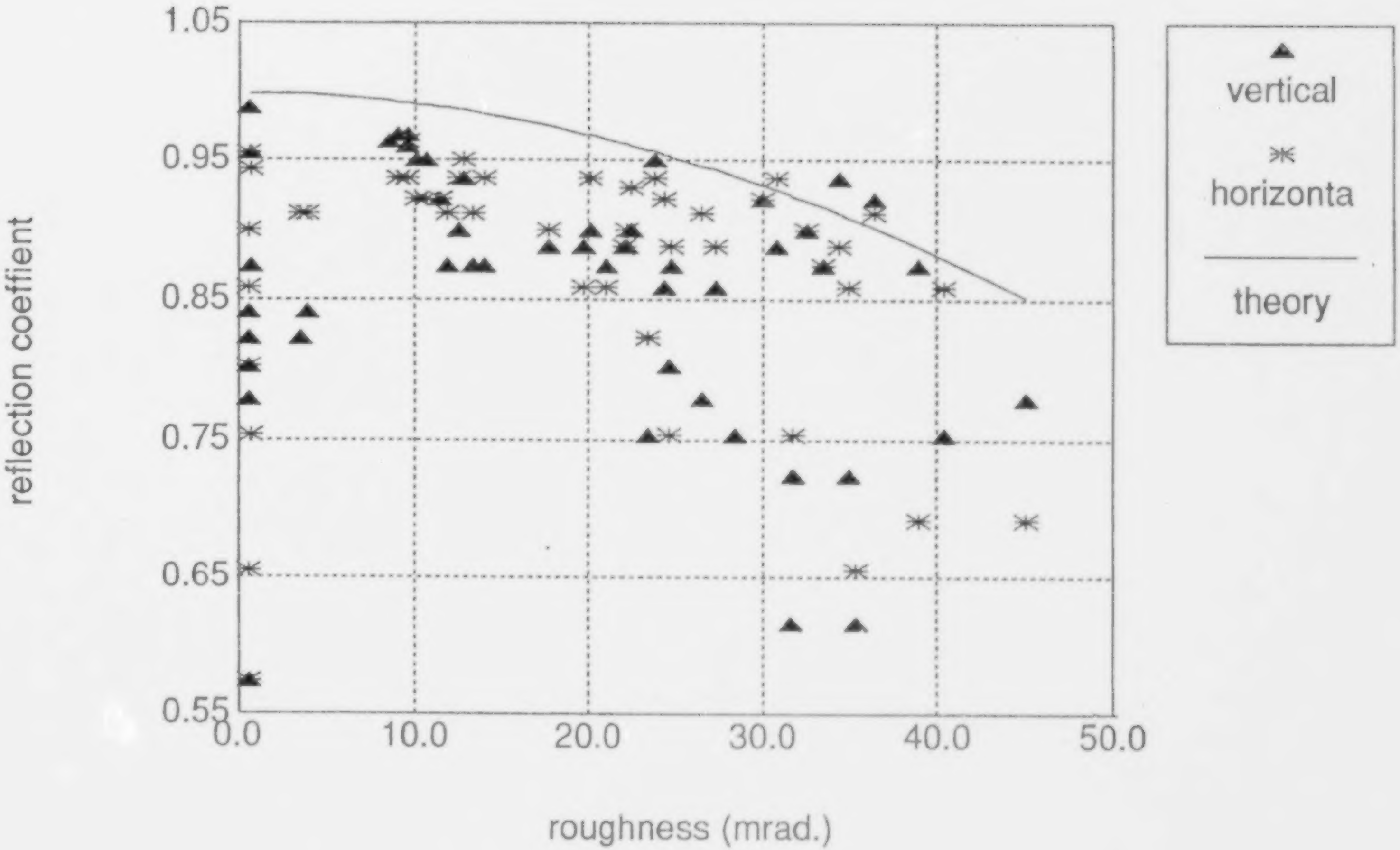

Fig. 6.1 Specular reflection coefficient as a function of roughness parameter.

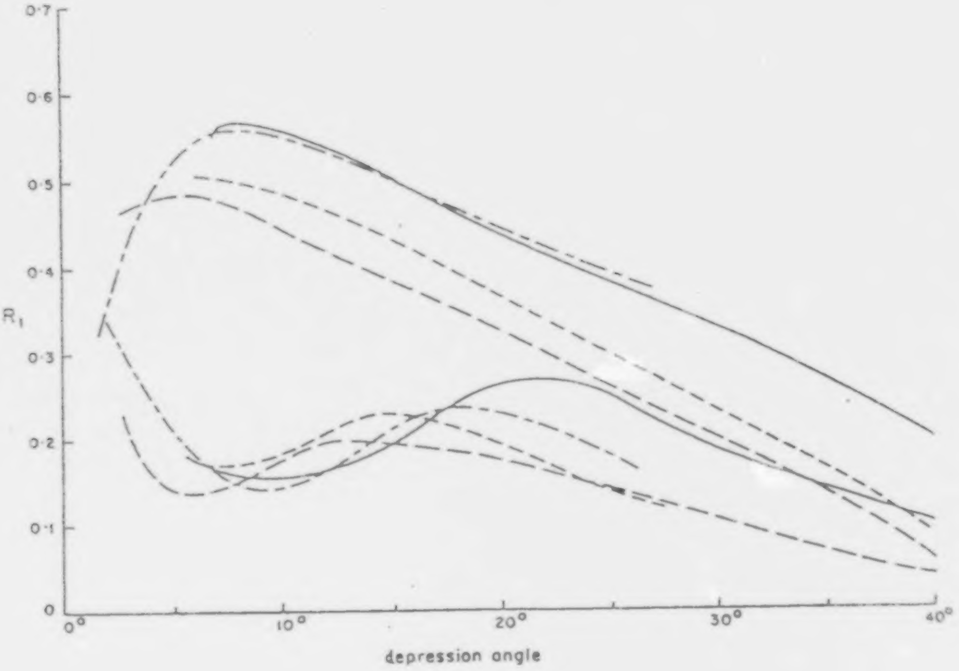

Summary of curves of voltage-reflection coefficient R_1

—— sea state 1
—— sea state 1–2
- - - - sea state 2–3
— — sea state 3–4
Upper curves, horizontal polarisation
Lower curves, vertical polarisation

Fig. 6.2 Reflection coefficient as a function of depression angle. (Source: M. Hunter and T. Senior, "Experimental Studies of Sea–Surface effects on Low–Angle Radars," Proc. IEE, vol. 113, no. 11, Nov. 1966.)

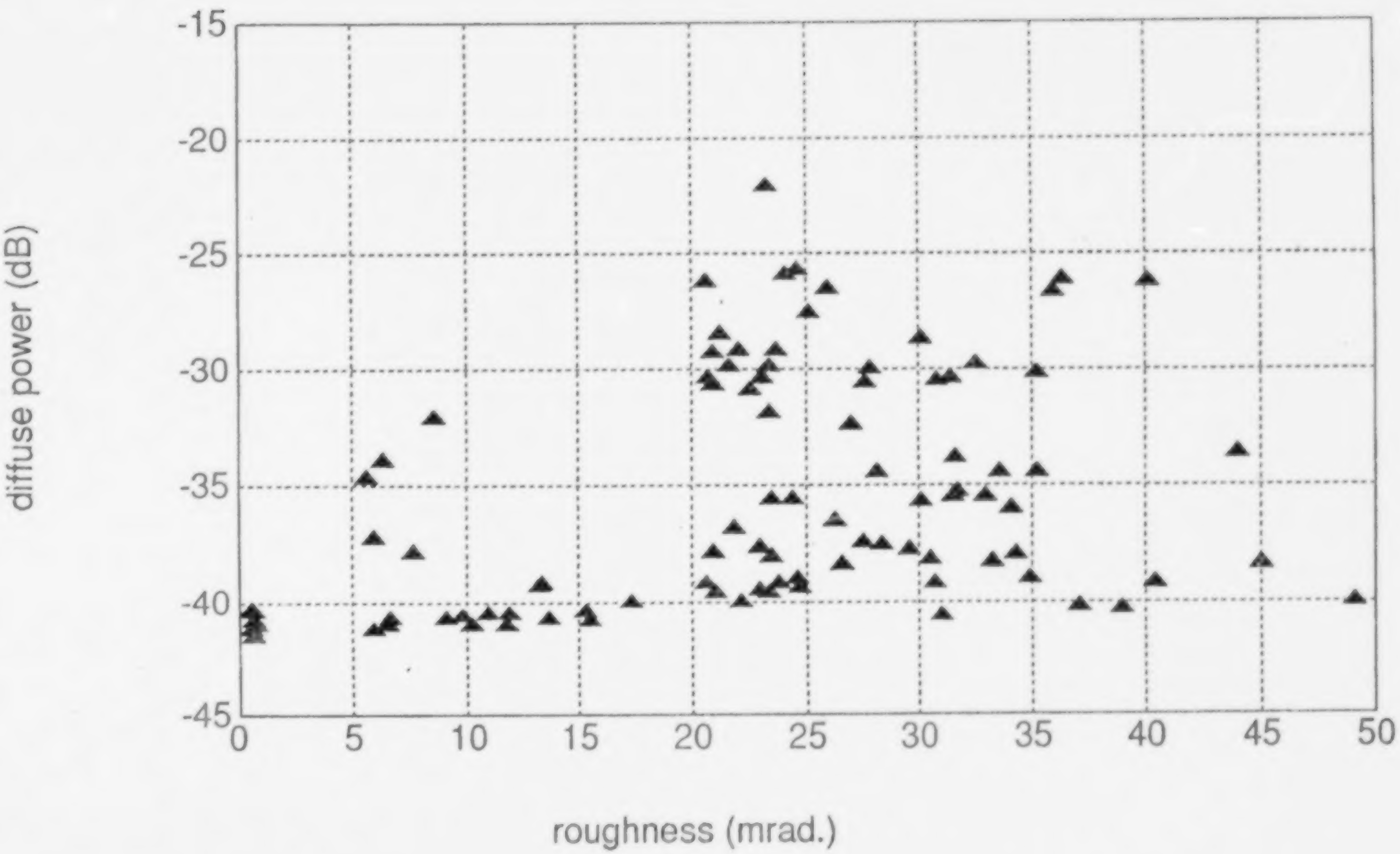

Fig. 6.3 The diffuse signal power of vertical polarization as a function of roughness parameter.

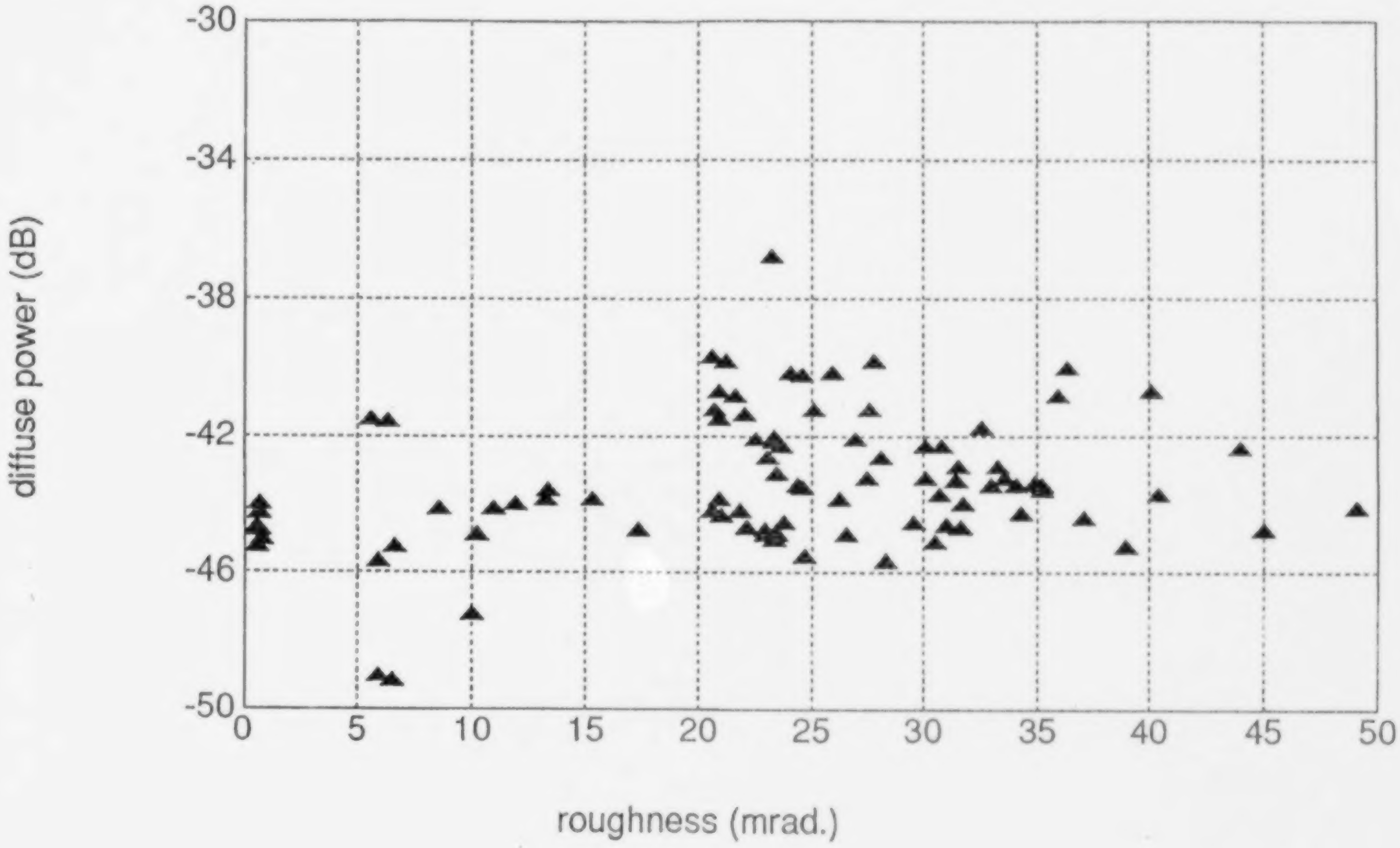

Fig. 6.4 The diffuse signal power of horizontal polarization as a function of roughness parameter.

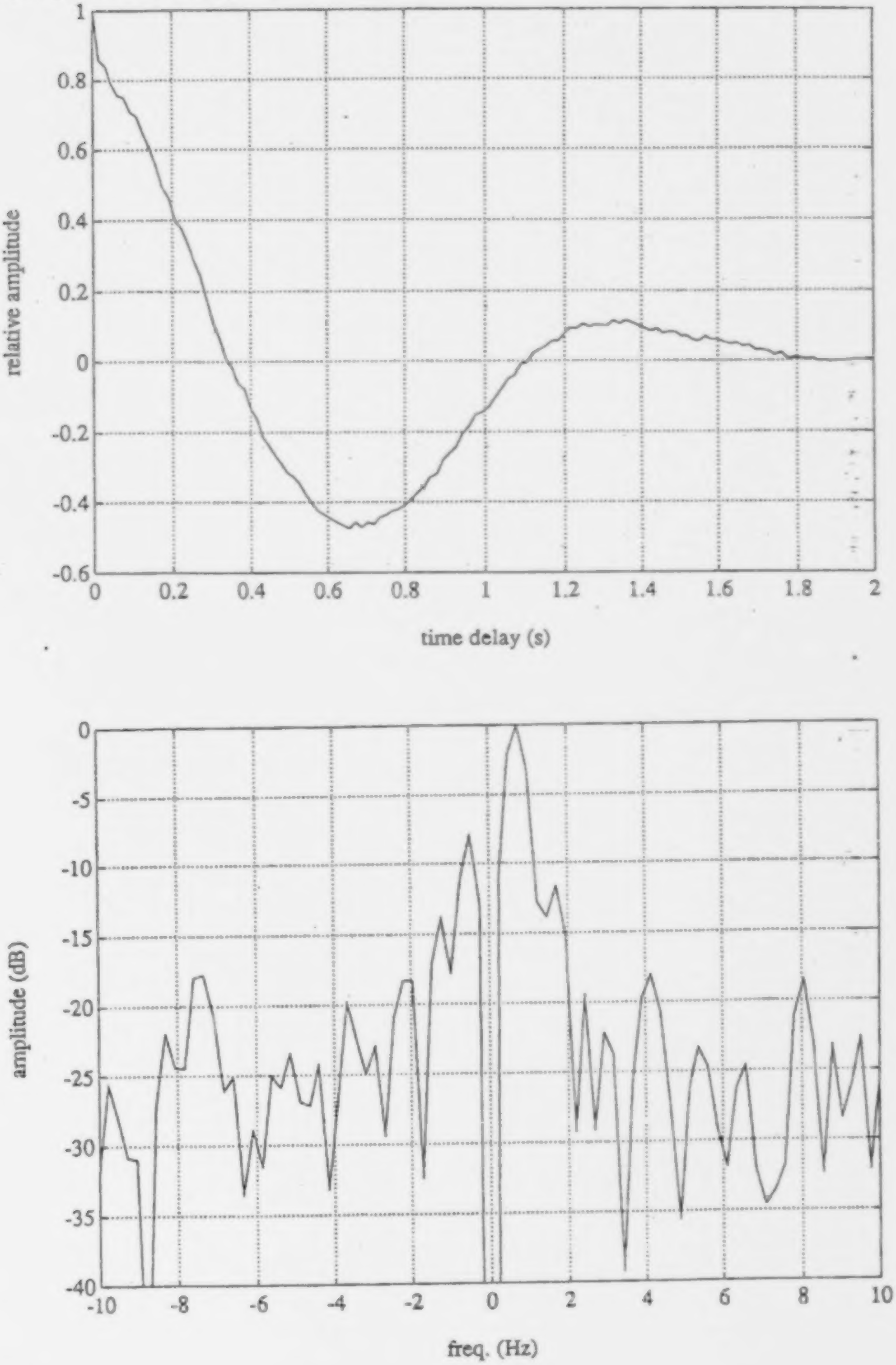

Fig. 6.5 Temporal auto–correlation function and power spectrum derived from a representative data set from Lake Huron trials. Recorded on Nov. 4, 1987, f = 10.2 GHz, horizontal polarization.

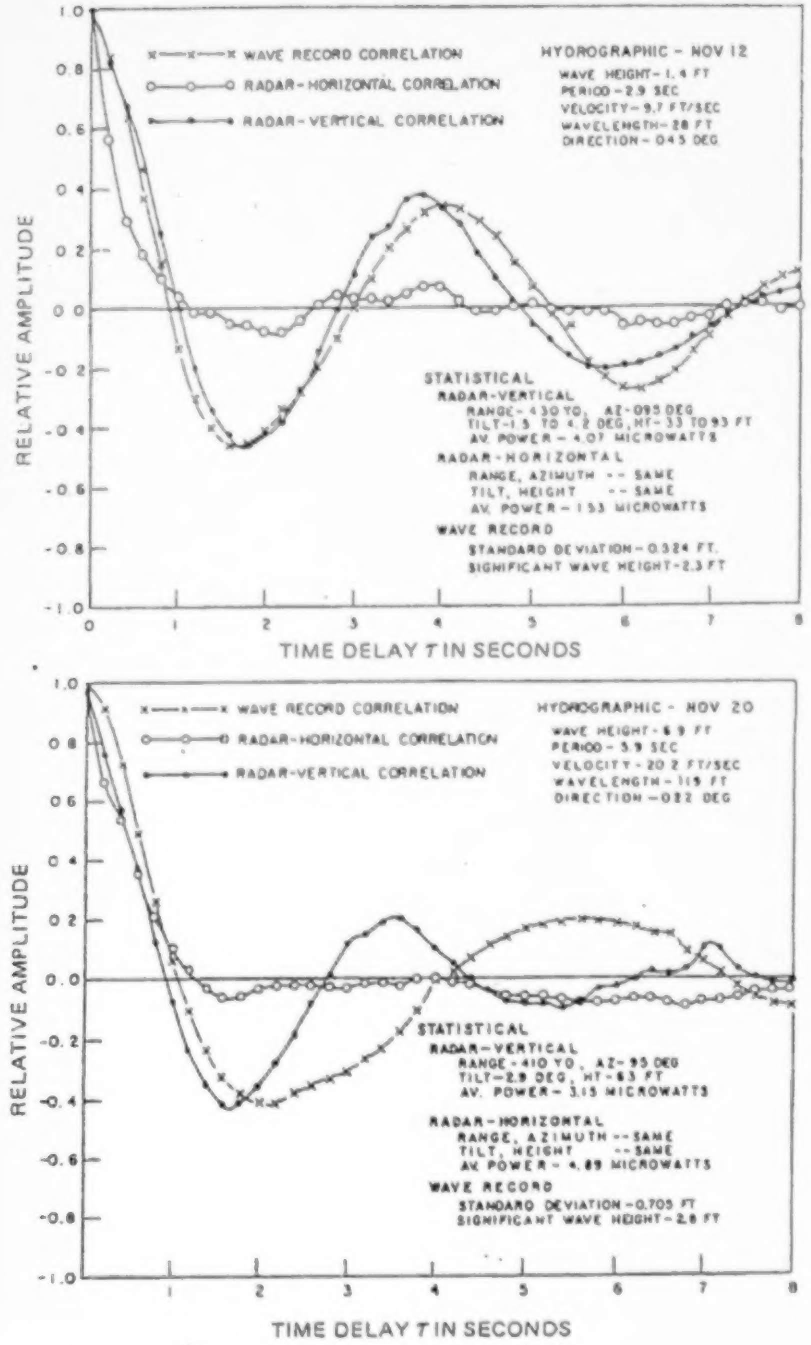

Fig. 6.6 Temporal auto-correlation function of backscattering signal. (Source: M. Long, *Radar Reflectivity of Land and Sea*, Artech House, Inc. 1983.)

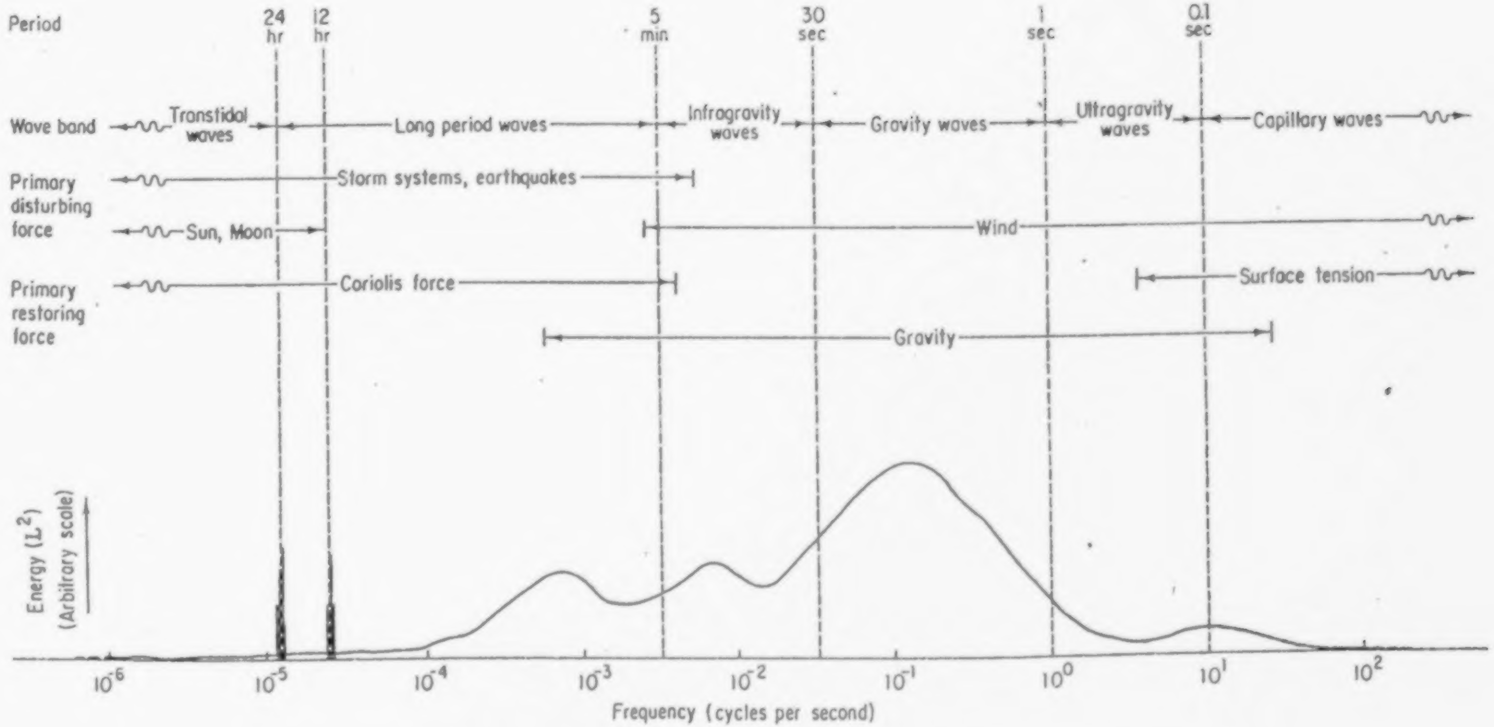

Fig. 6.7 The power spectrum of the surface waves of the oceans. (Source: B. Kinsman, *Wind Waves*, Prentice–Hall, 1965.)

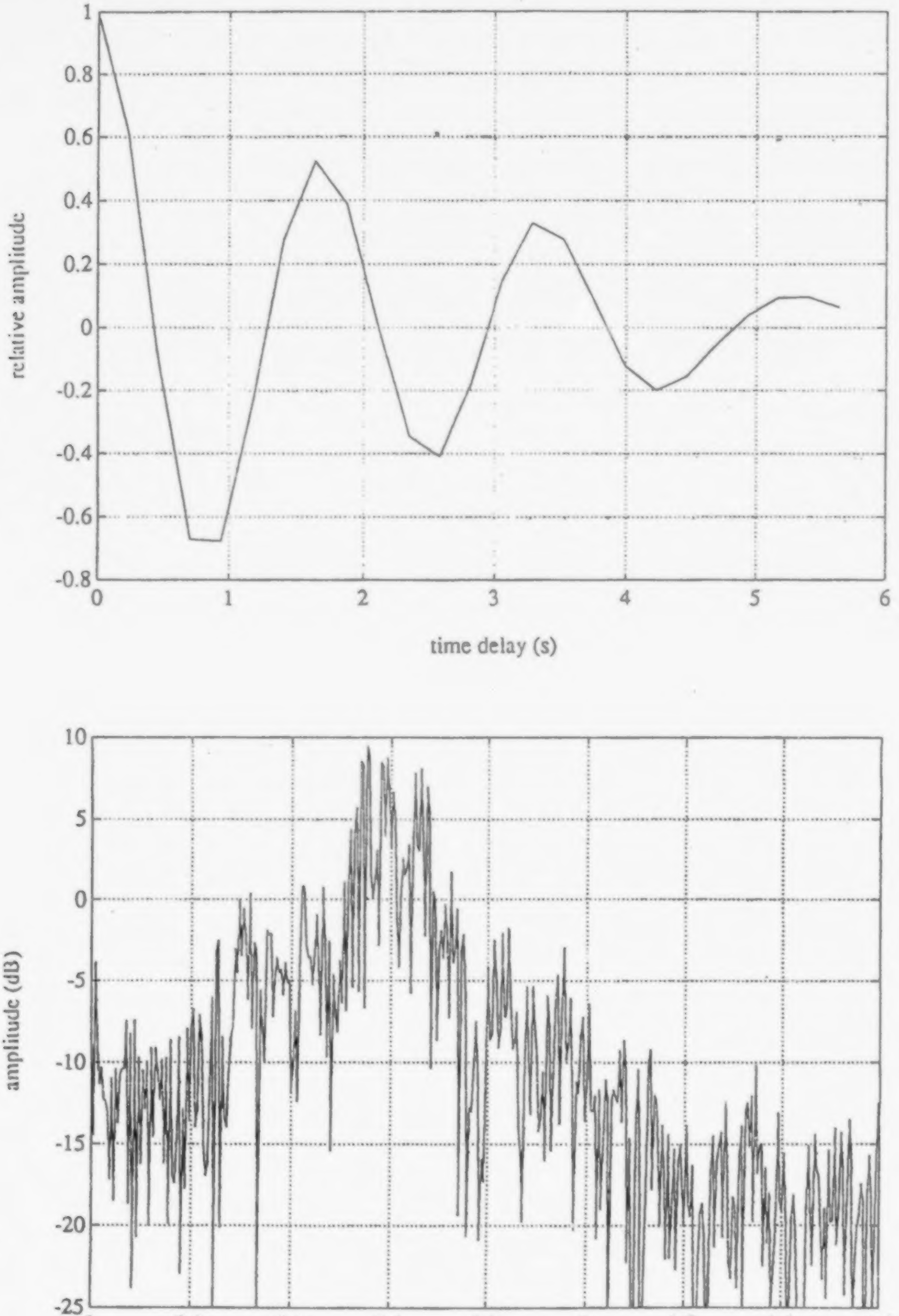

Fig. 6.8 Temporal auto-correlation function and power spectrum derived from a representative data set from Lake Ontario trials. Recorded on Nov. 17, 1988, f = 9.6 GHz, vertical polarization.

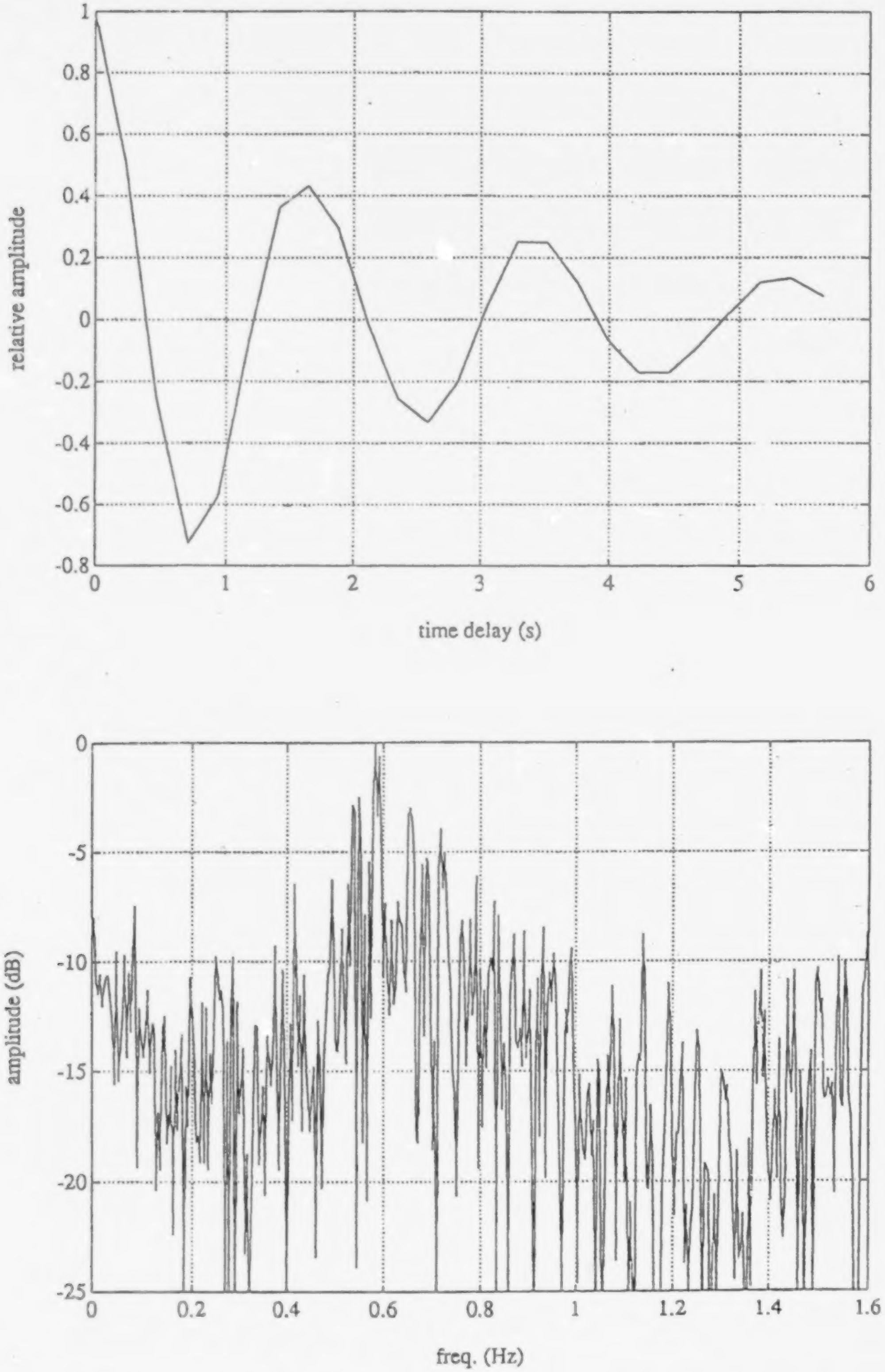

Fig. 6.9 Auto-correlation function and power spectrum derived from a representative data set from Lake Ontario trials. Recorded on Nov. 17, 1988, f = 9.6 GHz, horizontal polarization.

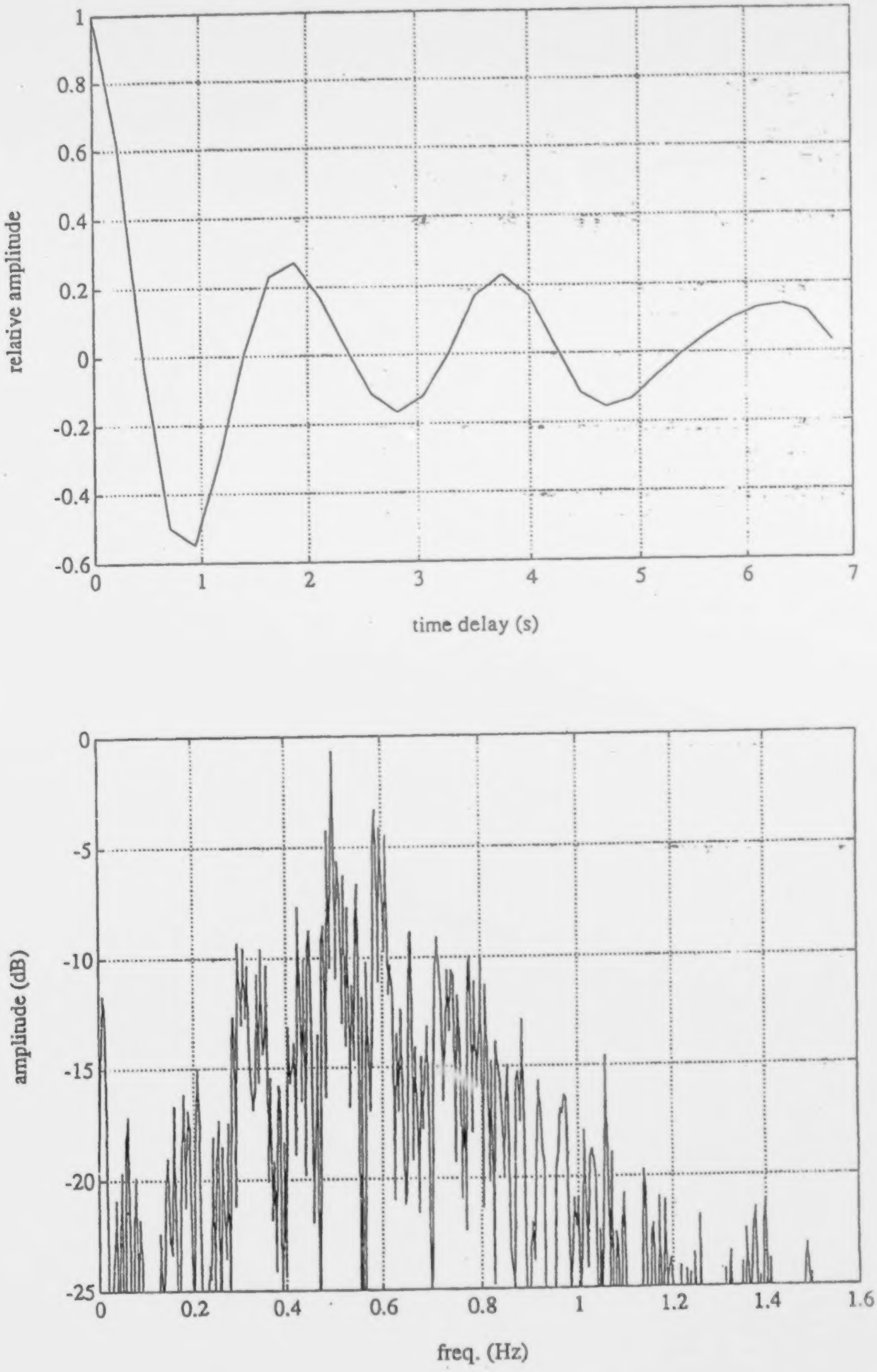

Fig. 6.10 Auto-correlation function and power spectrum derived from a representative data set from Lake Ontario trials. Recorded on Nov. 27,1988, f = 9.6 GHz, vertical polarization.

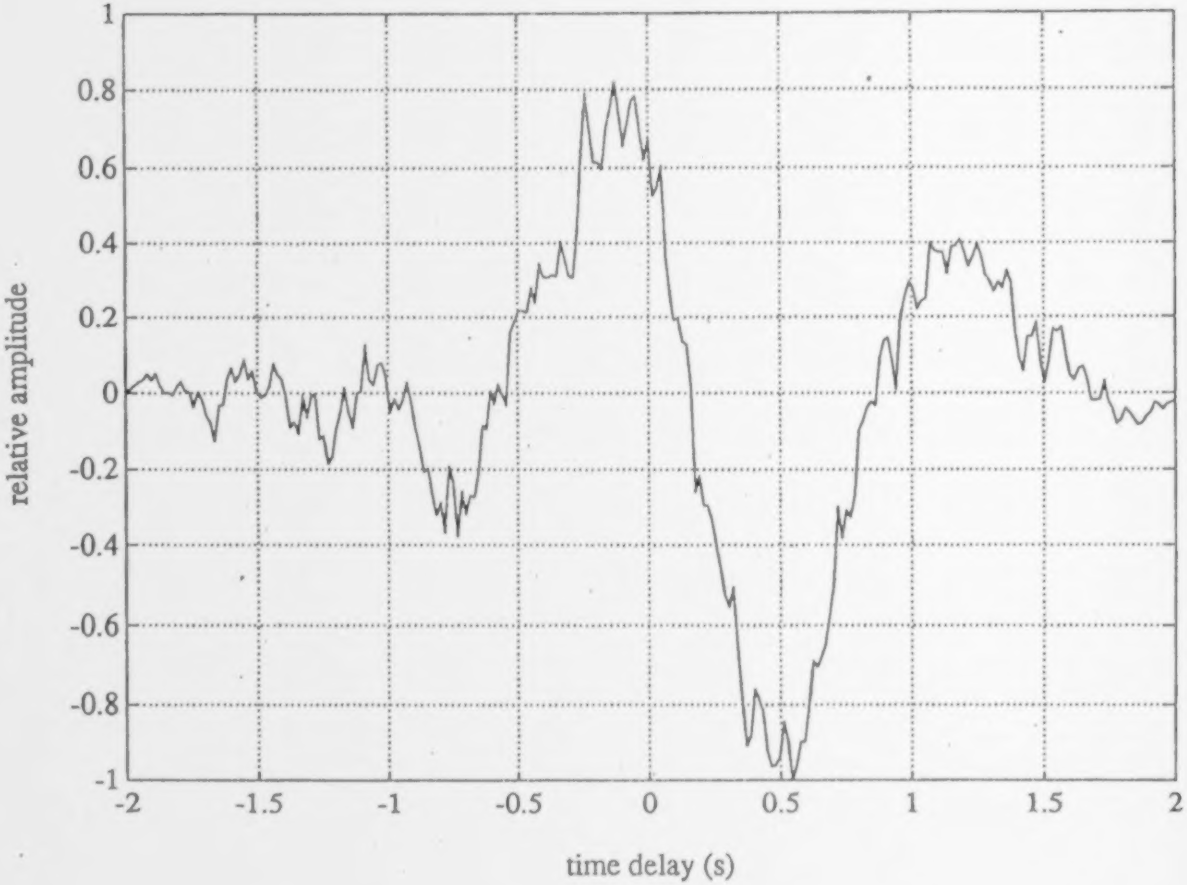

Fig. 6.11 Temporal cross-correlation function derived from a representative data set from Lake Huron trials. Recorded on Nov. 4, 1987, f = 10.2 and 8.05 GHz, horizontal polarization.

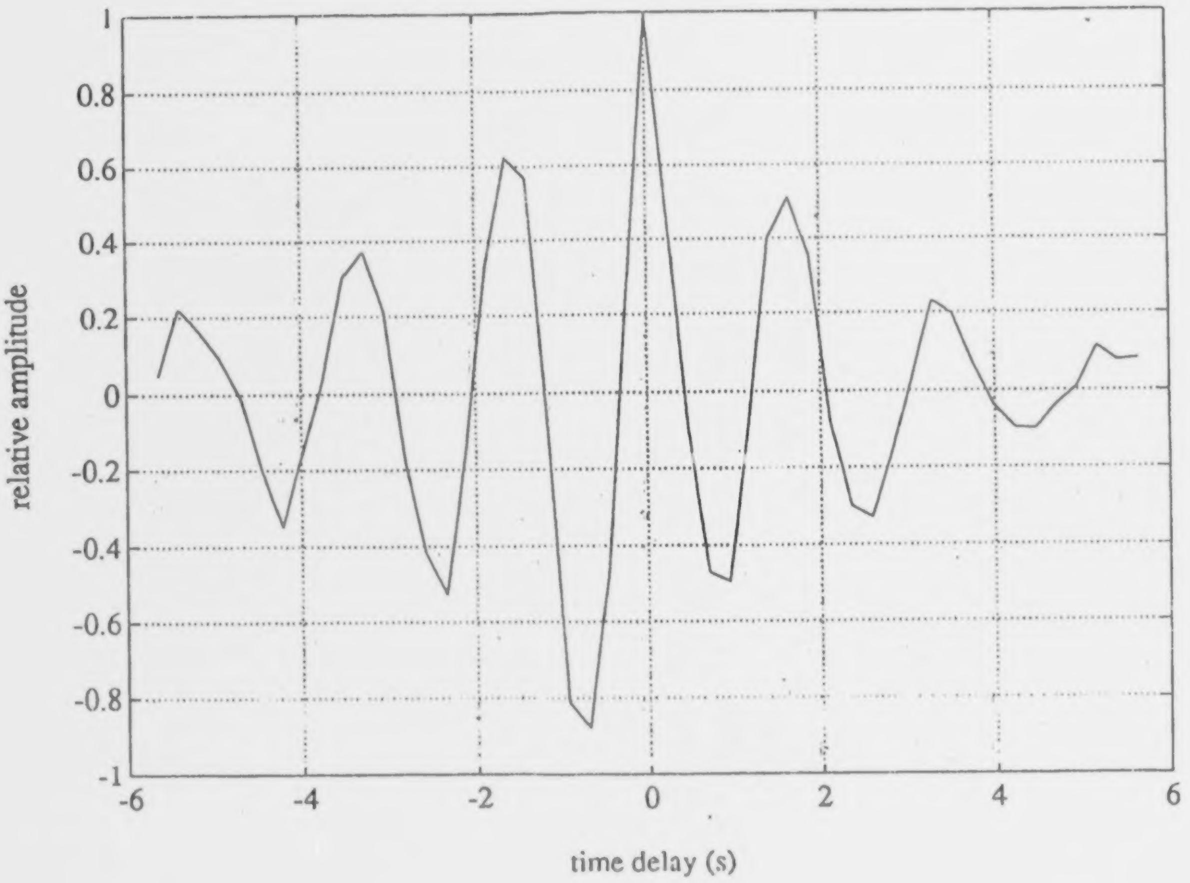

Fig. 6.12 Cross-correlation function derived from a representative data set from Lake Ontario trials. Recorded on Nov. 27,1988, f = 9.6 GHz, vertical polarization.

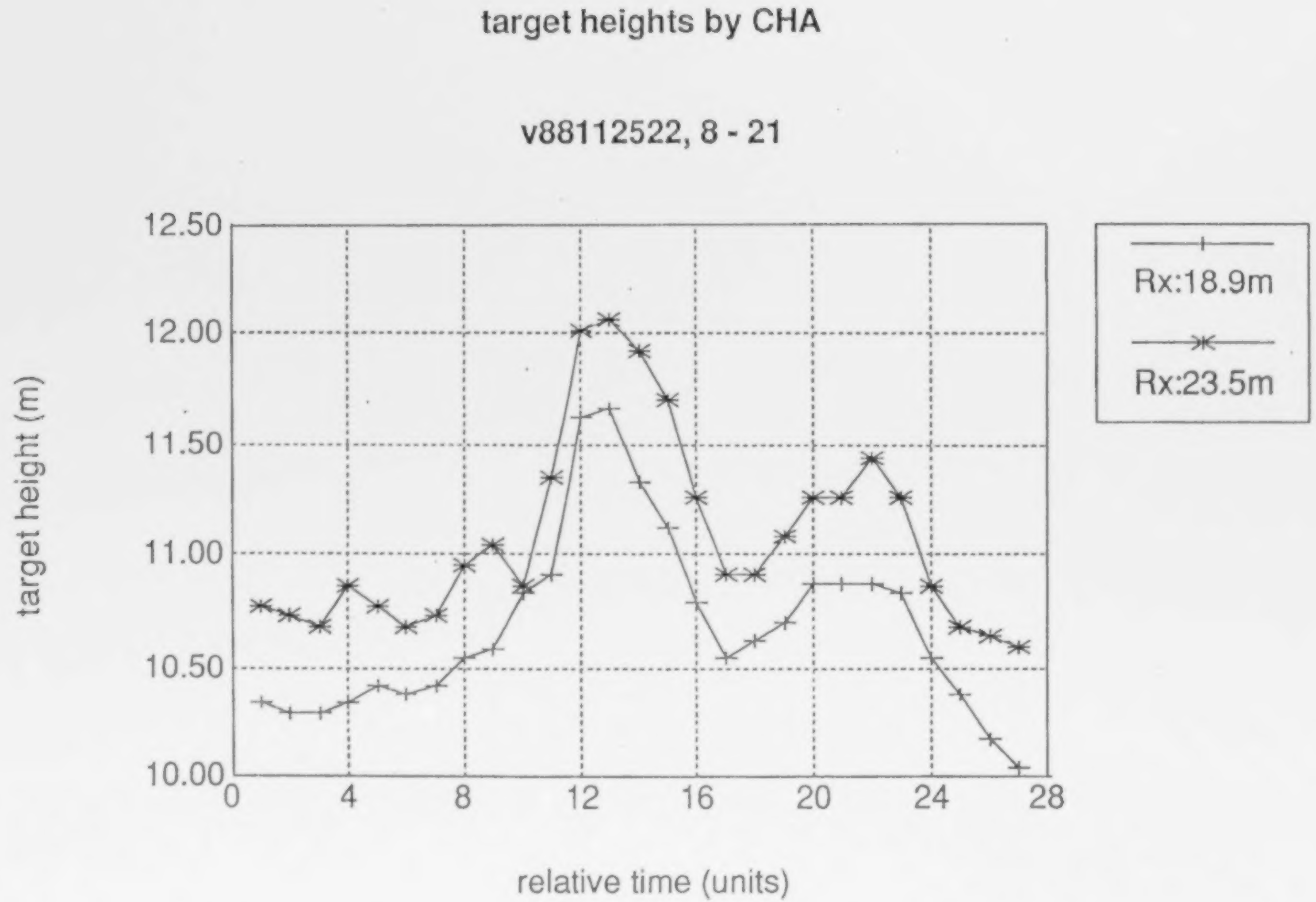

Fig. 7.1 Target heights given by CHA based on the data recorded on Nov. 25, 1988.

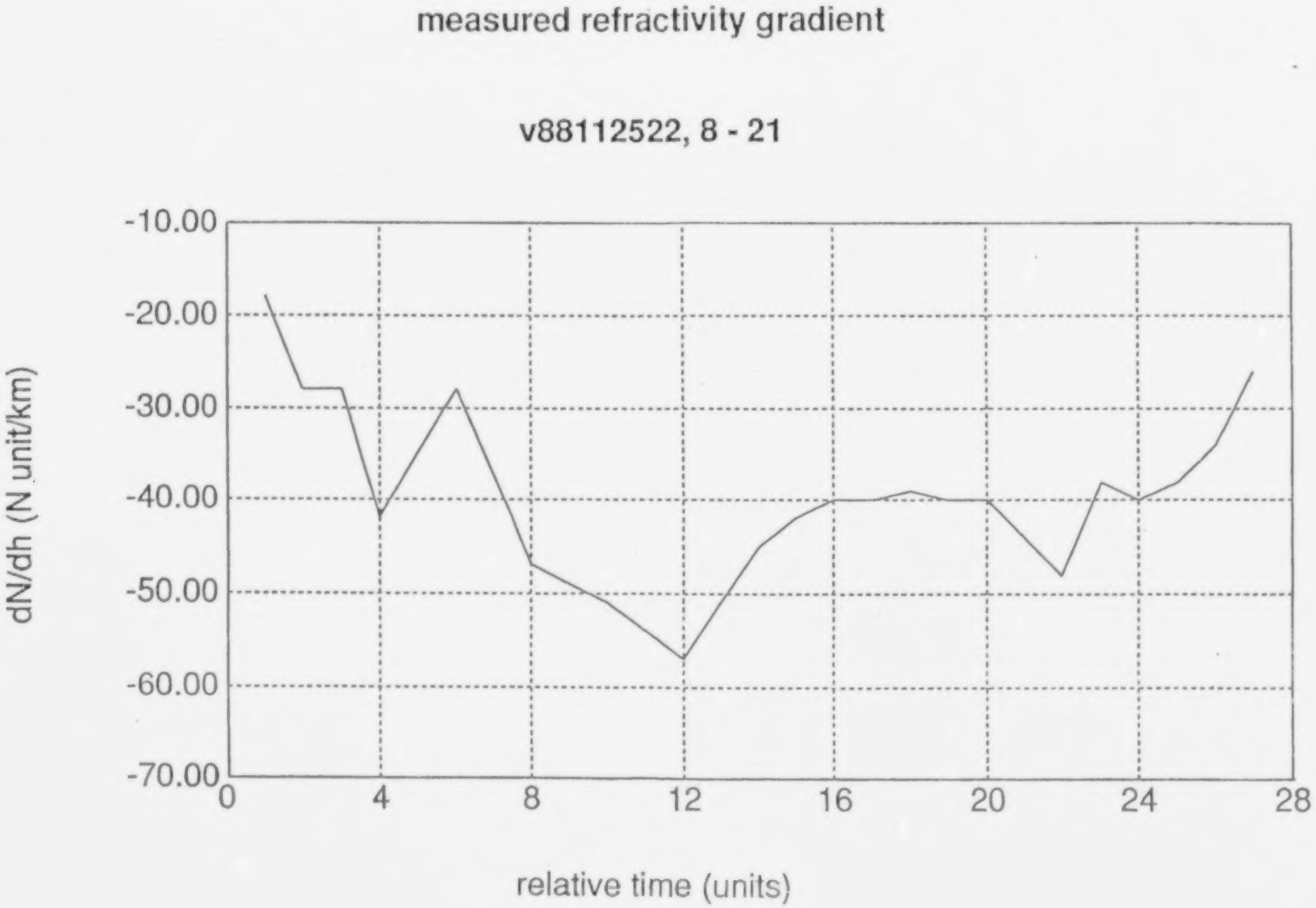

Fig. 7.2 Refractivity gradient measured during the period when the data used for Fig. 7.1 were recorded.

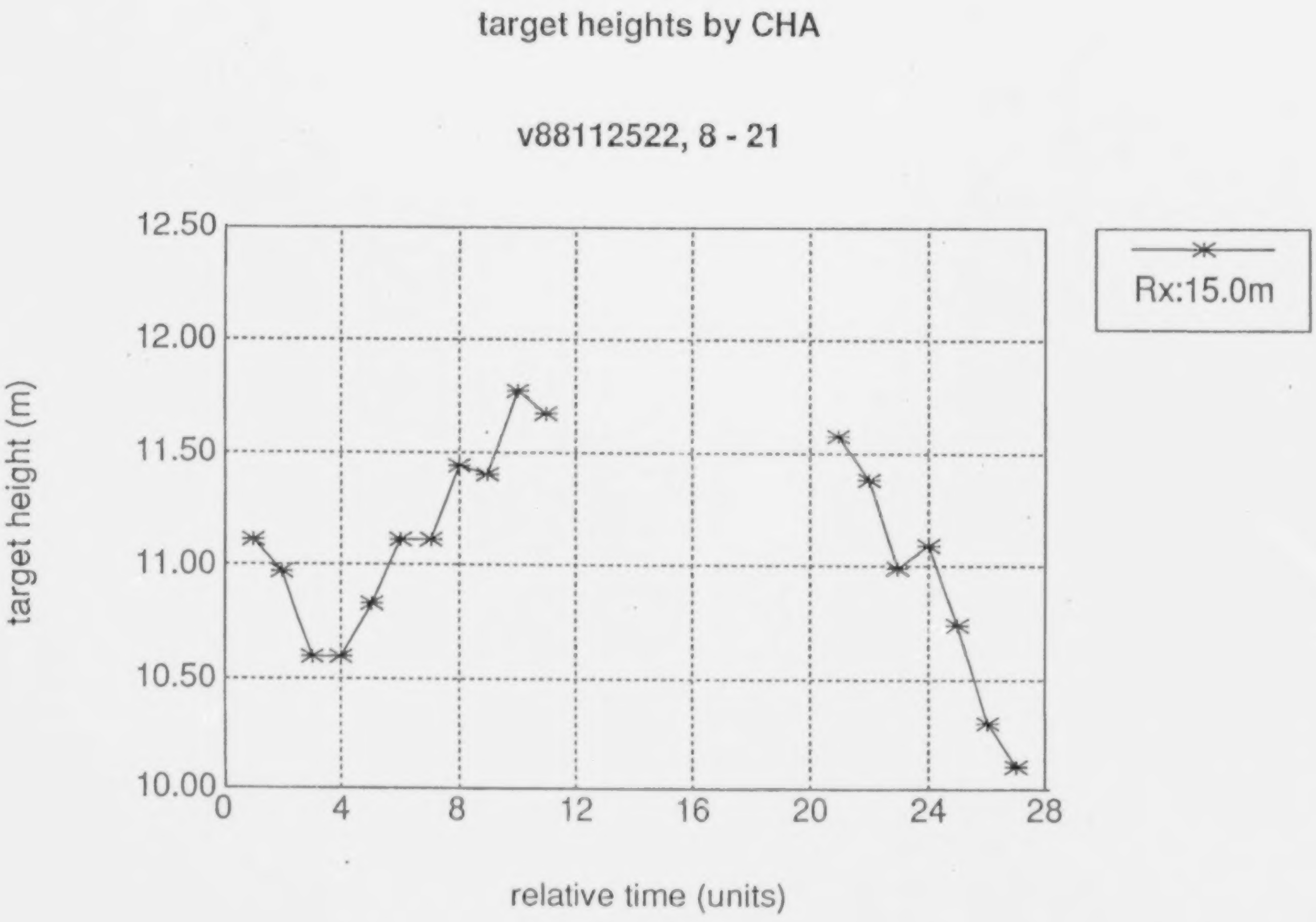

Fig. 7.3 Target heights given by CHA based on the data recorded on Nov. 25, 1988. The missing trace indicates the loss of track.

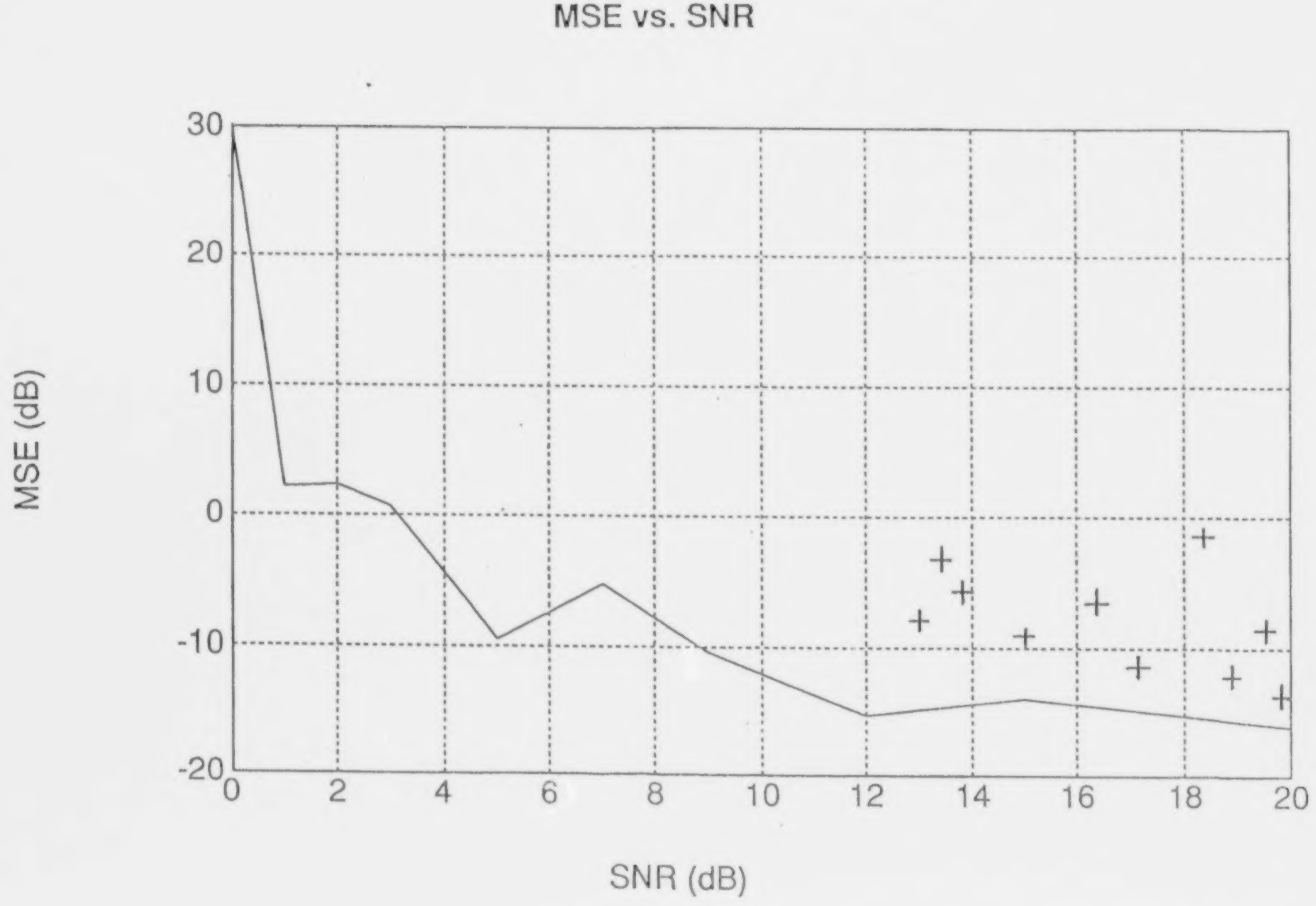

Fig. 7.4 MSE vs SNR.

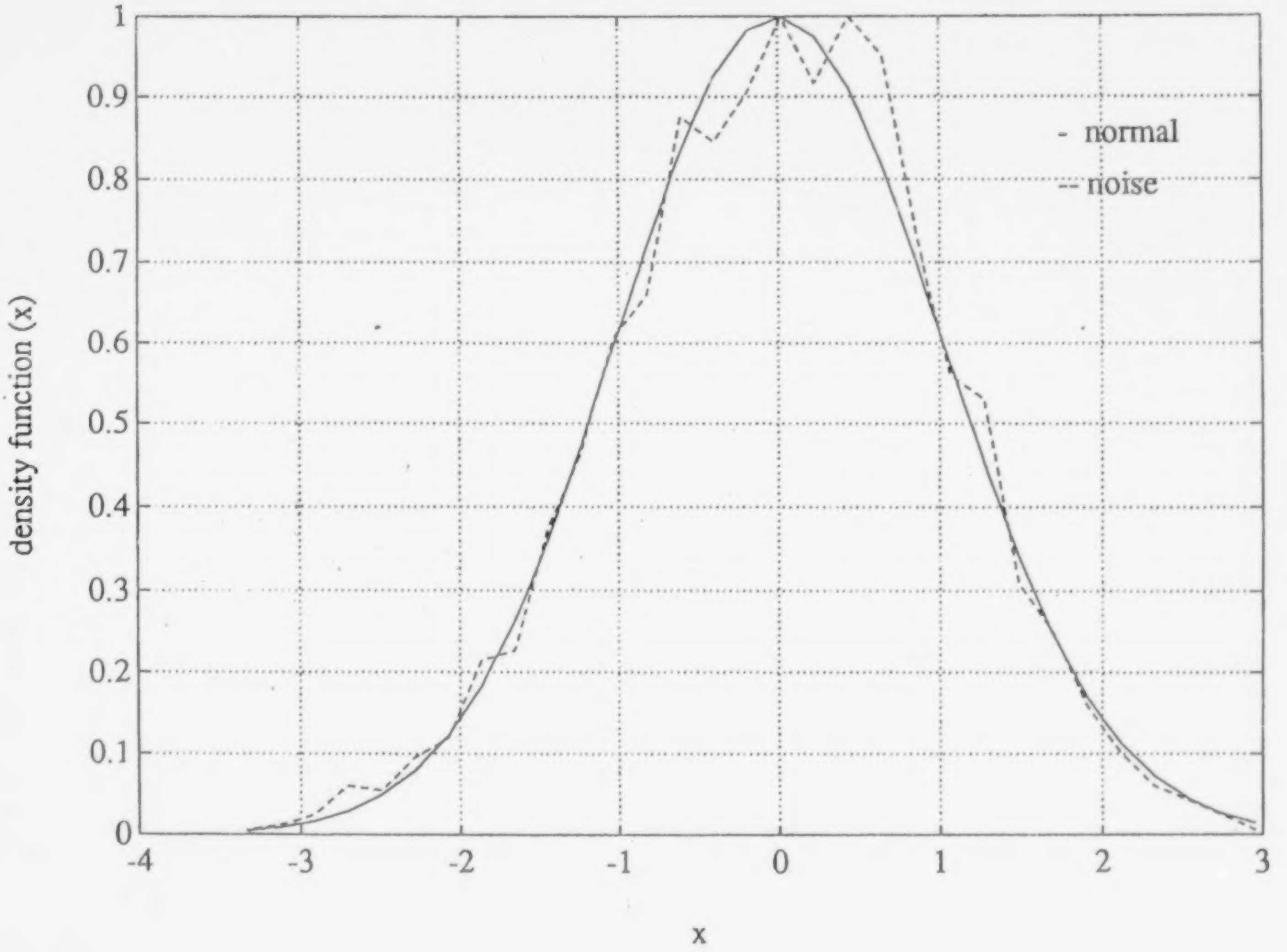

Fig. 7.5 The density distribution of the noise used in the simulation.

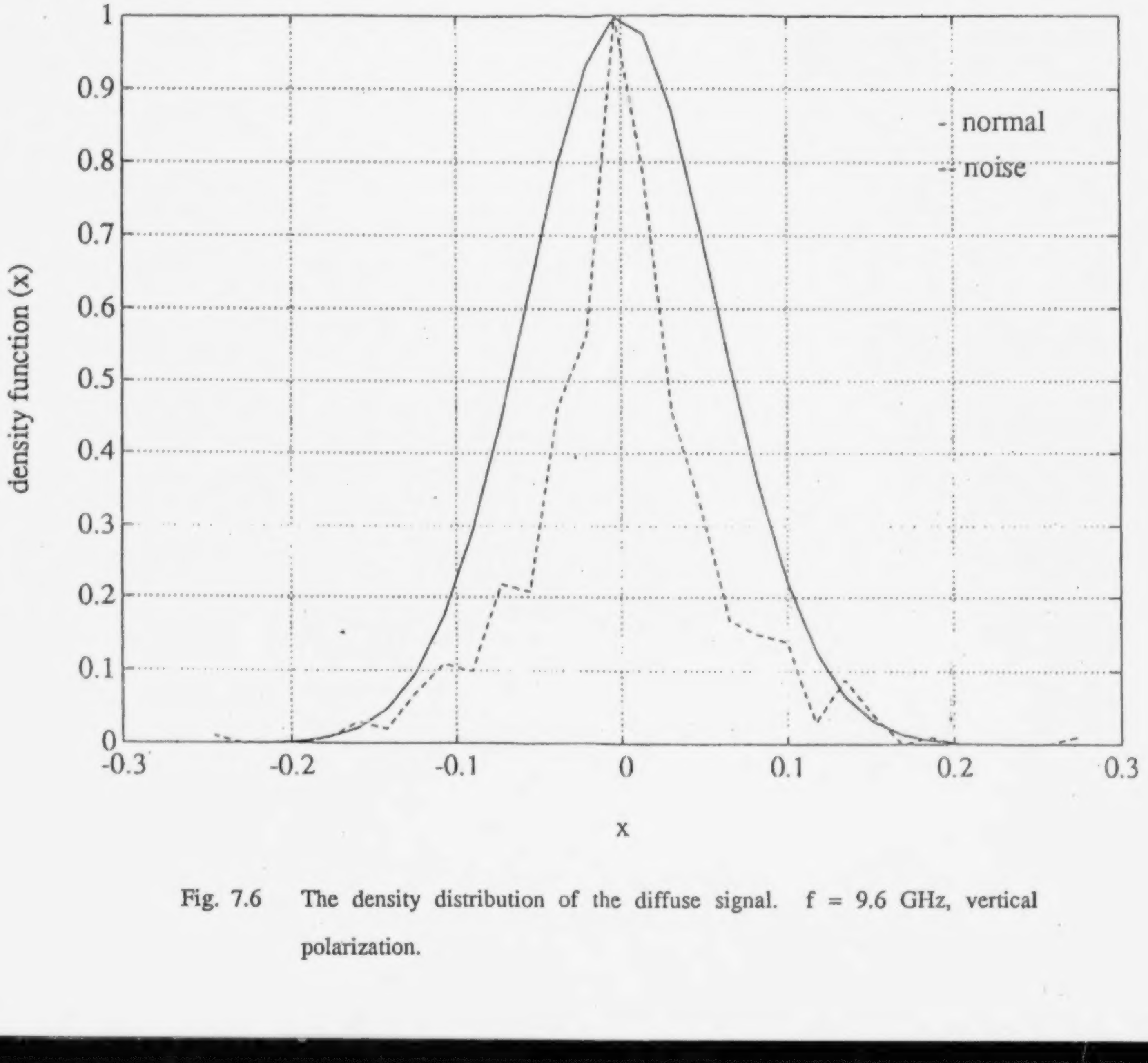

Fig. 7.6 The density distribution of the diffuse signal. f = 9.6 GHz, vertical polarization.

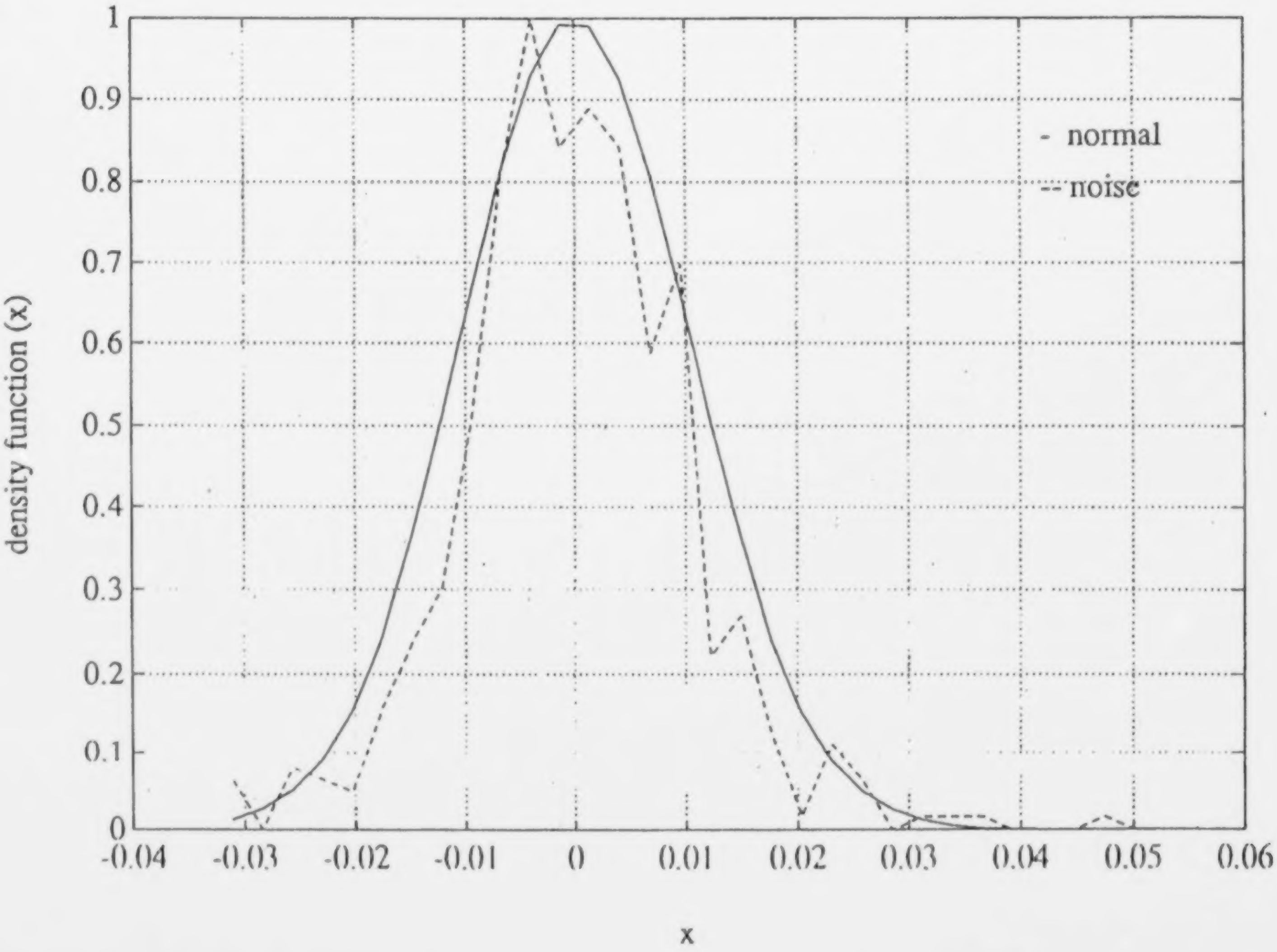

Fig. 7.7 The density distribution of the diffuse signal. f = 9.6 GHz, horizontal polarization.

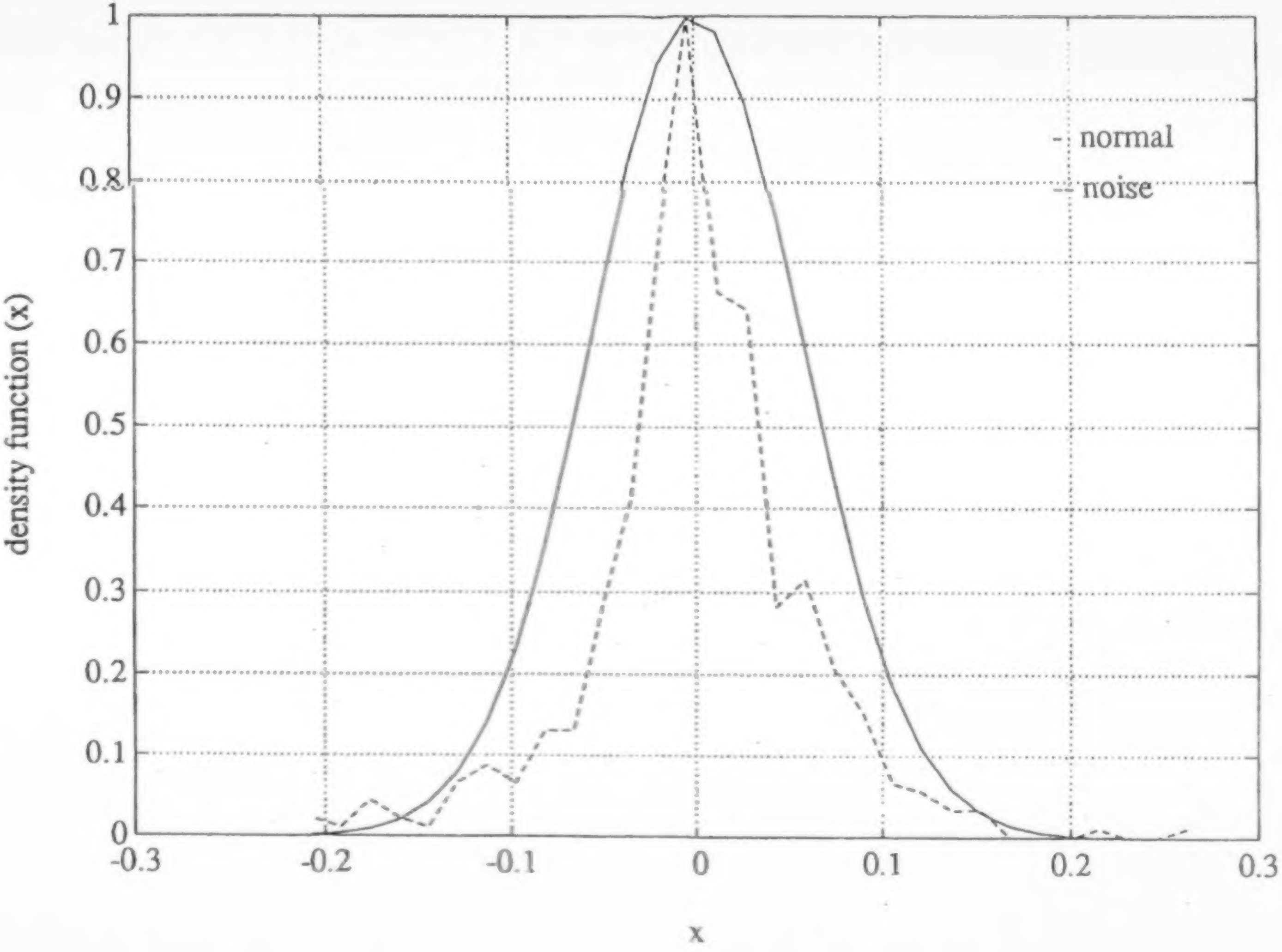

Fig. 7.8 The density distribution of the diffuse signal. f = 8.6 GHz, vertical polarization.

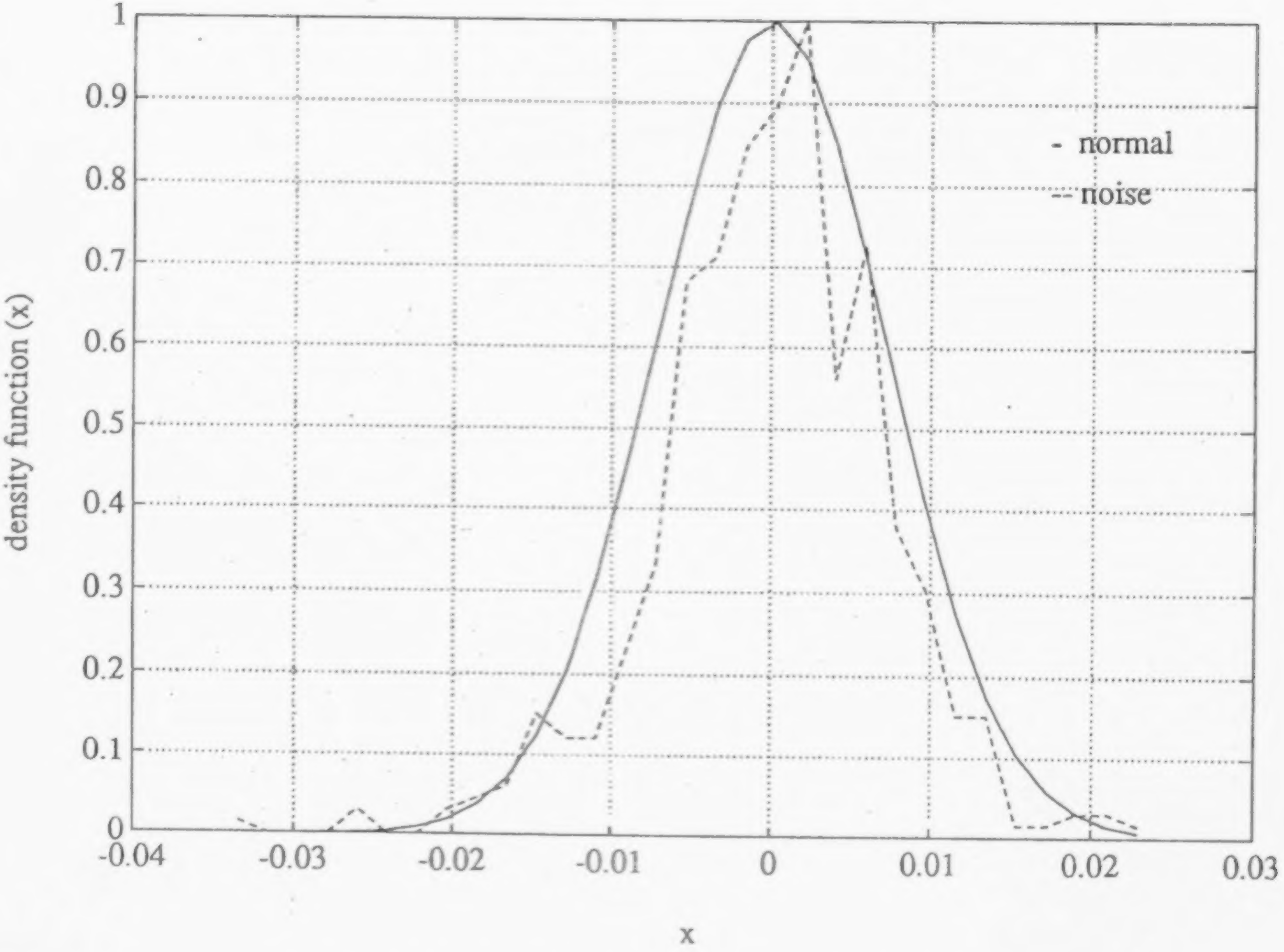

Fig. 7.9 The density distribution of the diffuse signal. f = 8.6 GHz, horizontal polarization.

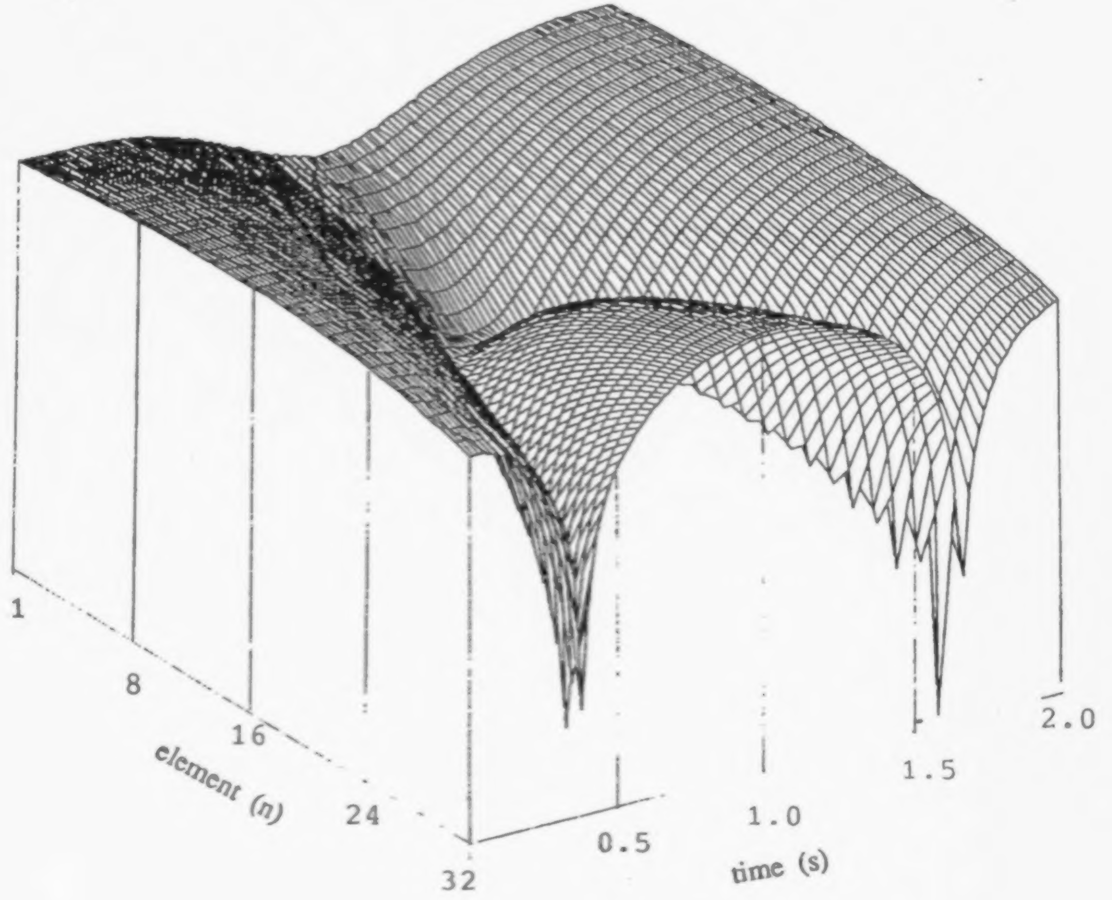

Fig. 7.10 The amplitude distribution of the interference pattern as a function of time. Swell propagation angle = 90 degrees.

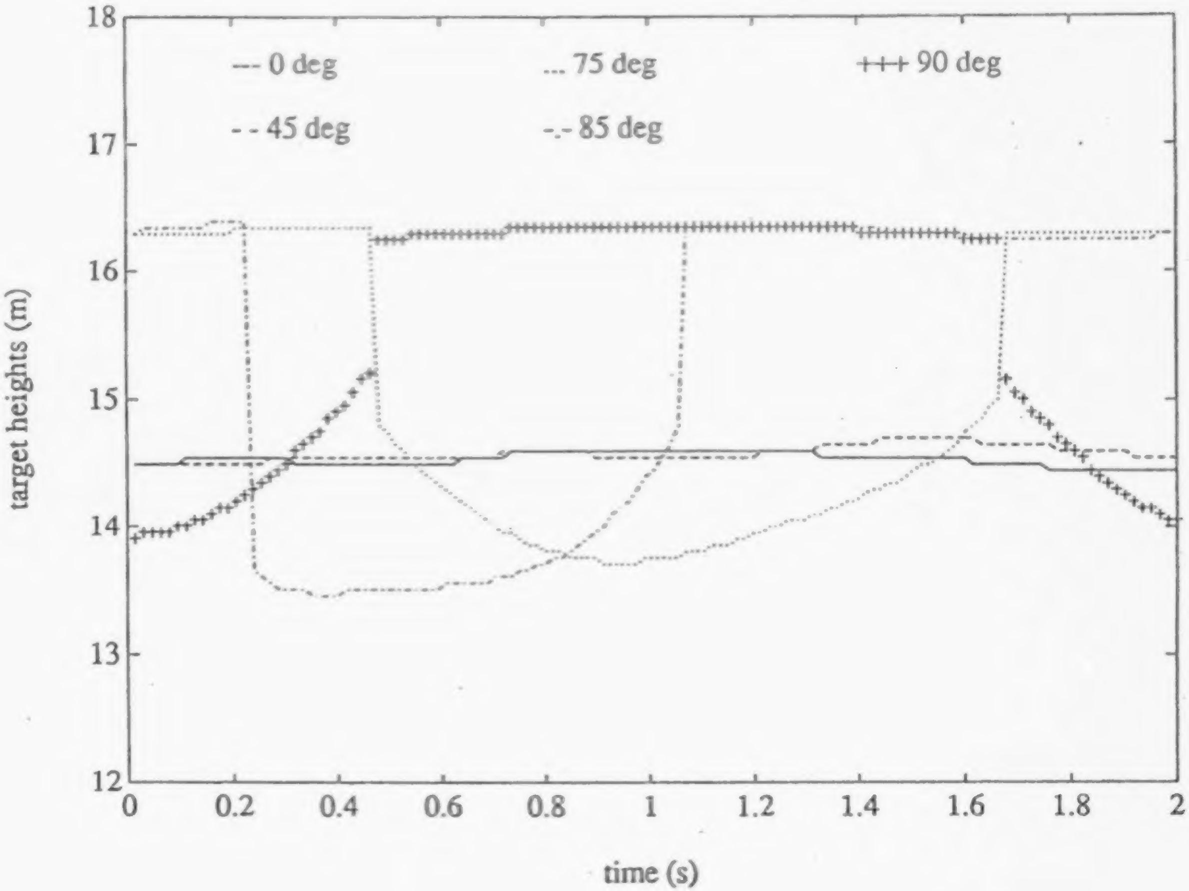

Fig. 7.11 Target heights given by the CHA algorithm under single sea swell condition.

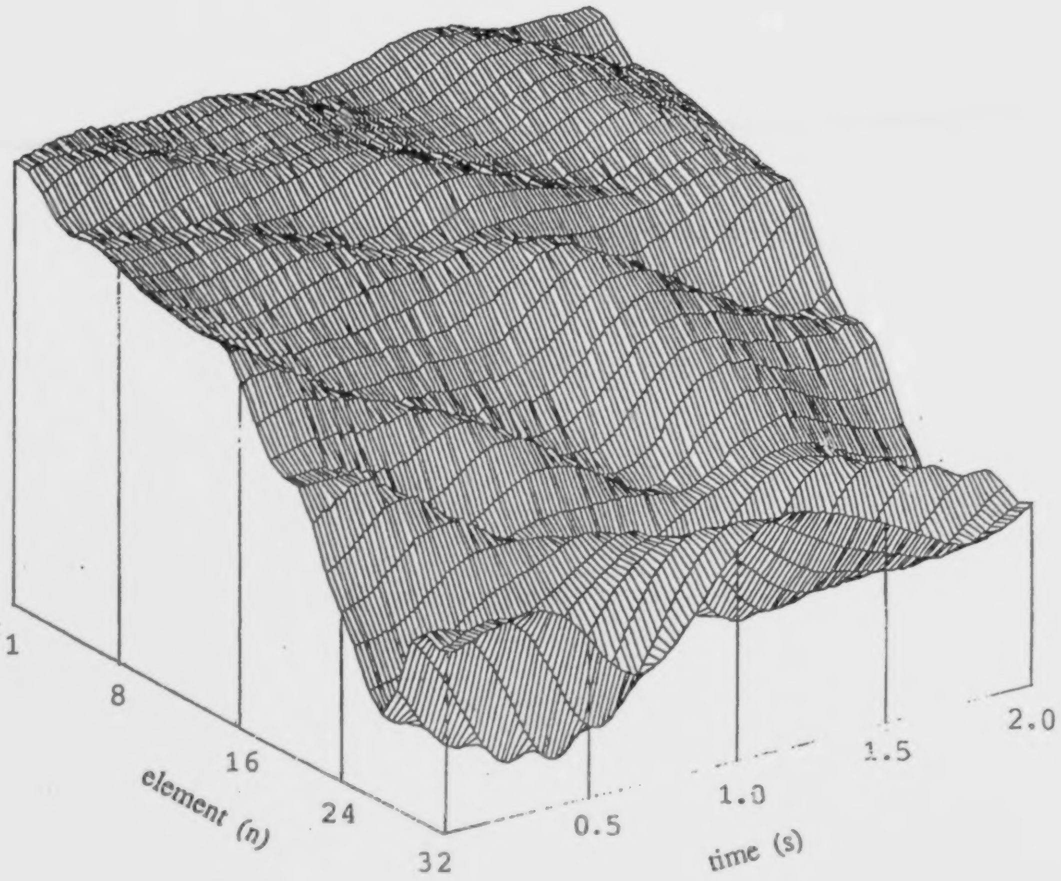

Fig. 7.12 The amplitude distribution of the interference pattern as a function of time. Swell propagation angle = 0 degrees.

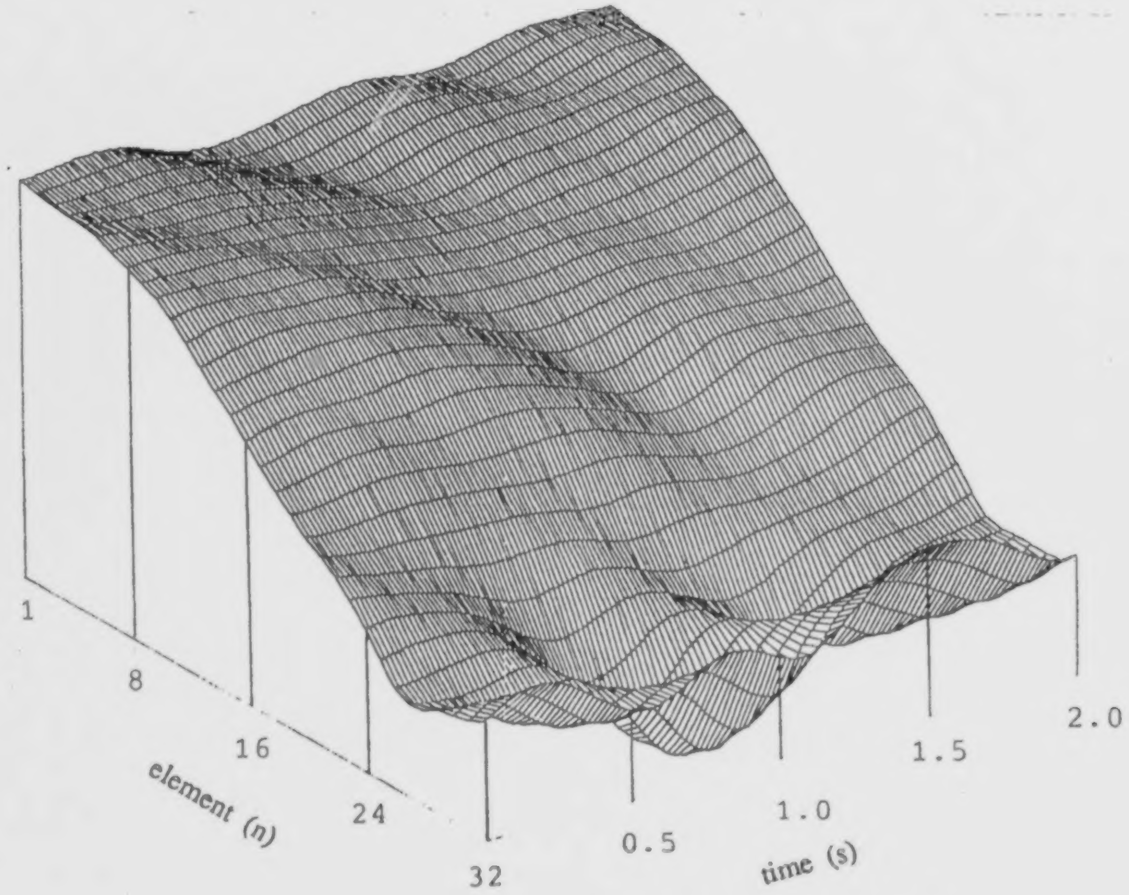

Fig. 7.13 The amplitude distribution of the interference pattern as a function of time. Swell propagation angle = 45 degrees.

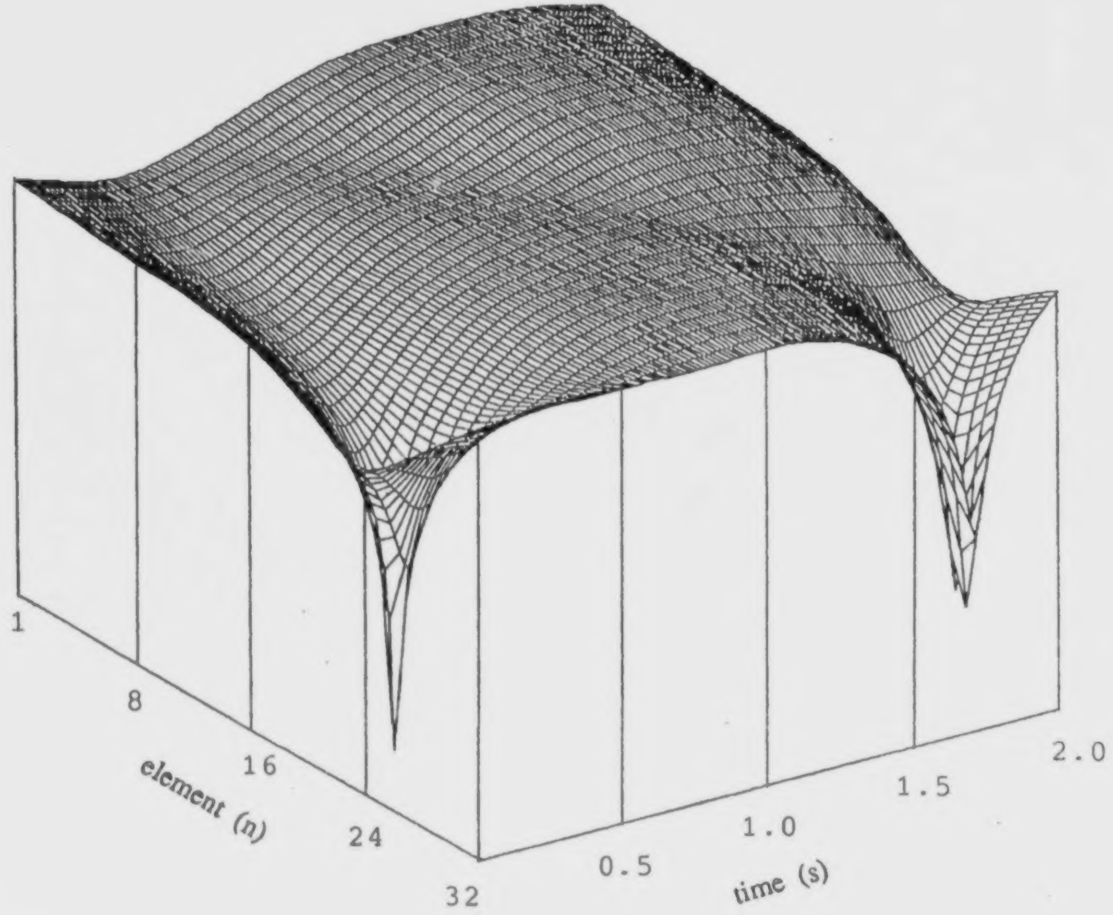

Fig. 7.14 The amplitude distribution of the interference pattern as a function of time. Swell propagation angle = 75 degrees.

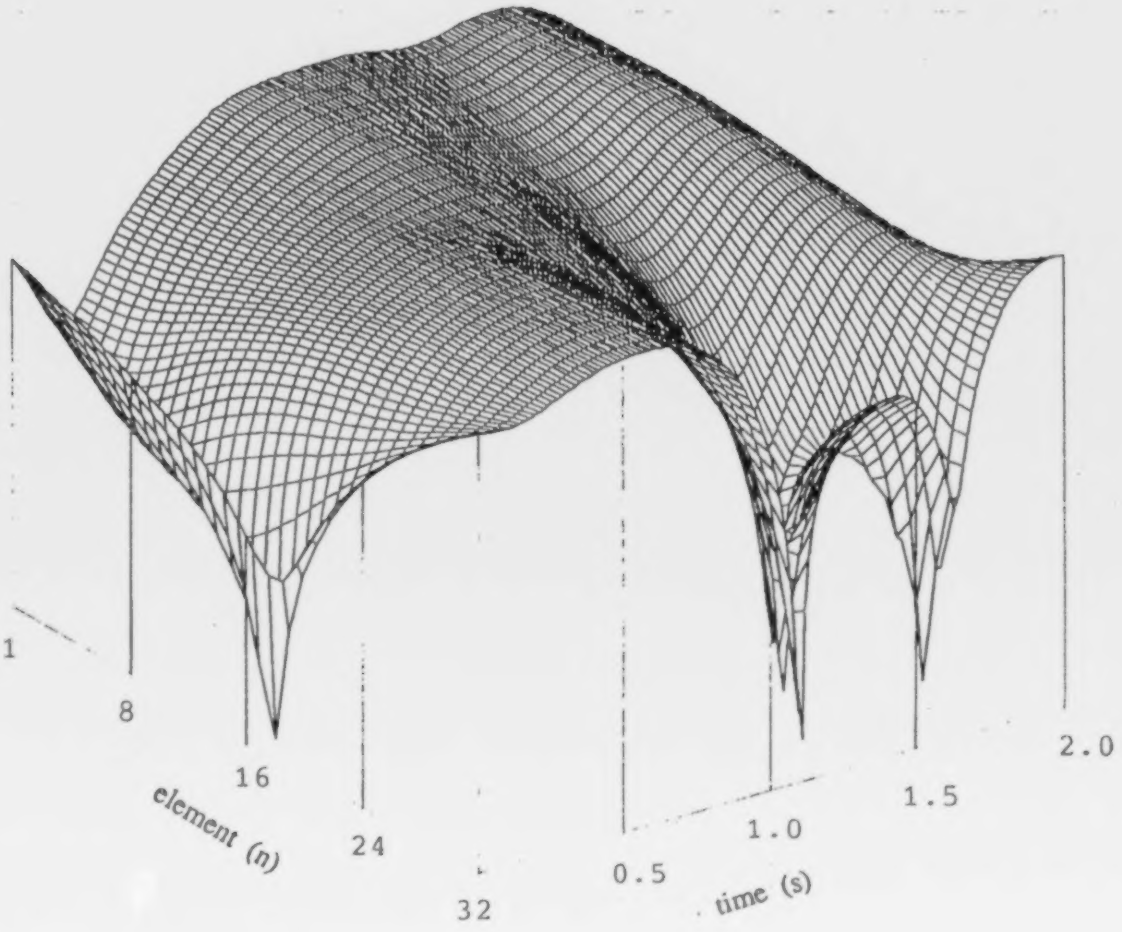

Fig. 7.15 The amplitude distribution of the interference pattern as a function of time. Swell propagation angle = 85 degrees.

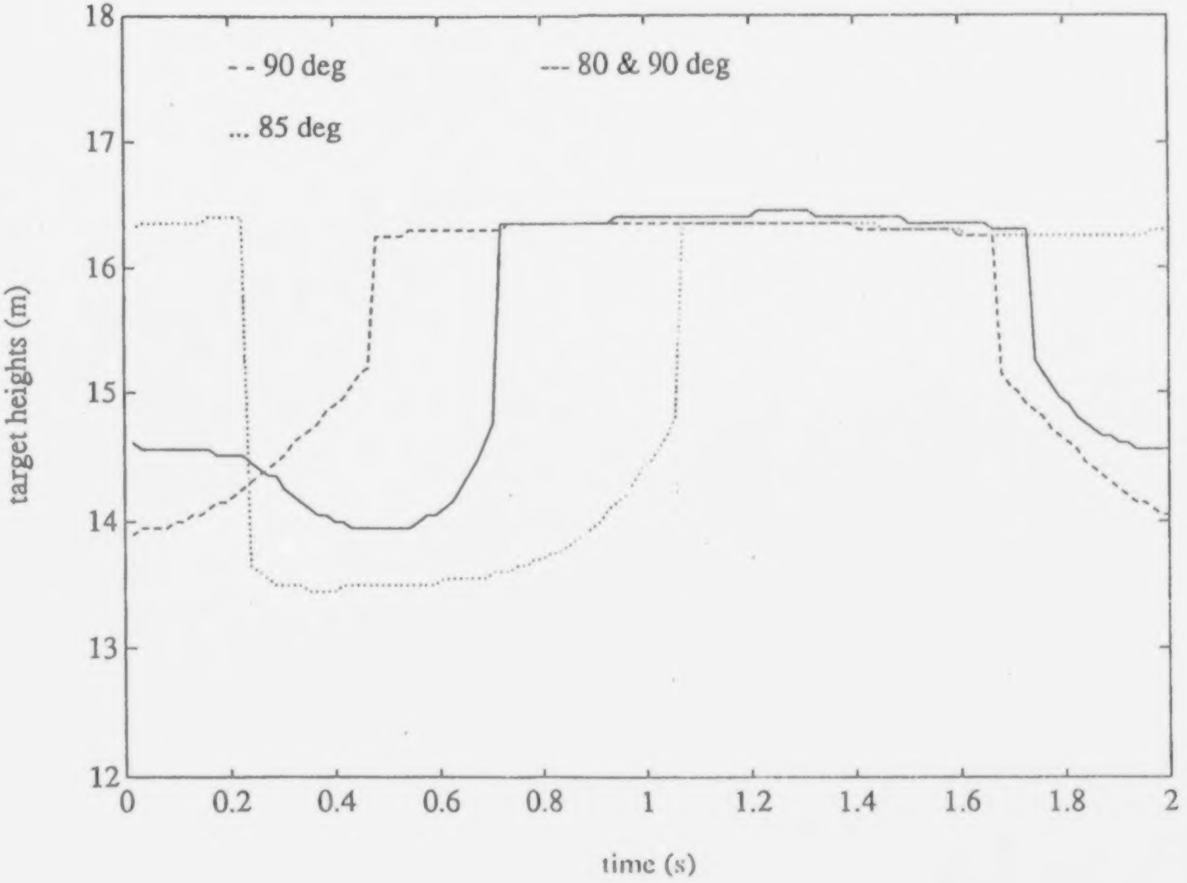

Fig. 7.16 Target heights given by the CHA algorithm under two sea swell condition.

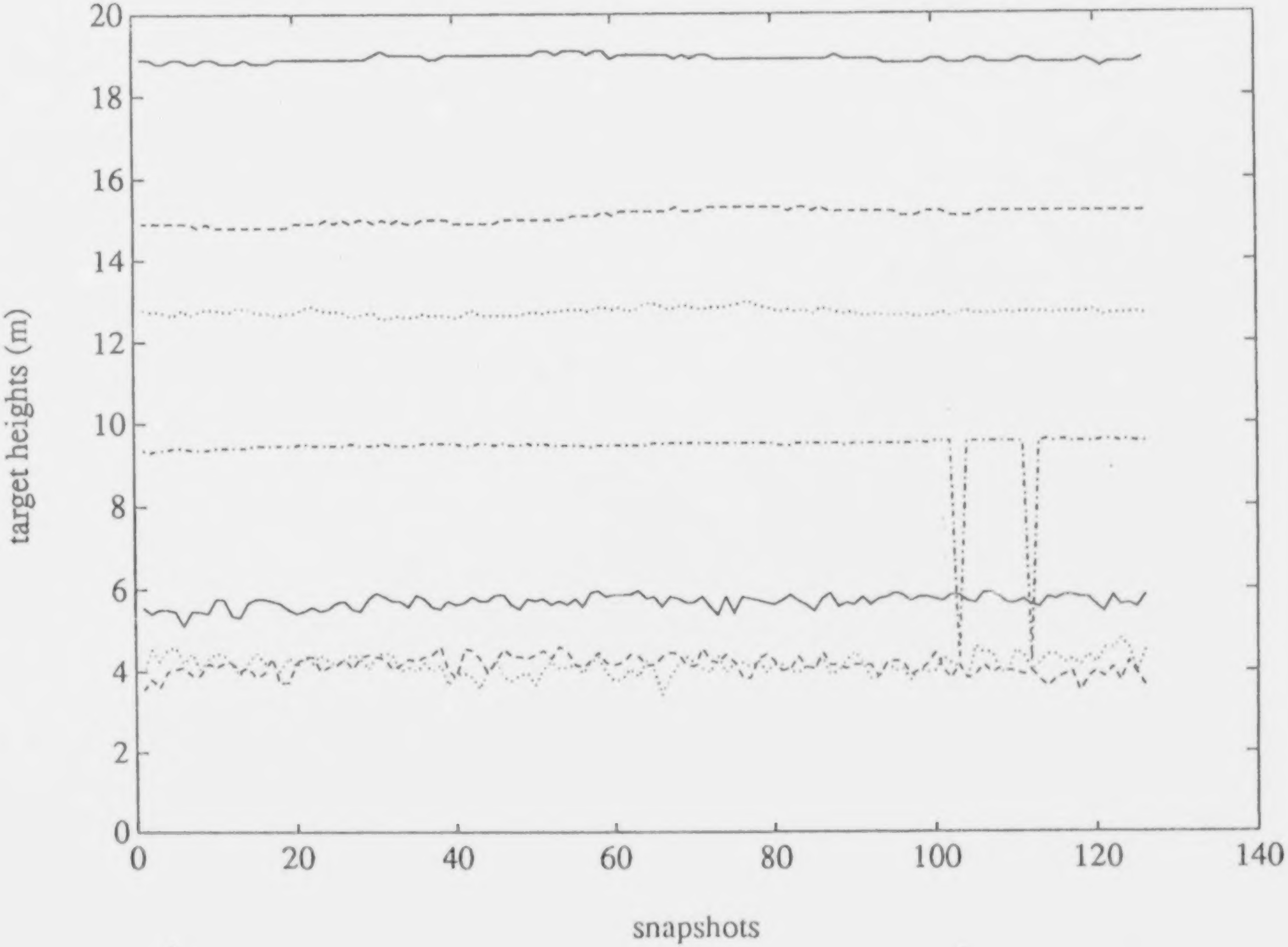

Fig. 7.17 Target heights given by the RML technique based on the Lake Huron data. Number of frequencies = 2.

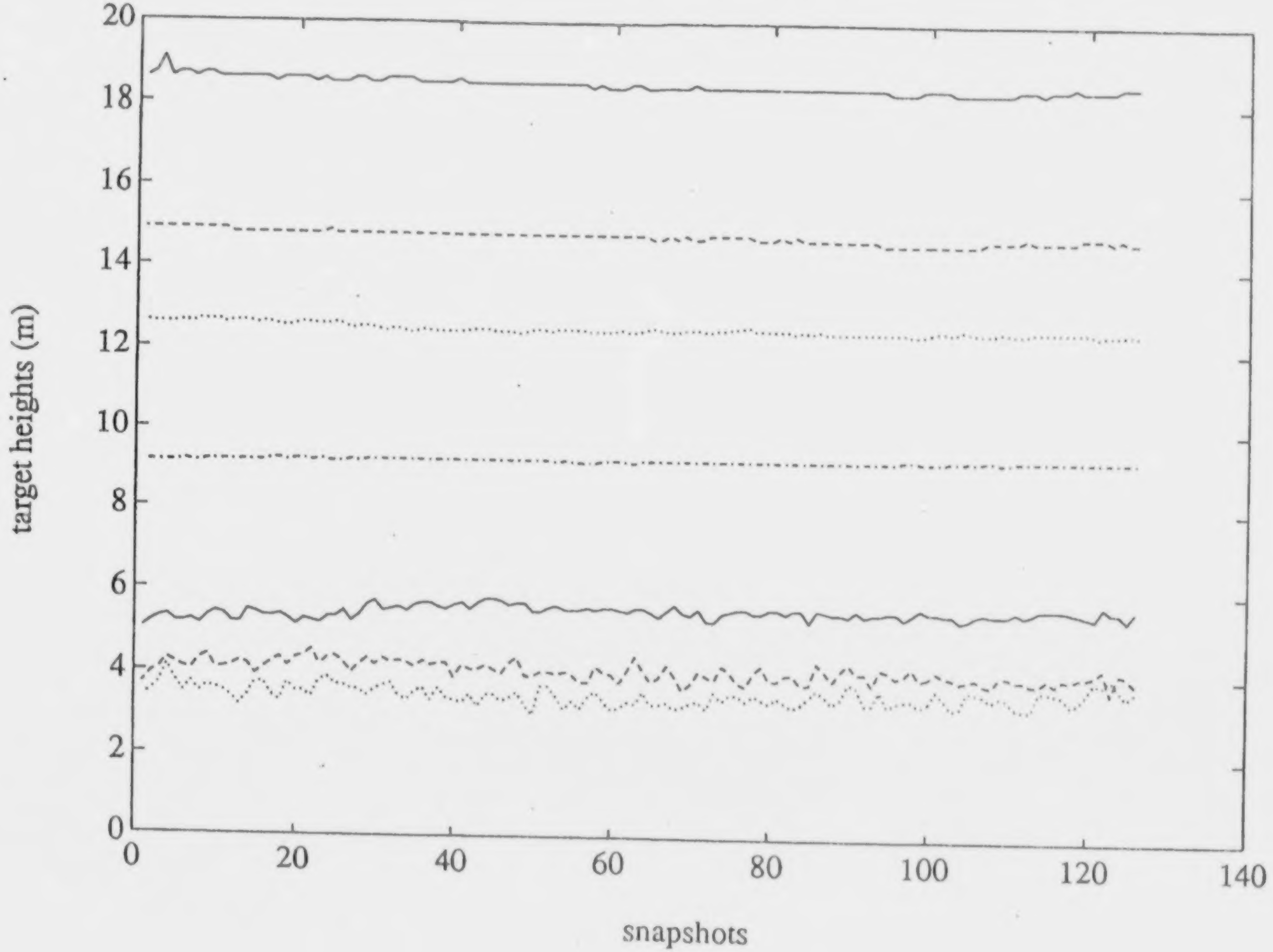

Fig. 7.18 Target heights given by the RML technique based on the Lake Huron data. Number of frequencies = 4.

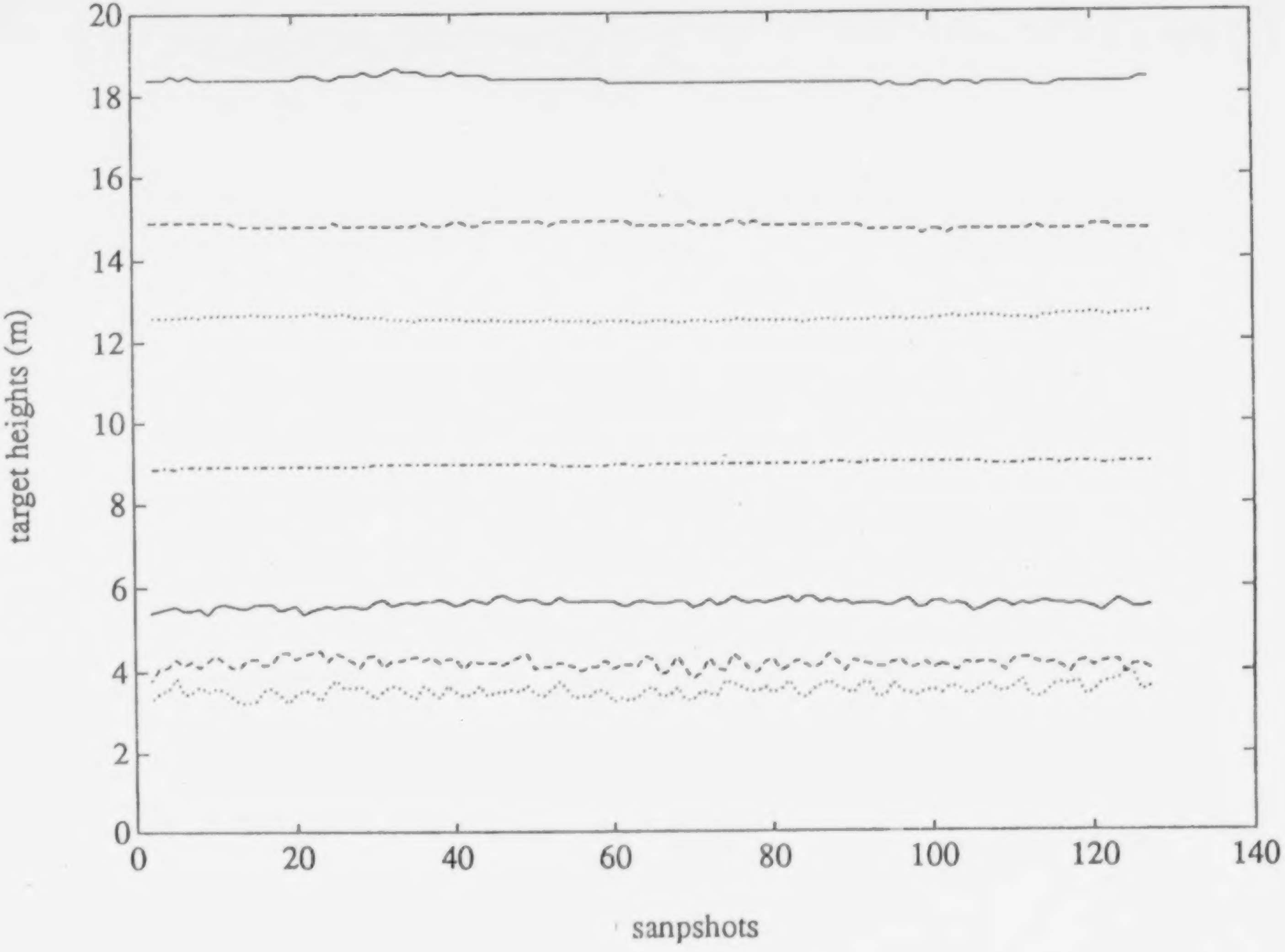

Fig. 7.19 Target heights given by the RML technique based on the Lake Huron data. Number of frequencies = 6.

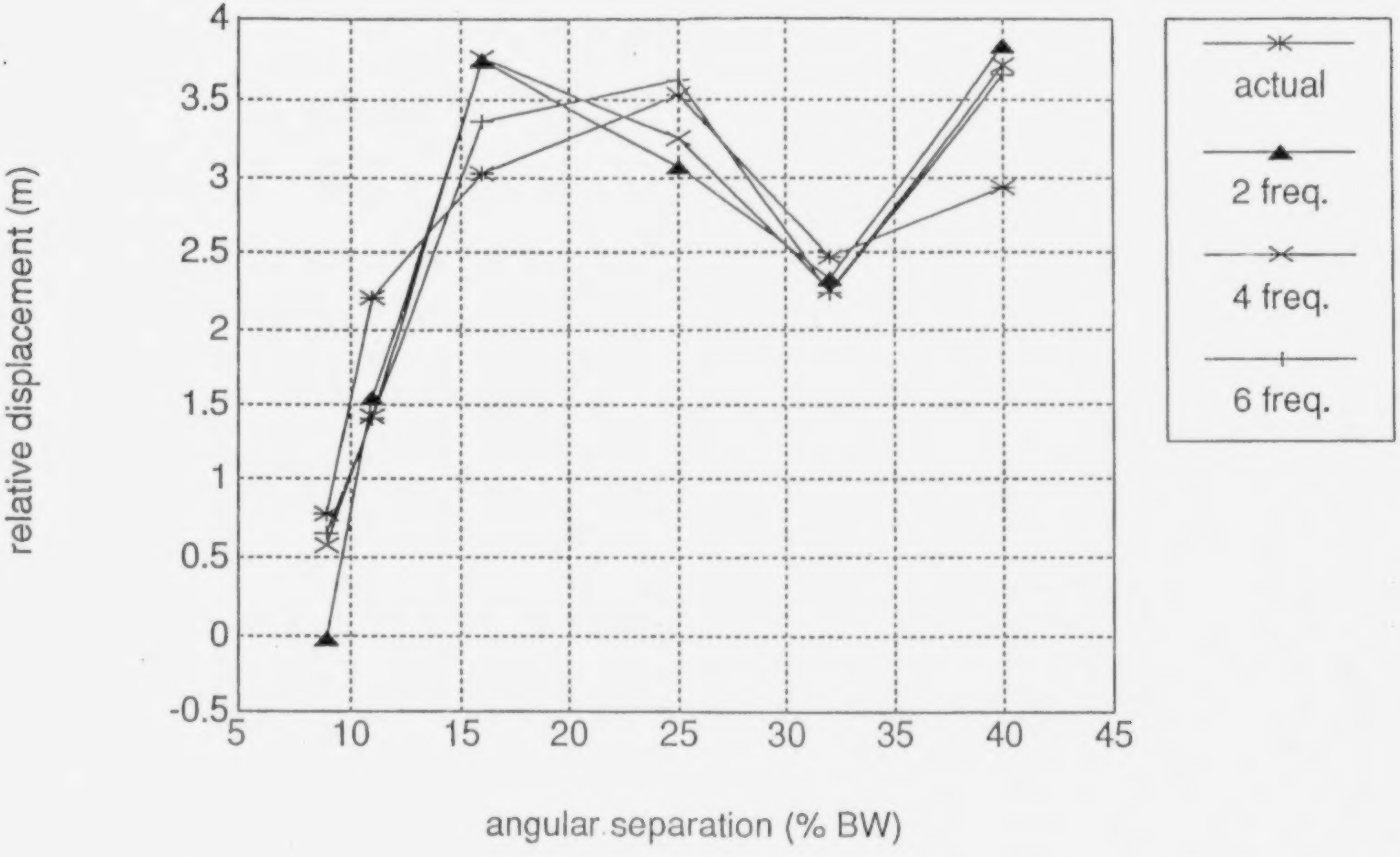

Fig. 7.20 Relative height displacements, showing that the estimates given by using six frequencies are closer to the actual ones.

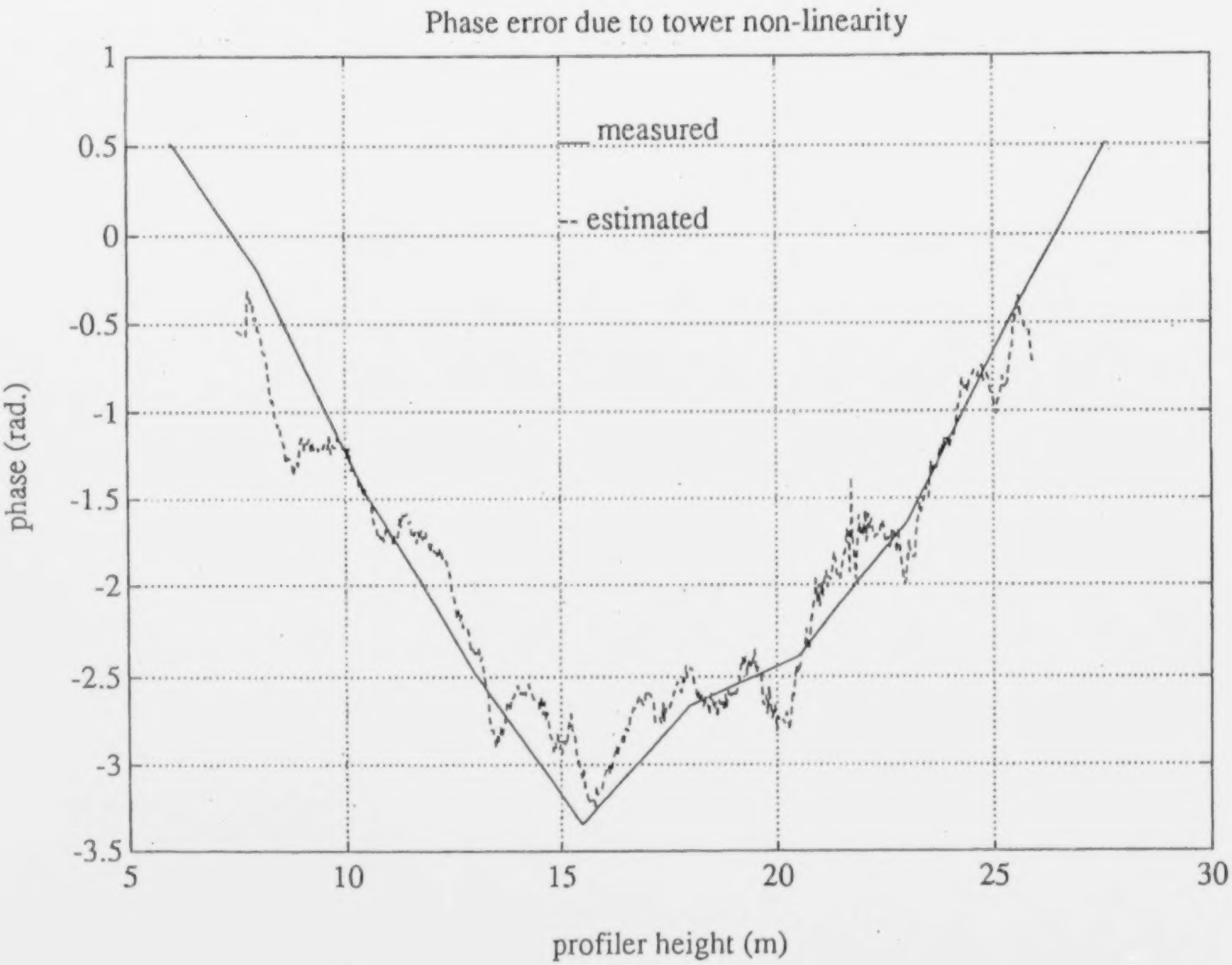

Fig. A1 Comparison of the measured and estimated phase errors due to the non-linearity of the profiler tower.

Table 7.1

The Lake Huron data files
used for estimation of target heights

actual target height(m)	file name	Two freqs. (GHz)	Four freqs. (added in) (GHz)	six freqs. (added in) (GHz)
18.5	n3dh4.dat	10.2, 11.92	8.62, 11.02	8.05, 9.22
15.5	n4dh9.dat	10.2, 8.05	8.62, 10.72	10.12, 9.22
13.1	n4dh8.dat	10.2, 8.05	8.62, 11.02	11.62, 9.22
9.5	n4dh1.dat	10.2, 8.05	8.62, 10.72	11.92, 9.22
6.5	n4dh2.dat	10.2, 8.05	8.62, 11.02	11.32, 9.22
4.3	n4dh5.dat	10.2, 8.05	8.62, 11.02	11.32, 9.22
3.5	n4dh6.dat	10.2, 8.05	8.62, 11.02	11.32, 9.22

Table 7.2

Means and variances of the estimated target heights

target heights (m)	angular separation (% BW)	Two freqs.		Four freqs.		six freqs.	
		mean	var	mean	var	mean	var
18.5	50	18.91	0.0079	18.48	0.0163	18.38	0.0105
15.5	40	15.08	0.0256	14.76	0.0064	14.80	0.0060
13.1	32	12.74	0.0073	12.51	0.0048	12.56	0.0048
9.5	25	9.40	0.4275	9.24	0.0015	8.95	0.0016
6.5	16	5.66	0.0578	5.49	0.0535	5.58	0.0297
4.3	11	4.11	0.0813	4.07	0.0543	4.17	0.0328
3.5	9	4.14	0.0747	3.49	0.0504	3.51	0.0307

SOME REPRESENTATIVE EXPERIMENTAL RESULTS FROM THE LAKE ONTARIO TRIALS

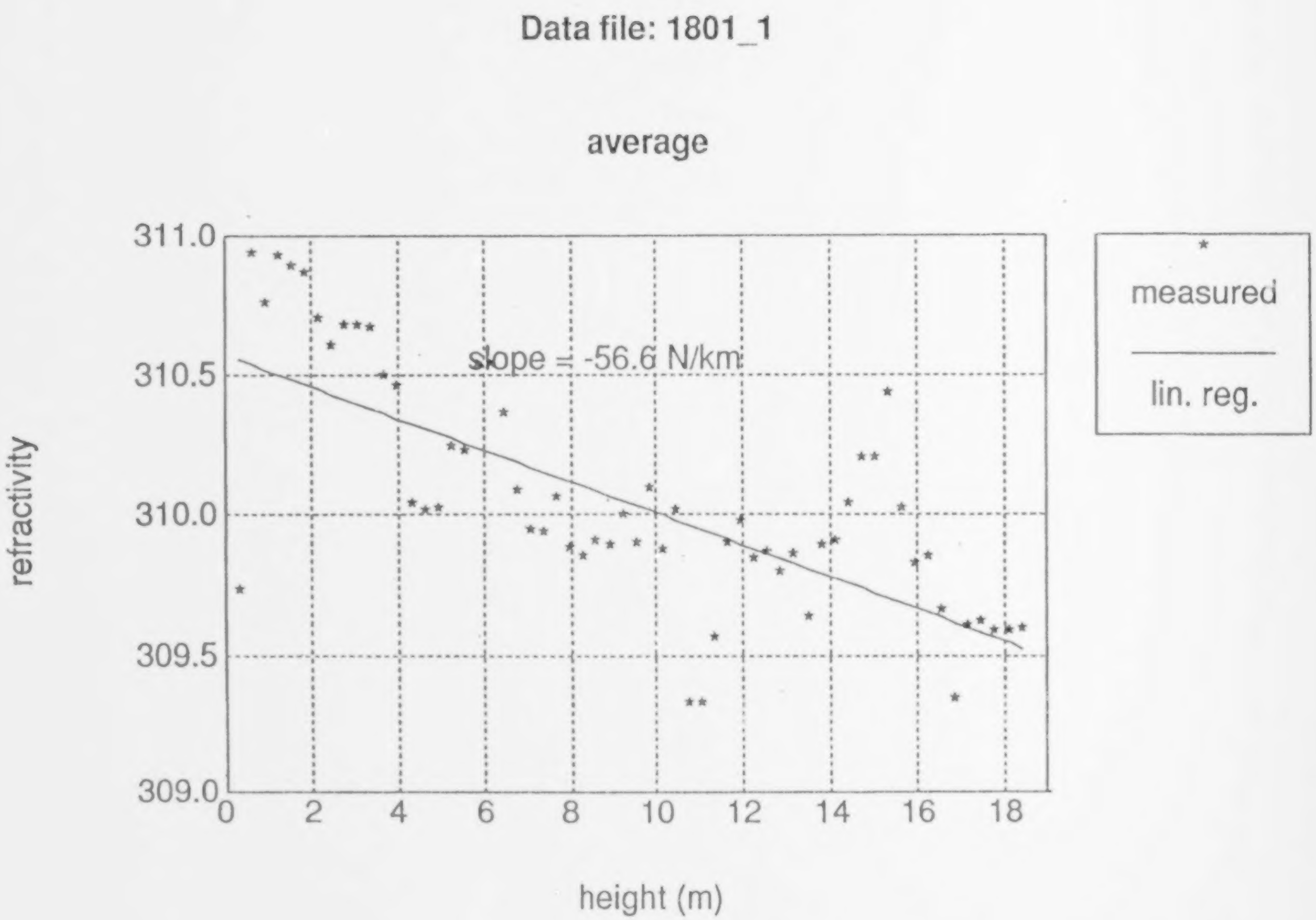
Data file: 1801_1
average
slope = -56.6 N/km
refractivity
311.0
310.5
310.0
309.5
309.0
0
2
4
6
8
10
12
14
16
18
height (m)
measured
lin. reg.

Fig. E1

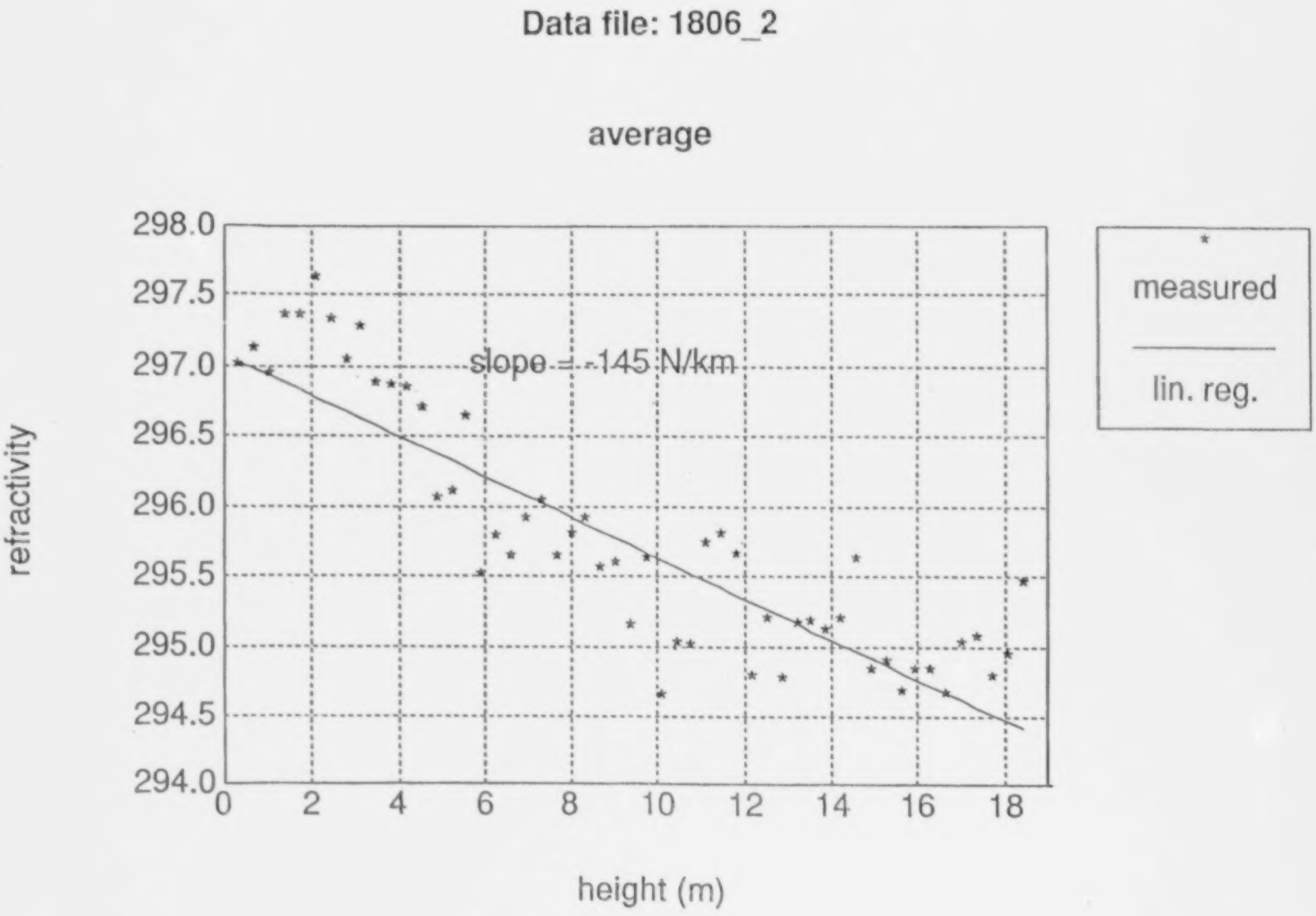
Data file: 1806_2
average
slope = -145 N/km
refractivity
298.0
297.5
297.0
296.5
296.0
295.5
295.0
294.5
294.0
0
2
4
6
8
10
12
14
16
18
height (m)
measured
lin. reg.

Fig. E2

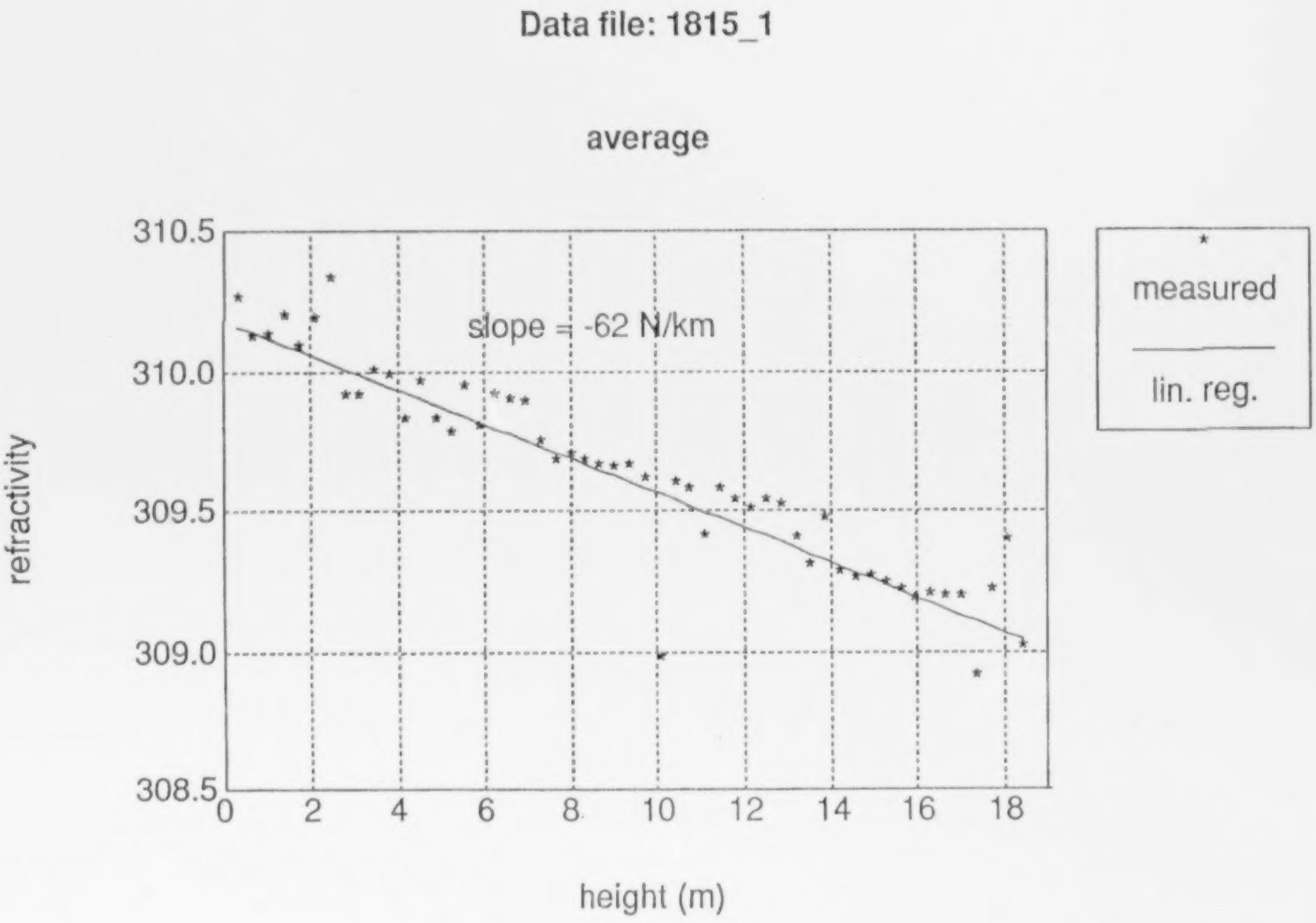
Data file: 1815_1
average
slope = -62 N/km
measured
lin. reg.
refractivity
310.5
310.0
309.5
309.0
308.5
0
2
4
6
8
10
12
14
16
18
height (m)

Fig. E3

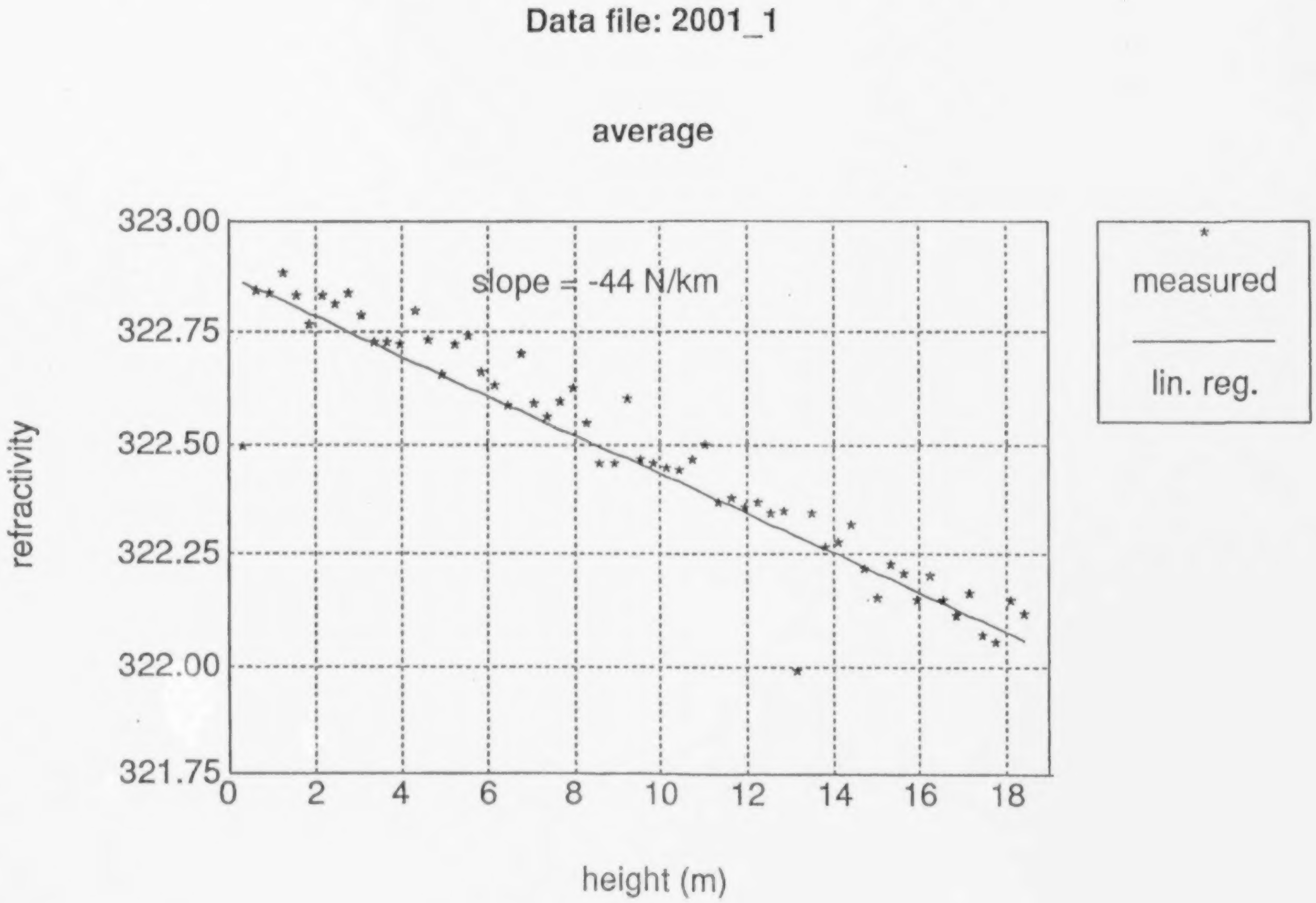
Data file: 2001_1
average
slope = -44 N/km
refractivity
323.00
322.75
322.50
322.25
322.00
321.75
0
2
4
6
8
10
12
14
16
18
height (m)
measured
lin. reg.

Fig. E4

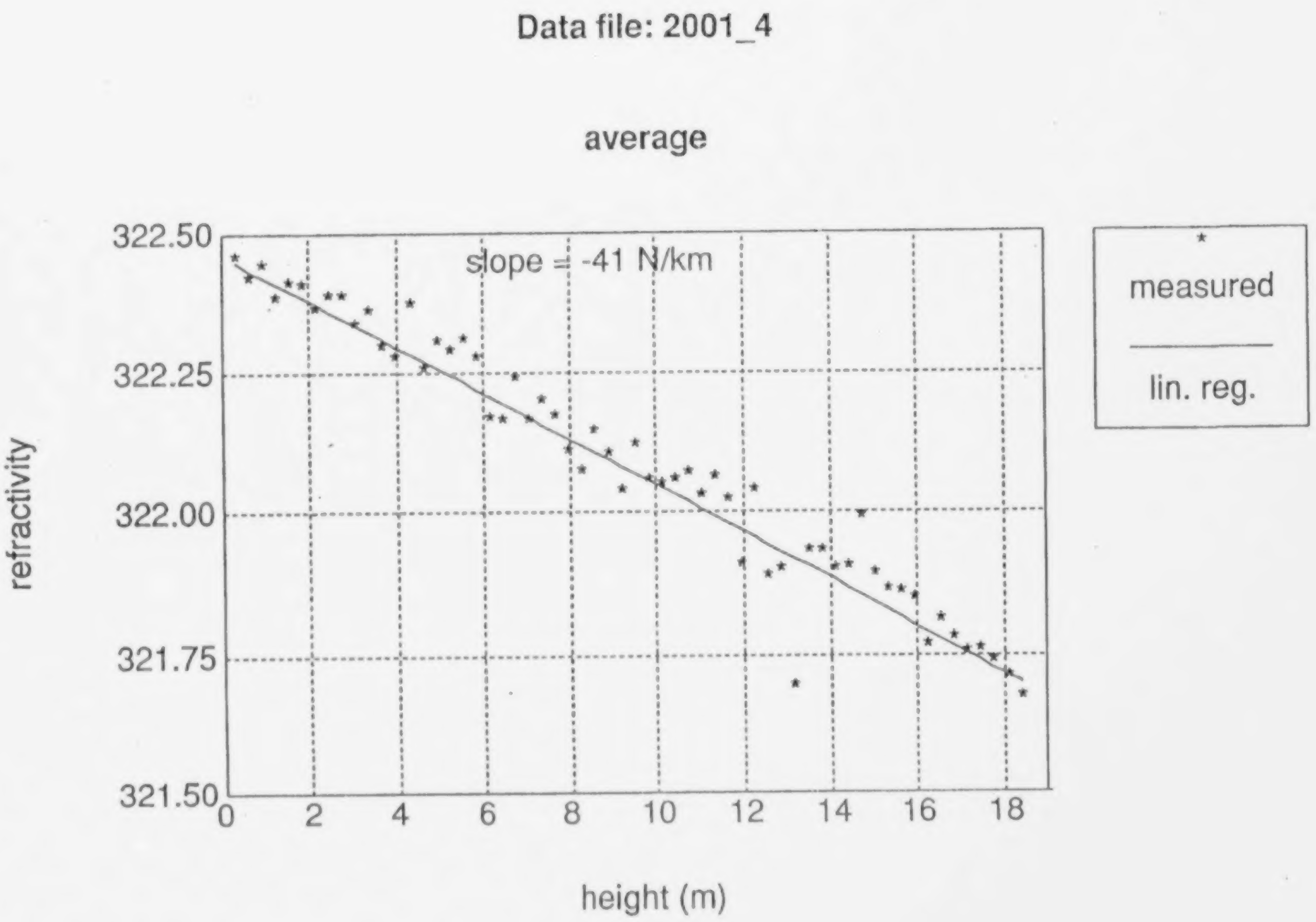
Data file: 2001_4
average
slope = -41 N/km
refractivity
322.50
322.25
322.00
321.75
321.50
height (m)
0
2
4
6
8
10
12
14
16
18
measured
lin. reg.

Fig. E5

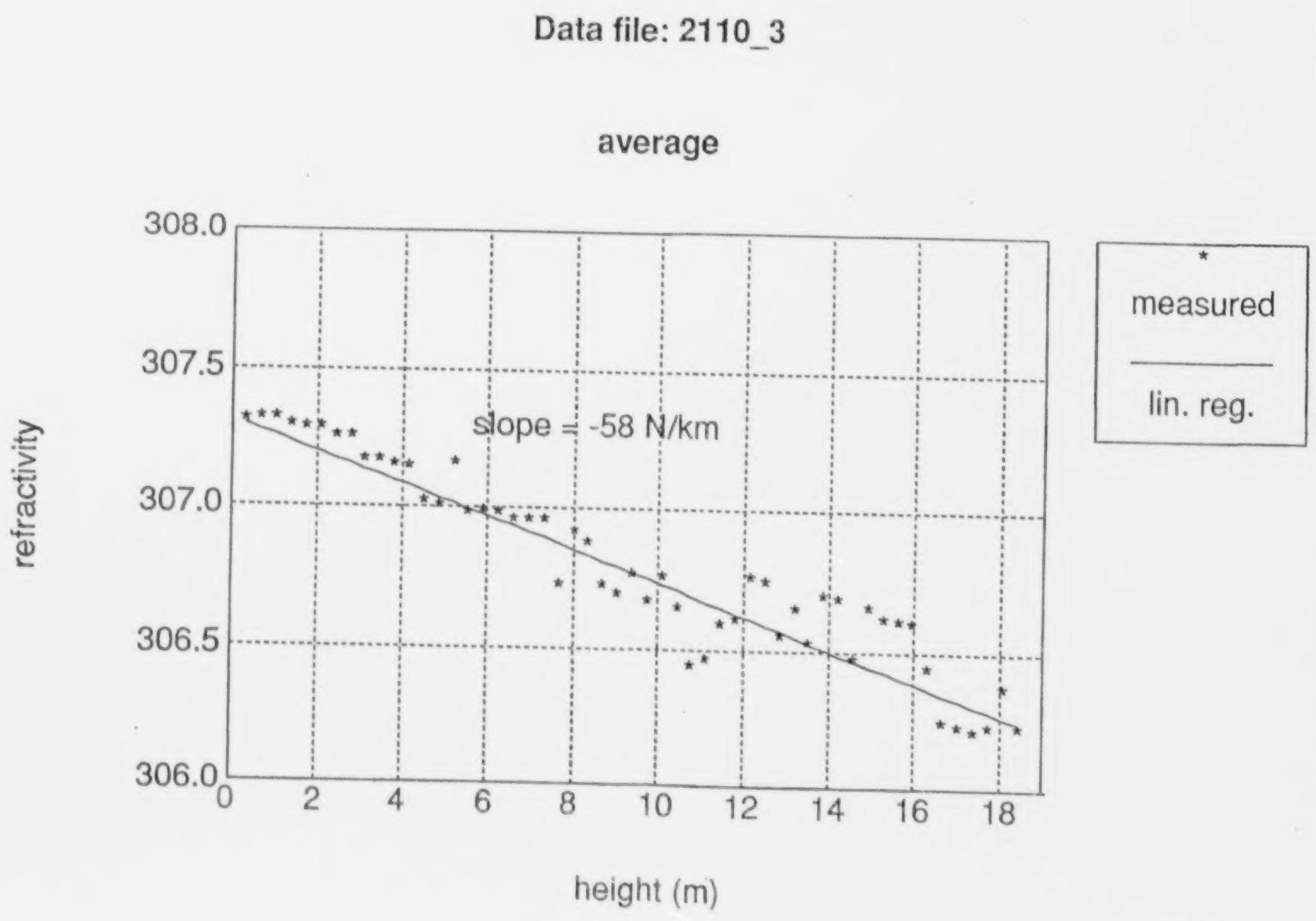
Data file: 2110_3
average
308.0
307.5
307.0
306.5
306.0
0
2
4
6
8
10
12
14
16
18
refractivity
height (m)
slope = -58 N/km
measured
lin. reg.

Fig. E6

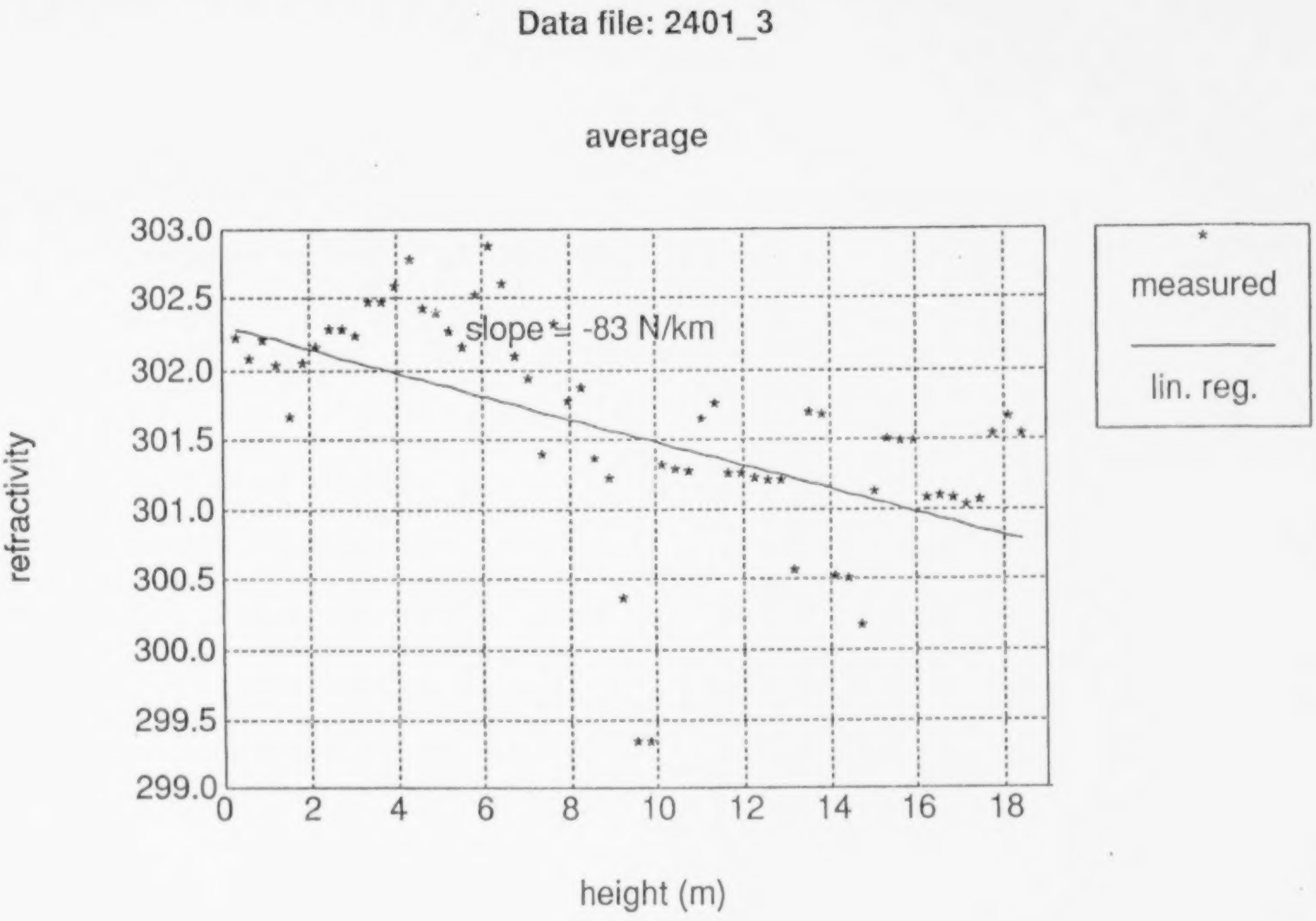
Data file: 2401_3
average
slope = -83 N/km
refractivity
303.0
302.5
302.0
301.5
301.0
300.5
300.0
299.5
299.0
0
2
4
6
8
10
12
14
16
18
height (m)
measured
lin. reg.

Fig. E7

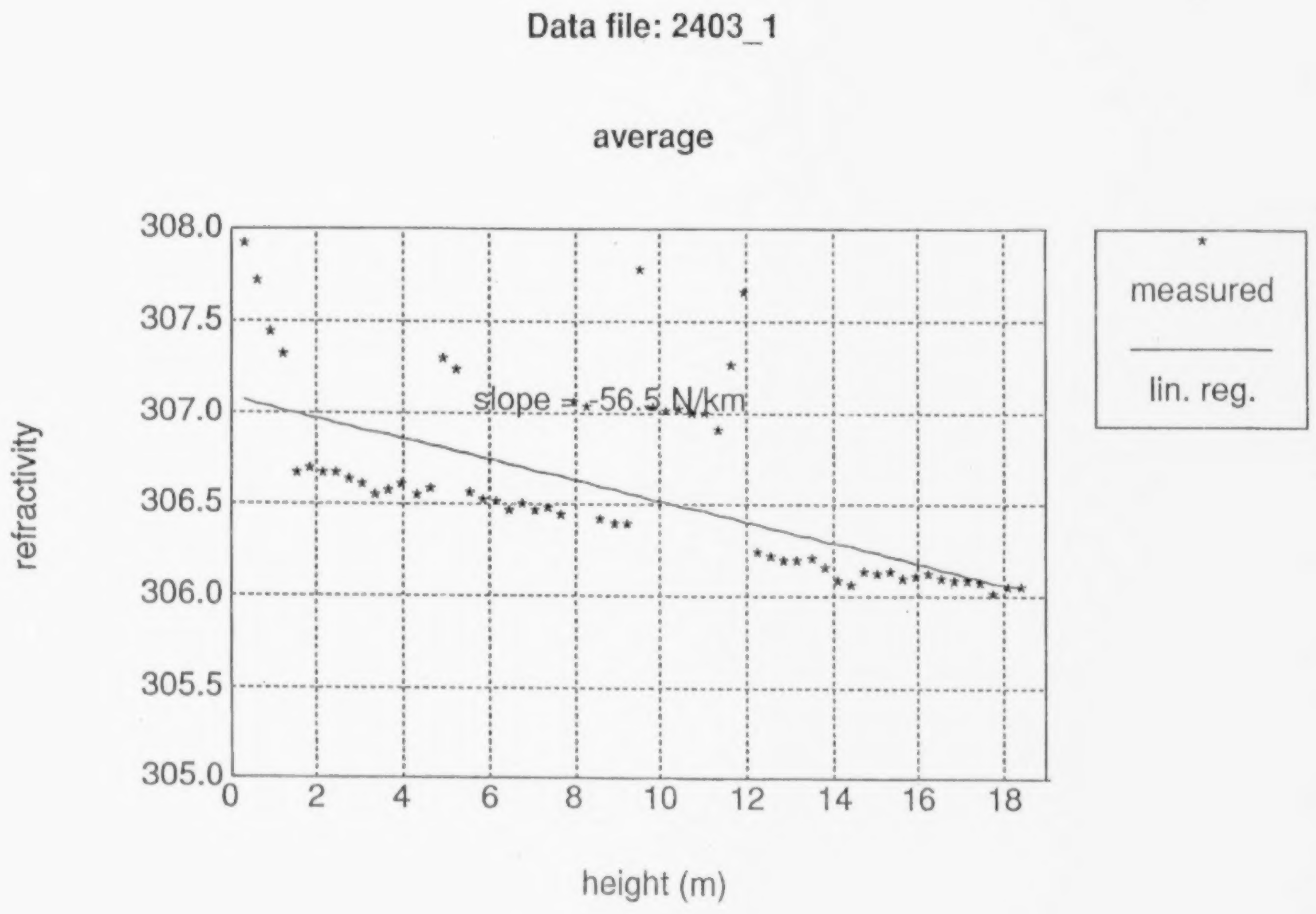
Data file: 2403_1
average
refractivity
308.0
307.5
307.0
306.5
306.0
305.5
305.0
0
2
4
6
8
10
12
14
16
18
height (m)
slope = -56.5 N/km
measured
lin. reg.

Fig. E8

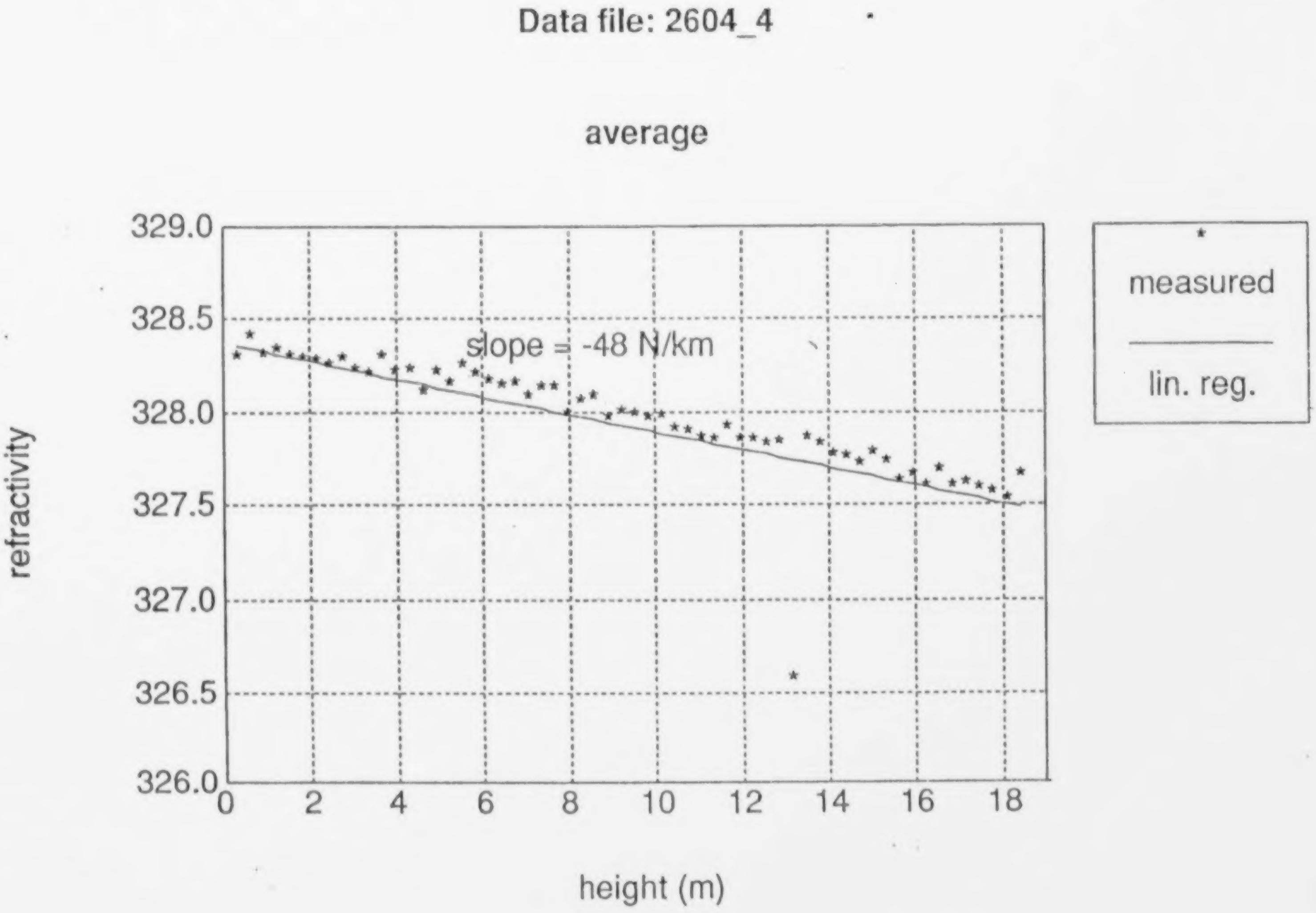
Data file: 2604_4
average
slope = -48 N/km
refractivity
329.0
328.5
328.0
327.5
327.0
326.5
326.0
0
2
4
6
8
10
12
14
16
18
height (m)
measured
lin. reg.

Fig. E9

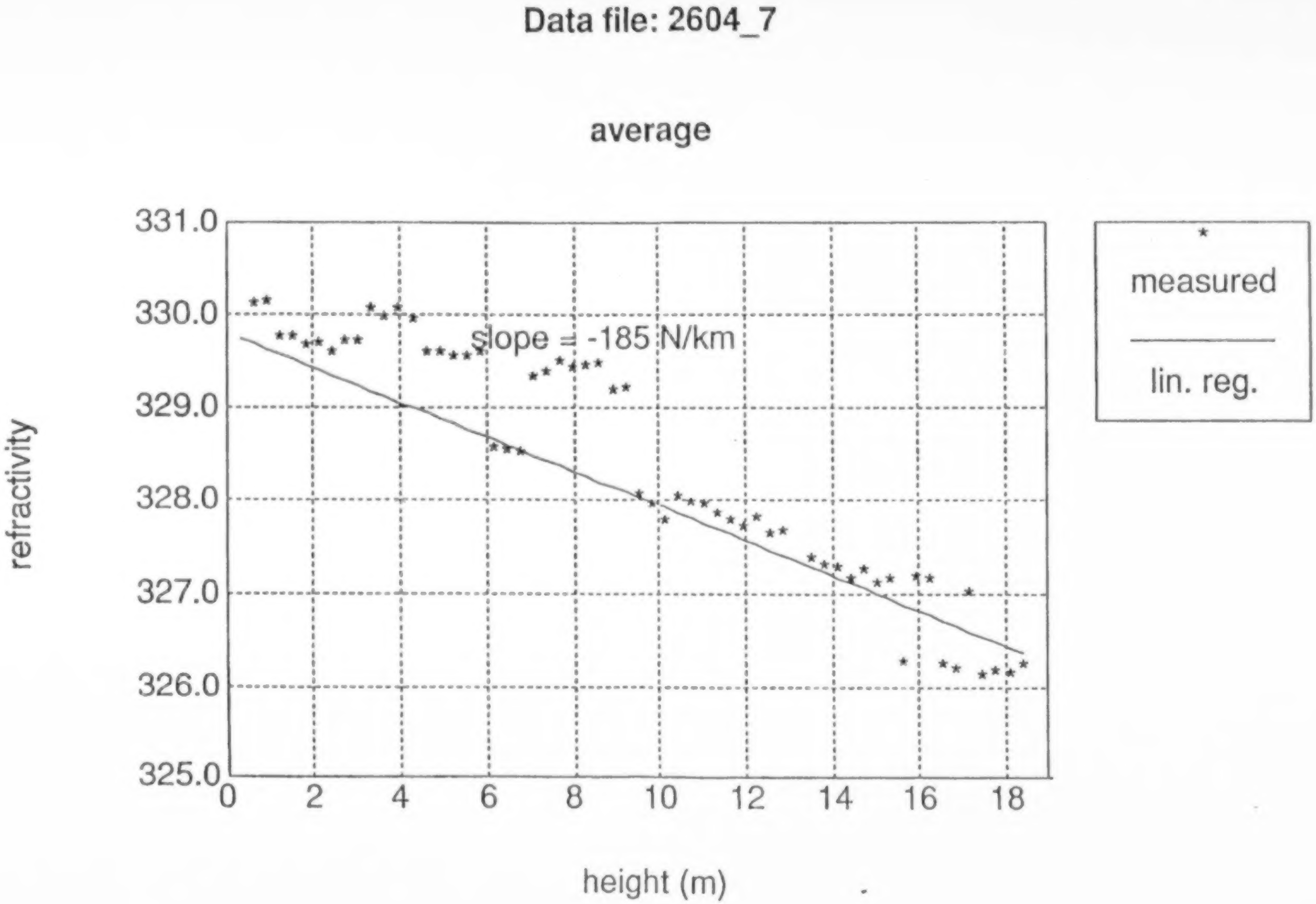
Data file: 2604_7
average
refractivity
331.0
330.0
329.0
328.0
327.0
326.0
325.0
0
2
4
6
8
10
12
14
16
18
height (m)
slope = -185 N/km
measured
lin. reg.

Fig. E10

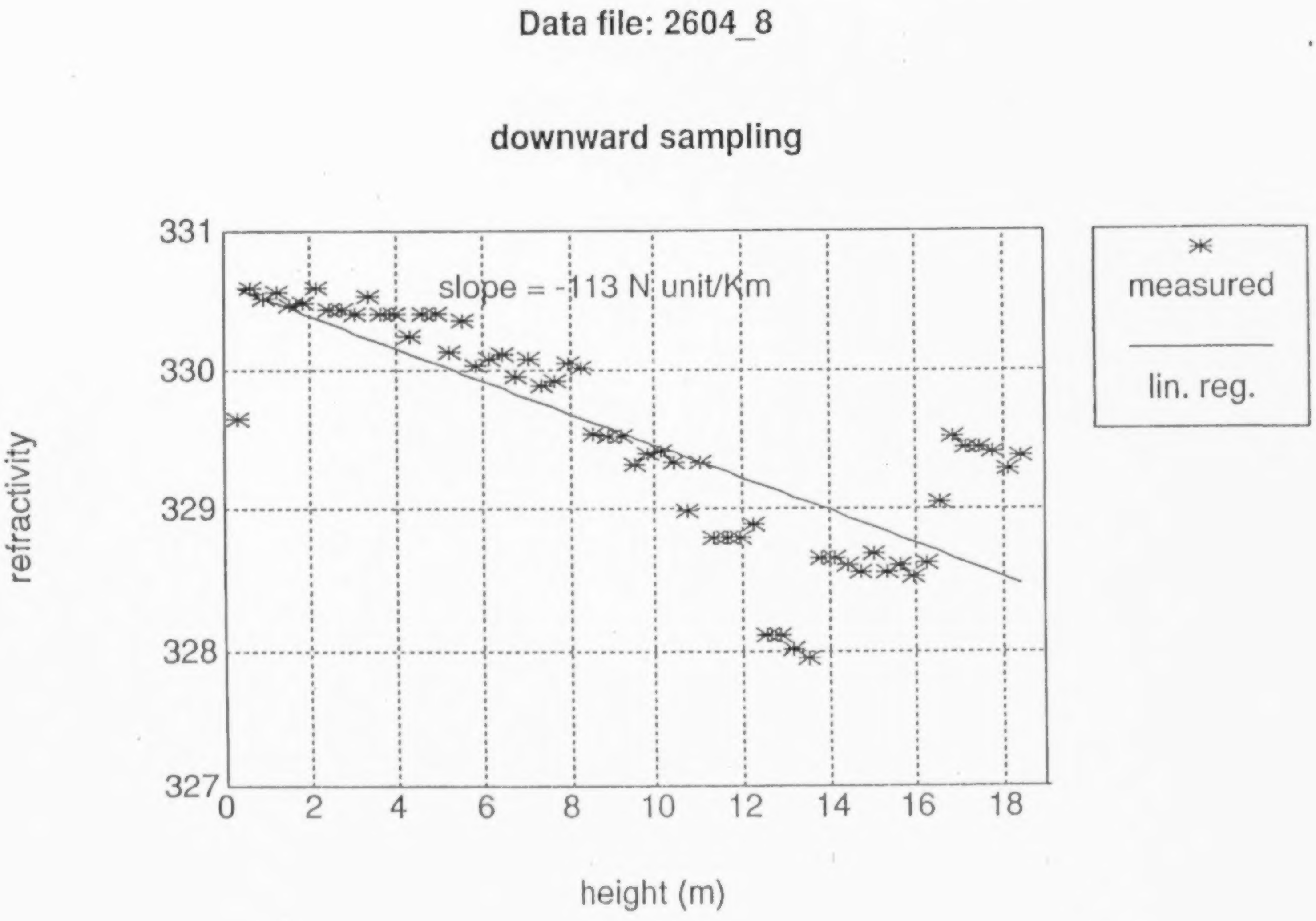

Data file: 2604_8

downward sampling

Fig. E11

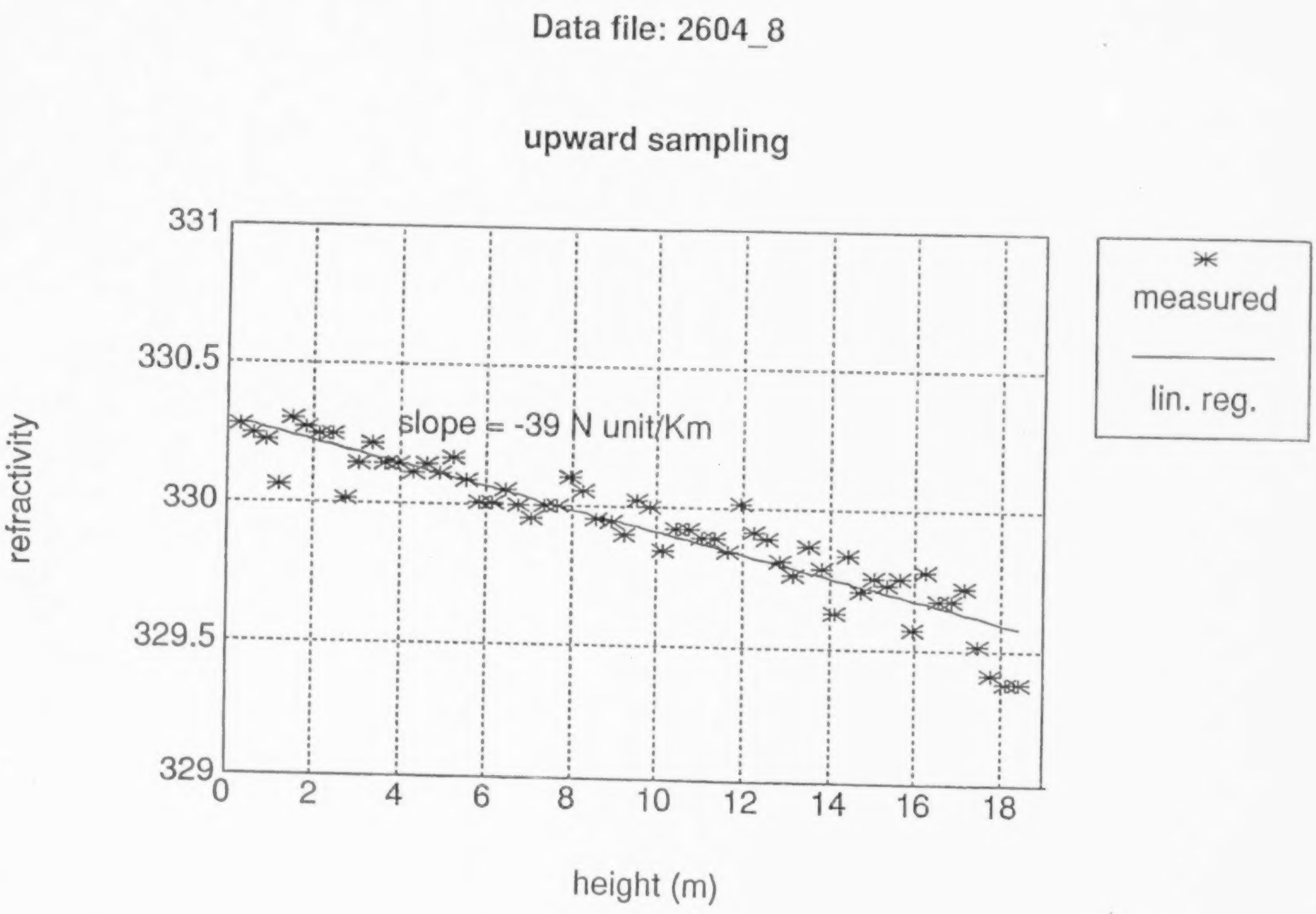
Data file: 2604_8
upward sampling
slope = -39 N unit/Km
refractivity
331
330.5
330
329.5
329
height (m)
0
2
4
6
8
10
12
14
16
18
measured
lin. reg.

Fig. E12

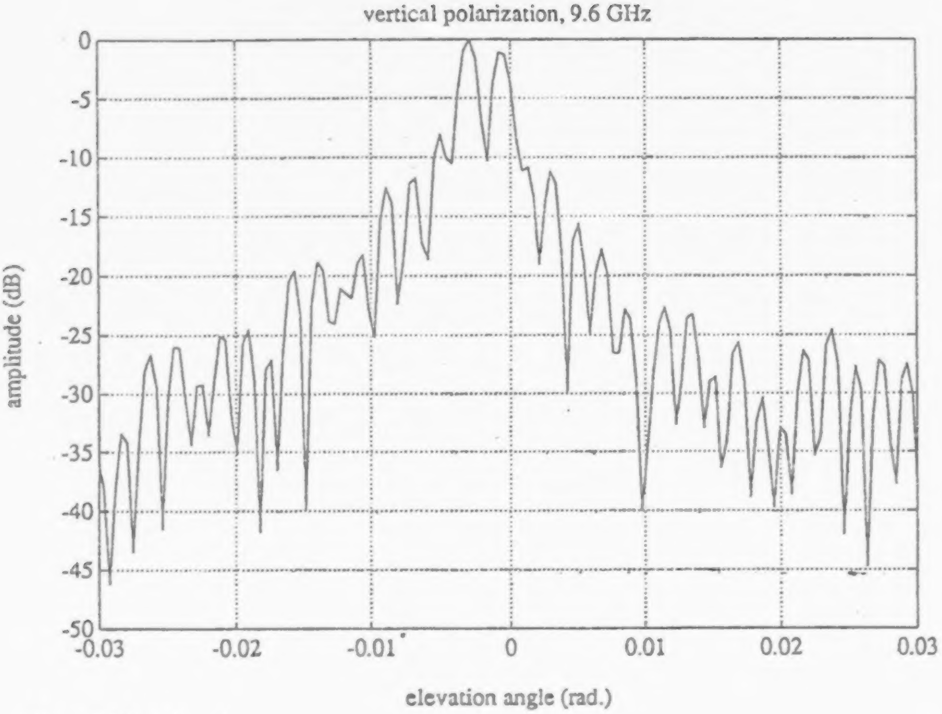

Fig. E13 (a)

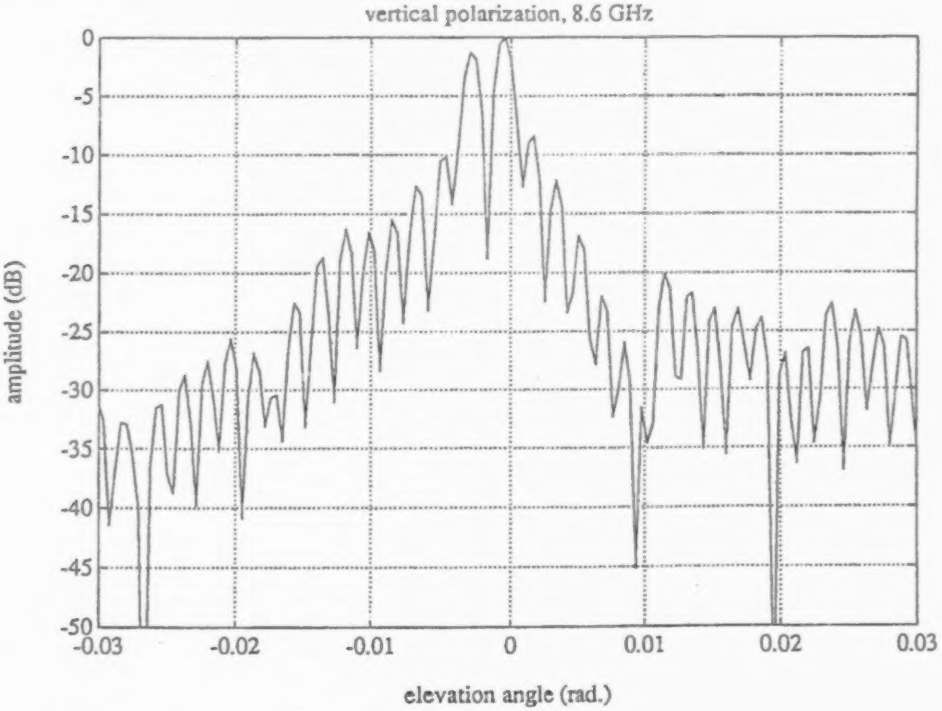

Fig. E13 (b)

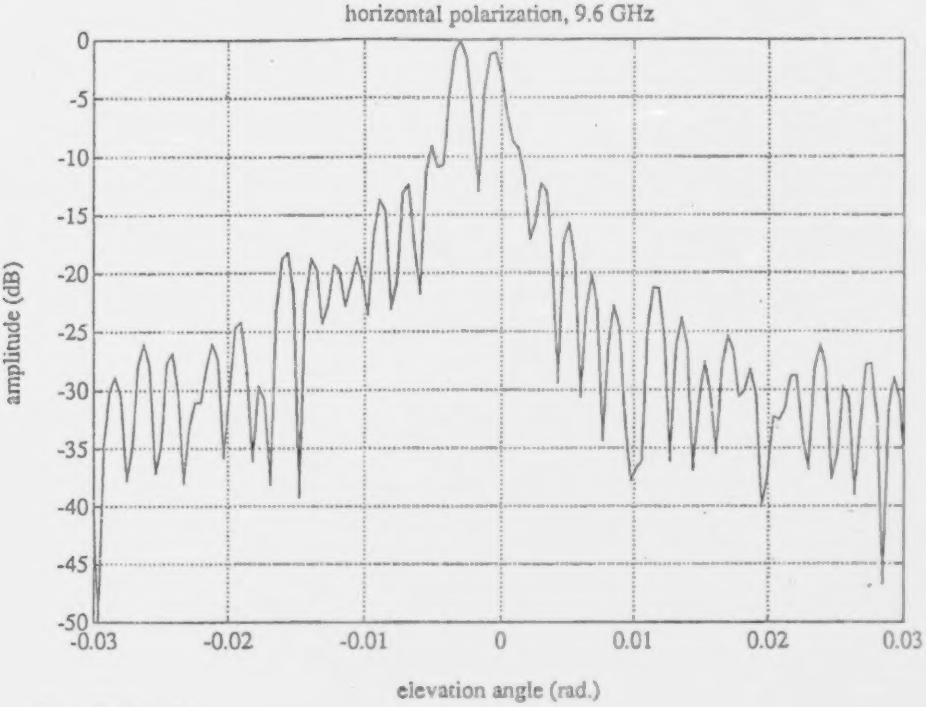

Fig. E13 (c)

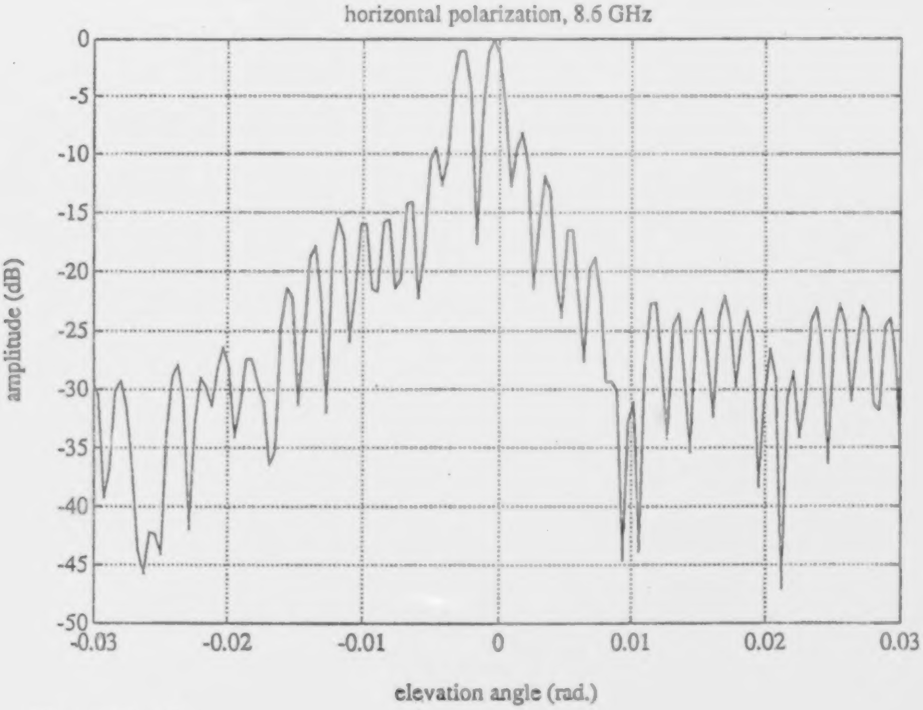

Fig. E13 (d)

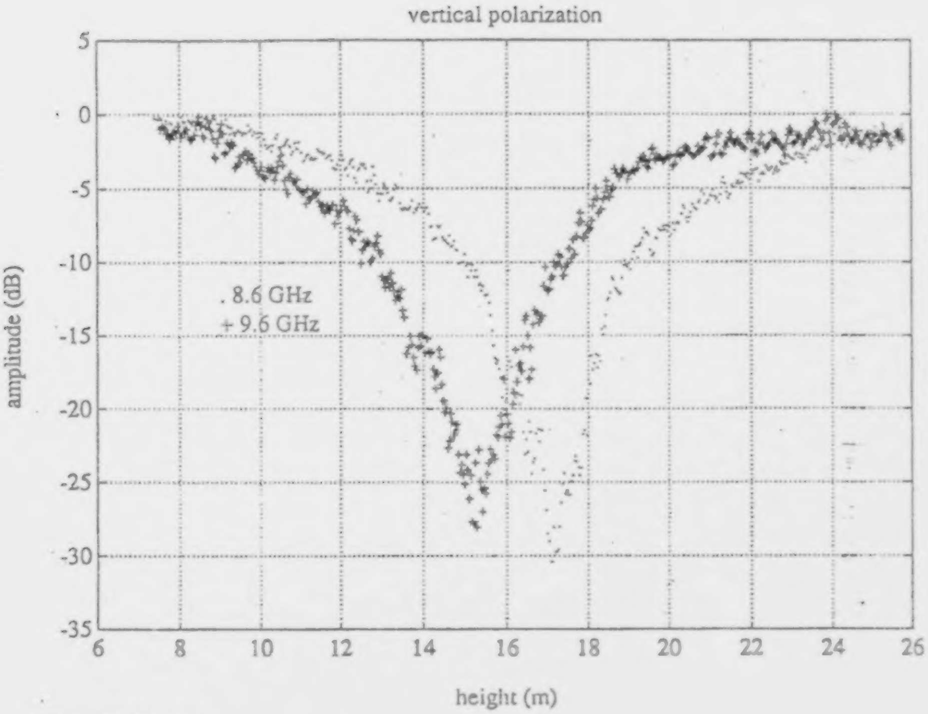

Fig. E13 (e)

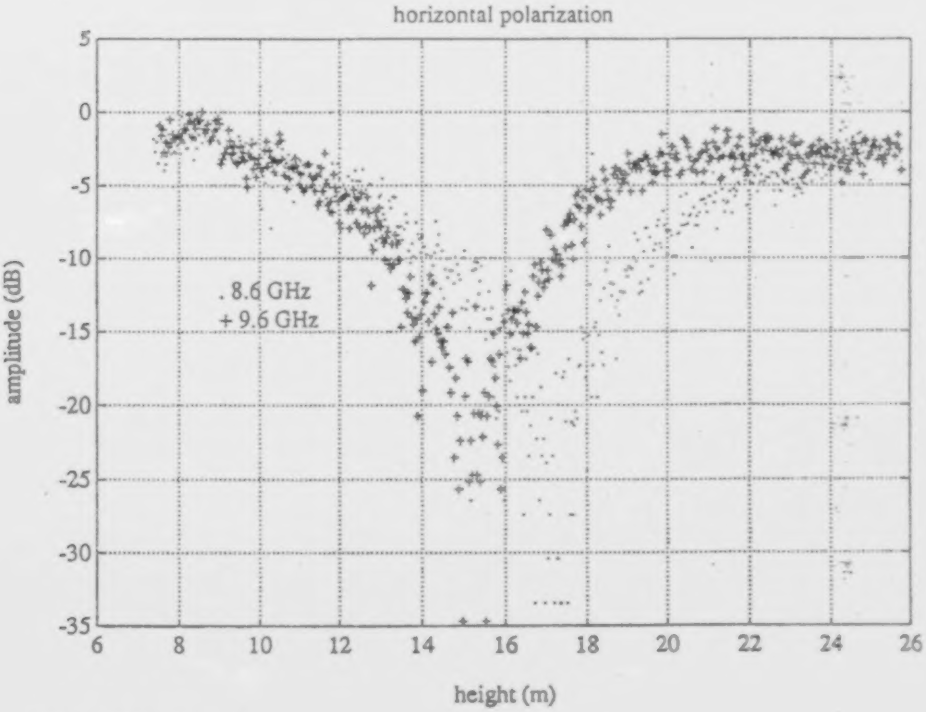

Fig. E13 (f)

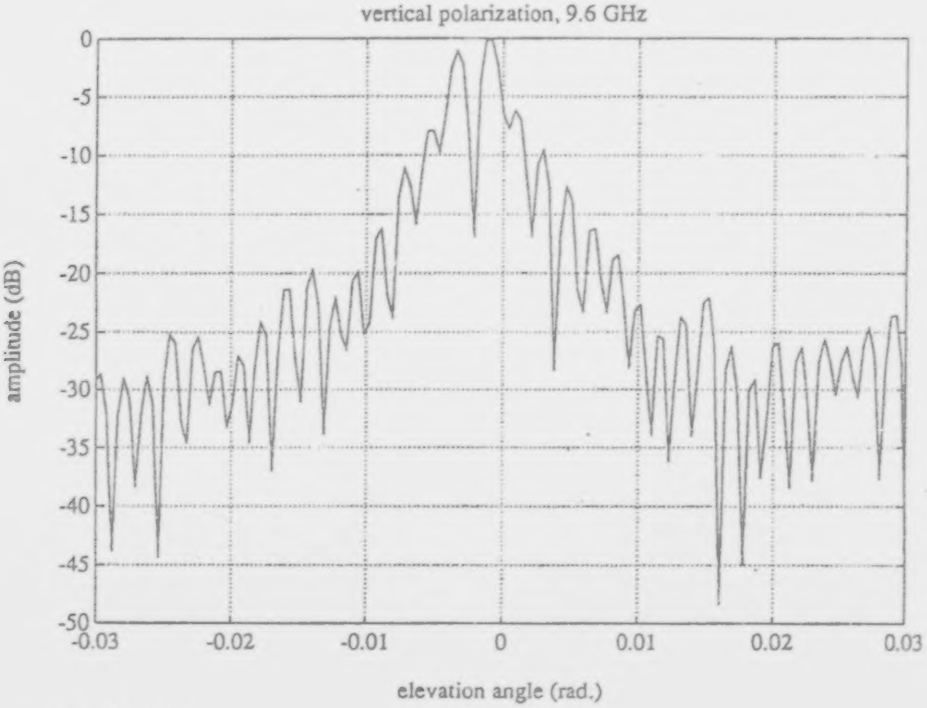

Fig. E14 (a)

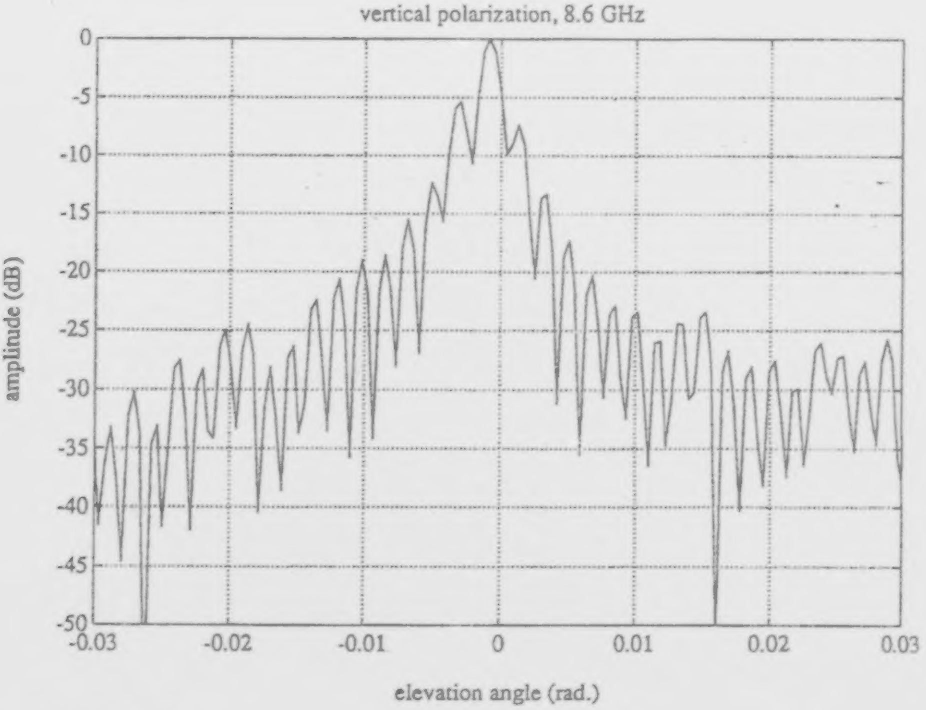

Fig. E14 (b)

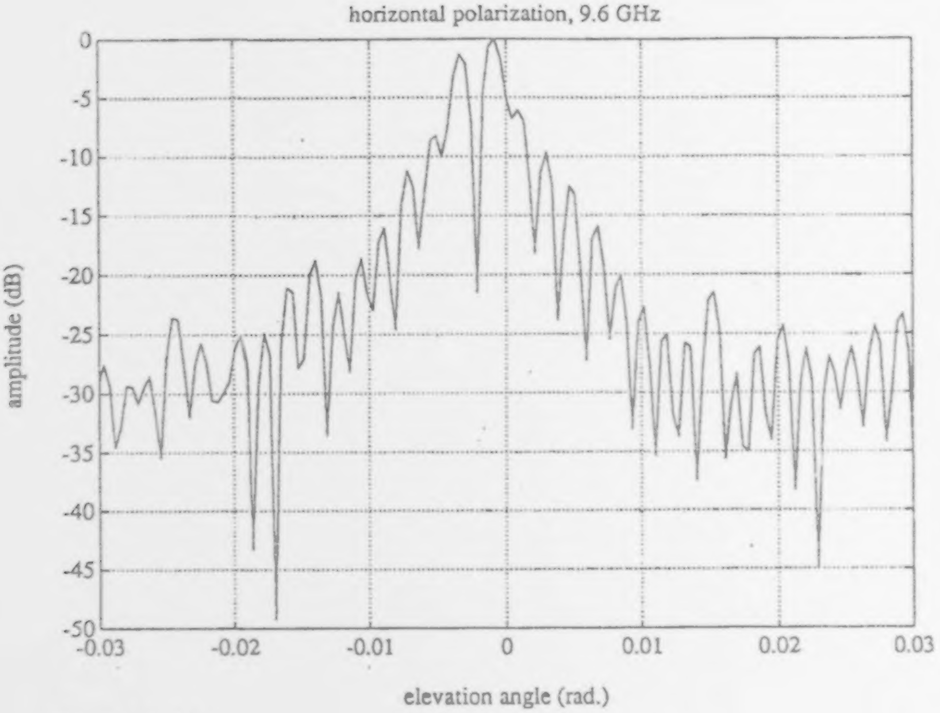

Fig. E14 (c)

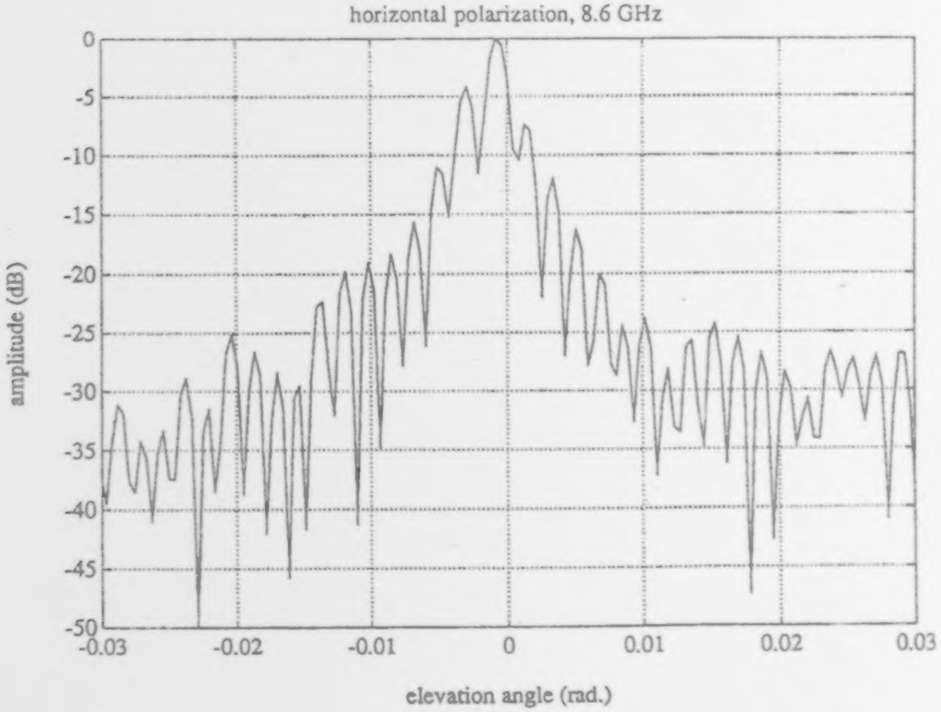

Fig. E14 (d)

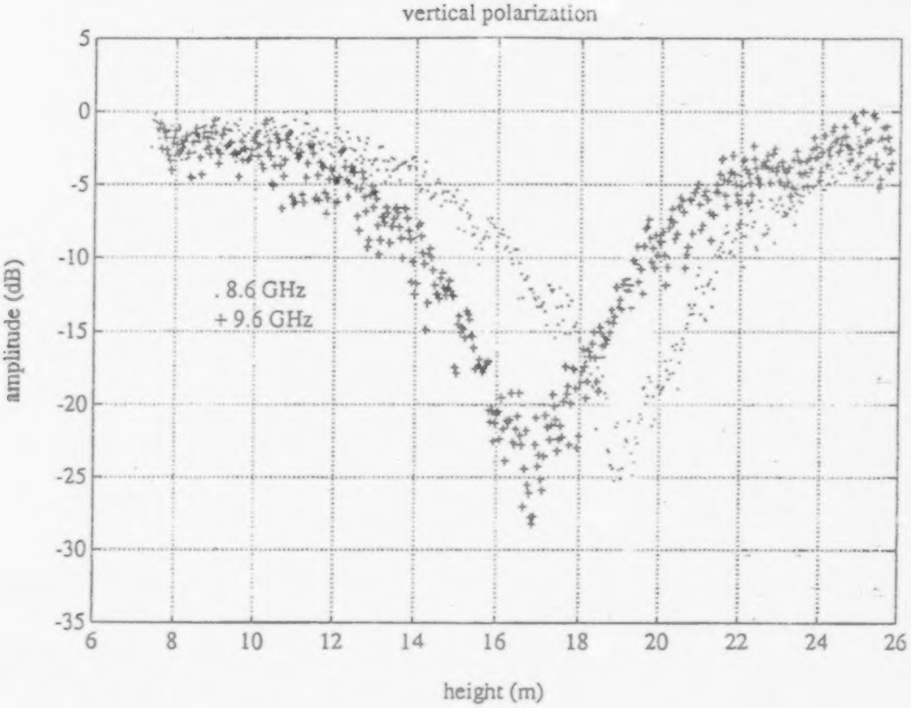

Fig. E14 (e)

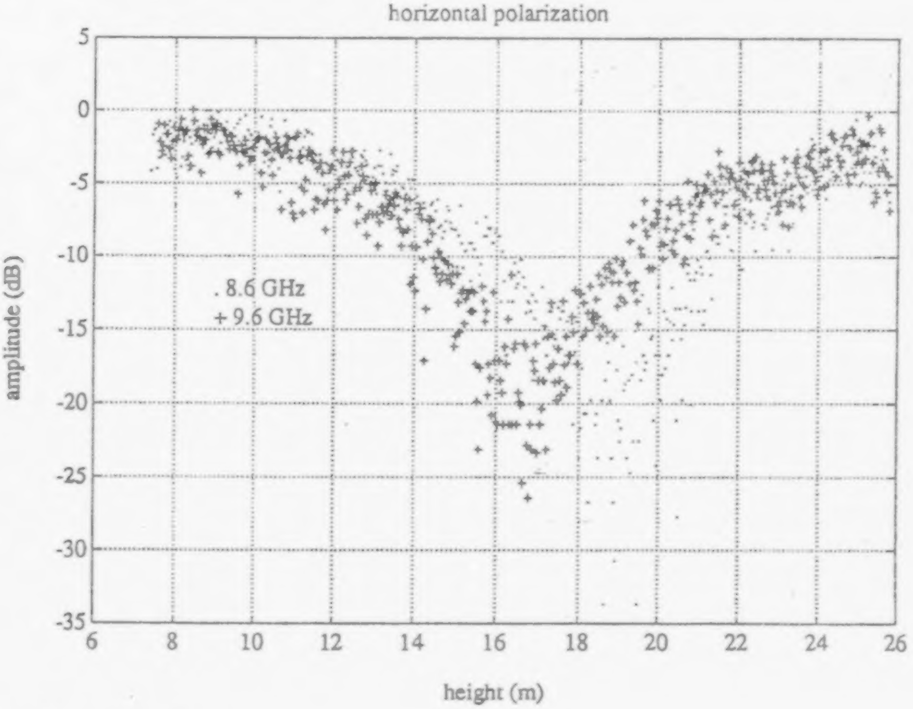

Fig. E14 (f)

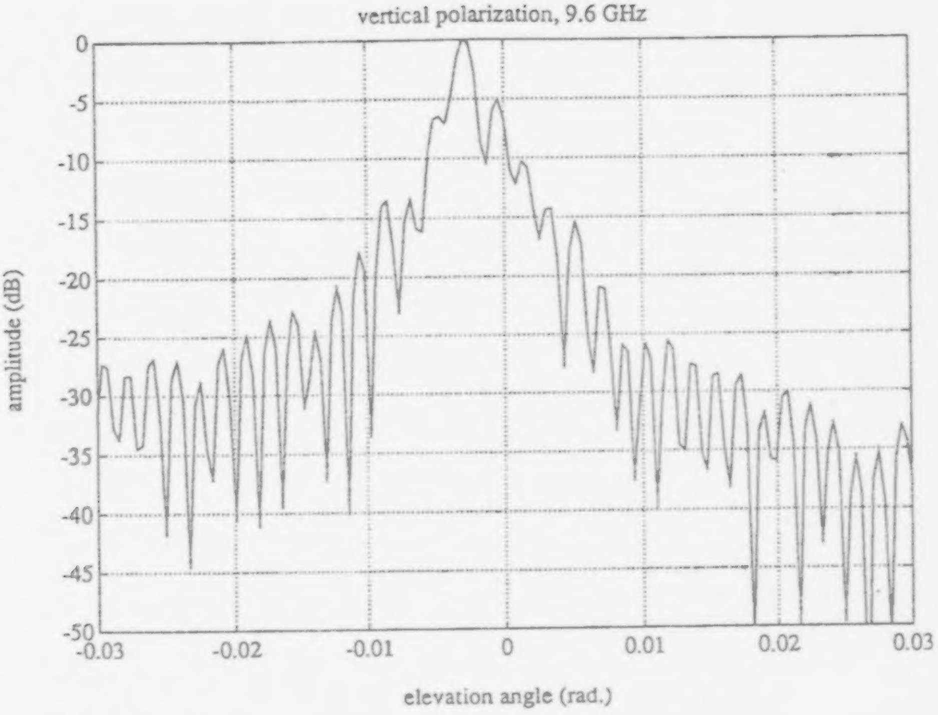

Fig. E15 (a)

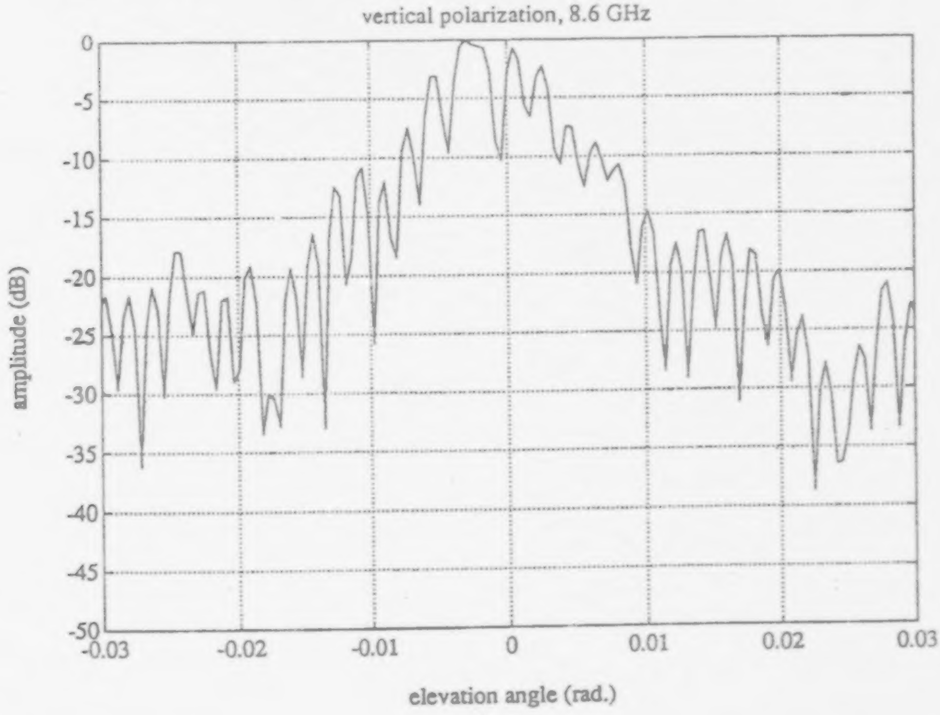

Fig. E15 (b)

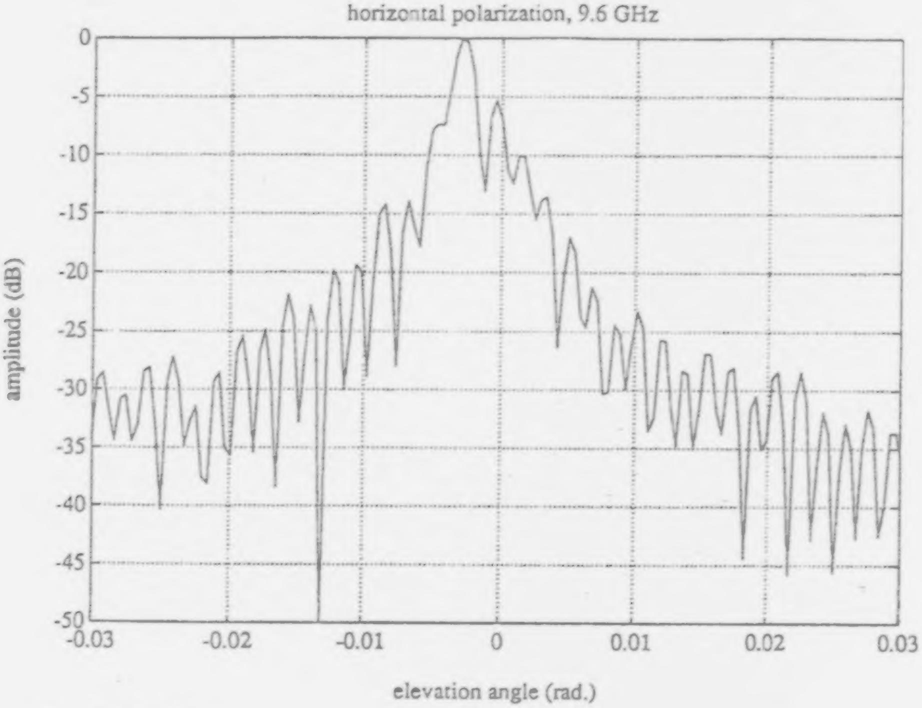

Fig. E15 (c)

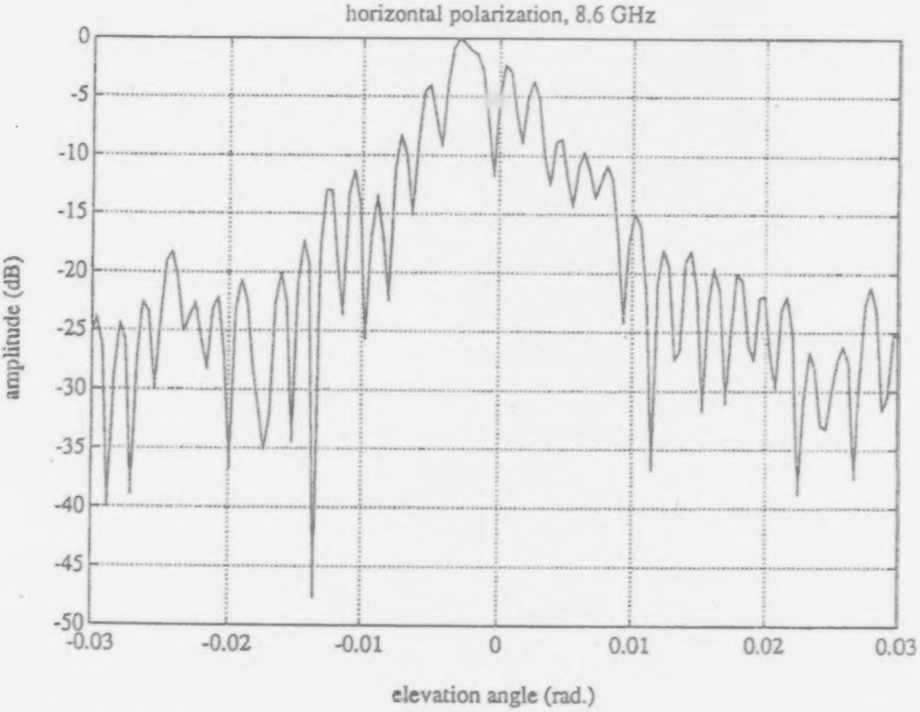

Fig. E15 (d)

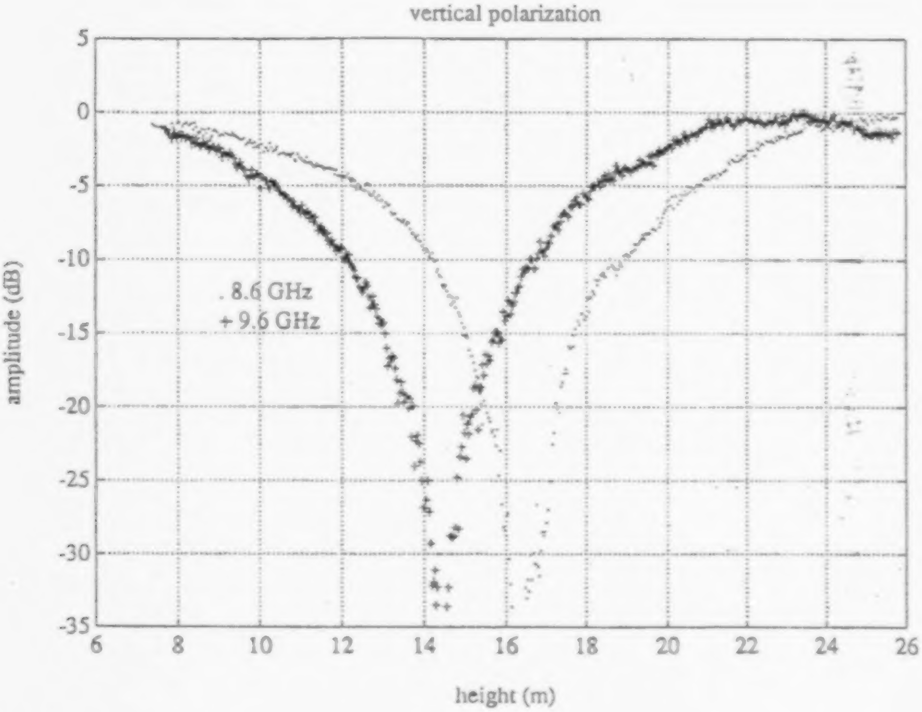

Fig. E15 (e)

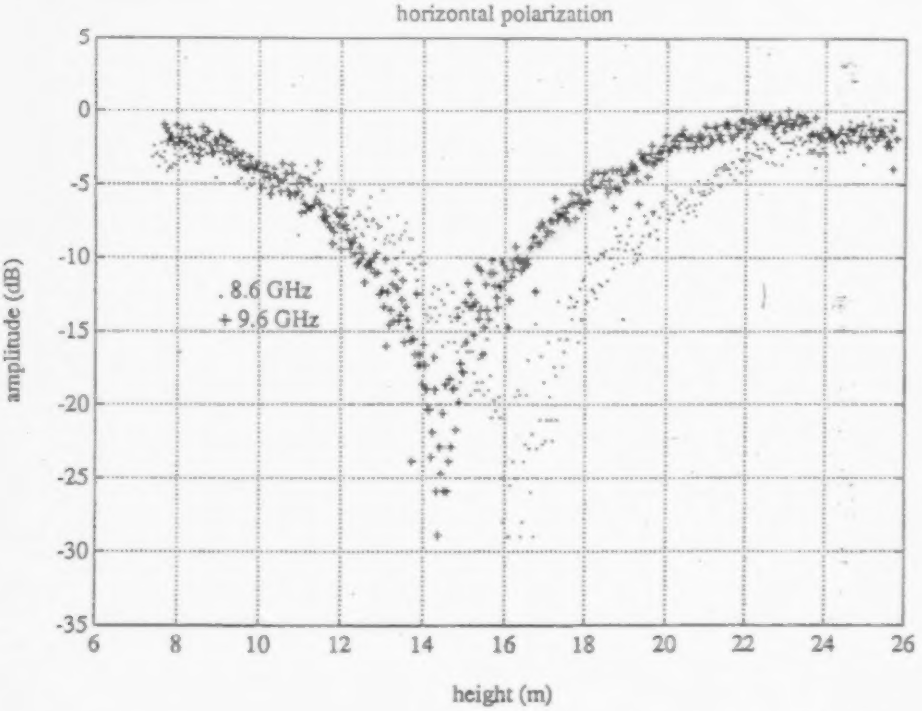

Fig. E15 (f)

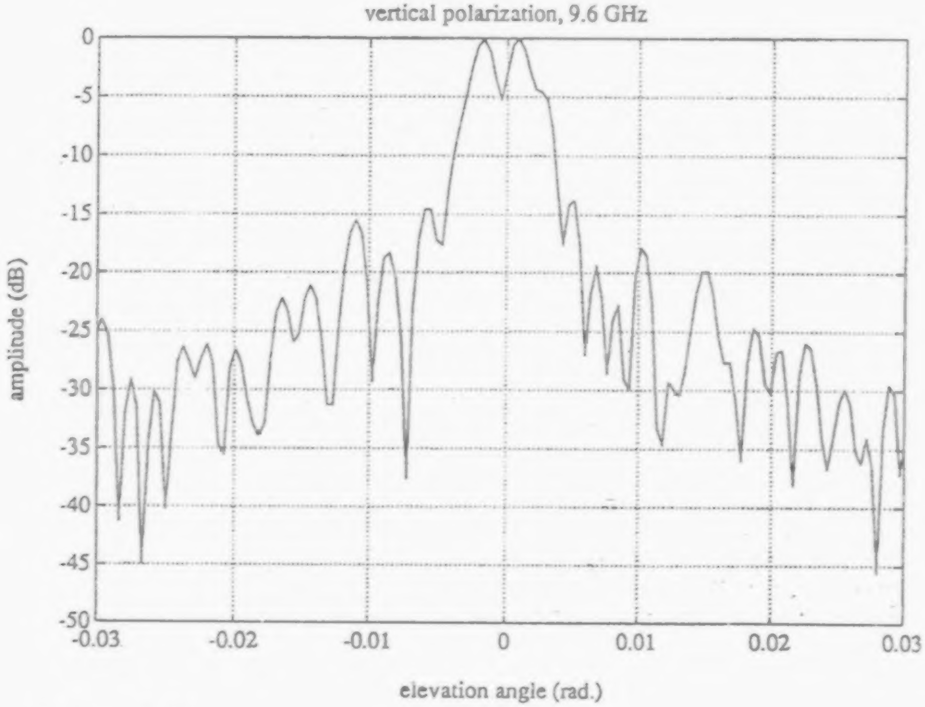

Fig. E16 (a)

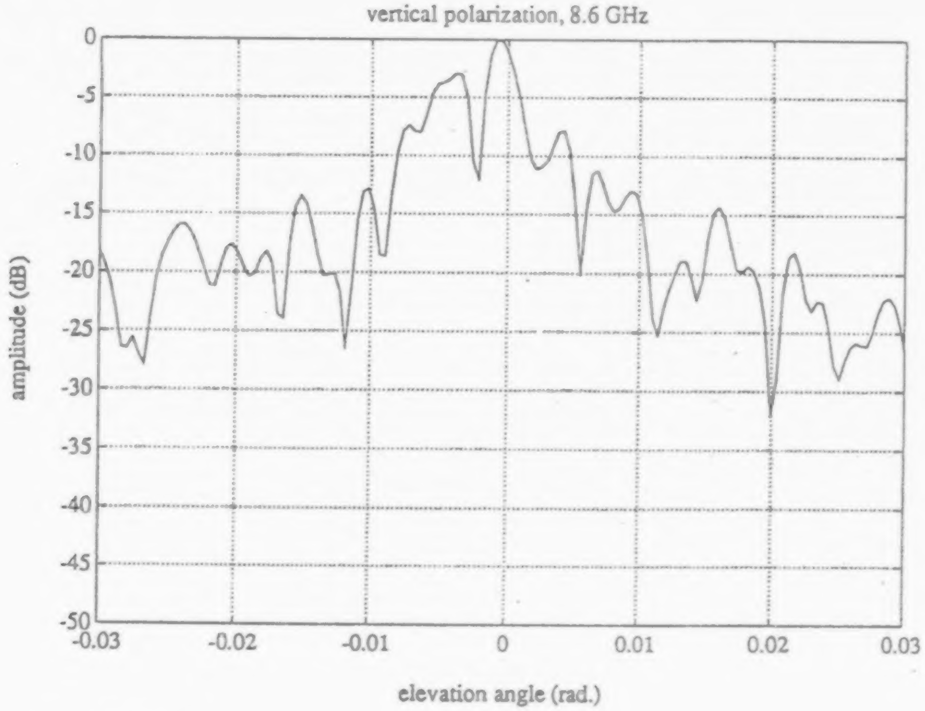

Fig. E16 (b)

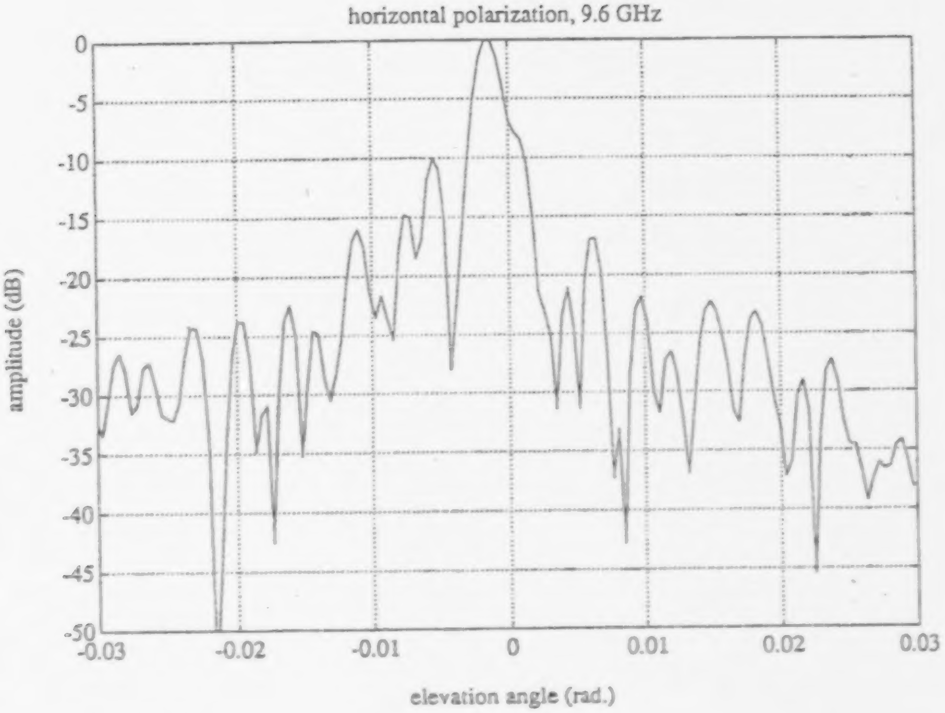

Fig. E16 (c)

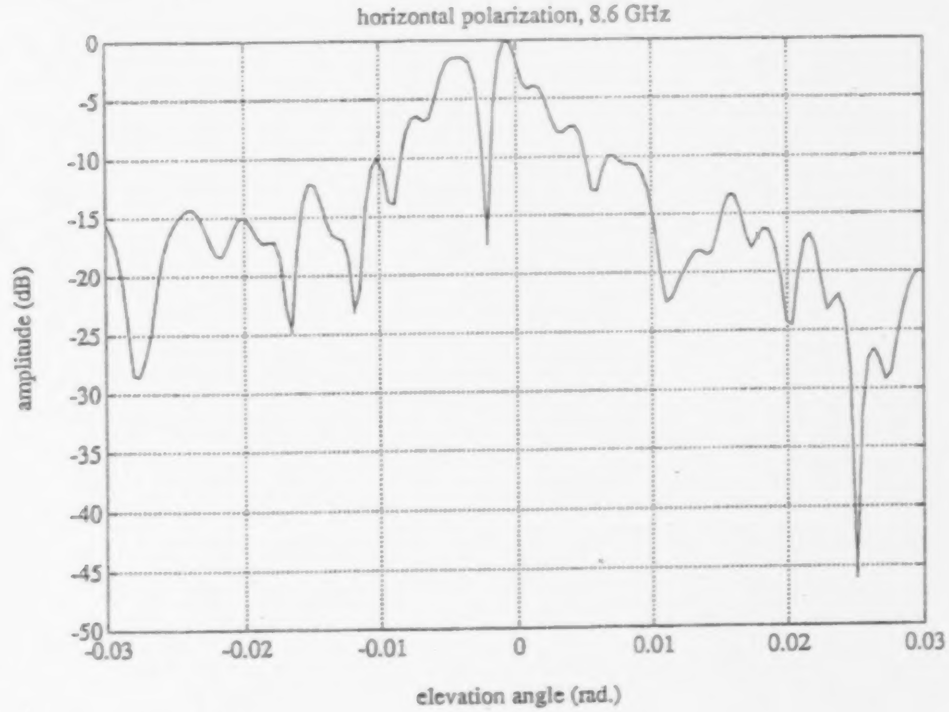

Fig. E16 (d)

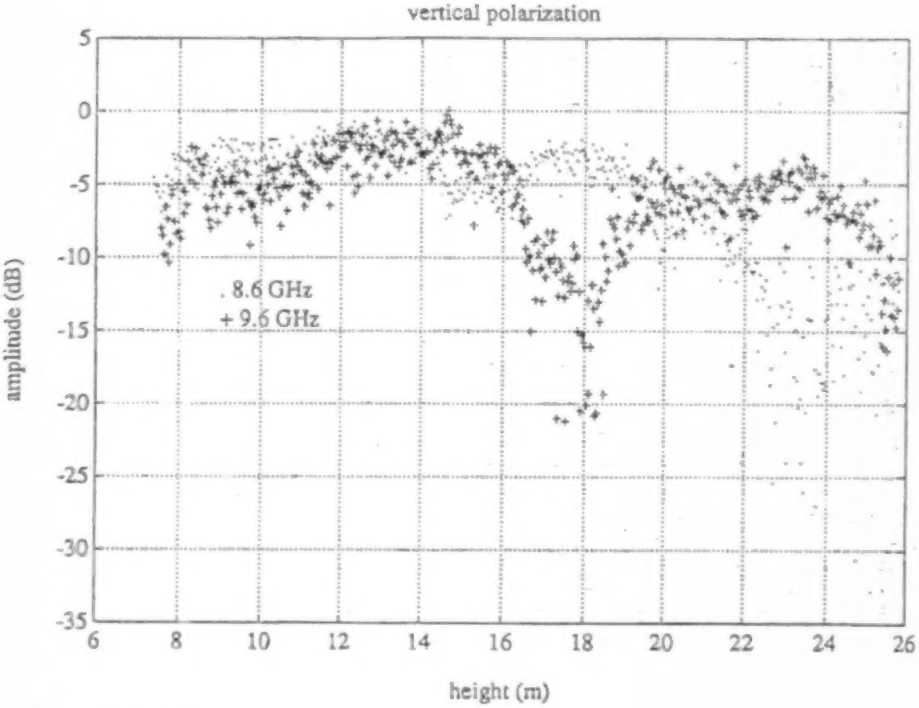

Fig. E16 (e)

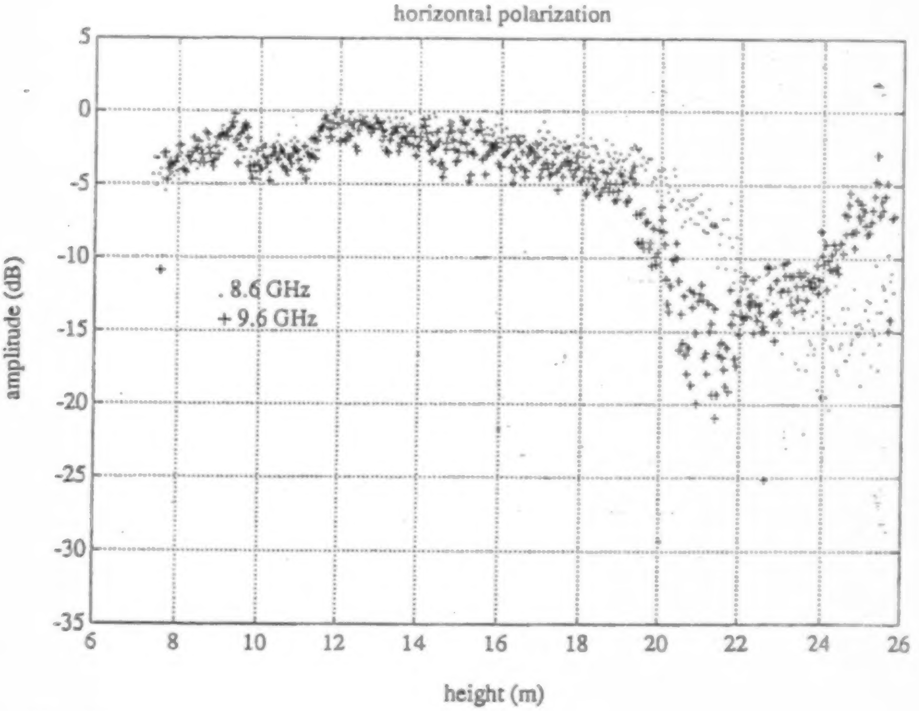

Fig. E16 (f)

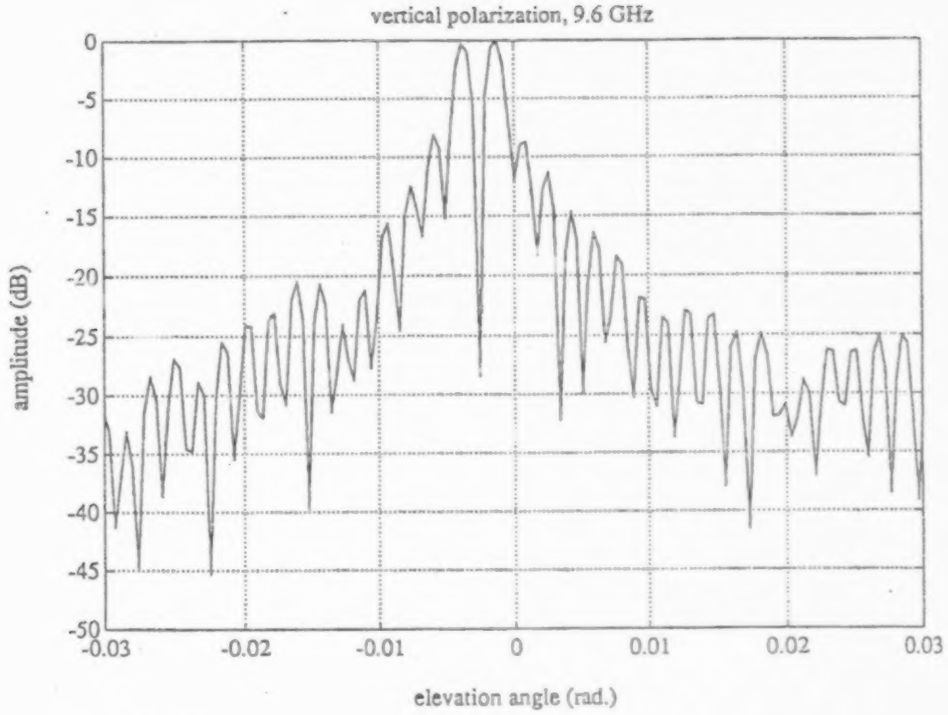

Fig. E17 (a)

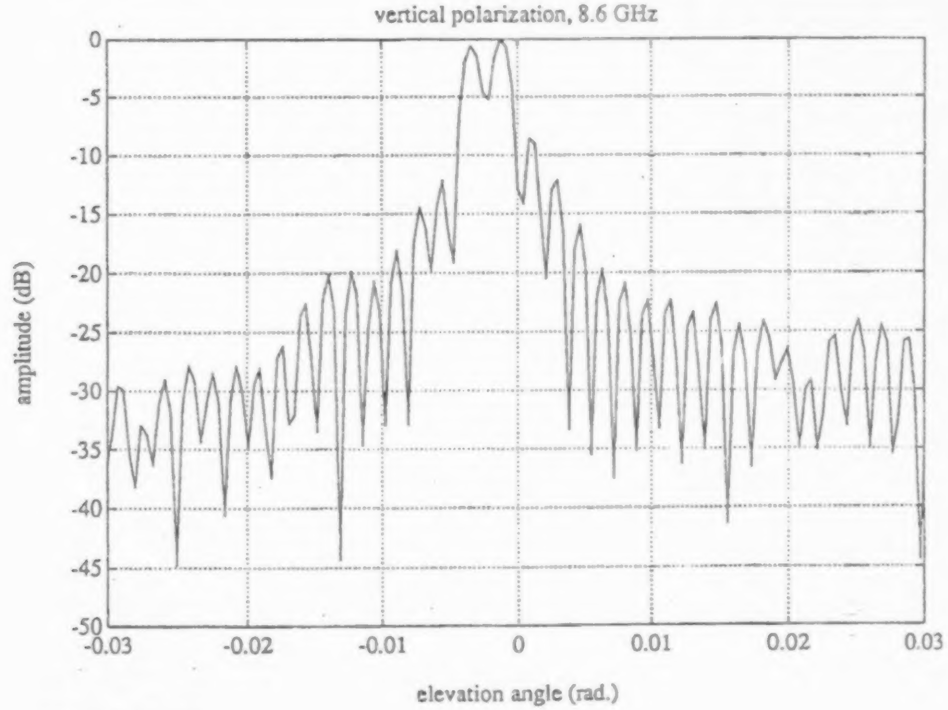

Fig. E17 (b)

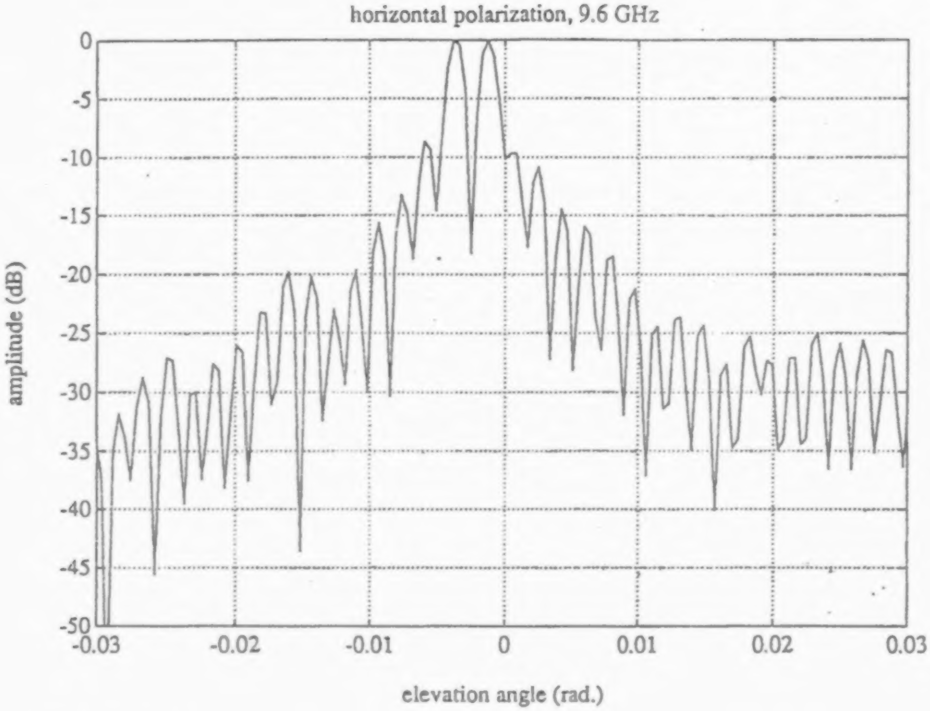
horizontal polarization, 9.6 GHz

Fig. E17 (c)

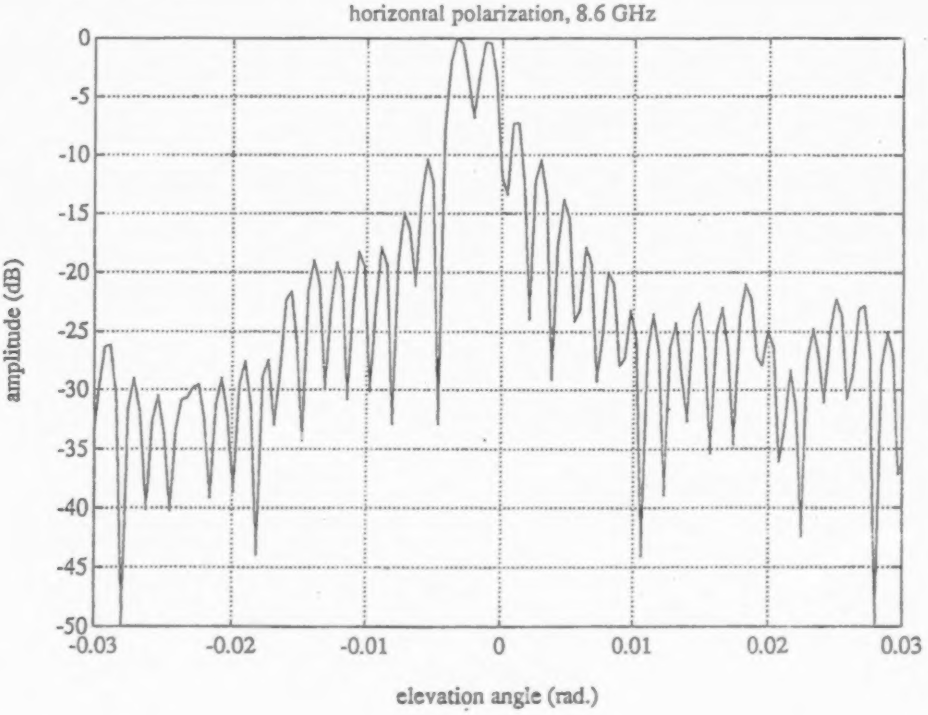
horizontal polarization, 8.6 GHz

Fig. E17 (d)

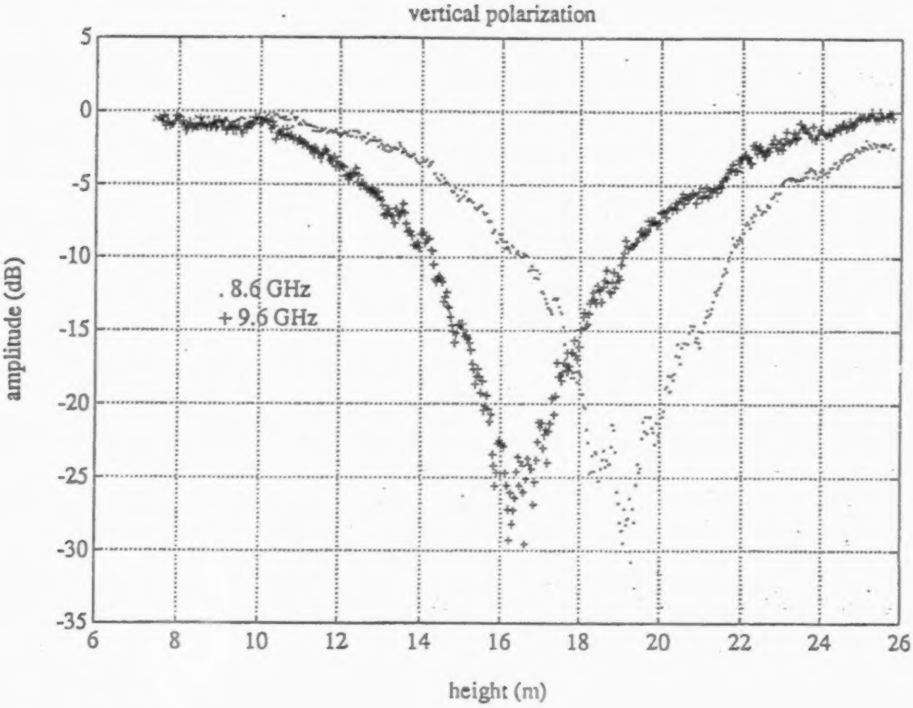

Fig. E17 (e)

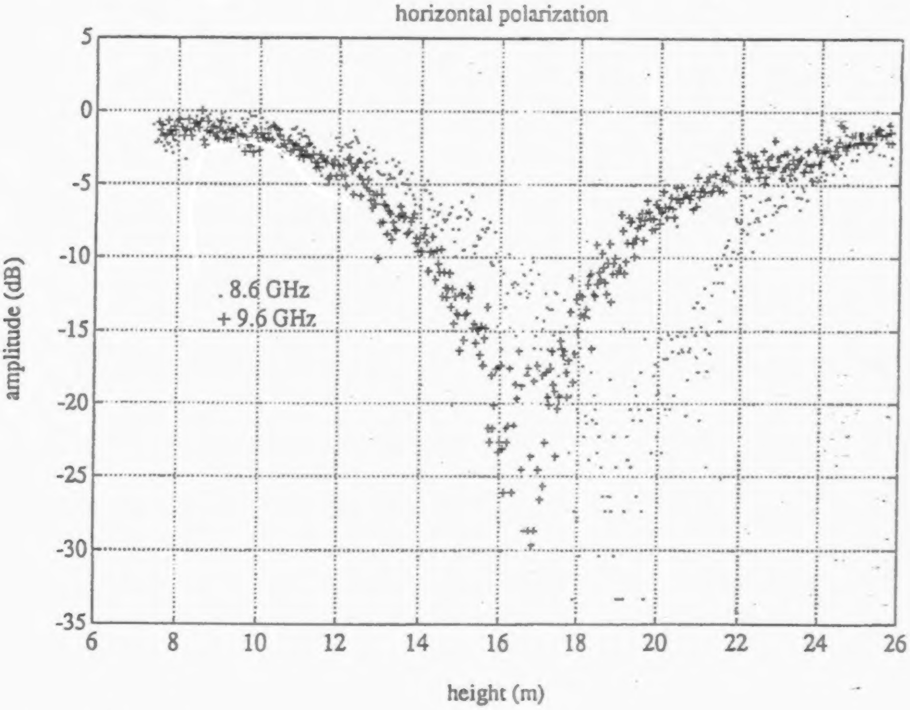

Fig. E17 (f)

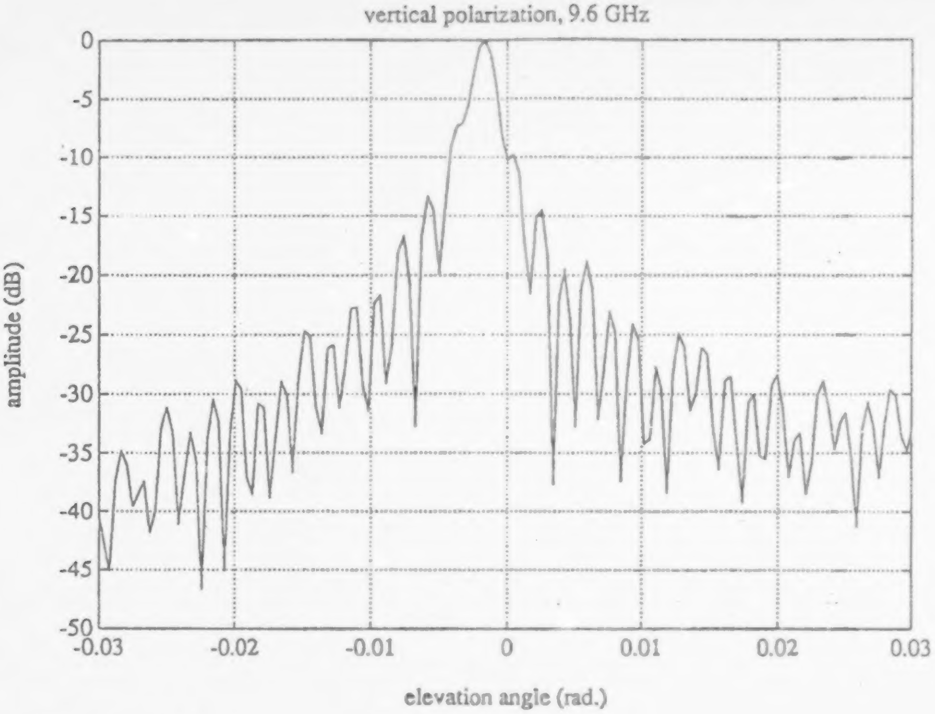

Fig. E18 (a)

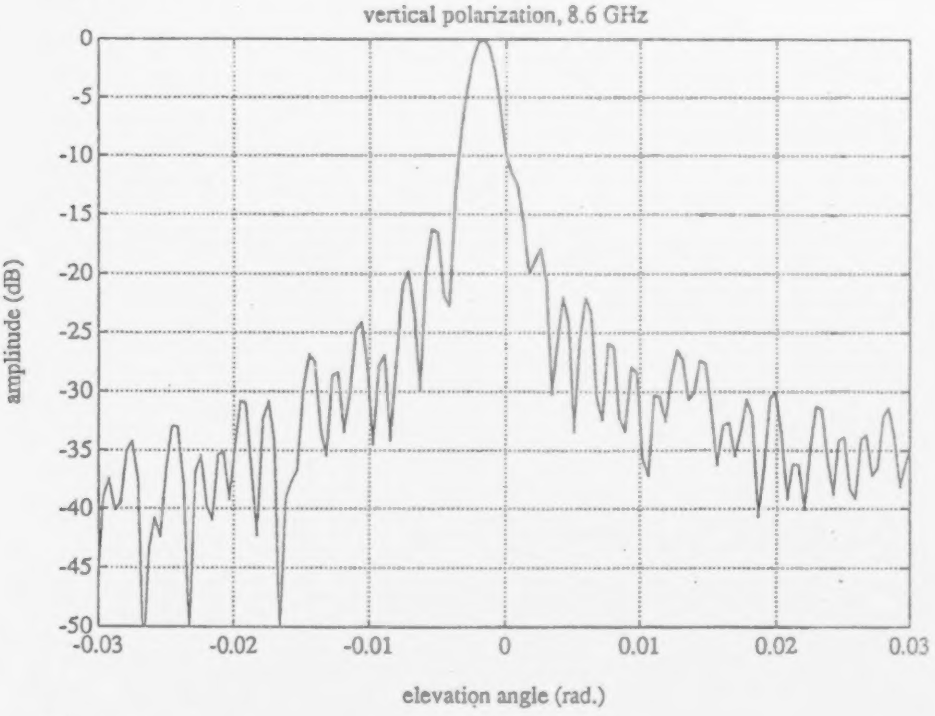

Fig. E18 (b)

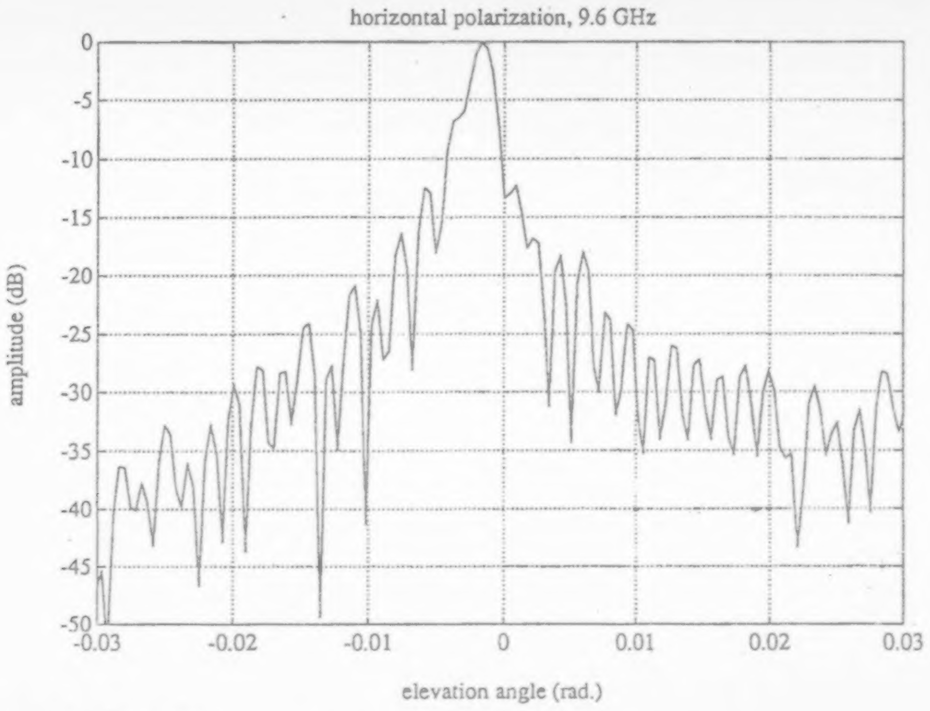

Fig. E18 (c)

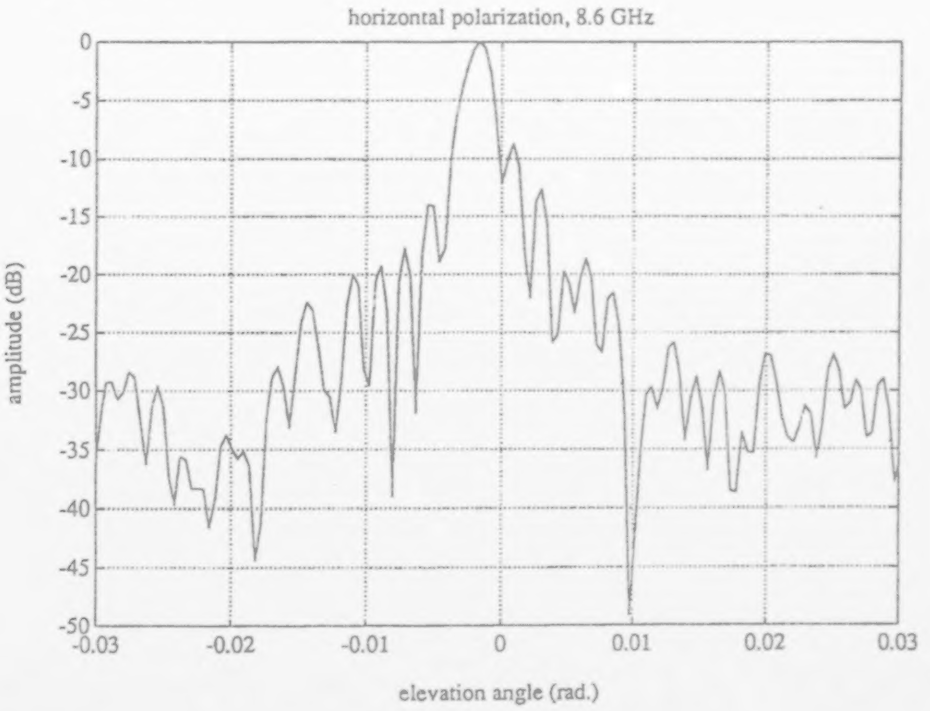

Fig. E18 (d)

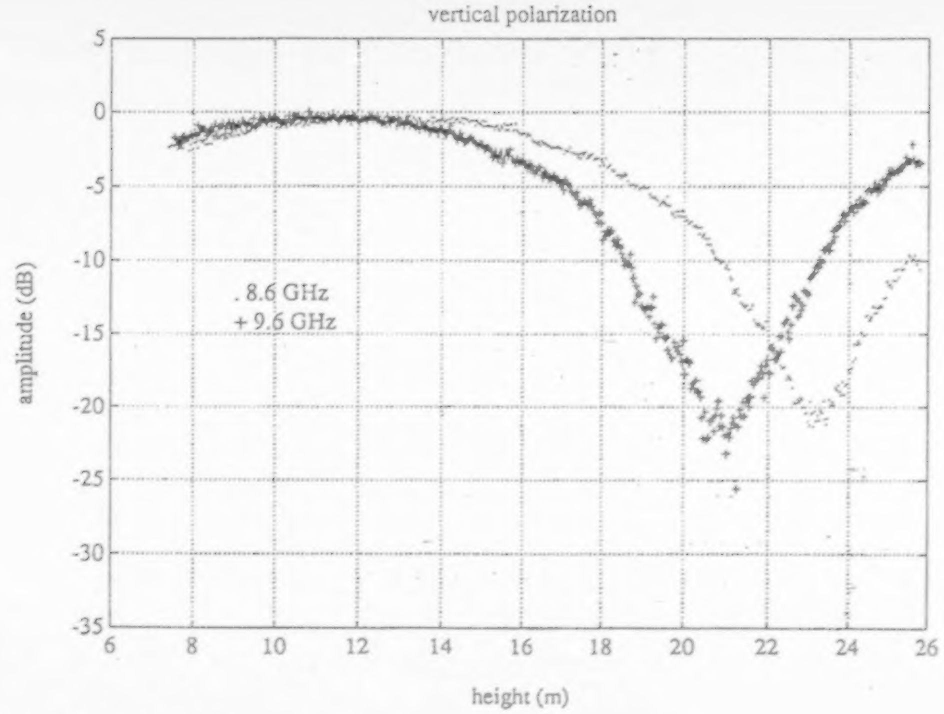

Fig. E18 (e)

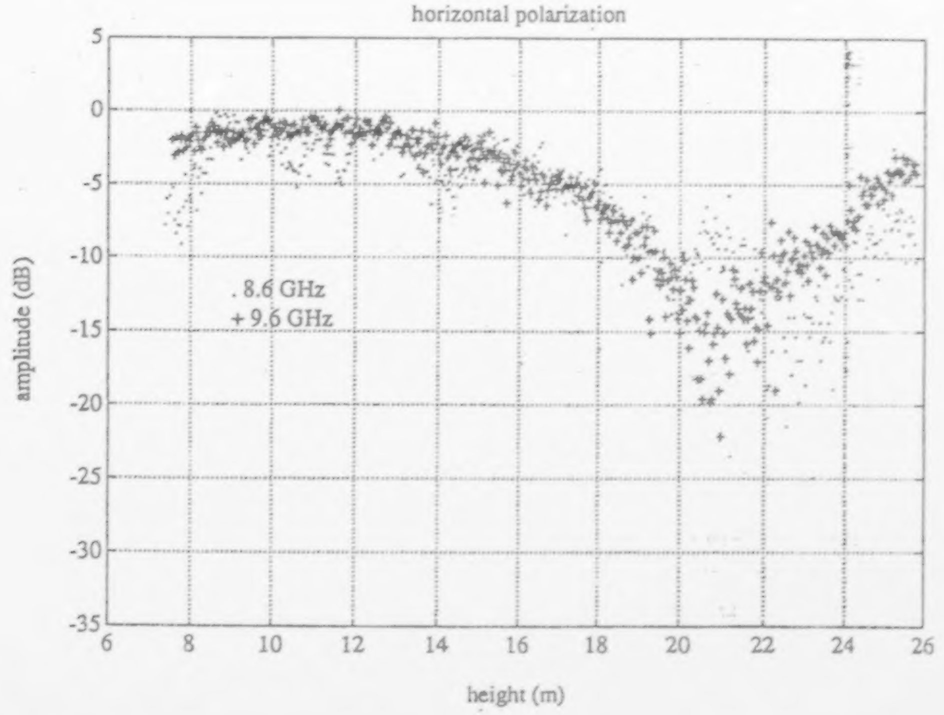

Fig. E18 (f)

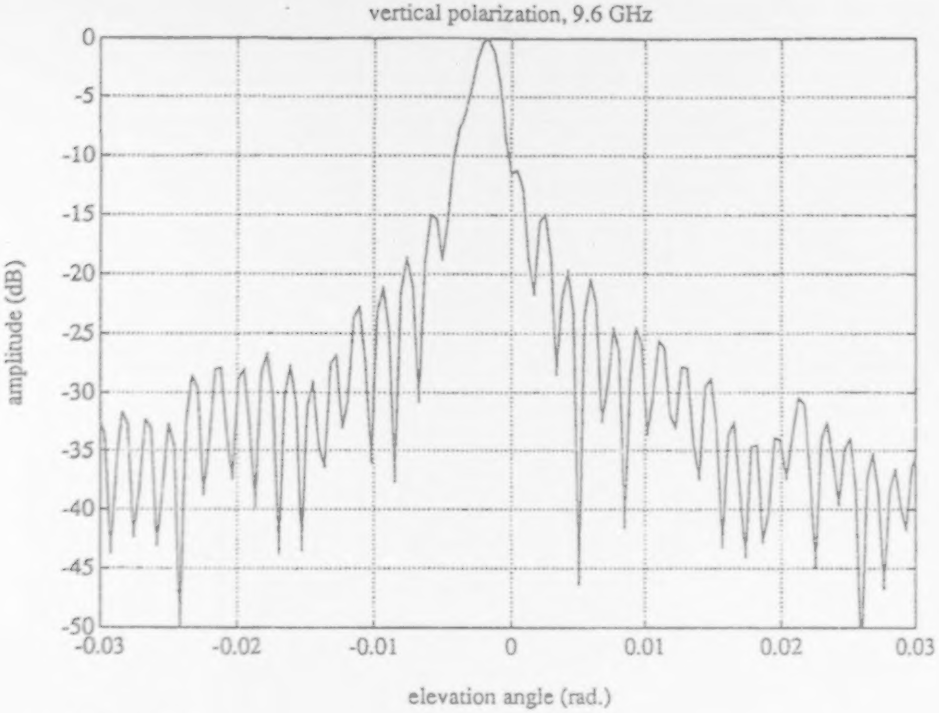

Fig. E19 (a)

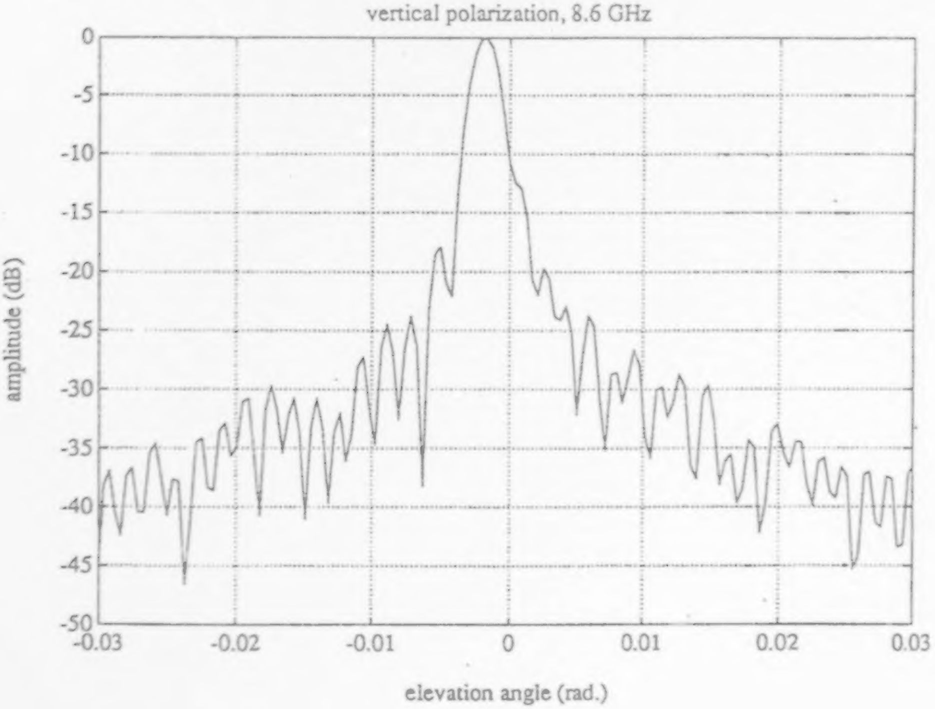

Fig. E19 (b)

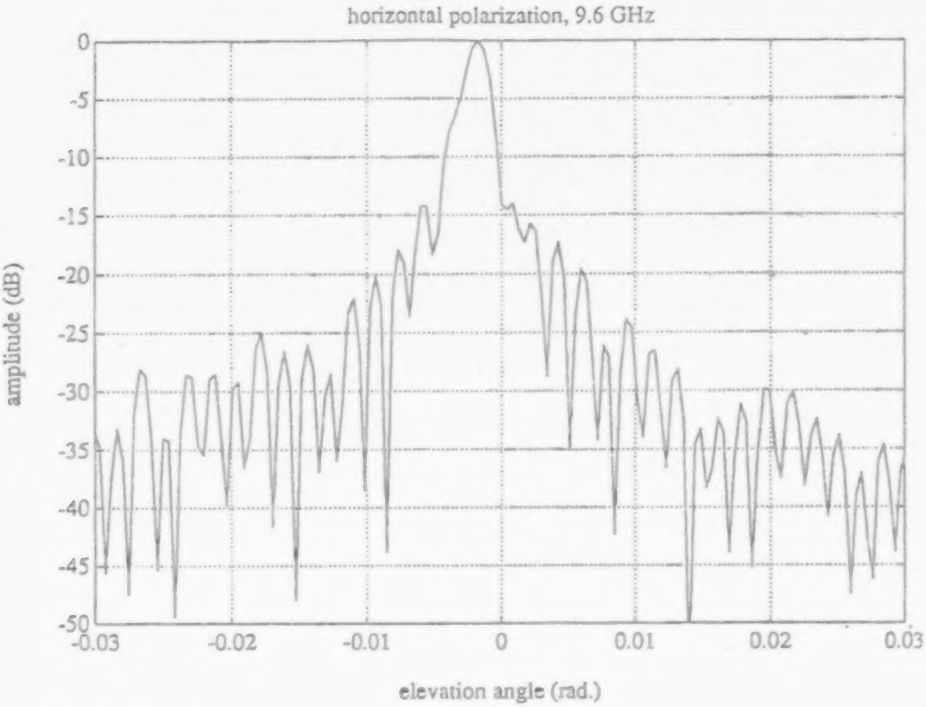

Fig. E19 (c)

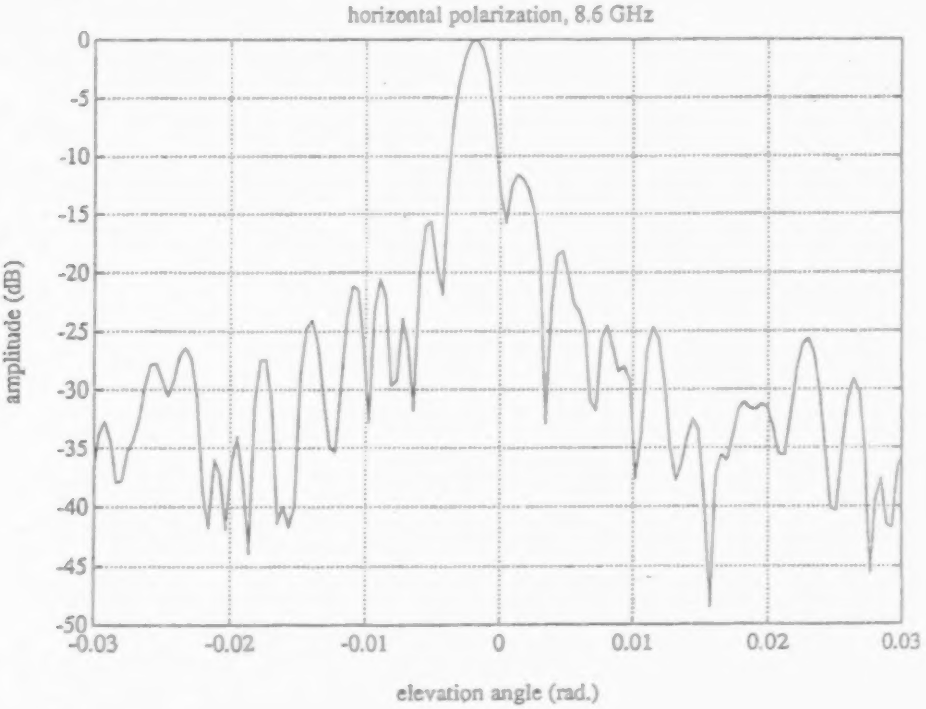

Fig. E19 (d)

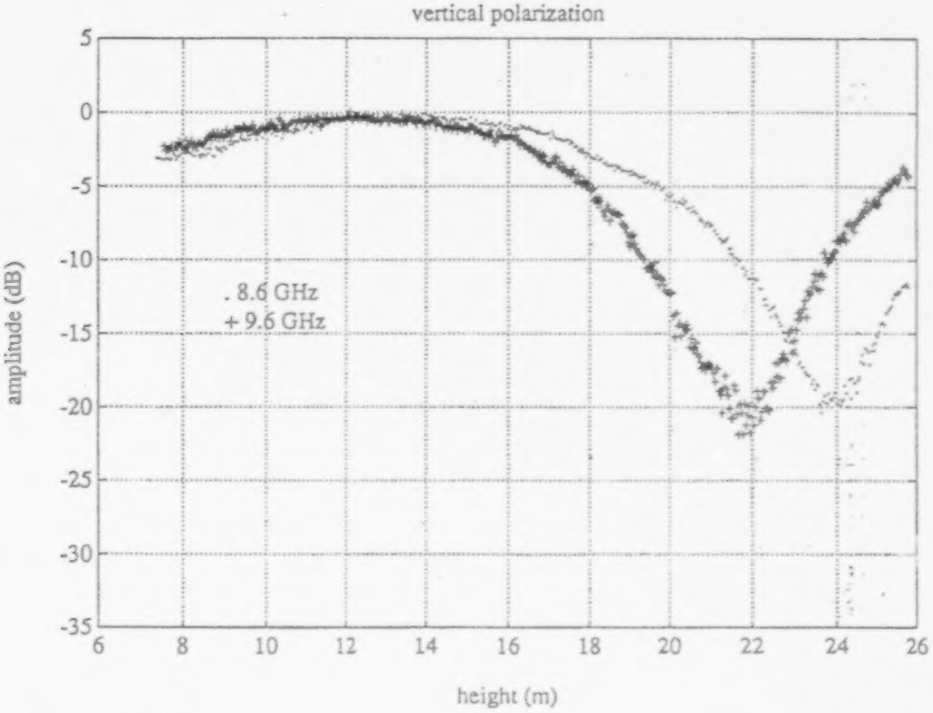

Fig. E19 (e)

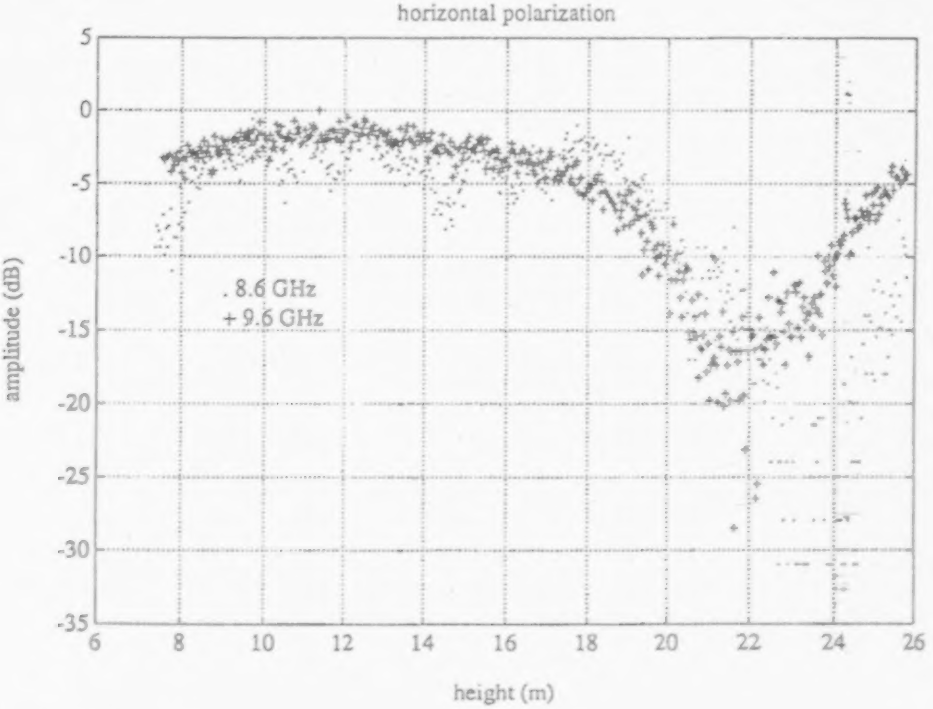

Fig. E19 (f)

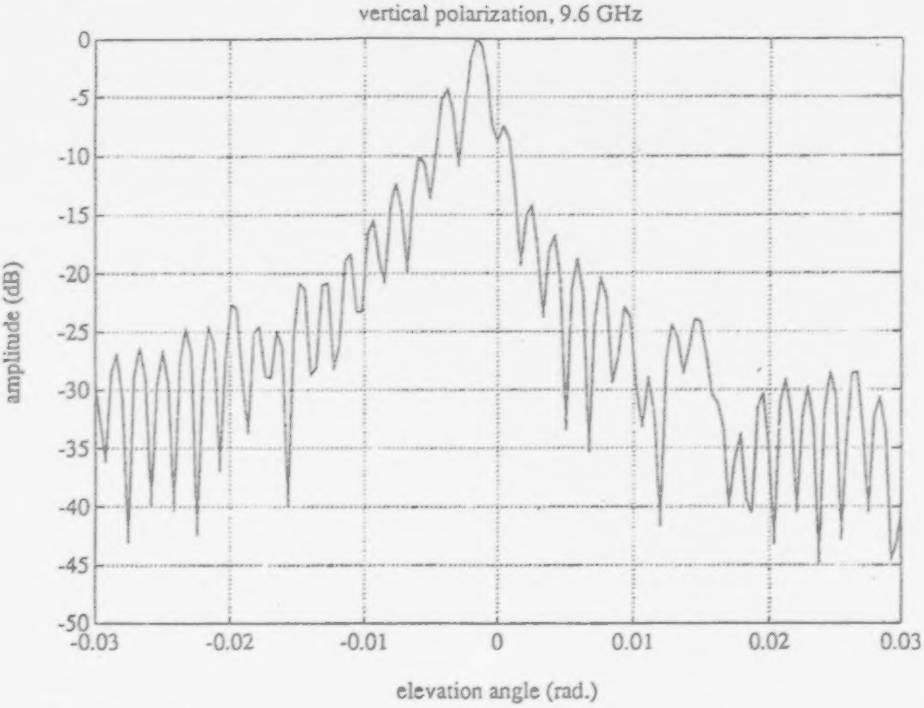

Fig. E20 (a)

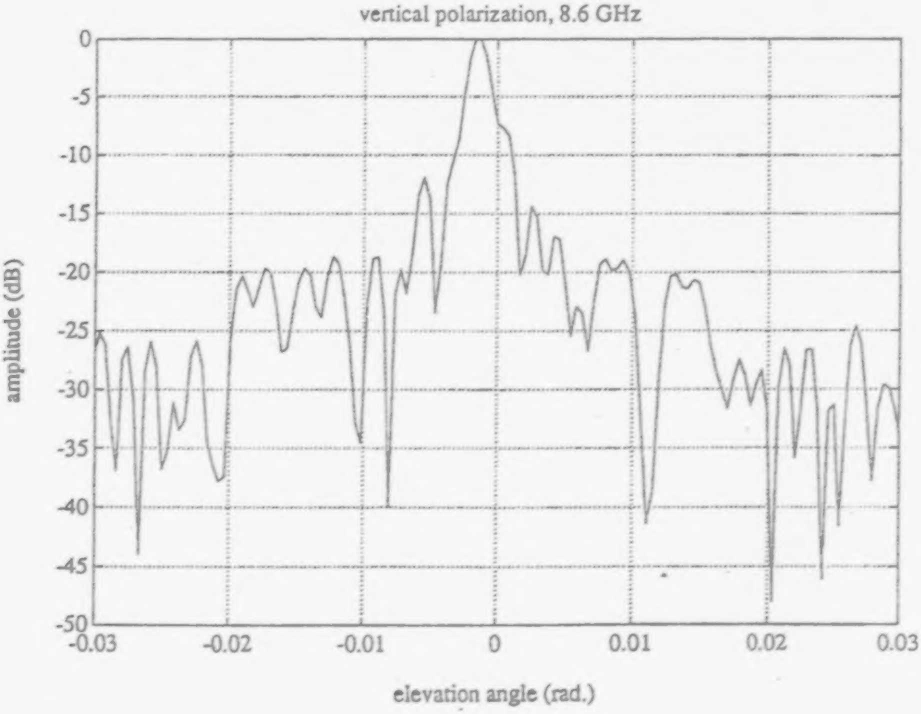

Fig. E20 (b)

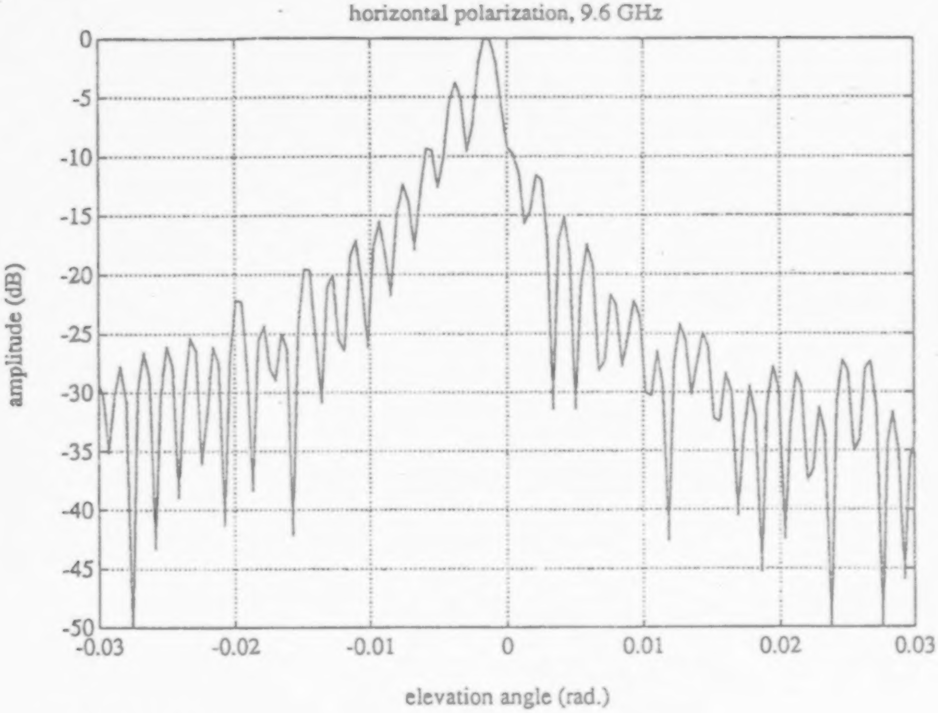

Fig. E20 (c)

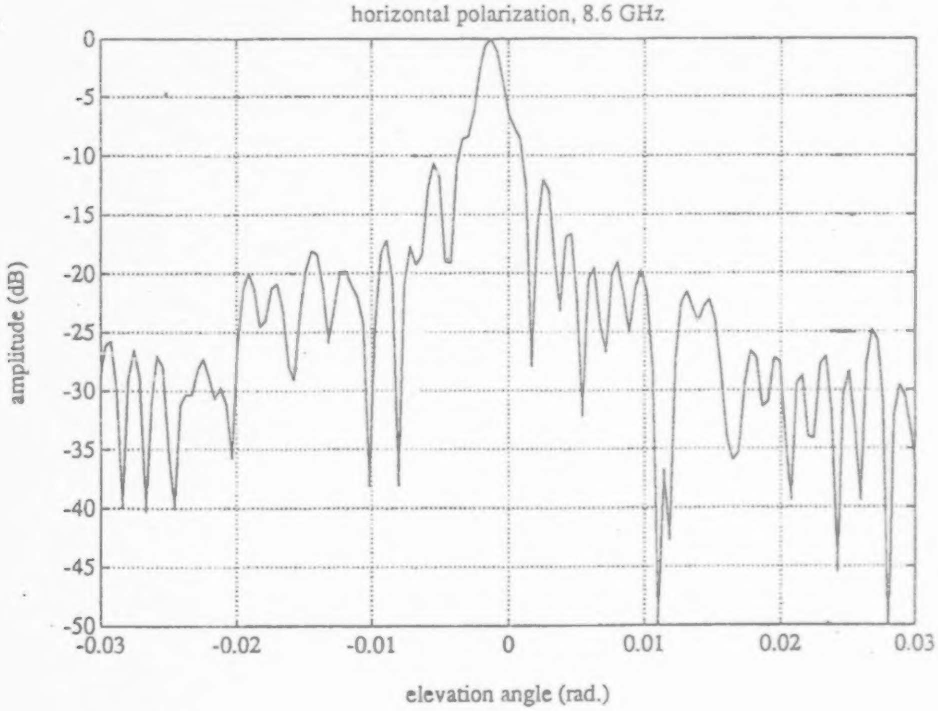

Fig. E20 (d)

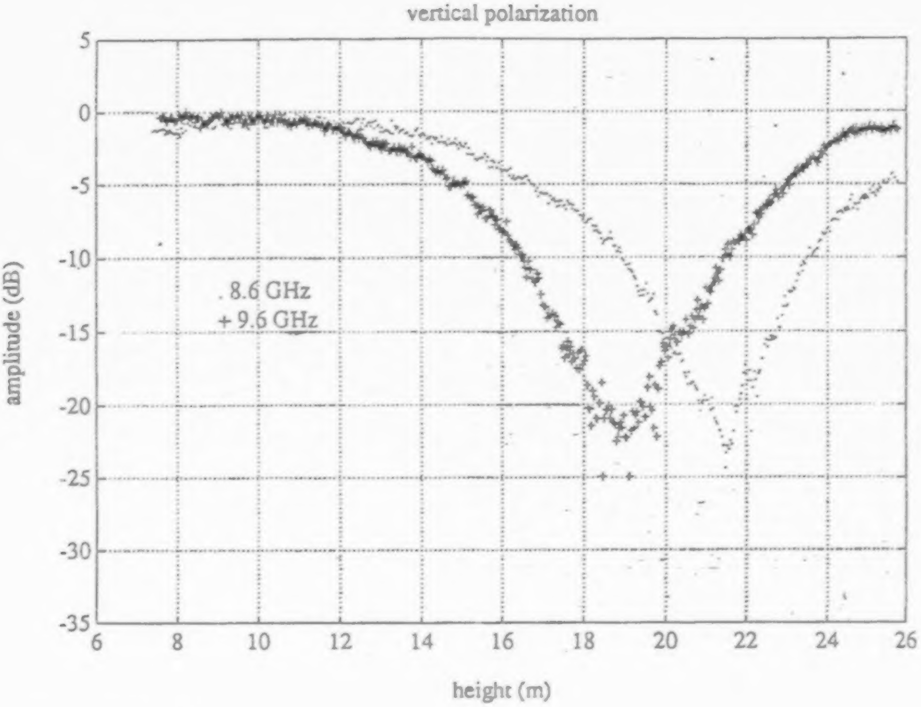

Fig. E20 (e)

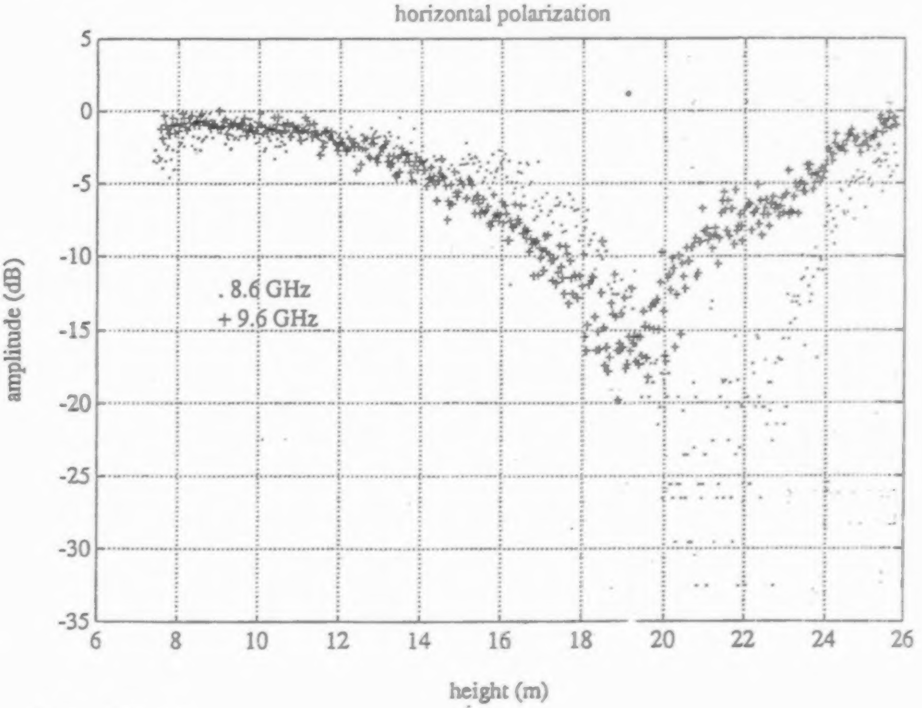

Fig. E20 (f)

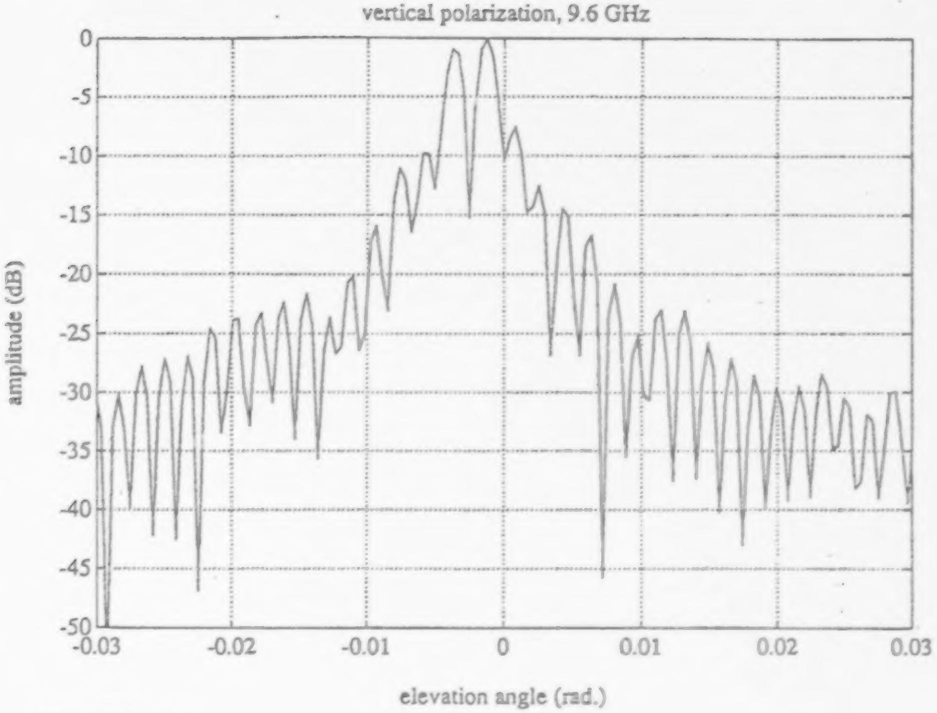

Fig. E21 (a)

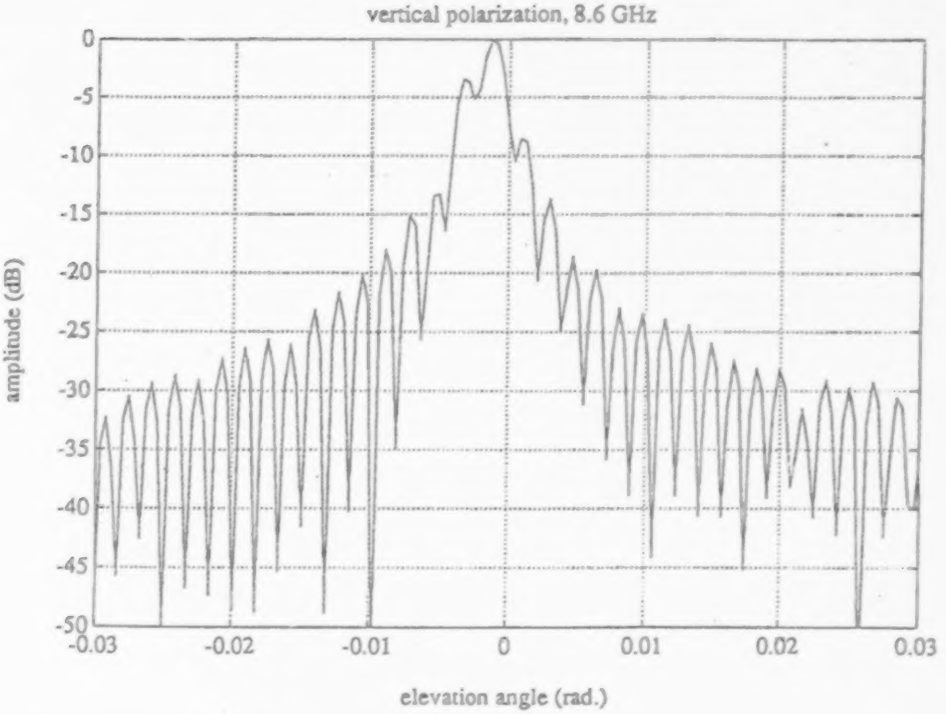

Fig. E21 (b)

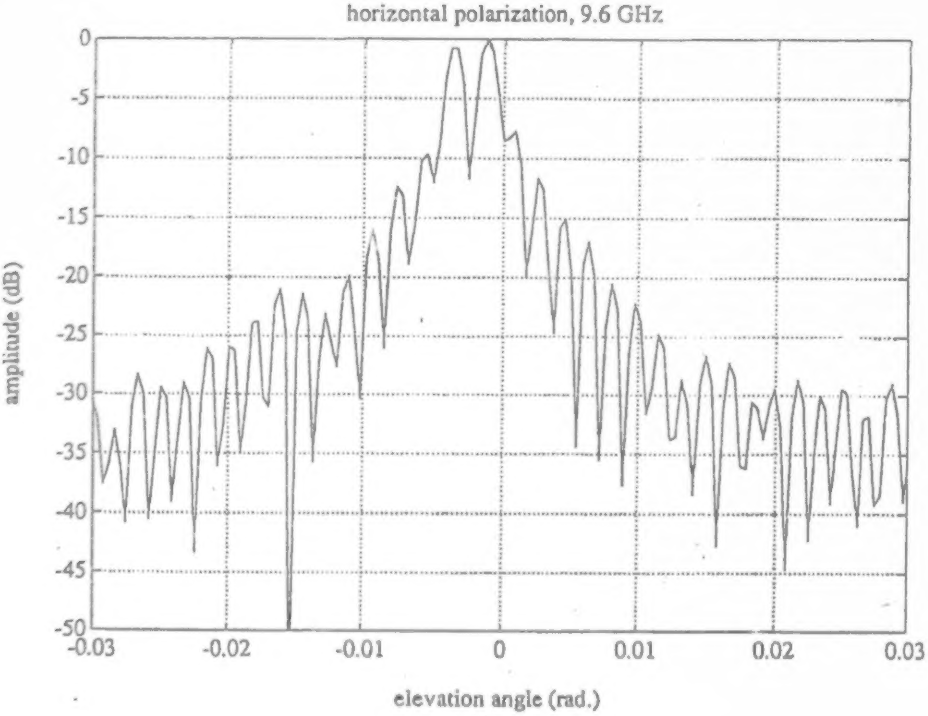

Fig. E21 (c)

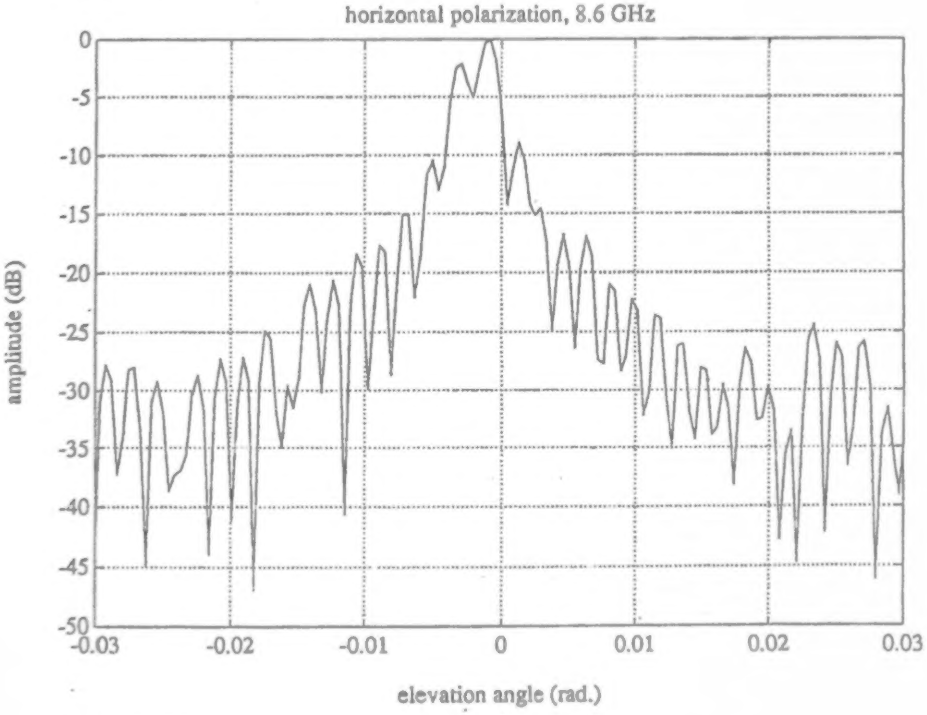

Fig. E21 (d)

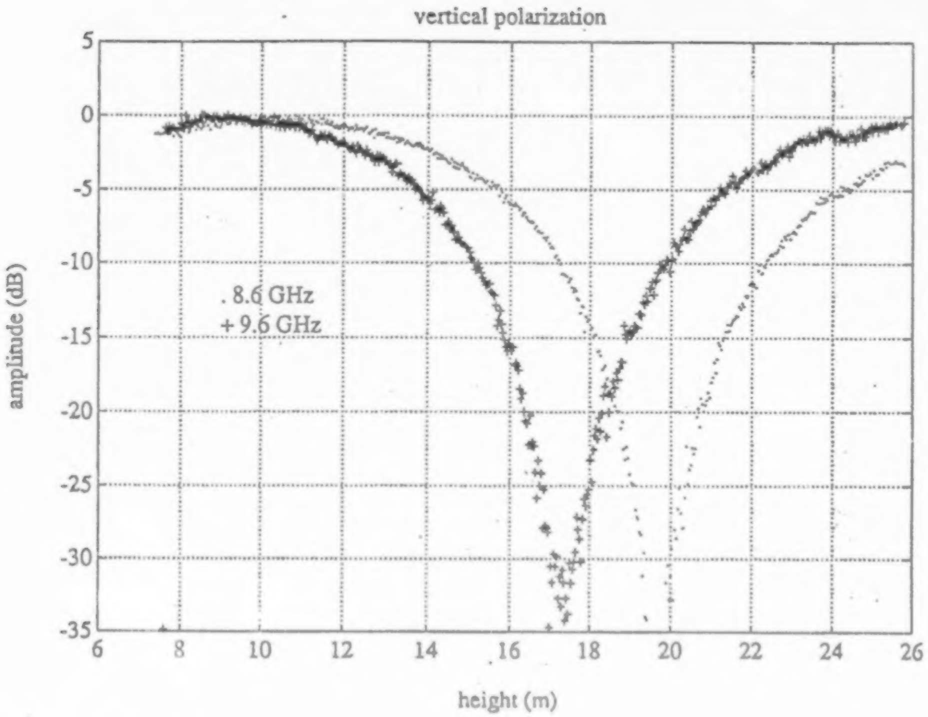

Fig. E21 (e)

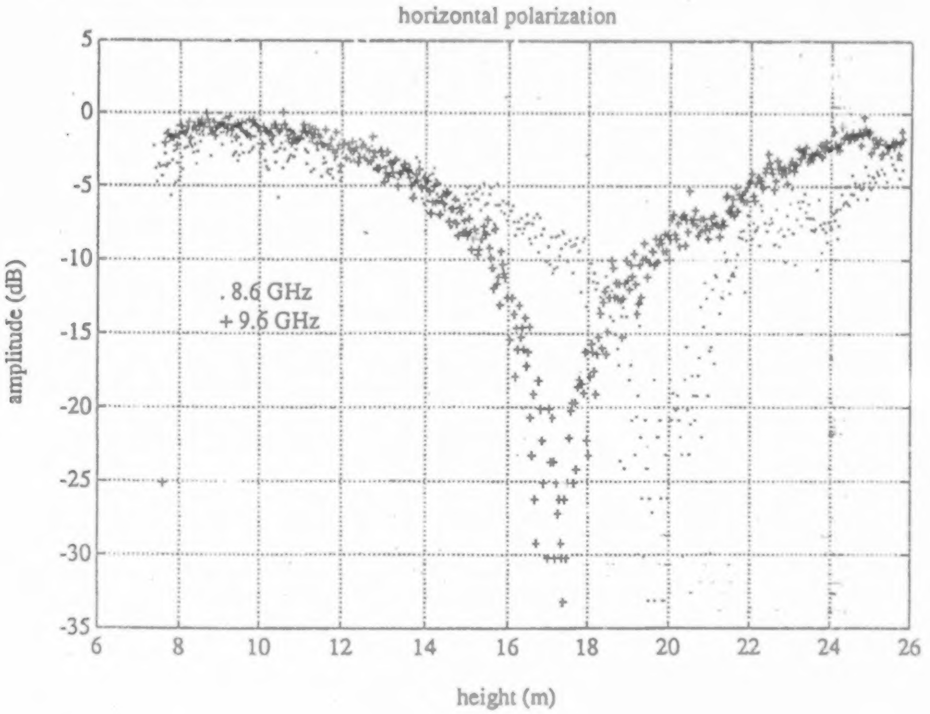

Fig. E21 (f)

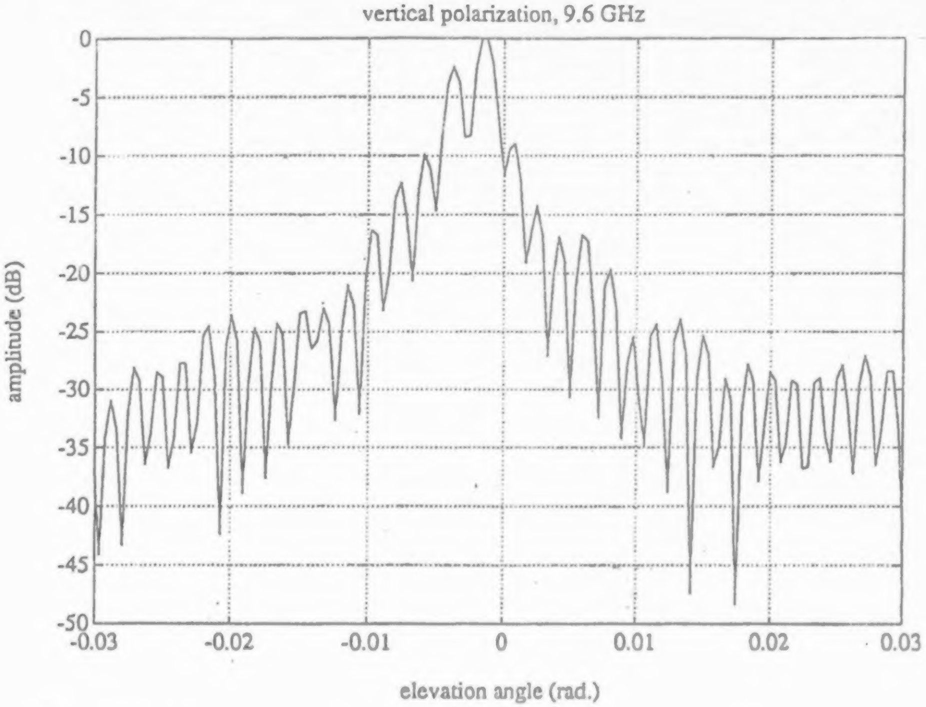

Fig. E22 (a)

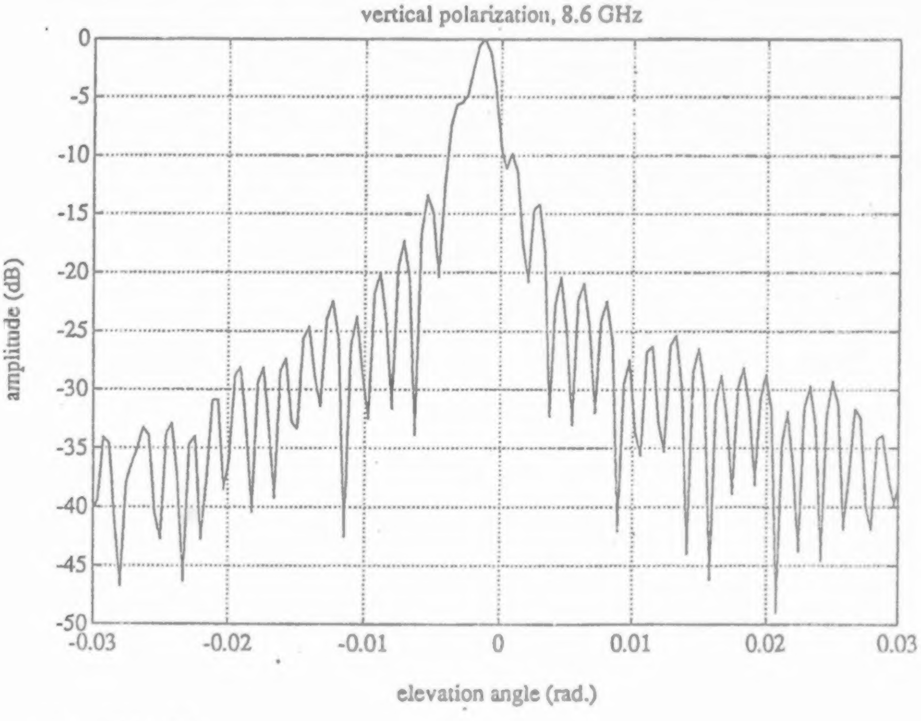

Fig. E22 (b)

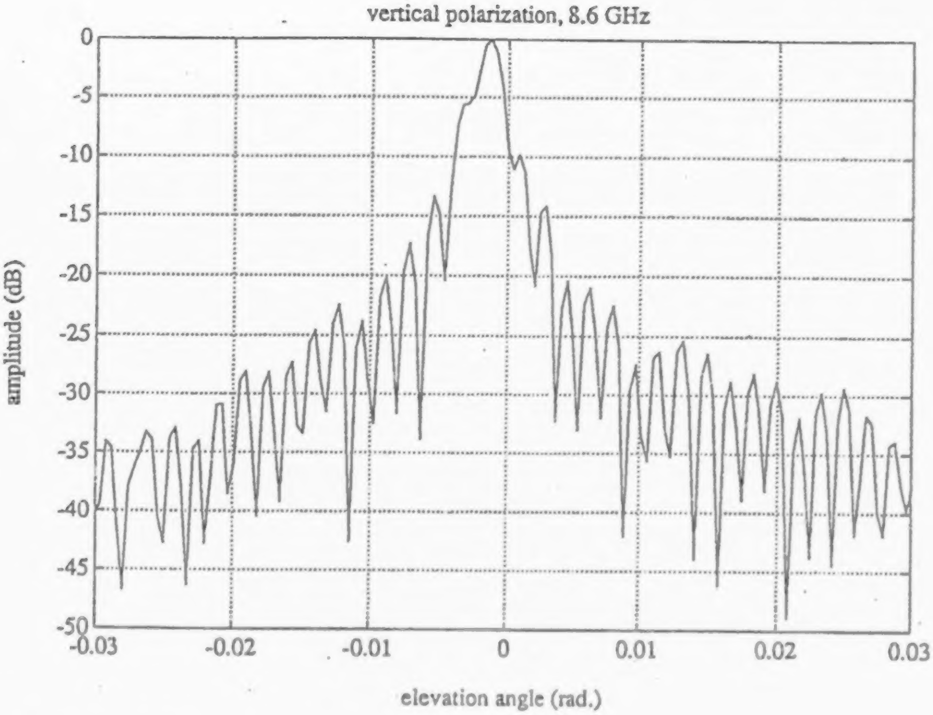

Fig. E22 (c)

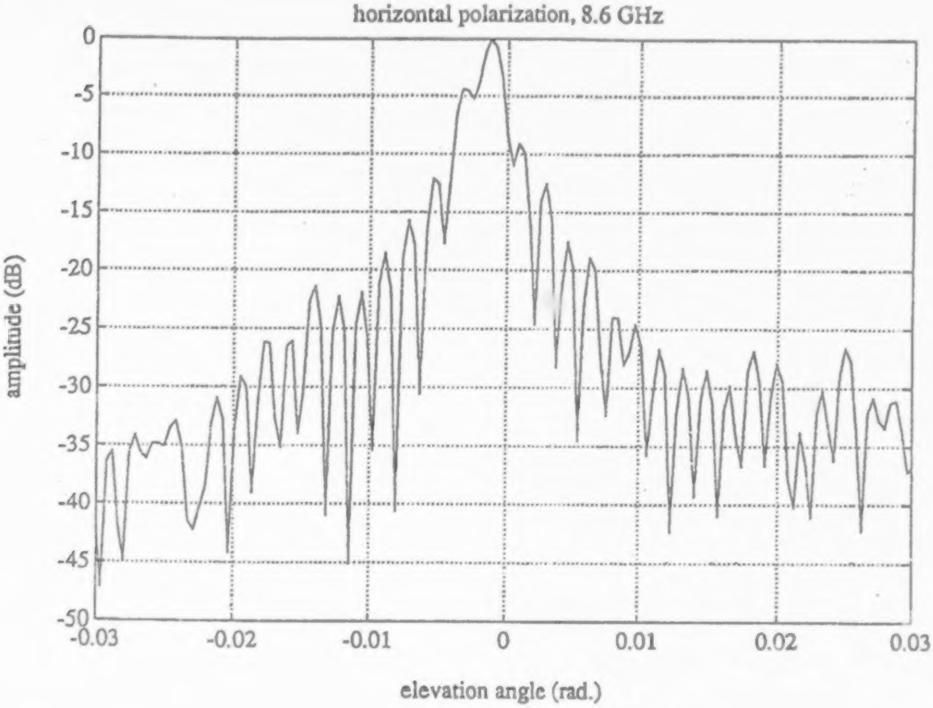

Fig. E22 (d)

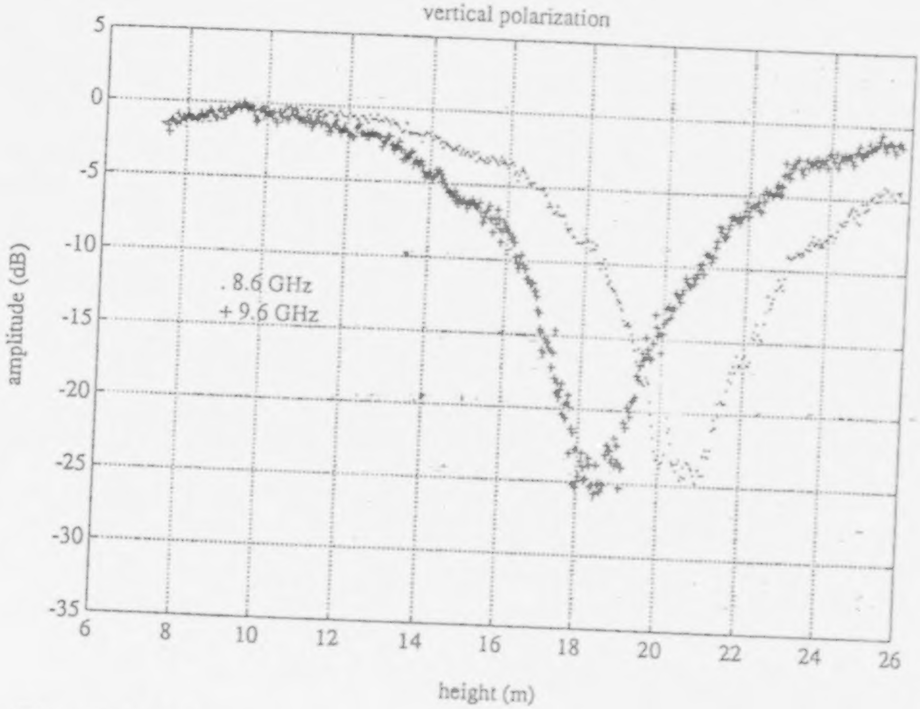

Fig. E22 (e)

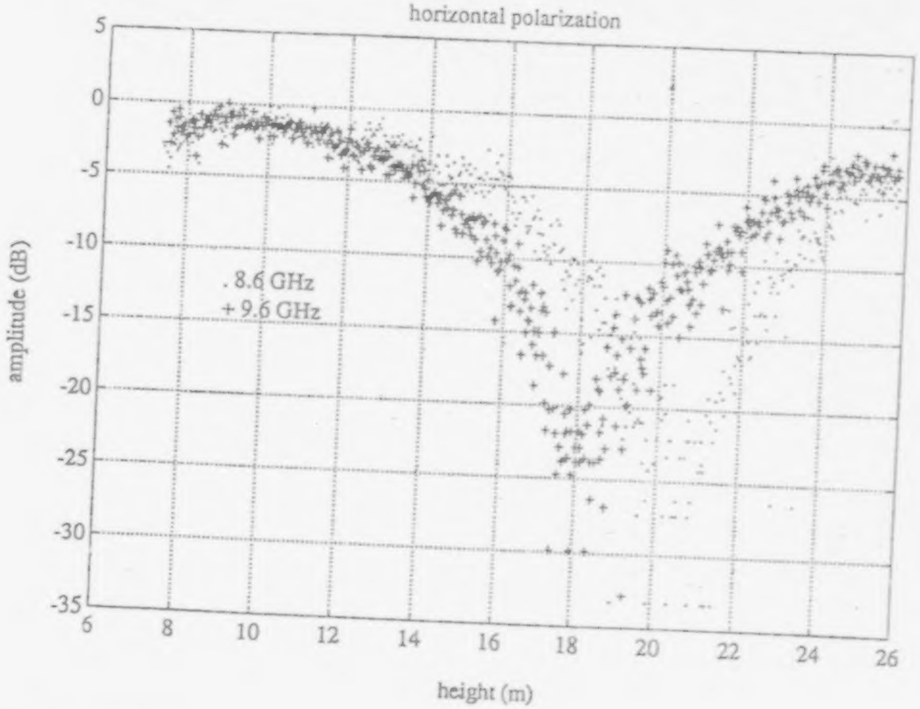

Fig. E22 (f)

UNCLASSIFIED
SECURITY CLASSIFICATION OF FORM
(Highest classification of Title, Abstract, Keywords)

DOCUMENT CONTROL DATA

(Security classification of title, body of abstract and indexing annotation must be entered when the overall document is classified)

1. **ORIGINATOR** (the name and address of the organization preparing the document. Organizations for whom the document was prepared, e.g. Establishment sponsoring a contractor's report, or tasking agency, are entered in section 8.)

McMaster University, 1280 Main Street West, Hamilton, Ont. L8S 4K1

2. **SECURITY CLASSIFICATION** (overall security classification of the document. Including special warning terms if applicable)

UNCLASSIFIED

3. **TITLE** (the complete document title as indicated on the title page. Its classification should be indicated by the appropriate abbreviation (S,C,R U) in parentheses after the title.)

Validation of Sea Swell Model, Analysis of Real Multipath Data, and Testing of the Cha Technique with Real and Simulated Data (U)

4. **AUTHORS** (Last name, first name, middle initial. If military, show rank, e.g. Doe, Maj. John E.)

T. Lo, L. Lai, J. Litva (Scientific Authority: Eloi Bossé)

5. **DATE OF PUBLICATION** (month and year of publication of document)

April 1990

6a. **NO. OF PAGES** (total containing information. Include Annexes, Appendices, etc.)

180

6b. **NO. OF REFS** (total cited in document)

25

7. **DESCRIPTIVE NOTES** (the category of the document, e.g. technical report, technical note or memorandum. If appropriate, enter the type of report, e.g. interim, progress, summary, annual or final. Give the inclusive dates when a specific reporting period is covered.)

Technical Report

8. **SPONSORING ACTIVITY** (the name of the department project office or laboratory sponsoring the research and development. Include the addre

Defence Research Establishment, Ottawa, 3701 Carling Ave, Ottawa, Ont. K1A 0Z4

9a. **PROJECT OR GRANT NO.** (if appropriate, the applicable research and development project or grant number under which the document was written. Please specify whether project or grant)

011LA

9b. **CONTRACT NO.** (if appropriate, the applicable number unde which the document was written)

052 SS.W7714-8-5674

10a. **ORIGINATOR'S DOCUMENT NUMBER** (the official document number by which the document is identified by the originating activity. This number must be unique to this document.)

94-612

10b. **OTHER DOCUMENT NOS.** (Any other numbers which may assigned this document either by the originator or by the sponsor)

11. **DOCUMENT AVAILABILITY** (any limitations on further dissemination of the document, other than those imposed by security classification)

(X) Unlimited distribution
( ) Distribution limited to defence departments and defence contractors; further distribution only as approved
( ) Distribution limited to defence departments and Canadian defence contractors; further distribution only as approved
( ) Distribution limited to government departments and agencies; further distribution only as approved
( ) Distribution limited to defence departments; further distribution only as approved
( ) Other (please specify):

12. **DOCUMENT ANNOUNCEMENT** (any limitation to the bibliographic announcement of this document. This will normally correspond to the Document Availability (11). However, where further distribution (beyond the audience specified in 11) is possible, a wider announcement audience may be selected.)

UNCLASSIFIED
SECURITY CLASSIFICATION OF FORM

13. **ABSTRACT** (a brief and factual summary of the document. It may also appear elsewhere in the body of the document itself. It is highly desirable that the abstract of classified documents be unclassified. Each paragraph of the abstract shall begin with an indication of the secu classification of the information in the paragraph (unless the document itself is unclassified) represented as (S), (C), (R), or (U). It is not necessary to include here abstracts in both official languages unless the text is bilingual).

Mathematical modelling and propagation data measurements of a continuous wave (CW) signal over a water path have been carried out to study the multipath phenomena and their effects on the performance of tracking radars operating against low flying objects and, eventually, to seek for solution to improve their presently unsatisfactory performance. The mathematical model, which is originated from sea swell modelling, is developed to study the mechanism of the forward scattering from rough sea surfaces or/and sea swells. It is based on the theory of representing a sea surface by a continuum of aperture antennas. Simulations were carried out and results were satisfactory. Two multipath measurements were conducted in the past two years. One was over Lake Huron in November, 1987 and the other over Lake Ontario in November, 1988.

14. **KEYWORDS, DESCRIPTORS or IDENTIFIERS** (technically meaningful terms or short phrases that characterize a document and could be helpf in cataloguing the document. They should be selected so that no security classification is required. Identifiers, such as equipment model designation, trade name, military project code name, geographic location may also be included. If possible keywords should be selected fro published thesaurus. e.g. Thesaurus of Engineering and Scientific Terms (TEST) and that thesaurus-identified. If it is not possible to select indexing terms which are Unclassified, the classification of each should be indicated as with the title.)

Multipath Modeling
Tracking Radars
Sea Swell
Scattering